Preparation of copper manganese oxide catalysts and their application for oxidation reactions.

Tomos J. Clarke

Submitted in fulfilment of the requirements for the degree of

PhD

September 2015

DECLARATION

This work has not been submitted in substance for any other degree or award at this or any other university or place of learning, nor is being submitted concurrently in candidature for any degree or other award.

Signed …………………………………… (candidate) Date …………………………

STATEMENT 1

This thesis is being submitted in partial fulfillment of the requirements for the degree of PhD

Signed …………………………………… (candidate) Date …………………………

STATEMENT 2

This thesis is the result of my own independent work/investigation, except where otherwise stated.

Other sources are acknowledged by explicit references. The views expressed are my own.

Signed …………………………………… (candidate) Date …………………………

STATEMENT 3

I hereby give consent for my thesis, if accepted, to be available online in the University's Open Access repository and for inter-library loan, and for the title and summary to be made available to outside organisations.

Signed …………………………………… (candidate) Date …………………………

Acknowledgments

There are so many people who over the years have helped me on my journey to writing this thesis. It would be impossible to list everyone but I am eternally grateful to all of you who have helped me along the way.

Firstly I have to thank my supervisor, Professor Stuart Taylor for the opportunity to study under his guidance, it has been a pleasure. A big thanks to all the postdocs in the group past and present, but especially Dr Dave Sellick, Dr James Hayward, Dr Simon Kondrat, and of course Dr Thomas Davies for their help and enthusiasm throughout the project.

Thank you to the technical staff down in the workshop, especially Steve and Alun. This project would not have been possible without their help.

Thanks to all the PhD students in the group, thanks for making the past 4 years fun and full of laughter. You guys make our office and labs a great place to work keep it going now I'm done. Keep the coffee flowing!

Thanks Morfydd, David and Gwesyn for welcoming me into your family so completely, you guys have been great throughout.

Thanks you to all my friends who have kept me sane over the course of all this. Robin, Chapple, Gypsy, Sam, Ben, Hannah, Sam, Helen, Baker and Rob, cheers guys.

A special thanks to my best friends Oli and Hannah, you guys are the best. I love you both dearly, thank you for all your love and encouragement through this PhD, it's meant everything to me.

To my whole family for their unending support, thank you. Mam and Dad you guys made this possible, this thesis only happened because you both encouraged (and tolerated) my curiosity. Thank you so so much. You too bro.

To my Grandmother, Jean, you are incredible. Thank you for your and Grandads love and support all these years. Grandad, I miss you. I'll keep the red flag flying for you.

None of this would have been possible without the love and support of my favourite Dormouse. You're the best, thank you for putting up with me throughout this.

This thesis is dedicated to my grandparents.

Peter and Jean Clarke

William and Winnie Murray

Abstract

The total oxidation of naphthalene using copper manganese oxide catalysts was investigated. A study on the effects of calcination temperature on the materials determined that the presence of a disordered $CuMn_2O_4$ phase gave superior naphthalene oxidation activity and selectivity towards CO_2 than a more crystalline material. The effects of doping catalysts with precious metals was also investigated for this reaction. Catalysts with various gold and silver loadings were prepared and tested. A lowering of the temperature of 50 % naphthalene conversion and CO_2 production was observed when doping with silver but no promotion was observed when using gold.

The preparation of copper manganese oxide catalysts by a mechanochemical route is reported. Investigation into the CO oxidation activity of samples prepared from oxide, acetate, and carbonate precursors was undertaken alongside investigations into the structure of the materials prepared. It was determined that use of carbonate precursors gave rise to the most active materials. The activity was attributed to migration of Cu^{2+} ions into the $MnCO_3$ lattice, which allowed facile formation of disordered $CuMn_2O_4$ upon calcination.

The effects of precipitating copper manganese oxide catalysts from various alcohol solvents was studied. The solvents investigated were linear alcohols with chain lengths from C2 to C5. It was found that the mixing of the aqueous base and alcoholic nitrate solutions had an effect on the oxidation state of both the precursor and calcined catalyst, which in turn affected the catalytic activity.

A study on the effects of washing the catalyst precursors with water and chelating agent solutions is also reported. It was found that washing with water was efficient at removing sodium from the material but that after a point, manganese was also removed, with an

adverse effect on activity. Washing with chelating agents was able to remove more Na$^+$ than washing with water with positive effects on activity.

Publication List

Total oxidation of naphthalene using copper manganese oxide catalysts

Catalysis Today. 2015

Tomos J. Clarke, Simon A. Kondrat, and Stuart Hamilton Taylor.

Mechanochemical synthesis of copper manganese oxide for the ambient temperature oxidation of carbon monoxide.

Applied Catalysis B: Environmental. Vol 164, page 222-231, 2015

Tomos J Clarke, Thomas Davies, Simon A. Kondrat, and Stuart Hamilton Taylor.

Abbreviation List

Abbreviation	Meaning
MP-AES	microwave plasma atomic emission spectroscopy
XPS	X-ray photoelectron spectroscopy
XRD	X-ray diffraction
SEM	Scanning electron microscopy
EDX	Energy dispersive X-ray analysis
TEM	Transmission electron microscopy
TGA	Thermal gravimetric analysis
TPR	Temperature programmed reduction
MvK	Mars van Krevelen
VOC	Volatile organic compound
PAH	Polycyclic aromatic hydrocarbon
ppm	Parts per million

Contents

Chapter 1

Introduction

1.1 Thesis Aims

The aim of this thesis is to investigate the activity of copper manganese oxide for the oxidation of naphthalene. Investigation into this area included a study on the effects of calcination temperature on catalytic activity and the effect of precious metal doping. Catalysts will be evaluated based on their ability to catalytically combust naphthalene in the gas phase.

Alongside this work to investigate the effect of preparation method on the activity of copper manganese oxide catalysts for CO oxidation was undertaken. This involved preparation of catalysts by dry mechanochemical methods and investigation of these materials. Another area of catalyst preparation that was investigated was the precipitation of coper manganese oxide from non-aqueous solvents, an area that was previously unstudied.

Finally the washing step of the precipitation process was studied in depth. The effect of washing volume was investigated alongside the effect of washing with additives with the aim of facilitating the removal of sodium. Work in this chapter will focus on monitoring the levels of sodium present in the catalyst using microwave plasma atomic emission spectroscopy (MP-AES) and X-ray photoelectron spectroscopy (XPS).

A wide range of characterisation techniques have been used to monitor changes in the catalyst structure and properties in all aspects of the work. Focus will be on the changing phases present in the materials monitored by XRD along with the surface area of the catalysts and how these two factors affect catalyst activity.

This chapter serves as an introduction to the research that has been undertaken in this area previously. All experimental details are located in Chapter 2.

1.2 Hopcalite

Hopcalite is the most commonly used CO oxidation catalyst in use currently. Carbon monoxide, a colourless odourless poisonous gas, requires treatment in a wide range of applications including, but not limited to, Firefighting, Mining[1], Diving and CO_2 lasers[2].

Gas masks are a common application for copper manganese oxide catalysts in both military and civilian applications.

1.2.1 Development of Hopcalite

During the First World War, with the advent of chemical warfare, there was much investigation into methods to protect soldiers from gaseous weaponry. One agent that was feared to be used as a chemical agent was carbon monoxide.

During the course of the war J W C Frazer and co-workers investigated the activity of copper oxide and manganese oxide mixtures for CO oxidation[3]. Previous studies on the oxidation of CO had focussed on the use of palladium and silver. These were deemed to be to costly however and focus was shifted towards base metal catalysts. The catalyst mixture developed was known as hopcalite, the work was largely a collaboration between groups from both John Hopkins University and The University of California – hence the name.

The original hopcalite catalyst consisted of a mixture of 50 % MnO_2, 30 % CuO, 15% Co_2O_3 and 5% Ag_2O. This catalyst was prepared by the separate precipitation followed by intimate mixing of the Mn, Cu and Co oxides. This was followed by the precipitation of the silver species onto the mixture. This catalyst was widely used in gas masks [4, 5].

A second formulation, Hopcalite 2, was developed shortly after and consisted of 60% MnO_2 and 40% CuO. This material was synthesised by the thermal decomposition of copper carbonate precipitated onto the MnO_2. Hopcalite 2 was found to be highly active for CO oxidation, along with the preferential oxidation of CO over H_2[6]. It was noted at this time

that water deactivated the catalyst[3, 6] and this was closely studied [7]. The addition of a desiccant to remove water from the gas stream was found to increase the lifetimes of hopcalite catalysts significantly[8].

1.2.2 Structure of Hopcalite

The mixed metal oxide $CuMn_2O_4$ phase is widely accepted to be the active structure of the Hopcalite catalyst. Its structure was determined by XRD by Sinha *et al.* to be an analogue of the cubic spinel[9]. This was unexpected as it was expected that $CuMn_2O_4$ would have a pseudo spinel structure analogous structure to $CuFe_2O_4$ [9]. Further neutron diffraction by Radhakrishnan *et al.* confirmed the spinel structure[10]. The spinel structure is named for the semi-precious gem of the same name ($MgAl_2O_4$), other spinels include the precious gems sapphire and aquamarine. The general formula for spinels is A B_2O_4. The overall structure is cubic, the A ion sits in the tetrahedral sites and the B ions in the octahedral sites. The charges of the ions within the structure may be +2 +3 for A and B respectively or +4 +2[11]. Figure 1 is Sickfaus *et al.*'s representation of the spinel structure[12] where the tetrahedral and octahedral primitive unit cells can be clearly seen within the overall cubic unit cell.
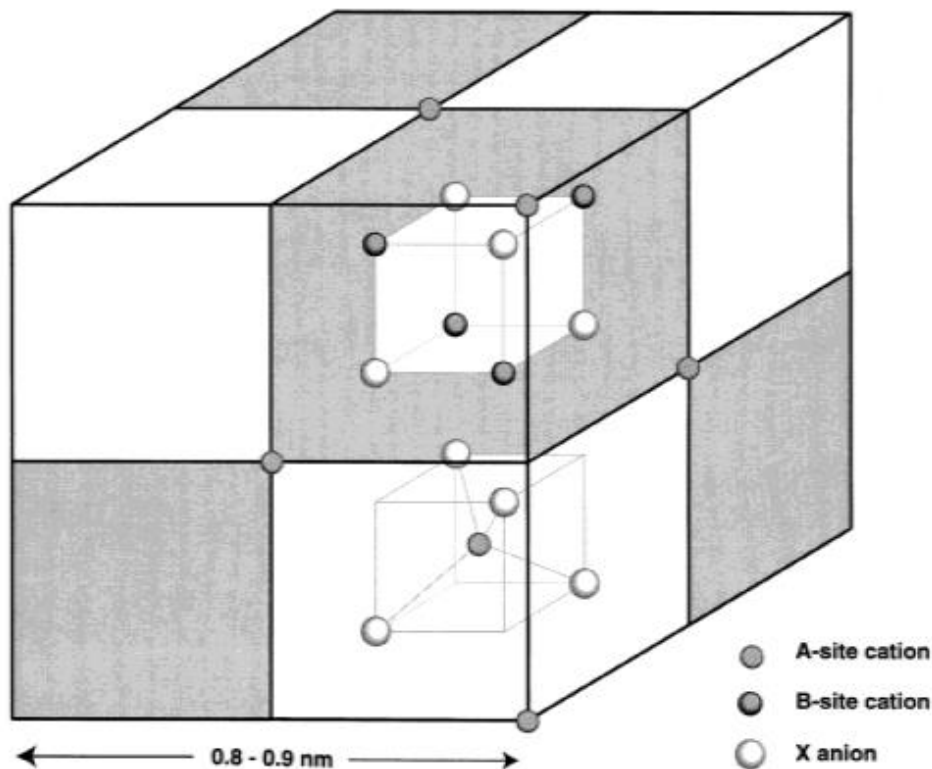
Figure 1: Structure of spinel type materials. The cation and anion locations for the primitive tetrahedral and octahedral unit cells are shown within the framework of the cubic structure. Figure adapted from Sickfaus et al.[12]

In the case of $CuMn_2O_4$ it was found that Manganese predominately was found to inhabit the octahedral sites of the structure with coper sitting in the tetrahedral sites. The structure is complicated by the inversion of part of the spinel. Verwey, in his 1947 paper in the Journal of Chemical Physics, states that inverse spinels are those where the A cation sits in the octahedral position and half the B cations sit in the A tetrahedral position[11]. Biswas *et al.* found that 25% of the hopcalite structure was inversed [10]. Further neutron studies by the same group determined that rather than satisfying the A 2+ and B 3+ criteria for spinel materials laid out by Verwey [11], the structure consisted of $(Cu_{0.5}^{2+}Cu_{0.25}^{1+}Mn_{0.25}^{3+})$ $(Cu_{0.25}^{2+}Mn_{1.5}^{3+}Mn_{0.25}^{4+})O_4$. In their proposed structure copper exists in multiple oxidation states in multiple co-ordination environments as do the manganese ions[13].

The structure is complicated further by Jahn Teller effects as both Cu2+ and Mn3+ are affected by the Jahn teller distortion. Shoemaker *et al.* demonstrated using PDF and XPS that a disproportionation reaction can occur between two tetrahedral Cu^{2+} ions to form Cu^{1+} and Cu^{3+} to minimise the number of Jahn-Teller active species in the tetrahedral sites[14]. The authors note the novelty of this as Cu3+ is rarely observed outside of copper oxides containing highly electropositive cations[15].

A dissenting study by Vandenberghe *et al.* studied the thermal properties of CuO $MnCO_3$ mixtures and their properties after sintering to form mixed metal oxides of varying Cu: Mn ratio[16]. They determined that that unlike the findings of Sinha *et al.* [9] the $CuMn_2O_4$ phase was not present and that instead a mixture of $Cu_{1.5}Mn_{1.5}O_4$ and Mn_2O_3 was present. Indeed they suggest that the cubic $CuMn_2O_4$ phase cannot be formed due to the destabilisation of the structure by Mn^{3+} clustering.

It is clear from the many studies regarding the true structure of $CuMn_2O_4$ that it is a complex system with many possible permutations that can be modified by preparation techniques and doping.

1.2.3 Active sites and reaction mechanism

Sinha *et al.* identified the presence of an electron transfer mechanism within the spinel structure that was initially identified to resolve the observed cubic symmetry versus the predicted tetragonal one[9]. Their proposed pathway is shown in Figure 2.

$$CuO + Mn2O \rightarrow Mn^{3+}[Cu^{1+}Mn^{3+}]O_4^{2-} \rightarrow Mn^{4+}[Cu^{1+}Mn^{3+}]O_4^{2-} \rightarrow Cu^{1+}[Mn^{3+}Mn^{4+}]O_4^{2-}$$
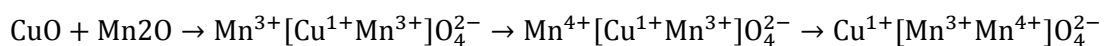
Figure 2: Electron transfer reaction proposed by Sinha et al[9]. Metal ions in [] are in the octahedral sites and those outside are in the tetrahedral sites.

This electron transfer was proposed to proceed via charge transfer through the adjacent p-orbital of the oxygen ions in the lattice as demonstrated by Zwolinski[17]. They suggested an irreversible and instantaneous e- transfer from Mn^{3+} to O^{2-} to Cu^{2+}. This is followed by the

relatively slow transfer of Cu1+ into the tetrahedral site of the structure in adherence with the Franck –Condon principle.

This redox process illustrates the ease at which this system can undergo redox changes. This redox change was identified by Kanungo as a key driver for the catalytic activity of the copper manganese materials[18, 19]. The ability to shuttle electrons between copper and manganese ions allowed the facile re-oxidation of the catalyst.

$$Cu^{2+} + Mn^{3+} \leftrightarrow Cu^{1+} + Mn^{4+}$$
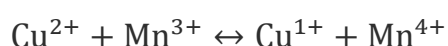
Figure 3: Redox couple proposed by Kanungo[20]

When the oxidation of CO is considered on the surface of $CuMn_2O_4$ this redox couple explains the observed activity. When the equilibrium is to the right CO adsorbs to Cu^{2+} while O_2 adsorbs to Mn^{3+}. This CO is oxidised to form $CO^+_{(ads)\ along}$ with Cu^+. Reduction of the adsorbed oxygen by the copper species results in Mn^{4+} and $O^-_{(ads)}$, this reduced O^- can then react with the $CO^+_{(ads)}$ to form CO_2. When the equilibrium is to the left the opposite reaction occurs with O_2 oxidising the Cu^+ and CO reducing the Mn^{4+} [19].   Direct evidence of this was given by Veprek *et al*. when they studied the XPS of the system in detail[21]. This was suggested to require the presence of an amorphous spinel phase by Puckhaber *et al*. as the Cu:Mn ratio on the surface changed considerably after the amorphous to crystalline phase transition [22].

A second explanation for the activity is that the reaction proceeds via a Mars van Krevelen mechanism (MvK). The MvK mechanism was proposed by Mars and van Krevelen to explain the observed reactivity of vanadium oxides[23]. It involved the direct oxidation of an adsorbed species by lattice oxygen. This leaves the catalyst in a reduced state and is the re oxidised by oxygen from the gas stream.

Buicman suggests that the activity of copper manganese oxide catalysts is due to a spillover type mechanism. By studying $CuMn_2O_4$, CuO, Mn_2O_3 and a mechanical mixture of the two single oxides they came to the conclusion that there was an alternative to the 'amorphous

spinel' model of activity. They assert that oxygen spillover occurs from Mn_2O_3 to CuO where it reacts with adsorbed CO. In their model they attribute deactivation of the catalyst to a solid state reaction between CuO and Mn_2O_3 to form the spinel phase.

1.2.4 Deactivation

Lamb, in their initial studies of hopcalite, identified the extreme sensitivity of the Hopcalite catalysts to moisture. Very small traces were observed to completely inhibit the activity of the catalyst for CO oxidation[3]. The mechanism for this is unclear, there are suggestions however that the deactivation is caused by water adsorbing onto O_2 adsorption sites[24]. It is not only limited to CO oxidation, work by Kang demonstrate that the activity for NOx SCR is impeded by the presence of moisture[25]. They were able to recover the catalysts activity by removing water from the surface. The catalyst also showed susceptibility to SO_2 poisoning.

Another aspect of deactivation was studied by Veprek *et al*. They were investigating the effect of temperature on catalyst activity when it was noted that a significant deactivation was associated with the crystallisation of the catalyst[24]. They noted that as the catalyst deactivated there was a phase change in the material from a disordered spinel to a crystalline one. Puckhaber *et al.* noted that this was accompanied by a change in the oxidation state of the surface to favour the Cu^+ state along with the Mn^{4+}. This served to disrupt the redox couple that is the source of the catalysts activity.

The presence of alkali metal poisons has also been linked with catalyst inactivity. Veprek showed that the activity was linked with the concentration of residual K^+ on the surface of the catalyst [24]. Work by Mirzaei *et al.* found a correlation between the concentration of Na^+ on the surface of the catalyst and activity[26]. This work is discussed further in section1.2.6.1.

1.2.5 Methods for the preparation of hopcalite

Since the discovery of hopcalite, many preparation techniques have been investigated for the synthesis of the material, taking into account the work on the structure of the material and its deactivation. This section details the investigations into this area.

1.2.5.1 Catalysts prepared by Co precipitation

The most studied method for the production of Hopcalite type catalysts in recent times has been via the co-precipitation method. The process begins with the precipitation of two salts together using a precipitating agent. There may then follow an aging step where the precipitated material is left to mature in the mother liquor. The precipitate is then recovered by filtration, washed to remove any precursor materials or poisons, dried to remove precipitation solvent and finally calcined to give the active oxide [27].

```
Precipitation  →  Aging  →  Recovery  →  Drying  →  Calcination
```

Figure 4: Schematic of the steps involved in producing a catalyst by coprecipitation.

A number of reagent systems have been studied. Principle among these is precipitation of metal nitrates with sodium carbonate, this subject is discussed at length in section 1.2.6.1 . Nitrates area attractive due to their solubility, they are non-toxic for the most part and straightforward to handle. Their solubility leads them to not remain in the precipitant as they can be easily rinsed out[28]. Other precipitants studied include formates [28], acetates and sulphates[29]. Other precipitating agents include hydroxides[29] and tetramethylammonium carbonate [30].

A variant of the coprecipitation method is confined coprecipitation. This involves coprecipitation inside the structure of a silica aqua-gel. The sample is then calcined inside the aqua-gel structure before removing it with NaOH. Marbán *et al.* demonstrated this technique and were able to produce a range of mixed metal oxides including $CuMn_2O_4$ [31].

The surface area of the $CuMn_2O_4$ synthesised by this route was in the region of $300 \ m^2 \ g^{-1}$ which is high compared to the $100 m^2 \ g^{-1}$ commonly reported for co-precipitated catalysts [32].

1.2.5.2 Impregnation

A straightforward method of producing hopcalite is by the impregnation method. Impregnation is the process whereby a metal salt is deposited on the surface of a solid by adding the solid to be impregnated to a solution of the salt. The volume of this solution is then reduced by heating until the salt deposits onto the surface. Lamb *et al.* produced copper manganese oxide materials by impregnating copper nitrate onto MnO_2 and calcining it [3, 6].

A second, and related, method is to co-impregnate both copper and manganese nitrate onto a support material before calcination to give the active catalyst. An example of this is work by Einaga *et al.* who impregnated copper and manganese nitrate onto SiO_2. Upon calcination, both the $CuMn_2O_4$ spinel and $Cu_2Mn_3O_8$ phases were observed[33]. This has been extended into mesoporous silica supports by Issa *et al.*[34]. Similarly Fang *et al.* demonstrated that it was possible to produce $CuMn_2O_4$ supported on TiO_2 by this method[35].

Larsson *et al.* produced Al_2O_3 supported $CuMn_2O_4$ by a similar impregnation method whereby they degassed the Al_2O_3 at 50 torr. They then introduced copper manganese nitrate at this reduced pressure before increasing the pressure to 760 torr [36]. Calcination then produced the active catalyst, which was found to consist of supported $CuMn_2O_4$.

Copper manganese oxide can also be prepared supported on monoliths by the impregnation method. Wu *et al.* prepared a range of cordorite monoliths by dipping the monolith into a Cu: Mn nitrate solution containing an alumina sol and calcining to give the active phase[37].

Other supports that have been investigated include high surface area silica, tin oxide[38] and titania[39].

A similar but separate preparation technique to impregnation is incipient wetness impregnation. Whereas impregnation uses an excess of solvent incipient wetness uses only enough solvent to fill the pores of the support. An example of the use of this method for prepare supported copper manganese oxide is a study by Chen *et al*. where supported copper manganese oxide on ZSM-5/PSSF fibres was produced by an incipient wetness method[40].

1.2.5.3 Supercritical antisolvent precipitation (SAS)

A similar technique to co-precipitation is supercritical antisolvent precipitation (SAS). While coprecipitation precipitates the desired product by modifying the pH using a precipitating agent SAS precipitates by the addition of a supercritical fluid as an antisolvent. When the antisolvent is mixed with the precursor solution it changes the solubility of the dissolved salts causing them to precipitate. This process has the added benefit of allowing the sample to be recovered easily by simply reducing the pressure and allowing the supercritical fluid to revert to a gas leaving the desired catalyst precursor behind. Work by Tang *et al.* demonstrated the viability of using supercritical CO_2 as an antisolvent to produce copper manganese oxide catalysts[41]. By dissolving copper and manganese acetate in DMSO and mixing with CO_2 at 110 bar they precipitated an amorphous copper manganese carbonate. This was calcined in static air to form the copper manganese oxide. This report is the first example of the production of a mixed metal oxide by this method. Further studys of supercritically precipitated copper manganese materials waereundertaken by Kondrat *et al*. who studied the effects of heat treatment on these catalysts[42]. They precipitated well mixed copper manganese acetates via a similar SAS method to Tang and calcined the materials under flowing air, static air and helium. Unsurprisingly the samples calcined in flowing air formed the CuMn2O4 phase, however some Mn_3O_4 was also observed suggesting

a degree of phase separation, which considering the well mixed nature of the precursor, was surprising. The sample calcined in helium exhibited a large degree of auto reduction due to the *insitu* formation of CO from acetate decomposition, this was observed to a lesser extent in the sample calcined in static air.

1.2.5.4 Redox method

Amorphous copper manganese oxide catalysts were prepared by Njagi *et al*. via a novel redox method[43]. This involved the reduction of potassium permanganate using a solution of manganese (II) acetate and copper nitrate. The resulting precursor was calcined at 300C to give the amorphous copper manganese oxide phase. They found however that as the $Cu(NO_3)_2$ was not directly involved in the redox reaction only around 5% was incorporated into the catalyst and that which was incorporated was trapped within the amorphous manganese framework. It was noted that compared to other preparation methods the surface area of 163 $m^2\,g^{-1}$ was high.

1.2.5.5 Sol gel

The Sol-gel method is a common method for the preparation of metal oxide catalysts. Hosseini *et al*. applied it to the preparation of copper manganese oxide[44]. Mixtures of copper and manganese nitrate alongside a stoichiometric amount of citric acid were heated at 60 °C until a gel formed. This gel was then warmed to 180 °C at which point the gel combusted forming a porous $CuMn_2O_4$ network[44]. Kraemer *et al*. also used a sol gel process to prepare copper manganese oxide[45]. They used the ethylene glycol method and were able to produce an amorphous copper manganese oxide. Calcination above 400 °C led to sintering and crystallisation of the catalyst.

1.2.5.6 Combustion

Sebusai *et al*. synthesised a range of copper manganese oxide catalysts with varying Cu: Mn ratio via a combustion method for the use in the direct epoxidation of propylene [46]. Mixtures of copper and manganese nitrate in an organic fuel were heated until combustion

took place resulting in production of the oxide. By changing the fuels that were used for the pyrolysis they were able to tune the crystallite size of the final $Cu_{1-x}Mn_xO_4$ phase. Use of glycerol resulted in the largest crystallites (45nm) whilst using citric acid gave the smallest (29nm). This was attributed to citric acid's ability to chelate the metal ions in solution whilst the glycerol could not do so as effectively leading to larger metal nitrate domains [46].

1.2.5.7 Flame Pyrolysis

Flame pyrolysis is a novel method for the production of nanoparticulate materials. Biemelt *et al*. synthesised $CuMn_2O_4$ nanoparticles by this route[47]. A copper manganese nitrate inverse micro-emulsion was sprayed through a nozzle with n-heptane and ignited. The resulting nanoparticulate oxides were 10-15nm in diameter with spherical and hollow morphologies observed.

1.2.5.8 Thermal decomposition

Another very straightforward preparation method for copper manganese oxide was presented by Gautier and co-workers [48]. They simply dissolved the appropriate ratio of copper and manganese nitrates, in a slightly acidified solution before drying. The resulting powder was thermally decomposed at 200 °C to give the mixed metal oxide.

1.2.5.9 Reactive grinding

Qian *et al*. report a novel synthesis method for synthesising copper manganese oxide using a soft reactive grinding method [49]. This involved grinding copper hydroxycarbonate and manganese carbonate with either oxalic or citric acid in a planetary ball mill. This was followed by calcination. The materials produced consisted of the $Cu_{1.5}Mn_{1.5}O_4$ phase. Unpublished work by our group has also demonstrated that a copper manganese oxide material can be prepared by grinding the nitrate salts with ammonium hydrogen carbonate in a pestle and mortar. This was following a method first reported by Yang *et al*. for synthesising cobalt nanoparticles [50].

Table 1: Comparison of various prep methods discussed in this chapter applied to CO oxidation

Preparation Method	Surface area / m^2g^{-1}	CO oxidation activity / %
Impregnation [6]	-*	90[a]
Co-precipitation [56]	94	90 [b]
Supercritical anti-solvent precipitation [41]	50	10 [b]
Redox method [43]	376	40 [c]

* No surface area reported, a 20 °C Catalyst bed of 5cm, 0.25% CO, Air, b 25 °C. Catalyst: 50 mg, space velocity: 17,000 mL h−1 gcat−1, feed gas: 0.5% CO, Synthetic air, c 25 °C. Catalyst: 100 mg, space velocity: 35,000 mL h−1 gcat−1, feed gas: 1% CO, 20

1.2.5.10 Preparation of doped hopcalite

There has been some interest in promoting the activity of Hopcalite catalysts by doping them with various other metal ions. Cole *et al*. demonstrated the viability of doping hopcalite with transition metals by substituting 1% Co in place of Cu[51]. This was done by coprecipitation of the three nitrate salts with sodium carbonate as discussed previously. Substitution of copper with cobalt was possible as the ionic radius of Co^{2+} was slightly smaller than that of Cu^{2+} and as such was able to fit into the tetrahedral sites of the spinel. Co-precipitation has also been shown to facilitate the incorporation of Zn and Al[52].

Du *et al*. produced copper manganese oxide catalysts with a range of transition metal dopants. Metals investigated included Ce, Zr, Zn, Fe and Al. These catalysts were formed by a urea combustion method[53].

Gold has also been added to hopcalite. One method of achieving this is to simply add the desired metal salt into the coprecipitation mixture as was done by Solsona *et al*.[54]. A second method is to deposit gold on the surface of the catalyst after it has been produced separately. Cole *et al*. produced gold modified hopcalite by adding 1 wt% gold to the surface by a deposition precipitation method[55].

1.2.6 Influence of preparation conditions on the oxidation of carbon monoxide

The principle use for hopcalite historically has been as a CO oxidation catalyst. Carbon monoxide is a colourless, odourless gas. Formed commonly from the incomplete combustion of hydrocarbon fuels it is often referred to as "the silent killer" for its propensity to cause unexpected death from undetected boiler or cooker faults.

The toxicity of CO lies in its strong affinity for haemoglobin. CO binds irreversibly with the enzyme preventing the transport of oxygen throughout the body. It is only when the haemoglobin is broken down at the end of the lifetime of the red blood cell that the effects of CO poisoning are mitigated.

1.2.6.1 CO Oxidation using Hopcalite

$$CO + \frac{1}{2}O_2 \rightarrow CO_2$$
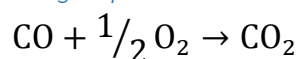
Figure 5: CO Oxidation reaction to form carbon dioxide

The most commonly studied catalyst in recent times for CO oxidation has been the coprecipitated copper manganese oxide catalyst. Co-precipitation is a complex preparation technique with a number of variables that all can have a profound effect on the activity of the final material.

1.2.6.2 Copper to manganese ratio

A study on the optimum Cu: Mn ratio for CO oxidation using coprecipitated copper manganese oxide catalysts was undertaken by Hutchings *et al.*[56]. They precipitated a number of catalysts at pH 9 and 80 °C varied the Cu: Mn molar ratio of the precipitation mixture from 100% Mn to 100% Cu. Once precipitated and dried all catalysts were calcined at 500 °C for 17h. The catalysts were tested for CO oxidation by flowing 0.5% CO / He at a space velocity of 33000 h^{-1} over a catalyst bed. The individual oxides of copper and manganese were active but less so than any of the mixed phases. Changing the Cu: Mn ratio from 4:1 to 1:1 was found to have little effect on the activity, all three catalysts tested

converted 65% of the CO stream. The sample with the 1:2 Cu: Mn ratio had the highest activity converting 90% of the CO gas stream. This was attributed to the presence of the stoichiometric $CuMn_2O_4$ phase in the catalyst. Increasing the Cu: Mn ratio further was detrimental to activity.

1.2.6.3 Effect of precipitation pH

Hutchings *et al*. studied the effect of precipitation pH on the activity of Hopcalite catalysts coprecipitated from nitrates using Na_2CO_3 for CO oxidation [23].   Varying the precipitation pH between 7 and 10, they found that 8.3 was the optimum. At lower pH they found Cu rich materials, a result of the lower precipitation pH of Cu^{2+} ions. The optimum range was between 8.3 and 9 with pH 9 giving the highest specific activity with 90% conversion observed.   However when surface area normalised rates were considered the sample precipitated at 8.3 was clearly superior. Both samples contained a spinel phase. The sample precipitated at 8.3 consisted of CuO, Mn_2O_3 and $CuMn_2O_4$ while precipitating at pH 9 resulted in a mixture of $Cu_{1.4}Mn_{1.6}O_4$ and Mn_2O_3 in agreement with Vandenberghe[16].

1.2.6.4 Effect of precursor aging

The aging step, along with the initial nucleation, is amongst the least understood of all the process of producing materials by co-precipitation. Hutchings *et al*. found that a short aging time of 30 mins or a long aging time of 300 mins resulted in the most active catalysts. Other aging times, shorter or in between these times, resulted in less active materials [27]. Further study illustrated that prolonged aging of 720 min resulted in materials that exceeded the 30 or 300 min for CO oxidation activity by a significant amount.

The aging step was shown to have an effect on the nature of the precipitated precursor. With no aging the precursor contained crystalline copper hydroxycarbonate alongside manganese carbonate. Upon aging this re dissolves and is not present in their samples. After calcination the XRD patterns broaden, indicative of a lowering of the crystallite size, and decrease in intensity. This is in agreement with Veprek, who stated that the amorphous

$CuMn_2O_4$ is the active species [24], in this case the sample aged for 12 h was least crystalline and most active.

Further work by Mirzaei *et al.* illustrated the change in the precursor by analysing it with TGA[57]. They found that the total mass loss decreased with increasing aging time. This suggests that an oxide phase, whether Mn_2O_3 or CuO, was formed during the aging process. This was confirmed with XRD to be CuO. TPR studies of the samples proved to be difficult to interpret with multiple reduction events overlapping with one another, however they were able to deduce that the Cu^{2+} reduction was being promoted with increased aging.

1.2.6.5 Effect of calcination

Cole *et al*. studied the effect on calcination temperature on the activity of copper manganese oxide catalysts. The materials were precipitated as in previous work by Hutchings *et al*.[56] and calcined at varying temperatures from 200-500 °C for varying periods of time. XRD showed that calcination at 300 °C resulted in a completely amorphous material, increasing the temperature to 400 °C caused the formation of a microcrystalline $CuMn_2O_4$ phase and above 450 °C the crystalline spinel was observed. This phase transition occurred at lower temperatures than previously reported [58].

The most active material was that calcined at 410 °C for 2h. This was also the material with the highest surface area. Testing the samples for CO oxidation. Calcination at higher or lower temperatures for retarded the surface area leading to less active materials. Calcination at higher temperatures also lead to the crystallisation of the catalyst and the presence of a Mn_2O_3 phase was detected [59].

1.2.6.6 Effect of Na+ poisoning

Veprek *et al*. identified that K^+ can decrease the activity of hopcalite towards CO oxidation. Mirzaei *et al*. investigated the effect of Na^+ on the activity of copper manganese oxide catalysts for CO oxidation[26]. They achieved this by monitoring the surface Na: Mn ratio using XPS for a series of catalysts produced by coprecipitation and aged for varying periods

of time and at various pH conditions. They found that CO oxidation activity can be directly related with Na^+ concentration on the surface and that the surface concentration of Na^+ can be controlled by manipulating the pH environment.

The link between activity and Na^+ concentration has lead researchers to investigate sodium free preparation of copper manganese oxide. Einaga *et al*. investigated the use of tetramethylammonium hydroxide as a precipitating agent in place of Na_2CO_3 [30]. The materials precipitated by this method were highly crystalline and as a consequence only exhibited ca 20% oxidation of a 5000ppm CO feed at room temperature. However the $CuMn_2O_4$ phase was successfully synthesised.

1.2.7   Effect of Doping

Previously in this chapter the preparation of hopcalite type materials doped with various other metals has been discussed. A number of groups have investigated the effect that doping can have on the activity of hopcalite.

Jones *et al*. replaced copper with varying amounts of cobalt [51]. They found that by replacing 1 wt% Cu with Co the activity of the catalyst for CO oxidation was doubled. The Co was incorporated into the lattice and changed the redox properties of the catalyst leading to improved activity.

Taylor and co-workers doped copper manganese oxide with gold via a co-precipitation method[74]. It was observed that the addition of 3 wt% gold lead to a catalyst that was twice as active as its un-doped analogue. Addition of 1 wt% and 6 wt% gold also improved catalytic activity but not to the extent of 3 wt%. The presence of gold also led to less catalyst deactivation than the undoped material. Further studies on gold addition have been undertaken by Cole *et al*. They deposited gold on the surface of gold catalysts using a deposition precipitation technique [55]. They found that deposition of 1 wt% gold resulted in the most active catalyst. Supported gold nanoparticles are well known CO oxidation

catalysts. The addition of nanoparticulate gold to the surface was expected to add activity through the presence of active sites associated with the gold. However they also found that the addition of gold to the surface modified the reducibility of the catalyst. Further studies using temporal analysis of products investigated the mechanism of CO oxidation on these gold doped catalysts [75]. Isotopic labelling was used to identify the relative contribution of the MvK and Langmuir-Hinshelwood mechanisms (LH). Both the undoped and doped catalyst exhibited evidence of both mechanisms at work. However the sample with gold on the surface exhibited a higher contribution from the MvK mechanism, they suggest that this is the result of gold on the surface increasing the availability of oxygen for reaction with CO. Multi pulse experiments suggest the presence of two oxygen species, one active for CO oxidation and one not active. The inactive species is more common than the active species by a factor of 10, the increased activity of the gold catalyst comes from promoting the activity of this inactive species.

1.3 Oxidation of volatile organic compounds using hopcalite

Alongside its primary use in the oxidation of CO, hopcalite has also been used in the oxidation for other waste products, notably volatile organic compounds.

Volatile organic compounds (VOC's) as defined by the 1999 EU paints directive are "organic compounds having at 293.15 K (i.e., 20°C) a vapor pressure of 0.01 kPa or more"[60]. [61]. A wide class of compounds, VOC's include diverse hydrocarbons from simple linear alkanes, complex polycyclic aromatics (PAH) and chlorinated materials [60, 61].

Due to their role in air pollution with many linked to health complications ranging from asthma[62] to cancer[63] there are strict controls on the production and emission of VOC's. Common sources of VOC's are from paints and incomplete combustion of hydrocarbon fuels.

The VOC discussed in this thesis is naphthalene, the simplest and is discussed at length in section 1.5 of this chapter.

1.3.1 Methods of dealing with VOC's

There are a number of methods for treating VOC's to prevent their emission. The simplest process is to simply thermally incinerate the VOC's using an extremely hot gas flame. This method has the advantage of low complexity, however if incomplete combustion occurs more VOC's may be emitted than if the gas stream was untreated. A very hot flame is also required with temperature in excess of 1000 °C required for some materials. This is energetically and financially very costly.

An alternative method is to adsorb the VOC's onto a filter. This can be extremely effective however the effectiveness of filters decreases with time and they must be replaced or regenerated. Common adsorbents include Carbon[64], Zeolites[65] and mesoporous polymers[66]

Catalytic combustion is a third option for regulating the emission of VOC's. This involves using a catalyst to decompose the compounds forming CO_2. This has the advantage of low operating temperature compared with thermal combustion and long potential operating lifetime compared with filters. A ubiquitous example of a catalytic combustor is the three way catalyst used in automobiles. One component that is treated with the catalytic converter is partially combusted fuel, this includes short chained olefins and alkanes that cannot be allowed to enter the atmosphere[67].

1.3.2 VOC Oxidation using Hopcalite

Hopcalite, alongside its well-known CO oxidation activity, has been identified by a number of studies as a promising oxidation catalyst for a number of classes of VOC.

Oxygenated hydrocarbons. Lintz studied the oxidation of some common oxygenated solvents in the gas phase by copper manganese oxide. They observed that it was possible to totally

oxidise acetone, butyl acetate and isopropanol to within legal limits. However partially oxidised products were also observed in all cases[68]. Total oxidation of ethanol has also been observed by Morales[69]. For catalysts with a 1:1 Cu: Mn ratio a temperature of 200 °C was sufficient to achieve 100% conversion to CO_2. It was observed that prolonged aging time was beneficial for these materials with the most active aged for 24h.

Saturated hydrocarbons. Morales *et al*. investigated the role of Cu-Mn mixed oxides for the total oxidation of propane[69]. They demonstrated that copper manganese oxides had higher conversion to CO_2 at lower temperatures than manganese or copper alone. They attribute the higher activity to the presence of the Cu1.5Mn1.5O4 phase alongside a disordered Mn_2O_3 phase predominantly on the surface. Solsona *et al*. have also studied the oxidation of propane with copper manganese oxide, however they doped their catalyst with gold[54]. Cole *et al*. have previously demonstrated the promoting effect of gold addition on hopcalite for CO oxidation, this is observed again in this study. They noted that the addition of gold lowered the temperature at which 50% of propane was oxidised to CO_2 from 245 °C to 230 °C. 3 wt% gold was the optimal loading and calcination at 300 °C the optimal calcination temperature. This was due to the nanocrystaline nature of the material precipitated with only a broad reflection corresponding to gold observed.

Unsaturated hydrocarbons. It has been identified that hopcalite is an active catalyst for the oxidation of ethylene. Njagi *et al*. report a 100% oxidation of ethylene to CO_2 at 200 °C using a copper manganese oxide catalyst prepared by a novel redox method[70]. This catalyst was previously reported to exhibit high activity for CO oxidation also[43]. Hopcalite has also been reported to be active for the oxidation of propene [71].

Chlorinated compounds. Vu *et al*. presented a study on the effectiveness of Cu-Mn oxide catalysts for the total oxidation of chlorobenzene [72]. They prepared a supported $CuMn_2O_4/TiO_2$ catalyst by the impregnation method and tested it by flowing a 500ppm

chlorobenzene stream over the catalyst at elevated temperature. It was observed that 100% oxidation of chlorobenzene to CO_2, H_2O and Cl_2 was observed by 350 °C. The catalyst deactivated rapidly to 75% activity but this was maintained for up to 3 days and 100% activity could be regenerated by re-oxidising the catalyst under flowing air at 350 °C. The catalyst demonstrated remarkable resistance to poisoning by chlorine, a poison for many catalyst systems.

Aromatic hydrocarbons. A range of aromatic compounds were shown to be oxidised using copper manganese oxide by the study of Geunino *et al*[73]. Toluene, xylene, benzene and ethyl-benzene were all oxidised and the results are summarised in Table 1

Table 1: Results of the study of Geunino et al. into aromatic VOC oxidation[73]

Aromatic VOC	Conversion at 250 °C / %
Benzene	44
Toluene	74
Ethyl benzene	37
p-Xylene	29
o-Xylene	27
m-Xylene	26

Toluene was found to be the most readily oxidised, followed by benzene, ethyl benzene and xylene. They identified that lattice oxygen was involved in the oxidation process as even in O_2 free conditions activity was still observed.

1.3.3   Other uses for hopcalite

Methanol steam reforming. Papavasiliou *et al*. investigated the activity of copper manganese oxide for methanol steam reforming. The catalysts were prepared by the combustion of nitrate precursors using urea and as a result have a very low surface area of

$8.6 \, m^2 \, g^{-1}$. Despite this their catalyst showed high selectivity towards H_2 out performing a copper ceria catalyst prepared by the same method.

Water gas shift. Tanaka *et al.* reported the activity of copper manganese catalysts produced from the reduction of $CuMn_2O_4$ for water gas shift reaction [76]. The catalyst was especially active when a high proportion of CO was used making it attractive for use in removal of CO from reformed hydrocarbon gas.

Epoxidation of propylene. Seubsai *et al.* demonstrated that $CuMn_2O_4$ was active for the epoxidation of propylene with the use of molecular oxygen as the oxidant[46]. They recorded 1.5% conversion propylene reactant with a 30-37% selectivity to propylene. The higher selectivity's were achieved by doping with NaCl, this served to cap acidic sites on the surface of the catalyst, preventing over oxidation to CO_2

NOx SCR. Sreekanth et al demonstrated the activity of titania supported CuMn2O4 catalysts for NOx SCR[77]. They found that the material was active at low temperatures with 100% selectivity to N_2 at 120 °C. Fang *et al.* found that compared with titania copper manganese catalysts, Cu Mn spinel materials were more resistant to poisoning by K^+ whilst still maintaining high activity[35].

1.4 Naphthalene Oxidation

Polycyclic aromatic hydrocarbons are a class of VOC that are associated with serious health conditions. Short term exposure can result in eye damage and respiratory problems, while prolonged exposure results in carcinogenic and mutagenic effects[78]. They are commonly produced when there is incomplete hydrocarbon combustion. A large source of this is exhaust from diesel motor vehicles[79] and wood burning stoves[80].

Naphthalene is the simplest of the polycyclic aromatic hydrocarbons and as such is of interest as a model. A common ingredient in mothballs until 2008[81], it is a white, crystalline solid with a melting point of 77 °C and a boiling point of 217 °C[82].

1.4.1 Naphthalene oxidation over metal catalysts

The total oxidation of naphthalene is an attractive method for air treatment purposes. Its only products are ultimately carbon dioxide and water with no toxic waste products.

$$C_{10}H_{12} + 14O_2 \rightarrow 10CO_2 + 8H_2O$$
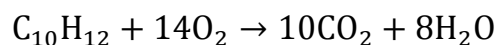
Figure 6: Total oxidation of naphthalene to form CO_2 and water exclusively

Zhang *et al.* studied the effectiveness of 6 metals on the total oxidation of naphthalene. Palladium, Ruthenium, Cobalt, Molybdenum and Tungsten were all impregnated onto a γ-Al_2O_3 support. Naphthalene TPD indicated that of the metals tested tungsten had the greatest affinity for naphthalene, naphthalene was totally desorbed by 500 °C. The sample impregnated with Cobalt retained the least naphthalene with total desorption by 200 °C. Palladium and platinum displayed similar adsorption characteristics with desorption occurring over a greater range on the Pd than the Pt. Adsorption characteristics are important as the longer the reactant spends on the surface the greater its chances for reaction.

The results of the naphthalene oxidation testing is shown in Table 2.

Table 2: Results of naphthalene oxidation testing reported by Zhang et al.[83]. 150mL min^{-1}100 vppm Naphthalene 10% O_2/He.

Catalyst	Naphthalene consumption		Carbon Dioxide production	
	T 10 / °C	T 90 / °C	T 10 / °C	T 90 / 10 °C
1% Pt/γ-Al_2O_3	194	203	240	280
1% Pd/γ-Al_2O_3	197	206	253	285
1% Ru/γ-Al_2O_3	296	299	325	433
5% Co/γ-Al_2O_3	374	380	370	410
5% Mo/γ-Al_2O_3	248	254	415	487

| 5% W/γ-Al_2O_3 | 251 | 302 | 337 | 487 |

The platinum and palladium catalysts were found to be the most active with Pt slightly more active than Pd. For all samples there was a clear difference between the temperatures of Naphthalene consumption and the CO2 production. This suggested that there was some partial oxidation underway at lower temperatures. Using a kinetic study it was established that the naphthalene oxidation reaction was 1st order with respect to O_2 and as such was proceeding via a Langmuir-Hinshelwood mechanism.

Zhang went on to study the discrepancy between naphthalene consumption and CO_2 production in further detail for the Pt and Co containing Al_2O_3 catalysts [84]. By using on-line and offline GC-MS they were able to identify a number of by-products falling into 3 categories; Naphthalene by-products, Naphthalene derivatives and polymerised PAH's. Naphthalene by-products consisted of partially oxidised naphthalene fragments, these included phthalic anhydride, oxalic acid and benzaldehyde amongst others. The production of these was attributed to the partial oxidation to phallic anhydride, this then oxidised further before desorption. Naphthalene derivatives consisted of oxidised naphthalene species such as 1, 4-naphthalenedione. The formation of these was due to alkylation and coupling reactions taking place on the surface via a radical mechanism. This was confirmed by EPR spectroscopy. Finally polymerised PAH's consisted of large, multi-ring systems both with and without oxygen. These were formed by the dimerization of naphthalene via a cationic intermediate. When compared with the Co catalyst there were far more side products from reaction over the Pt catalyst. When the TPD data from their previous study was considered[85] they determined that lower residence times on the surface was beneficial for total oxidation of naphthalene.

Further study on the effectiveness of Platinum supported on alumina for naphthalene was undertaken by Njainjua et al.[86]. They produced vanadium doped Pt/Al2O3 catalysts. It was found that low levels of vanadium (0.5 wt%) improved the activity of the catalysts, with a promotion of the T50 from 200°C for the undoped material to 175 °C for the vanadium doped catalyst. Addition of more vanadium served to retard the activity of the catalyst due to the formation of a V_2O_5 species. The activity of the 0.5 wt% V 0.5 wt% Pt/Al_2O_3 catalyst was attributed to the presence of a highly redox active vanadium species that was identified in the TPR of the material.

Other support materials were investigated by Ntainjua et al. with the activity of 0.5 wt% Pt supported on silica, alumina, tin oxide, titania and ceria all compared [87]. It was found that Pt/SiO_2 was far and away the most active catalyst. They observed over 50% conversion to CO_2 at 100 °C. In comparison Pt/Al_2O_3 is inactive at this temperature. They identified using XPS that the silica supported catalyst was the only one that contained metallic platinum, the others had oxide species on their surface. This, coupled with the large platinum particle size on the Pt/SiO_2 catalyst combined to make the material exceptionally active.

Sellick et al. further investigated the activity of platinum supported on silica[88]. A series of catalysts with varying Pt levels ranging from 0.1 to 5 wt % were prepared. It was observed that loading with 2.5 wt% Pt resulted in the most active catalysts. This was attributed to the large Pt particles on this sample along with the presence of both metallic and oxidic platinum species.

1.4.2 Naphthalene oxidation over metal oxide catalysts

Metal oxide catalysts have the advantage of relatively low costs compared with supported noble metal materials. They also have the added advantage of potentially higher stability due to the thermodynamically stable nature of the materials.

Pt/CeO$_2$ was briefly discussed previously in its relation to Pt/SiO$_2$ however there has been much research into the activity of CeO$_2$ alone for the total oxidation of naphthalene. Garcia *et al*. investigated CeO$_2$ prepared by a number of varying coprecipitation methods for naphthalene oxidation[89]. Precipitation using urea resulted in a material with 90% CO$_2$ production at 175 °C whereas precipitation from carbonate resulted in 90% CO$_2$ production at 290 °C. They also observed that at low temperatures the CeO$_2$ catalysts were very efficient at adsorbing naphthalene. This was noted to be potentially useful in any "cold start" applications with the catalyst acting as a filter at low temperature before combusting the adsorbed material at elevated temperatures.

Garcia *et al*. went on to study the oxidation capability of a range of metal oxides[90]. Ceria produced by both the urea (CeO$_2$ (U)) and carbonate (CeO$_2$ (P)) coprecipitation methods was compared with manganese oxide, cobalt oxide, iron oxide, zirconia, titania and alumina.
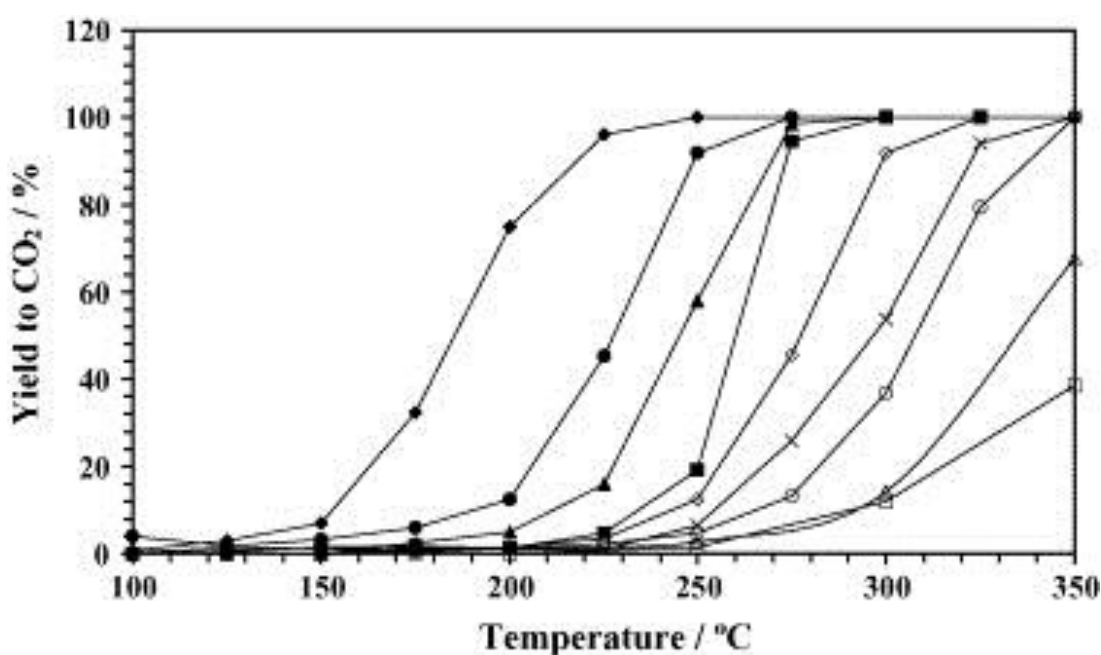
Figure 7 : Comparison of catalytic activities of several metal oxide catalysts. ♦ CeO$_2$ (U), ● MnOx, ▲ CoOx, ■ CuOx, ◇ Fe$_2$O$_3$, × CeO$_2$ (P), ○ ZnO$_2$, △ TiO$_2$ and □ Al$_2$O$_3$. Reproduced from [90]

As illustrated in Figure 7 the order of activity for the oxides studied was CeO2(U) > MnOx > CoOx > CuOx > Fe2O3 >CeO2 (P) >TiO2 > Al2O3. They considered the isoelectric properties of the oxides and noted that there was no correlation. They also noted that the activity of the catalysts was not directly related to their reducibility.

In the same study Garcia *et al*. also investigated the synergistic effect of co-precipitating copper and zinc oxide together[90]. Copper zinc oxide is a well-known catalyst used for the synthesis of methanol [91]. They observed that mixing the two oxides promoted the decomposition of naphthalene and production of CO_2. They attributed this increase in activity to the increase in surface area and reducibility of the mixed catalyst compared with the individual oxides. This has also been observed by Taylor *et al*. who were investigating CuZnO for CO oxidation [92].

Of the oxides studied, CeO_2 produced by the urea coprecipitation route was the most active, however the MnOx catalyst was the second most active. As manganese oxide is a cheap readily available material Garcia *et al*. investigated its effectiveness further. In their review of the subject of polycyclic aromatic hydrocarbons Ntainjua and Taylor identified that reducibility and surface area were key variables that played a role in determining manganese oxidation activity. Garcia decided to use a nanocasting approach in order to attempt to maximise these variables. Using KIT-6, a mesoporous silica, as a template they produced a mesoporous manganese oxide catalyst. Calcination at 600 °C yielded a material with a surface area of 78 $m^2 g^{-1}$. This compared favourably with the control sample, prepared by the thermal decomposition of manganese nitrate, which had a surface area of 7 $m^2 g^{-1}$. This high surface area was due to the mesoporous structure of the material which was clearly observed in TEM. XRD analysis indicated that both samples calcined at this temperature contained Mn_2O_3. However calcination at 500 °C resulted in mixtures of Mn_2O_3 and MnO_2. TPR analysis suggested that producing the catalyst in this manner also increased its

reducibility, illustrated by the earlier onset of reduction and a broadening of the reduction profile. T50 for this mesoporous catalyst was 215 °C while the control sample had a T50 of 310 °C.

1.4.3   Oxidation of mixtures of VOC's containing naphthalene

In the majority of real world applications VOC's are not produced alone, rather they are produced in mixtures. As such it is important that catalysts are able to treat multiple VOC's at the same time.

Carno *et al*. investigated the oxidation of a naphthalene, methane and CO stream using both a commercial platinum on alumina catalyst and a supported copper manganese oxide catalyst on alumina[93]. They observed that the Pt/Al2O3 catalyst was more active than the supported metal oxide. All hydrocarbons except methane were oxidised by 500 °C. These results were compared with testing on the flue gasses of a 15 kW wood burner and were found to be comparable. The metal oxide catalyst however was not active enough to be tested using the flue gasses[93].

Neyestanaki *et al*. investigated the activity of metal ion exchanged zeolites for the oxidation of a stream of methane, propane, naphthalene and CO[94]. The zeolite that was tested was a Pd exchanged ZSM-5. They found that more active materials were prepared by exchanging with the ammonium form of ZSM-5 rather than the sodium form. This was attributed to the changing acid-base properties of the material. The choice of Pd salt was also observed to have an effect with catalysts produced from Pd nitrate solutions more active than their chloride counterparts. The catalysts tested were resistant to deactivation for both ethane and naphthalene oxidation however methane oxidation activity decreased with time online. The group investigated the addition of zirconium and lanthanum as dopants, this had the effect of preventing deactivation towards methane. It also had the added effect of improving the low temperature activity for the catalysts. Notably these catalysts were resistant to poisoning by sulfur and were not deactivated by presence of water vapour.

The majority of studies focus on naphthalene as a model PAH, due to the ease of running experiments investigating it. Weber *et al*. however studded the oxidation of mixtures of other PAH's using commercial V_2O_5-WO_3/TiO_2. Their gas stream included pyrene, biphenyl, dibenzofuran and dibenzodioxins along with chlorinated analogues of these. They observed 90% oxidation of the non-chlorinated polyaromatics at 150 °C whilst the chlorinated aromatics proved more difficult to oxidise due to the electron withdrawing effects of the chlorine substituents [95].

1.5 Mechanochemistry

A novel catalyst preparation technique that has been the subject of much interest recently is Mechanochemistry. In their review of the subject, James *et al*. state that "Mechanochemistry refers to reactions, normally of solids, induced by the input of mechanical energy" [96]. The work of Takacs suggest that the first recorded example of a mechanochemical reaction is the production of mercury from cinnabar, as described by Theophrastus of Eresus in the 4th century BC in his book "On Stones"[97]. The advantage of mechanochemistry is its avoidance of solvent use and the associated generation of waste. One of the central themes of green chemistry is the avoidance of solvent waste generation.

Mechanochemistry offers advantages in catalyst preparation not only due to the green considerations but in producing more active materials. Mechanochemically produced materials can have more active sites than their precipitated analogues due to the introduction of stacking faults from the mechanical action[98] and the increased contact through grain boundaries[99].

James *et al*. offer caution in their review on the subject. They illustrate that scalability, purification of product and mechanistic understanding of the processes that are being undertaken in the grinding process are barriers to mechanochemistry moving from a nieche technique to a mainstream synthesis process. They suggest more use should be made of full

life cycle energy as this can help illustrate If a mechanochemical process is indeed more sustainable than a traditional solvent based method[96].

1.5.1 Production of binary oxides using Mechanochemistry.

Perovskites are binary oxides of the type ABO_3 and have been widely synthesised by mechanochemical routes. $LaMnO_3$ was produced by grinding manganese oxides with lanthanum oxide in a 1:1 molar ratio by Escobedo *et al*.[100]. A number of various perovskites have been produced by this method including $BaTiO_3$[101], $LaFeO_3$[102] and $La_{1-x}Sr_xFeO_3$[103].

James *et al*. discuss a second route for oxide synthesis whereby one of the metals is ground in a reduced state [96]. When ground in an inert atmosphere this reduced metal reacts with the oxide of the second metal. This has the net effect of lowering the required grinding time considerably. An example of this is the synthesis of $TiFeO_3$ as described by Crisóbal et al[104]. They used Ti metal and ground it with Fe_2O_3 to form the binary metal oxide.

1.6 References

[1]   A. Kumar, P.C. Mondal, J. Mines, Met. Fuels 55 (2007) 499-501.
[2]   D.N. Gavrilov, G.A. Musakin, N.F. Fedorov, E.A. Zobov, E.M. Apostolevskaya, Zh. Prikl. Khim. (Leningrad) 62 (1989) 391-393.
[3]   A.B. Lamb, W.C. Bray, J.C.W. Fraser, J. Ind. Eng. Chem. (Washington, D. C.) 13 (1920) 213-221.
[4]   A.C. Fieldner, S.H. Katz, S.P. Kinney, Tech. Paper 292 (1922) 27 pp.
[5]   J.A.S. Ritson, W.E.T. Hartley, Colliery Guardian J. Coal Iron Trades 129 (1925) 1135-1136.
[6]   A.B. Lamb, C.C. Scalione, G. Edgar, J. Am. Chem. Soc. 44 (1922) 738-757.
[7]   A.B. Lamb, W.E. Vail, J. Am. Chem. Soc. 47 (1925) 123-142.
[8]   H. Callut, J. Bracke, Ann. Mines Belg. (1969) 704-715.
[9]   A.P.B. Sinha, N.R. Sanjana, A.B. Biswas, The Journal of Physical Chemistry 62 (1958) 191-194.
[10]   N.K. Radhakrishnan, A.B. Biswas, J. Indian Chem. Soc. 51 (1974) 274-280.
[11]   E.J.W. Verwey, E.L. Heilmann, The Journal of Chemical Physics 15 (1947) 174-180.

[12]   K.E. Sickafus, J.M. Wills, N.W. Grimes, Journal of the American Ceramic Society 82 (1999) 3279-3292.
[13]   N.K. Radhakrishnan, A.B. Biswas, Phys. Status Solidi A 44 (1977) 45-49.
[14]   D.P. Shoemaker, J. Li, R. Seshadri, Journal of the American Chemical Society 131 (2009) 11450-11457.
[15]   R. Berger, L.-E. Tergenius, Journal of Alloys and Compounds 203 (1994) 203-207.
[16]   R.E. Vandenberghe, G.G. Robbrecht, V.A.M. Brabers, Materials Research Bulletin 8 (1973) 571-579.
[17]   B.J. Zwolinski, R.J. Marcus, H. Eyring, Chemical Reviews 55 (1955) 157-180.
[18]   S.B. Kanungo, J. Catal. 58 (1979) 419-435.
[19]   G.M. Schwab, S.B. Kanugo, Z. Phys, Chem 107 (1977) 109.
[20]   S.B. Kanungo, Journal of Catalysis 58 (1979) 419-435.
[21]   D.L. Cocke, S. Vepřek, Solid State Communications 57 (1986) 745-748.
[22]   L.S. Puckhaber, H. Cheung, D.L. Cocke, A. Clearfield, Solid State Ionics 32–33, Part 1 (1989) 206-213.
[23]   P. Mars, D.W. van Krevelen, Chemical Engineering Science 3 (1954) 41-59.
[24]   S. Vepřek, D.L. Cocke, S. Kehl, H.R. Oswald, Journal of Catalysis 100 (1986) 250-263.
[25]   M. Kang, E.D. Park, J.M. Kim, J.E. Yie, Catalysis Today 111 (2006) 236-241.
[26]   A.A. Mirzaei, H.R. Shaterian, R.W. Joyner, M. Stockenhuber, S.H. Taylor, G.J. Hutchings, Catalysis Communications 4 (2003) 17-20.
[27]   G.J. Hutchings, A.A. Mirzaei, R.W. Joyner, M.R.H. Siddiqui, S.H. Taylor, Catal. Lett. 42 (1996) 21-24.
[28]   V. Koleva, D. Stoilova, D. Mehandjiev, Journal of Solid State Chemistry 133 (1997) 416-422.
[29]   L.-N. Cai, Y. Guo, A.-H. Lu, P. Branton, W.-C. Li, Journal of Molecular Catalysis A: Chemical 360 (2012) 35-41.
[30]   H. Einaga, A. Kiya, S. Yoshioka, Y. Teraoka, Catalysis Science & Technology 4 (2014) 3713-3722.
[31]   G. Marbán, A.B. Fuertes, T. Valdés-Solís, Microporous and Mesoporous Materials 112 (2008) 291-298.
[32]   C. Jones, K.J. Cole, S.H. Taylor, M.J. Crudace, G.J. Hutchings, Journal of Molecular Catalysis A: Chemical 305 (2009) 121-124.
[33]   H. Einaga, N. Maeda, S. Yamamoto, Y. Teraoka, Catalysis Today 245 (2015) 22-27.
[34]   T. Tsoncheva, G. Issa, I. Genova, M. Dimitrov, J. Porous Mater. 20 (2013) 1361-1369.
[35]   D. Fang, J. Xie, D. Mei, Y. Zhang, F. He, X. Liu, Y. Li, RSC Advances 4 (2014) 25540-25551.
[36]   P.O. Larsson, A. Andersson, Appl. Catal., B 24 (2000) 175-192.
[37]   D. Wu, W. Li, R. Gao, Journal of Chemical Technology & Biotechnology 89 (2014) 1559-1564.
[38]   G. Issa, M. Dimitrov, T. Tsoncheva, Nanosci. Nanotechnol. (Sofia, Bulg.) 13 (2013) 47-50.
[39]   H. Liu, L. Bo, X. Wang, H. Zhang, J. Sun, L. Yang, L. Cai, Huanjing Kexue Xuebao 33 (2013) 1720-1727.
[40]   H. Chen, H. Zhang, Y. Yan, Industrial & Engineering Chemistry Research 52 (2013) 12819-12826.
[41]   Z.-R. Tang, C.D. Jones, J.K.W. Aldridge, T.E. Davies, J.K. Bartley, A.F. Carley, S.H. Taylor, M. Allix, C. Dickinson, M.J. Rosseinsky, J.B. Claridge, Z. Xu, M.J. Crudace, G.J. Hutchings, ChemCatChem 1 (2009) 247-251.
[42]   S.A. Kondrat, T.E. Davies, Z. Zu, P. Boldrin, J.K. Bartley, A.F. Carley, S.H. Taylor, M.J. Rosseinsky, G.J. Hutchings, Journal of Catalysis 281 (2011) 279-289.

[43]   E.C. Njagi, C.-H. Chen, H. Genuino, H. Galindo, H. Huang, S.L. Suib, Applied Catalysis B: Environmental 99 (2010) 103-110.

[44]   S.A. Hosseini, A. Niaei, D. Salari, S.R. Nabavi, Ceramics International 38 (2012) 1655-1661.

[45]   M. Kraemer, T. Schmidt, K. Stoewe, W.F. Maier, Appl. Catal., A 302 (2006) 257-263.

[46]   A. Seubsai, M. Kahn, B. Zohour, D. Noon, M. Charoenpanich, S. Senkan, Industrial & Engineering Chemistry Research 54 (2015) 2638-2645.

[47]   T. Biemelt, K. Wegner, J. Teichert, S. Kaskel, Chemical Communications 51 (2015) 5872-5875.

[48]   E. Ríos, S. Abarca, P. Daccarett, H. Nguyen Cong, D. Martel, J.F. Marco, J.R. Gancedo, J.L. Gautier, International Journal of Hydrogen Energy 33 (2008) 4945-4954.

[49]   Q. Liu, L.-C. Wang, M. Chen, Y.-M. Liu, Y. Cao, H.-Y. He, K.-N. Fan, Catalysis Letters 121 (2008) 144-150.

[50]   H. Yang, Y. Hu, X. Zhang, G. Qiu, Materials Letters 58 (2004) 387-389.

[51]   C. Jones, S.H. Taylor, A. Burrows, M.J. Crudace, C.J. Kiely, G.J. Hutchings, Chemical Communications (2008) 1707-1709.

[52]   M. Zimowska, A. Michalik-Zym, R. Janik, T. Machej, J. Gurgul, R.P. Socha, J. Podobiński, E.M. Serwicka, Catalysis Today 119 (2007) 321-326.

[53]   X. Du, Z. Yuan, L. Cao, C. Zhang, S. Wang, Fuel Processing Technology 89 (2008) 131-138.

[54]   B. Solsona, T. Garcia, S. Agouram, G.J. Hutchings, S.H. Taylor, Applied Catalysis B: Environmental 101 (2011) 388-396.

[55]   K. Cole, A. Carley, M. Crudace, M. Clarke, S. Taylor, G. Hutchings, Catalysis Letters 138 (2010) 143-147.

[56]   G.J. Hutchings, A.A. Mirzaei, R.W. Joyner, M.R.H. Siddiqui, S.H. Taylor, Applied Catalysis A: General 166 (1998) 143-152.

[57]   A.A. Mirzaei, H.R. Shaterian, M. Habibi, G.J. Hutchings, S.H. Taylor, Applied Catalysis A: General 253 (2003) 499-508.

[58]   P.A. Wright, S. Natarajan, J.M. Thomas, P.L. Gai-Boyes, Chemistry of Materials 4 (1992) 1053-1065.

[59]   R.E. Vandenberghe, G.G. Robbrecht, V.A.M. Brabers, Mater. Res. Bull. 8 (1973) 571-580.

[60]   EU, Council Directive 1999/13/EC 1999.

[61]   EU, Directive 2004/42/CE European Union, 2004.

[62]   N. Tagiyeva, A. Sheikh, Expert Rev. Clin. Immunol. 10 (2014) 1611-1639.

[63]   S.L. Simonich, R.A. Hites, Nature (London) 370 (1994) 49-51.

[64]   S. Sircar, T.C. Golden, M.B. Rao, Carbon 34 (1996) 1-12.

[65]   X.S. Zhao, Q. Ma, G.Q. Lu, Energy Fuels 12 (1998) 1051-1054.

[66]   K. Dettmer, W. Engewald, Anal Bioanal Chem 373 (2002) 490-500.

[67]   J. Kašpar, P. Fornasiero, M. Graziani, Catalysis Today 50 (1999) 285-298.

[68]   H.G. Lintz, K. Wittstock, Catalysis Today 29 (1996) 457-461.

[69]   M.R. Morales, B.P. Barbero, L.E. Cadús, Applied Catalysis B: Environmental 67 (2006) 229-236.

[70]   E.C. Njagi, H.C. Genuino, C.K. King'ondu, S. Dharmarathna, S.L. Suib, Applied Catalysis A: General 421–422 (2012) 154-160.

[71]   G.N. Pirogova, N.M. Panich, R.I. Korosteleva, Y.V. Voronin, Izv. Akad. Nauk, Ser. Khim. (1996) 2666-2669.

[72]   V.H. Vu, J. Belkouch, A. Ould-Dris, B. Taouk, Journal of Hazardous Materials 169 (2009) 758-765.

[73]   H.C. Genuino, S. Dharmarathna, E.C. Njagi, M.C. Mei, S.L. Suib, The Journal of Physical Chemistry C 116 (2012) 12066-12078.

[74]   B. Solsona, G.J. Hutchings, T. Garcia, S.H. Taylor, New Journal of Chemistry 28 (2004) 708-711.
[75]   K. Morgan, K.J. Cole, A. Goguet, C. Hardacre, G.J. Hutchings, N. Maguire, S.O. Shekhtman, S.H. Taylor, Journal of Catalysis 276 (2010) 38-48.
[76]   Y. Tanaka, T. Utaka, R. Kikuchi, T. Takeguchi, K. Sasaki, K. Eguchi, Journal of Catalysis 215 (2003) 271-278.
[77]   P.M. Sreekanth, D.A. Pena, P.G. Smirniotis, Ind. Eng. Chem. Res. 45 (2006) 6444-6449.
[78]   Department of Health and Human Services, Agency for Toxic Substances and Disease Registry (ATSDR) (1995).
[79]   P.F. Nelson, Fuel 68 (1989) 283-286.
[80]   D.J. Freeman, F.C.R. Cattell, Environmental Science & Technology 24 (1990) 1581-1585.
[81]   Regulation (EU) 1272/2008, EU, (2008).
[82]   Handbook of Chemistry and Physics, 73 ed., Chemical Rubber Publishing Company, 1993.
[83]   X.W. Zhang, S.C. Shen, L.E. Yu, S. Kawi, K. Hidajat, K.Y. Simon Ng, Applied Catalysis A: General 250 (2003) 341-352.
[84]   X.-W. Zhang, S.-C. Shen, K. Hidajat, S. Kawi, L. Yu, K.Y. Simon Ng, Catalysis Letters 96 (2004) 87-96.
[85]   X.-W. Zhang, S.-C. Shen, L.E. Yu, S. Kawi, K. Hidajat, K.Y. Simon Ng, Applied Catalysis A: General 250 (2003) 341-352.
[86]   E. Ndifor, T. Garcia, S. Taylor, Catalysis Letters 110 (2006) 125-128.
[87]   E. Ntainjua N, A.F. Carley, S.H. Taylor, Catalysis Today 137 (2008) 362-366.
[88]   D. Sellick, D. Morgan, S. Taylor, Catalysts 5 (2015) 690-702.
[89]   T. Garcia, B. Solsona, S. Taylor, Catalysis Letters 105 (2005) 183-189.
[90]   T. García, B. Solsona, S.H. Taylor, Applied Catalysis B: Environmental 66 (2006) 92-99.
[91]   M. Bowker, R.A. Hadden, H. Houghton, J.N.K. Hyland, K.C. Waugh, Journal of Catalysis 109 (1988) 263-273.
[92]   S.H. Taylor, G.J. Hutchings, A.A. Mirzaei, Catalysis Today 84 (2003) 113-119.
[93]   J. Carnö, M. Berg, S. Järås, Fuel 75 (1996) 959-965.
[94]   A. Kalantar Neyestanaki, L.E. Lindfors, T. Ollonqvist, J. Väyrynen, Applied Catalysis A: General 196 (2000) 233-246.
[95]   R. Weber, T. Sakurai, H. Hagenmaier, Applied Catalysis B: Environmental 20 (1999) 249-256.
[96]   S.L. James, C.J. Adams, C. Bolm, D. Braga, P. Collier, T. Friscic, F. Grepioni, K.D.M. Harris, G. Hyett, W. Jones, A. Krebs, J. Mack, L. Maini, A.G. Orpen, I.P. Parkin, W.C. Shearouse, J.W. Steed, D.C. Waddell, Chemical Society Reviews 41 (2012) 413-447.
[97]   L. Takacs, JOM 52 (2000) 12-13.
[98]   V.V. Molchanov, R.A. Buyanov, Y.T. Pavlyukhin, Kinetics and Catalysis 44 (2003) 788-792.
[99]   A. Rougier, S. Soiron, I. Haihal, L. Aymard, B. Taouk, J.M. Tarascon, Powder Technology 128 (2002) 139-147.
[100]   C.A. Cortés Escobedo, F. Sánchez de Jesús, A.M. Bolarín Miró, J. Muñoz-Saldaña, physica status solidi (c) 4 (2007) 4054-4063.
[101]   P. Dulian, W. Bąk, K. Wieczorek-Ciurowa, C. Kajtoch, Mater Sci-Pol 31 (2013) 462-470.
[102]   T. Uchiyama, M. Nishibori, H. Einaga, Y. Teraoka, Journal of the American Ceramic Society 98 (2015) 1047-1051.

[103]   I.S. Yakovleva, L.A. Isupova, S.V. Tsybulya, A.V. Chernysh, N.N. Boldyreva, G.M. Alikina, V.A. Sadykov, Journal of Materials Science 39 (2004) 5517-5521.
[104]   A.A. Cristóbal, E.F. Aglietti, M.S. Conconi, J.M. Porto López, Materials Chemistry and Physics 111 (2008) 341-345.

Experimental

This chapter details the procedures used to synthesis the catalysts discussed within this thesis. Also detailed are the characterisation and testing techniques that were used along with a brief introduction to the theory underpinning their operation.

2.1 Preparation of Catalysts

2.1.1 Coprecipitation with autotitrator

The majority of the catalysts prepared by coprecipitation utilised a Metrohm Titrando autotitrator to control the co-addition of nitrate salts and precipitating agent. There has been much work previously on the optimum preparation conditions for coprecipitated copper manganese oxide catalysts as discussed in Chapter 1. The conditions used, detailed in Table 3, were chosen after referring to this previous work.

The system monitors pH and temperature using an integrated pH probe and doses the appropriate reagents, using two Dosino dosing units, at the appropriate rate to maintain the pH at the desired value. The Dosino units are computer controlled syringe pumps with the ability to dose between 50 μL min^{-1} and 50 mL min^{-1}. At very low dosing rates anti-diffusion tips prevent precipitation occurring in the lines. In this case the nitrate solution was added at a constant rate and the base addition was varied to maintain the pH at 8.3. The general precipitation conditions are shown in Table 3.

Table 3: Conditions chosen for co-precipitation of hopcalite using autotitrator

Variable	Value
Precipitation temperature	80 °C [1]
Stirring rate	400 rpm
pH	8.3 [2]

Aging time	0.5 h [3]
Base concentration	2 M [4]
Rate of nitrate addition	5 mL min^{-1}
Total volume of nitrate	150 mL
Calcination time	415 °C [4]
Calcination temperature	4 h [4]

Before each precipitation the pH probe was calibrated using a three point calibration at pH 4, 7 and 10 (Fisher). To prepare the catalysts copper nitrate (Sigma Aldrich, 99.99 %, 0.25 M) and manganese nitrate (Sigma Aldrich, 99%, 0.25M) solutions were premixed in a 1:2 ratio. This solution was placed in a glass bottle with a Dosino unit attached via a standard screw fitting. A sodium carbonate solution (sigma, 99 %, 2 M) was placed in a separate bottle, to which the second Dosino was attached.

The two reagent vessels were placed into a water bath and heated to the maximum rated temperature of the Dosino units, 50 °C. The precipitation vessel was preheated to 80 °C before 20 mL of the nitrate solution was dosed to ensure full immersion of the pH probe. Sodium carbonate solution was then dosed to bring the pH to the desired 8.3. Following this 130 mL of nitrate solution was dosed at a constant rate (5 mL min^{-1}) and base was added at an appropriate rate to maintain a pH of 8.3. Spikes in the pH of the solution were observed periodically as the dosing unit pumps re-filled. Other than these inconsistencies the pH remained stable. Once all of the nitrate solution had been added the mixture was aged for 30 mins before the precipitate was recovered by filtration and washed with 6 L of boiling water to remove any residual sodium. The resulting filter cake was dried overnight (16 h, 120 °C) before calcination to form the active catalyst (415 °C, 2 °C min^{-1}, 4 h). All catalysts were stored in a desiccator to avoid moisture.
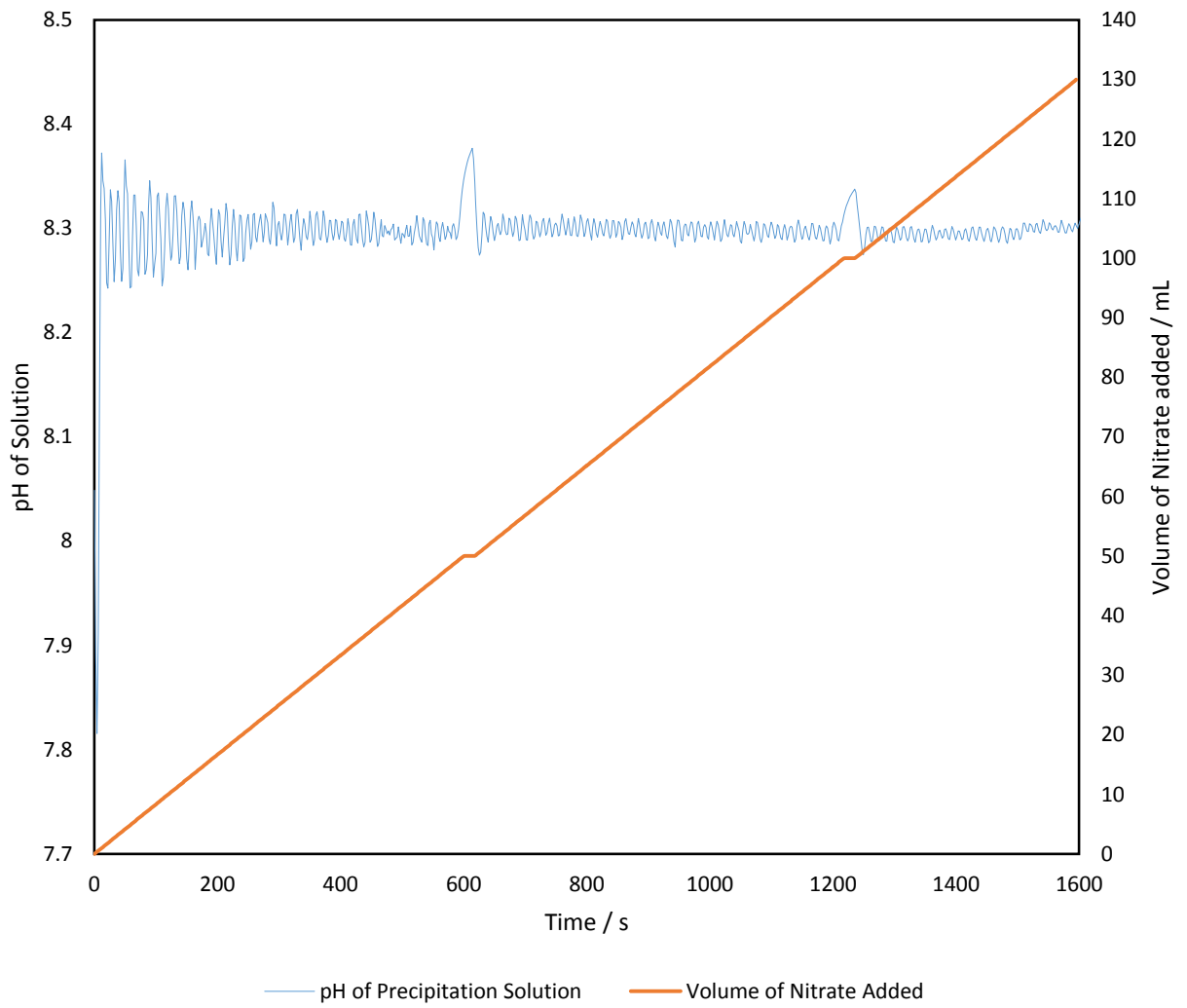
Figure 8: Representative example of the pH trend during the co-addition step illustrating the high accuracy possible using the auto titrator system.
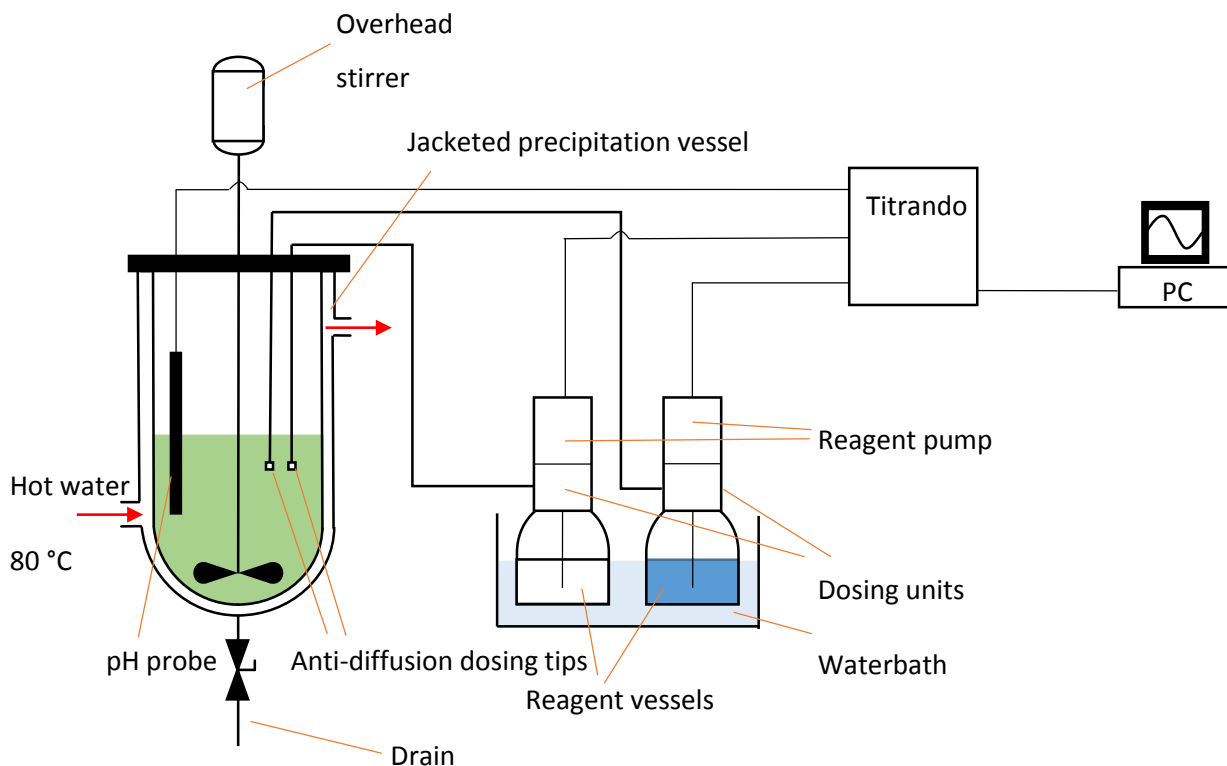
Figure 9: Schematic representation of the co-precipitation apparatus.

2.1.2 Addition of precious metals

For preparation of hopcalite catalysts containing precious metals an appropriate amount of copper was replaced with the desired metal. This resulted in a material with the molecular formula $Cu_{1-x}A_xMn_2O_4$ whereby A represents the precious metal. Two metals were investigated, silver and gold. For synthesis of the silver-containing catalyst solid $Ag(NO_3)$ (Aldrich, 99 % ACS reagent) was used as a silver source and was dissolved into the nitrate solution. The gold source was a solution of chloroauric acid (Aldrich, 99.999 %). The method for the preparation of the catalysts was the same as the undoped materials except for two factors which differed. The concentration of sodium carbonate was 0.25 M rather than 2 M in order to replicate the work of Solsona *et al* [5]. As a result the rate of nitrate addition was reduced from 5 mL min^{-1} to 2 mL min^{-1}.

2.1.3 Washing with water

To investigate the effects of washing on the catalyst material a sample of hopcalite was precipitated using the same method as discussed in section 2.1.1. However the addition of base and nitrates was controlled by two peristaltic pumps rather than the autotitrator system.

After filtering the aged catalyst precursor the material was washed with aliquots of boiling water and samples of the washed precursor were taken after every washing (*ca.* 0.25 g). The sample was washed with a total of 10 L of boiling water. Each sample was dried overnight (120 °C, 16 h) before being calcined to form the active material (415 °C, 2 °C min^{-1}, 4 h).

2.1.4 Washing with chelating agents

For this study a sample of hopcalite was prepared using the method detailed in section 2.1.1. After filtering the sample was split into 8 equal portions. Other than one portion that was left unwashed, each portion was washed with 200 mL of chelating agent solution (table 2) and 200 mL of water. The portions washed with water were washed with 400 mL of water. Samples were then dried overnight (120 °C, 16 h) and calcined (415 °C, 2 °C min^{-1}, 4 h)

Table 4: Solutions used to wash the catalyst precursours

Sample	Concentration / mol L^{-1}
Unwashed	N/A
Water (25 °C)	N/A
Hot water (90 °C)	N/A
15-Crown-5	0.00403
Citric acid	0.00403
Oxalic acid	0.00403
EDTA (0.2 M KOH)	0.00403
Hydrochloric Acid	0.1

2.1.5   Mechanochemistry

In order to prepare catalysts using mechanochemical methods a Retsch PM 100 planetary ball mill was used. The planetary ball mill operates by rotating a grinding vessel around a central point, as it spins the vessel also spins on its axis. This allows for more energy transfer into the materials.   All grinding processes described here were dry grinds with no added lubricant. They were also non-reactive grinds with no chemical reaction taking place.
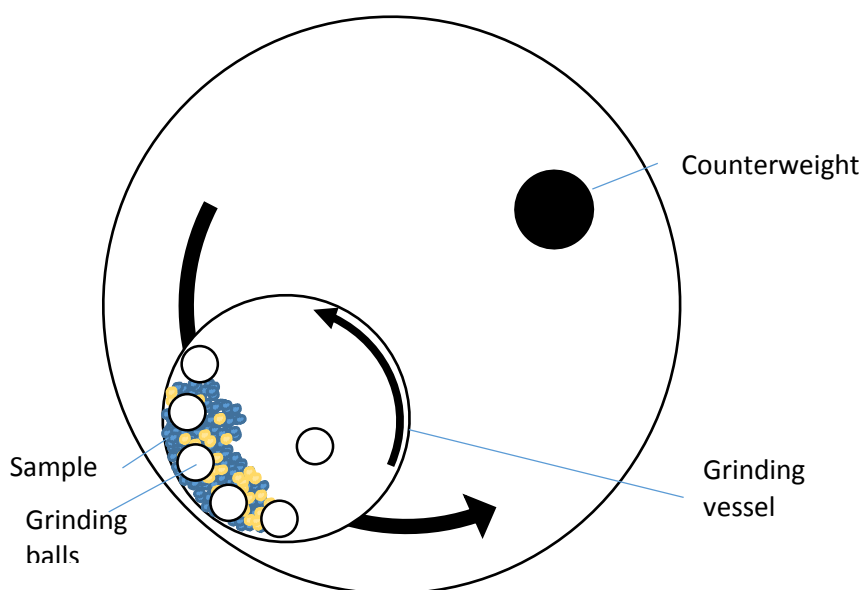
Figure 10: Schematic representation of planetary ball mill

2.1.5.1 Oxides

Powdered CuO (Sigma Aldrich, 99.99%) and Mn_2O_3 (Sigma Aldrich, 99.9%) were placed in the ball mill in a 1:2 molar ratio. The powders were ground for varying periods of time (0.5–72 h) at 400 rpm. The resulting dry solid powders were recovered and stored in a desiccator.

2.1.5.2 Carbonates

Powdered $Cu_2(OH)_2CO_3$ (Sigma Aldrich, 95 %) and $MnCO_3$ (Sigma Aldrich, 99.9 %) were placed in the ball mill in a 1:2 molar ratio. The powders were ground for varying periods of time (0.5–72 h) at 400 rpm. The resulting dry solid powders were recovered, calcined (415 °C, 2 °C min^{-1}) and stored in a desiccator.

$Cu(CO_2CH_3)_2$ (Sigma Aldrich, 98 %) and $Mn(CH_3CO_2)_2$ (Sigma Aldrich, 99.9 %) were placed in the ball mill in a 1:2 molar ratio. The materials were ground for varying periods of time (0.5–72 h) at 400 rpm. The resulting hard material was recovered, calcined (415 °C, 2 °C min^{-1}) and stored in a desiccator.

2.2 Testing

The activity of these catalysts was established using continuous flow reactor setups. This section details the apparatus along with their use.

2.2.1   Naphthalene oxidation
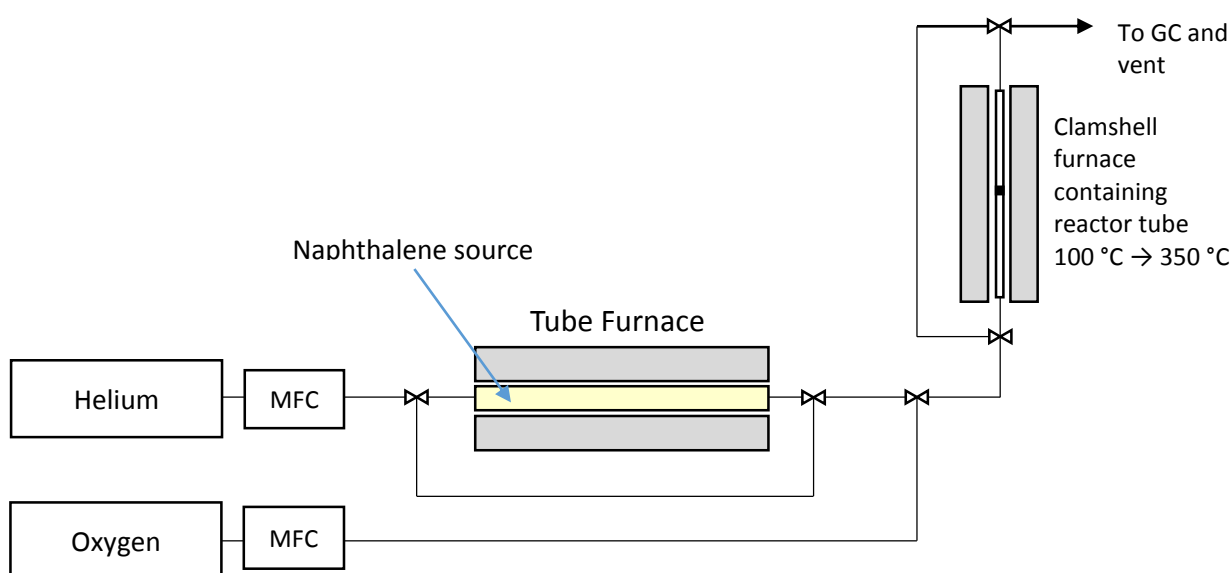
Figure 11: Schematic representation of the naphthalene oxidation apparatus

Figure 11 shows the reactor setup for the naphthalene oxidation reactor setup used for this testing. Gas flow was controlled by a pair of Brooks MFCs that were calibrated to give known flow rates. Helium was flowed through a bed of naphthalene heated to 40 °C in order to establish a flow of 100 vppm naphthalene. O_2 was then mixed in giving a gas mixture of 80 % He 20 % O_2. The naphthalene gas mixture is then flowed through a clamshell furnace where the catalyst bed was located. An appropriate volume of catalyst was used in order to

establish a gas hourly space velocity (GHSV) of 45000 h^{-1}. The clamshell furnace can be heated up to 350 °C. The gas flow then proceeds to a gas chromatograph for analysis. All lines were constructed using Swagelok and 1/8 inch stainless steel tubing. These were heated using heating cord and wrapped in glass fibre insulation. This was to prevent precipitation of naphthalene and any partial reaction products in the reactor.

2.2.1.1 Gas Chromatography

A gas chromatograph separates gases based on their relative affinity for the stationary phase situated on the column, compared with the mobile gas phase flowing through it. It is a useful technique for analysing gases. In this case two separate columns were used. The first, an OV-17 column was used to separate the naphthalene. Following this was a Carbosphere 80/100 column to separate the permanent gasses, O_2 and CO_2 from the gas mix.

2.2.1.2 Sampling of products

The gas stream was sampled using a 6-port valve fitted with a 500 μL sample loop. A large sample loop was required in order to introduce sufficient gas in order to detect the low concentrations of naphthalene studied. When in the fill position the loop was filled with gas from the reactor. When switched to the inject position the volume of the sample loop was flushed into the OV-17 column by the carrier gas which was He.

2.2.1.3 Separation of products

The two columns were located in series within the column oven. The OV-17 was located in the first position with the Carbosphere 80/100 following it. The Carbosphere 80/100 was also fitted with a bypass that used a restrictor valve in order to maintain the appropriate

column   pressure.
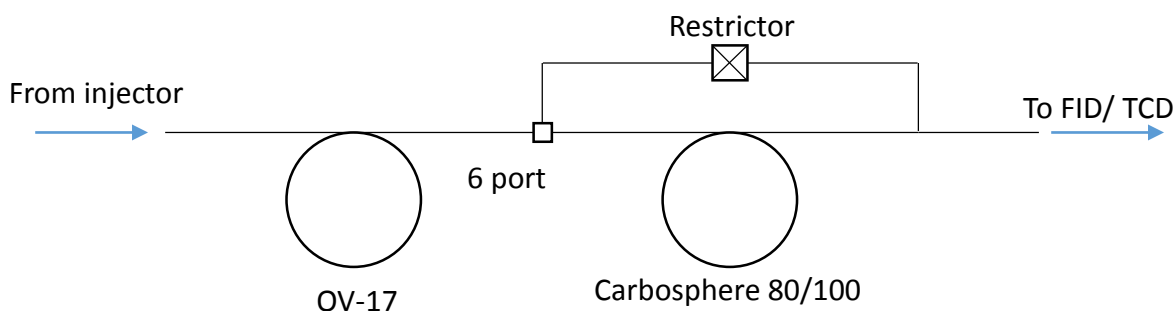
Figure 12: Schematic representation of the columns used to separate products of naphthalene oxidation.

Initially the gas stream flowed through the OV-17 then through the the Carbosphere 80/100.

Following this the 6-port valve controlling the bypass would switch to bypass the Carbosphere 80/100. This was necessary as the nature of the Carbosphere column prevents naphthalene or other heavy hydrocarbons from passing through it.

Table 5: Valve timings for the naphthalene oxidation GC. 1 refers to the sample valve and 2 to the column select valve. + denotes the valve in its initial position and - the second position.

Time / min	Valve position	Column Temperature / °C
0	+1, +2	100
0.01	-1, +2	100
1.25	+1, +2	100
12.00	+1, -2	200

In Table 3 the valve timings are displayed. Initially the sample loop is filling with the reactant gas. When the analysis starts this valve changes position to flow the sample into the OV-17 column only, the Carbosphere 80/100 is bypassed. Emptying the sample loop takes 1.25 min and after this time the injector valve returns to its initial state. After 12 min all permanent gases have flowed through the OV – 17 column, and at this point the Carbosphere bypass valve changes position in order to flow gas through this column to separate naphthalene from any potential partial oxidation products that may be present.

The Carbosphere 80/100 column allows the separation of CO_2 from O_2 at 100 °C. However due to its nature naphthalene will not travel through the OV-17 column at an acceptable rate. This necessitated the bypass of the Carbosphere column. Another factor that needed to be addressed is that at 100 °C the naphthalene would not travel; through the OV-17 column at an appropriate rate, therefore a temperature ramp from 100 to 200 °C increasing at 50 °C min^{-1} was programmed when the column switch occurred.

2.2.1.4 Analysis of products

A thermal conductivity detector (TCD) analysed the CO_2 produced by the reaction. This operates by monitoring the change in thermal conductivity of the gas passing over a hot filament compared with a reference He stream. As the thermal conductivity of the gas changes, so does the resistance of the filament. In order to quantify the amount of CO_2 produced the catalytic reaction was always taken to a point where the CO_2 response did not increase as the temperature increased. As CO_2 is the most thermodynamically stable product of the reaction it was taken that this value corresponded with 100 % CO_2 production. At lower temperatures the number of counts that corresponded to CO_2 were compared with this 100 % value in order to give a result for CO_2 produced.

$$\% \ CO_2 \ Production = \frac{Counts \ CO_2}{Counts \ 100 \ \% \ CO_2} \times 100$$

Following analysis by TCD a flame ionisation (FID) detector was used to analyse the naphthalene levels travelling through the reactor. It is important to locate the FID following the TCD as the FID destroys the sample by passing it into a hydrogen flame and combusting it. This results in ionisation of the sample, which is detected. At the beginning of experiment three injections, bypassing the reactor, were performed and the average naphthalene counts were used to determine the baseline of 100 vppm naphthalene for the experiment. As the

temperature was increased and the reaction undertaken this 100 % value was used to determine the levels of naphthalene consumption.

$$\% \; Naphthalene \; consumption$$

$$= 100 - \left(\frac{Counts \; Naphthalene}{Counts \; 100\% \; Naphthalene} \times 100 \right)$$

Partial oxidation is known to occur in this reaction system[6]; by comparing the naphthalene consumption and carbon dioxide production it is possible to identify if this is occurring. If there is a discrepancy between the CO_2 consumption and naphthalene production this suggests the presence of a partial oxidation pathway.

Elution of products occurred at the following times:

$O_2 - 3 \; minutes$

$CO_2 - 9 \; minutes$

$Naphthalene - 15 \; minutes$

2.2.2 CO Oxidation
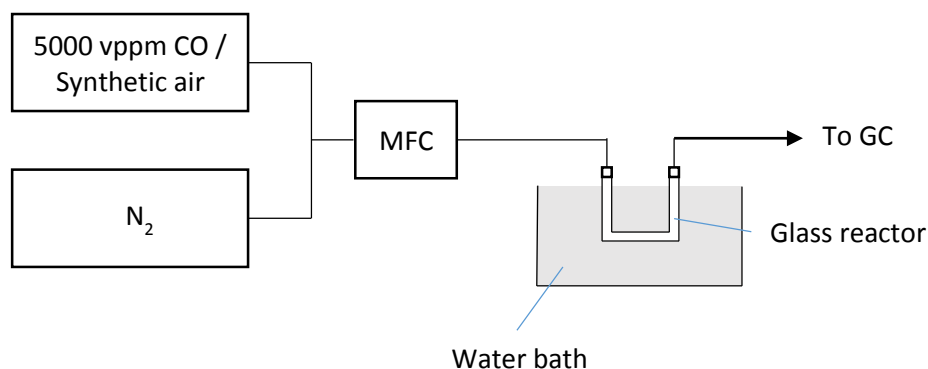
Figure 13: Schematic representation of CO oxidation apparatus.

5000 ppm CO in synthetic air (BOC) was flowed through a glass micro reactor containing 50 mg of the catalyst under investigation. This flow then proceeded to a gas chromatograph for analysis. Mass flow controllers maintained the flow at 20 mL min^{-1} while a water bath ensured that the catalyst bed remained at 25 °C. The use of a water bath was necessary to prevent temperature rises in the catalyst bed as a result of the exothermic CO $\rightarrow$ CO$_2$ reaction. Catalysts were typically tested for 1 hour. Nitrogen was used before and after each test to flush the system and prevent exposure to CO. CO alarms were present at all times during testing.

2.2.2.1 Gas Chromatography

A Supelco Carbosieve column (3 m x 35 mm) was used to separate CO$_2$ from the CO/ synthetic air mix. As CO and N$_2$ have similar polarity it was not possible to separate CO. Therefore all conversions reported are based on CO$_2$ production. The column oven was maintained at 195 °C during the analysis. Three peaks were observed in the GC trace, the first corresponded with the CO/ synthetic mix, the second with CO$_2$, and finally water.

The GC program resulted in the following retention times:

Synthetic air / CO mix – 1 min

CO$_2$ – 2 min

Water – 4 min

2.2.2.2 Analysis of products

The value for 100 % conversion of the 5000 vppm CO to CO$_2$ was established by using a World Gold council standard gold on iron oxide catalyst which is known to give 100% conversion of CO at low temperatures [7]. This was then used to compare the conversions observed.

$$\% \, CO_2 \, Production = \frac{Counts \, CO_2}{Counts \, 100 \, \% \, CO_2} \times 100$$

2.3 Characterisation

A wide variety of analysis techniques were used to investigate the physical properties of the catalysts and these are described in this section.

2.3.1 Powder X-ray diffraction (XRD)

A Panalytical powder diffractometer was used to analyse the samples using X-ray diffraction. Samples were ground to a fine powder and mounted in metal sample holders, or on non-diffractive silicon wafers. These were placed in the diffractometer where they were irradiated using monochromatic X-rays from a Cu source at 40 kV and 40 mA. The X-ray patterns resulting from this were compared with the International Centre for Diffraction Data (ICDD) database to identify the phases present.

2.3.1.1 Background

In 1913 Bragg described the diffraction of X-rays as they pass through crystalline materials [8]. His study found that when passing through the lattice of crystalline materials X-rays were diffracted by a value given by the equation $n\lambda = 2dsin\theta$ where λ is the wavelength of the irradiating X-ray, d is the lattice spacing and θ the angle diffracted. This became known as Bragg's law.
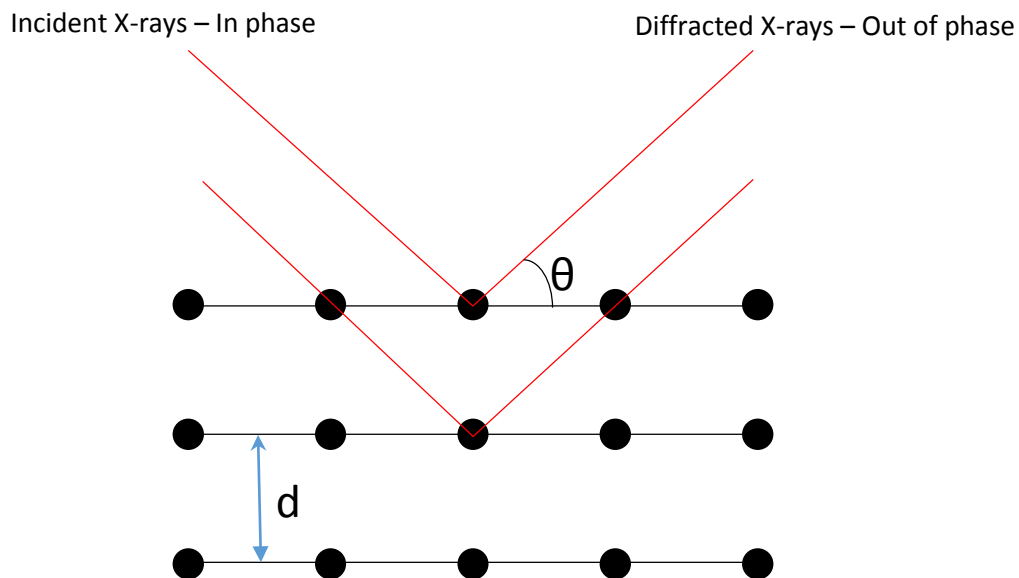
Figure 14: The diffraction of X-rays by a crystalline sample as described by Bragg.

The incident X-rays are in phase, up to the point where they come into contact with the sample. As the X-rays are diffracted, it is the resulting change path distance that causes constructive and destructive interference of the X-rays to take place. A powder sample gives of a cone of X-ray diffraction, the detector moves in an arc through this cone and measures the intensity of X-rays . As differing crystal structures and d-spacings will result in different diffraction patterns it is possible to identify phases by cross referencing the observed pattern with a library of patterns. In this work the library referenced is the ICDD database. Care should be taken, however, as materials of the same structure group will have similar patterns; in this case care was taken to correctly identify $CuMn_2O_4$ and Mn_3O_4 as both share the spinel structure.

2.3.1.2 Scherrer equation for determining crystallite size

Scherrer demonstrated that small particles broaden the diffraction angle for X-rays due to the shape of the particle having an effect on the path distance for a significant amount of the X-rays diffracted [9]. The practical application of this is that it is possible to estimate the particle size of a sample by studying the broadness of the peak. The following

equation, known as the Scherrer equation, was used to estimate the particle size of the catalysts.

$$D_{hkl} = \frac{K\,\lambda}{B_{hkl}\,Cos\,\theta}$$

D_{hkl} refers to the particle size of the material in relation to its Miller indices, K is the crystalline shape factor which may change depending on the morphogy of the particles, λ is the wavelength of the diffracted X-rays, B_{hkl} is the full width half maximum (FWHM) of the peak and θ the angle at which the X-rays have been diffracted. It is worth noting that this method has drawbacks. The sample must be highly crystalline to avoid interference from defects and strain within the lattice, which can cause erroneous results[10]. The signal-to-noise ratio for the FWHM is important as if the crystallite is too small then the noise will introduce error into the calculation.

2.3.1.3 Rietveld refinement to analyse non crystalline phases

X-ray diffraction is very powerful when analysing crystalline materials, however when the materials are non-crystalline or nanocrystalline in nature then it cannot detect them as repeating, well-defined lattice planes are required to give the requisite X-ray interference. Rietveld refinement is a technique whereby an estimate can be made of the amorphous content of the material by building a model of the X-ray pattern[11]. Using the least squares method a line profile can be made that matches with the observed diffraction. By comparing with a highly crystalline reference such as silicon it is possible to estimate the percentage of the material that is unaccounted for in the observed diffraction *i.e.* amorphous.

Panalytical pro X-pert software was used to perform the analysis. The line fitting was done using a pseudo-Voight function. The parameters were then refined using order of scale factors, zero shift, cell parameters, thermal parameters peak shape function and finally preferred orientation in order to refine a suitable pattern.

In order to investigate the changes in the phase makeup of the materials during the calcination process an *in situ* XRD study was undertaken. Catalyst precursors were heated under static air conditions in an Anton Paar 900 K *in situ* cell. A diffraction pattern at room temperature was taken before heating to 600 °C at a rate of 2 °C min^{-1} to replicate the conditions found during calcination. Further diffraction patterns were recorded every 25 °C to record the decomposition of the precursor to form the catalyst.

2.3.2   Brunauer–Emmett–Teller surface area analysis (BET)

A small quantity of sample was degassed under flowing nitrogen at 120 °C for 30 mins. This degassed sample was then placed in a Micromeretics Gemini instrument. Using liquid N_2 to chill the sample a five-point adsorbtion isotherm was generated and used to determine the surface area of the sample. The nature of the analysis technique used and the instrument lead to a 10 % error in the measurement.

2.3.2.1 Background

The BET isotherm method of measuring surface area was developed by Brunauer, Emmett and Teller [12] and is an extension on previous work performed by Langmuir[13]. The BET method is used to determine surface area by adsorbing a gas, usually N_2, onto the surface of the material under investigation at the condensation temperature of the gas. For N_2 adsorbtion this is 77 K. The isotherm is acquired by plotting the amount of gas adsorbed onto the surface of the sample at this temperature against the pressure. The Langmuir adsorbtion isotherm assumes that the coverage of adsorbate will form a monolayer and not adsorb further.
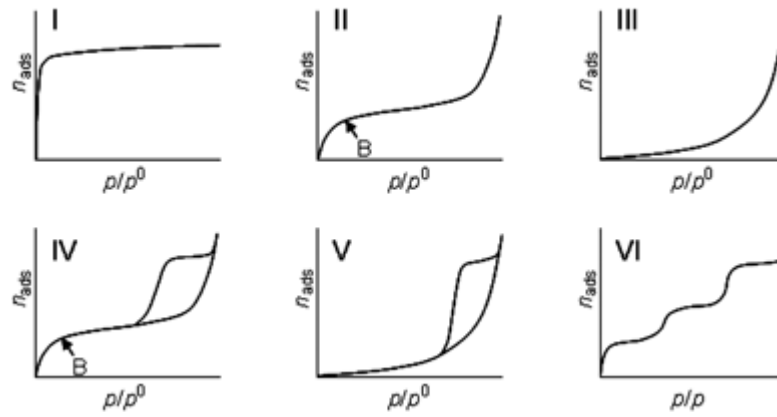
Figure 15: The various adsorbtion isotherms possible. I represents the Langmuir isotherm while II is the BET isotherm. B refers to the point at which monolayer coverage has been established. Adapted from [14]

The BET isotherm takes this further and accommodates multilayer formation on the surface of the material under investigation. It assumes that initially a monolayer will form. Only at pressures where there is complete coverage will the adsorbate adsorb atop the monolayer to form multilayers. The BET adsorption equation is displayed below.

$$\frac{P}{V(P_oP)} = \frac{1}{V_mC} + \frac{(C-1)P}{CV_mP_o}$$

Where P refers to pressure, P_o is the saturation pressure, V_m is the volume of a monolayer per unit mass and C is a constant. The constant is the result of the assumptions that must be made to accommodate the possibility of multilayer adsorption. It is assumed that the first layer is physisorbed with an associated heat of adsorption (E_l). Further layers adsorb with a heat of adsorption equal to the heat of condensation for the adsorbate (E_L). The adsorption process is a dynamic equilibrium, between the adsorbed layer and the gas phase; considering this the following equation can be described:

$$C = \frac{(E_lE_L)}{RT}$$

If P/V(P$_o$P) is plotted against (P/P$_o$) then V$_m$ can be calculated. As the area of an N$_2$ molecule is known to be 14 Å^2 this can be used to establish the surface area of the material under investigation.

2.3.3 X-ray photoelectron spectroscopy (XPS)

X-ray photoelectron spectroscopy was used to analyse the surface composition of the catalysts. A Kratos Axis Ultra DLD photoelectron spectrometer was used to gather spectra of the materials studied. The spectrometer was fitted with an Al source giving a photon energy of 1486.6 eV and all spectra were calibrated to adventitious carbon at binding energy 284.7 eV. High resolution scans were performed with pass energies of 40eV and the wide scan used a pass energy of 160 eV. The analysis area was 700 x 300 microns.

2.3.3.1 Background

X-rays are known to cause the ejection of core electrons from atoms upon absorbtion. When electrons are ejected due to the influence of electromagnetic irradiation they are known as photoelectrons. Due to the law of conservation of energy, it is possible to determine the binding energy (E$_b$) of the ejected photoelectrons electrons if the energy of the incident x-ray is known (hv) along with the kinetic energy of the ejected electron (E$_{kin}$).

$$E_{kin} = hv - E_b$$

The kinetic energy is therefore characteristic of the species under investigation and can be used to identify the elements present along with their respective oxidation states.
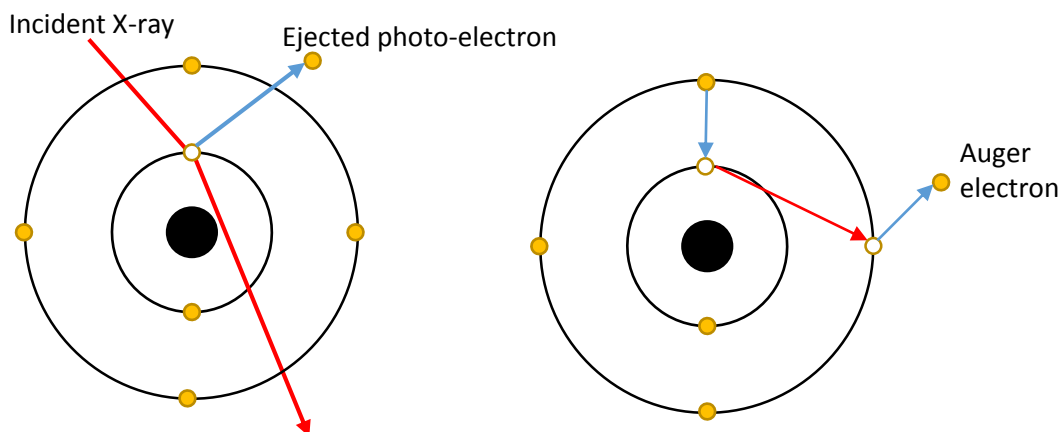
Figure 16: Schematic of x-ray photo-electron emmision and subsequent Auger emmision

When a core electron vacancy is generated a high-energy electron can transfer into the lower energy state. The excess energy of the electron is then released, either as x-ray emission or into another electron which is ejected. If a second electron is ejected it is referred to as an Auger electron. Auger spectroscopy is a useful second technique to assess the oxidation state of materials and was used to study copper in this case.

2.3.4 Microwave plasma atomic emission spectroscopy (MP-AES)

Microwave plasma atomic emission spectroscopy was used to determine the precise elemental composition of the catalysts prepared in this thesis. An Agilent 4200 MP-AES was used. A known mass of catalyst was dissolved in 5 mL of *aqua regia* and diluted up to 50 mL to form the solutions to be analysed. These samples were then sprayed through a nitrogen plasma using a single-pass nebuliser. The pressure of the spray was 240 kPa and no air injection was used. The emission lines used for analysis are detailed in Table 4. Each sample was run three times and the average result used.

Table 6: Emission lines used to analyse elemental composition of catalysts by MP-AES

Element	Emission line used / nm	
Cu	324 .8	327.1
Mn	404.1	403.4
Na	588.9	589.5
Au	242.8	267.6
Ag	328.1	338.3

Between samples a 10 % *aqua regia* rinse was applied to the instrument to clean it. Calibration was performed using 5000 ppm metal standards (Sigma Aldrich) diluted to the appropriate concentration using 10 % *aqua regia*.

2.3.4.1 Background

Microwave plasma atomic emission spectroscopy (MP-AES) operates by the same principles as traditional atomic emission spectroscopy (AES) changing only the method of exciting the metal ions under study[15]. In this case an Ar catalysed N_2 plasma is used to excite the metal ions under investigation. As the excited ions return to the ground state they shed the excess energy by emitting photons. These photons are characteristic to each element and as such allow identification of the elements present and their relative concentration.
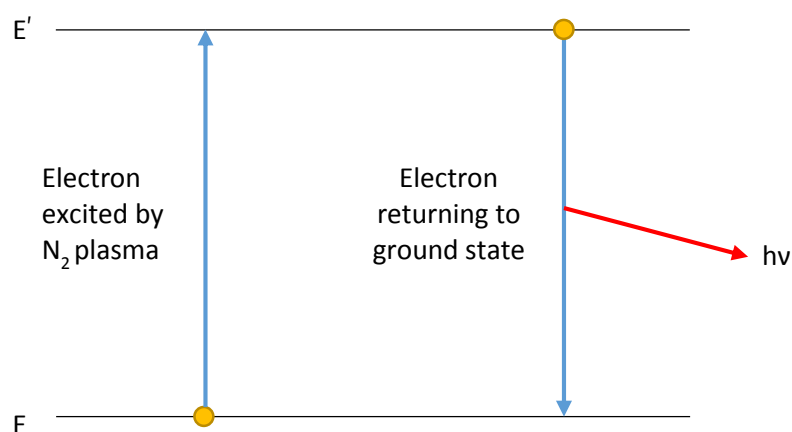

Figure 17: Atomic emission from excited electrons

2.3.5 Thermogravimetric analysis (TGA)

A Perkin-Elmer TGA 4000 fitted with auto sampler was used to analyse the thermal decomposition of catalyst precursors. 20-50 mg of sample was loaded into ceramic crucibles. The samples were loaded into the TGA using a robotic auto sampler, heated from room temperature to 600 °C at a rate of 5 °C min^{-1} in an atmosphere of static air, and the mass profile was recorded. This mass profile was expressed as a percentage of the initial mass of the sample loaded.

2.3.5.1 Background

When samples are calcined to form the active species it is important to investigate the thermal decomposition of the sample to determine appropriate calcination conditions as well as offer more information regarding the nature of the catalyst precursor. Thermogravimetry allows investigation of this by monitoring the mass of sample as it is heated, in this case in air, using a sensitive balance located in a furnace. In the case of the carbonate precursors that this thesis mainly focuses on, the samples it will initially lose adsorbed water. As the temperature increases we can expect loss of mass associated with the decomposition of carbonates to form CO_2 by the following process.

$$MCO_3 \rightarrow MO_x + CO_2$$
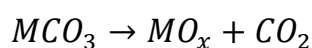
Different carbonate species will decompose at different temperatures and rates. This allows the identification of species that may not be detectable by other means such as XRD.

2.3.6 Thermal programmed reduction (TPR)

A Quantochrome ChemBet was used to perform TPR experiments. A known quantity of catalyst was loaded into a glass u-tube packed between two wads of glass wool. The tube was then connected to the analysis instrument by ultra-torr fittings and placed in an

external furnace. 10 % H_2 in argon was then flowed over the sample (30 mL min^{-1}) as it was heated from room temperature to 800 °C (15 °C min^{-1}). The hydrogen consumption over this temperature range was monitored by use of a TCD and quantified by calibration of the hydrogen consumption of known amounts of CuO over the same range.

2.3.6.1 Background

As oxides are heated under a flow of hydrogen they react to form more reduced species. TPR investigates this and quantifies the ease with a material is reduced. H_2 abstracts oxygen from the lattice of oxides and differing species will react with hydrogen at different temperatures. By monitoring the hydrogen consumption we can investigate the bulk oxidation state of materials as well as quantify the relative amounts of each species. The rate at which hydrogen consumption increases can be related to the ease at which the sample is reduced. The reducibility of materials can be related to the oxygen mobility of an oxide. If a sample has a high hydrogen consumption over a small temperature range then it is likely that the sample is highly reducible with high oxygen mobility. If consumption is lower over a larger range than it likely has low oxygen mobility and is not reducible as a result. This is significant as many reactions proceed by a mechanism where the mobility of lattice oxygen plays a role[16].

2.3.7 Scanning electron microscopy (SEM)/ Energy-dispersive X-ray spectroscopy (EDX)

A Zeiss scanning electron microscope was used to acquire SEM images for this thesis. This was fitted with a liquid N_2 cooled Oxford Instruments energy dispersive X-ray analyser. The EDX data was analysed using INCA software.

Samples were mounted on adhesive carbon disks attached to aluminium stubs. These were mounted within the chamber which was evacuated of air. Images were collected with an accelerating voltage of 25 keV and I-probe values of 0.5-1 nA. EDX data was

acquired with i-probe values of 25 nA to give sufficient X-ray production. Images were acquired with both secondary electron and back scattered electron detectors.

2.3.7.1 Background – SEM

High energy electrons emitted from a tungsten filament are used to investigate the surface morphology of materials. Under high vacuum electrons from the filament are focussed through a series of magnetic lenses and directed at the sample under investigation. Secondary electrons are generated by interaction between the beam and the sample which are detected in order to get topographical information. Conduction band electrons are ejected from the sample when the electron beam impacts it. Electrons from the beam can also be back scattered, as elements with higher atomic numbers back scatter more efficiently this can be used to gain elemental information. The electron beam is then rastered back and forth across the surface of the sample in order to build up an image.
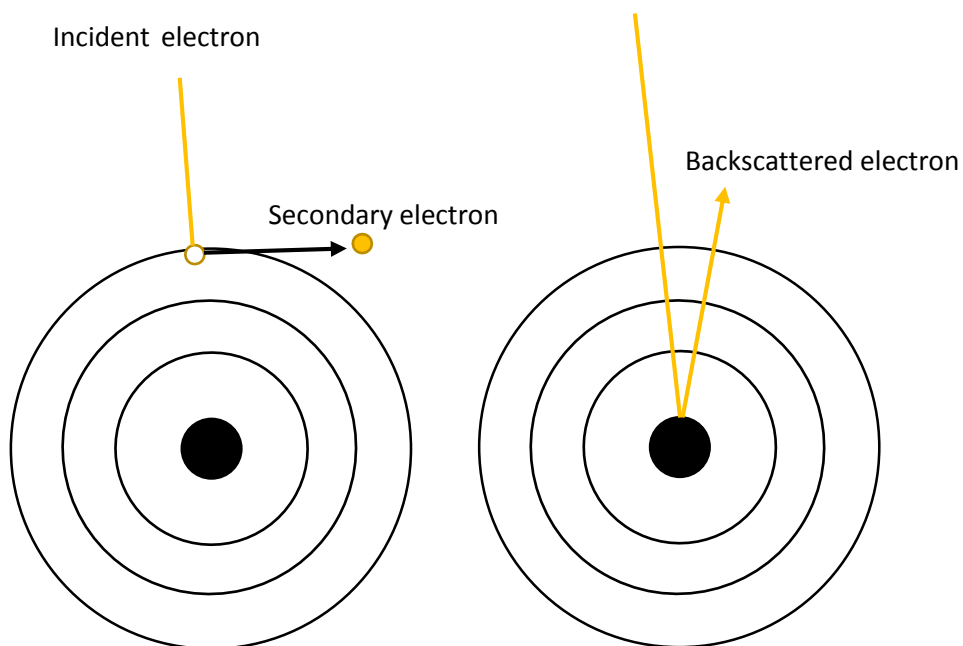

Figure 18: Illustration of the two electron-sample interactions used for imaging purposes, Secondary electron emission (left) and electron backscattering (right).

The secondary electron detector is usually located to the side of the sample whereas the backscatter detector is located around the electron gun aperture.

There are two variables that are manipulated to control image quality; accelerating voltage and i-probe. In this work the accelerating voltage was maintained at 25 keV for consistency however on samples that are susceptible to beam damage a lower voltage can be used. I-probe is a measure of the beam current. An illustration of the effects of varying I-probe can be seen in Figure 11. Low I-probe values allow the beam to be focussed to a fine tip and allow imaging of detailed surface features. However as the electron flux will be lower images may have a high signal-to-noise ratio.
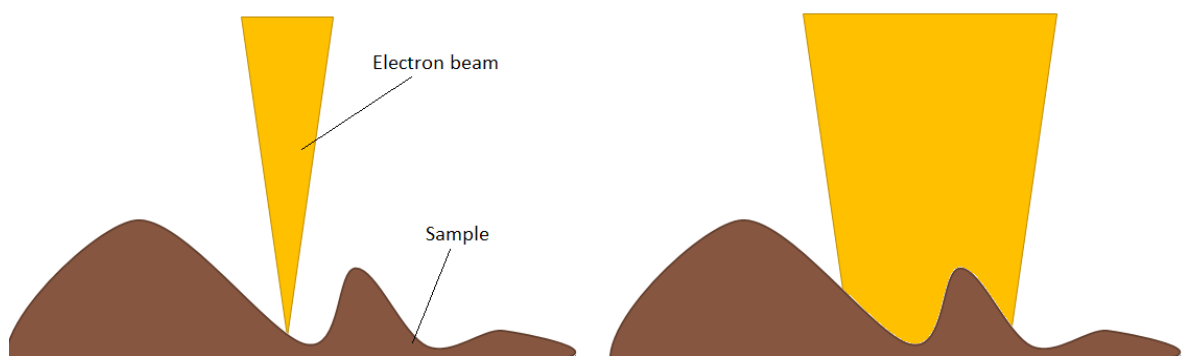
Figure 19: Illustration of the difference between imaging with a low I-probe value (left) and a high I-probe value (right)

High I-probe values on the other cannot be focussed to the same extent and as a result details and small structural features may not be detected. However the high electron flux allows for clearer images. Charging of samples can also occur when using high I-probe values, especially for samples that are poorly conducting such as metal oxides.

2.3.7.2 Background – EDX

Along with secondary electrons emitted by excitation of conduction band electrons, core electrons may be removed in a similar process to that which occurs in XPS. When this occurs a high-energy electron can relax into the vacancy generated and emit a photon to remove the excess energy it has. This photon will have a characteristic energy associated with it depending on the element and as such can be used to identify elements present in the material. High I-probe values are required in order to get sufficient X-ray emission to have a

representative study of a sample and as a result imaging while undertaking EDX analysis is difficult. However it can be useful as it is possible to determine the origin point of X-rays that are generated and as such can map the relative location of elements within a sample.

2.3.8   Transmission electron microscopy (TEM)

Transmission electron microscopy was used to image the nanostructure of the catalysts. A JEOL 2100 microscope located at the Rutherford Appleton laboratory in the Harwell research complex was used to acquire images. The microscope was fitted with a LaB_6 filament and operated at 200 keV. Samples were suspended in methanol before being deposited on holey carbon TEM grids and loaded into the microscope through an airlock.

2.3.8.1 Background

TEM was developed by Ernst Ruska who received a share of the 1986 Nobel Prize for physics for his invention[17]. A focussed, high-energy electron beam is directed at a sample. The electron beam passes through the sample, and depending on its density some electrons are absorbed and others transmit through. The transmitted electron beam is then focussed onto a fluorescent screen or camera at the base of the microscope where the image is generated. As electrons behave as waves as well as particles some of the beam is diffracted as it passes through the sample. This diffraction can be used to identify crystalline phases present within the material studied.

2.4 References

[1]   G.J. Hutchings, A.A. Mirzaei, R.W. Joyner, M.R.H. Siddiqui, S.H. Taylor, Catal. Lett. 42 (1996) 21-24.
[2]   G.J. Hutchings, A.A. Mirzaei, R.W. Joyner, M.R.H. Siddiqui, S.H. Taylor, Applied Catalysis A: General 166 (1998) 143-152.
[3]   A.A. Mirzaei, H.R. Shaterian, M. Habibi, G.J. Hutchings, S.H. Taylor, Applied Catalysis A: General 253 (2003) 499-508.
[4]   C. Jones, K.J. Cole, S.H. Taylor, M.J. Crudace, G.J. Hutchings, Journal of Molecular Catalysis A: Chemical 305 (2009) 121-124.
[5]   B. Solsona, T. Garcia, S. Agouram, G.J. Hutchings, S.H. Taylor, Applied Catalysis B: Environmental 101 (2011) 388-396.
[6]   X.-W. Zhang, S.-C. Shen, L.E. Yu, S. Kawi, K. Hidajat, K.Y. Simon Ng, Applied Catalysis A: General 250 (2003) 341-352.

[7]   M. Haruta, S. Tsubota, T. Kobayashi, H. Kageyama, M.J. Genet, B. Delmon, Journal of Catalysis 144 (1993) 175-192.

[8]   W.H. Bragg, W.L. Bragg, The Reflection of X-rays by Crystals, 1913.

[9]   P. Scherrer, Nachrichten von der Gesellschaft der Wissenschaften zu Göttingen, Mathematisch-Physikalische Klasse 1918 (1918) 98-100.

[10]   J.I. Langford, A.J.C. Wilson, Journal of Applied Crystallography 11 (1978) 102-113.

[11]   H. Rietveld, Journal of Applied Crystallography 2 (1969) 65-71.

[12]   S. Brunauer, P.H. Emmett, E. Teller, Journal of the American Chemical Society 60 (1938) 309-319.

[13]   I. Langmuir, Journal of the American Chemical Society 40 (1918) 1361-1403.

[14]   C. Weidenthaler, Nanoscale 3 (2011) 792-810.

[15]   W. Li, P. Simmons, D. Shrader, T.J. Herrman, S.Y. Dai, Talanta 112 (2013) 43-48.

[16]   P. Mars, D.W. van Krevelen, Chemical Engineering Science 3 (1954) 41-59.

[17]   E. Ruska, Angewandte Chemie International Edition in English 26 (1987) 595-605.

A study on the use of copper manganese oxide catalysts for the total oxidation of naphthalene.

3.1 Introduction

Volatile organic compounds (VOCs) are defined by the EU in the 1999 Paints Directive as "organic compounds having at 293.15 K (i.e., 20°C) a vapour pressure of 0.01 kPa or more"[1]. Levels of VOCs are strictly controlled under EU law, as many have toxic and carcinogenic properties[1-3] .Treatment of volatile organic compounds (VOC's) by catalytic oxidation is widely recognised as an effective method for controlling theirn their emission[4]. In recent years to comply with increasing levels of regulation[5] there has been much attention focused on VOC oxidation. However, the subclass of polycyclic aromatic hydrocarbons (PAHs) has received relatively little attention[6]. PAHs are produced from incomplete combustion of organic matter, such as wood, and can be a contributing factor in serious health issues such as breathing conditions and cancer[7]. PAH's can be extremely toxic to handle, as such research concentrates on the total oxidation of the simplest PAH, naphthalene. With its low sublimation temperature and relatively benign properties, it is the ideal model to study as its activity can be extrapolated to PAHs containing more ring systems.

Studies of naphthalene oxidation were pioneered by Zhang *et al.*[8]. Their initial work focussed on the use of supported metals on γ-Al$_2$O$_{3.}$ It was found that catalysts containing platinum were the most active[9, 10]. The support used also shows a strong influence on naphthalene oxidation, with platinum supported on silica exhibiting very high activity[11].

The rarity and expense of the platinum group metals has driven research towards more abundant, cheaper metal oxides. Previous work by Taylor and co-workers has investigated a range of precipitated metal oxides including Co_3O_4, Mn_2O_3, ZnO, CuO, Fe_2O_3 and CeO_2 [12]. It was found that nanocrystaline ceria was the most active of these, due to its good oxygen storage capacity and redox properties. Mn_2O_3 has been shown to have appreciable naphthalene oxidation activity. Studies based on nanocasting also demonstrate that high surface area Mn_2O_3 is very active[13].

The mixed copper manganese oxide spinel catalyst, known as hopcalite, is well known for its low temperature CO oxidation activity[14], and has been studied for the best part of a century[15]. Studies also suggest that hopcalite oxidised a wide range of VOCs, including both aliphatic[16] and aromatic hydrocarbons[17] along with their chlorinated equivalents[18]. To date there have been no studies on the activity of hopcalite for the total oxidation of PAHs. This chapter details our investigations into the activity of Hopcalite as a naphthalene oxidation catalyst and the effect of doping using silver and gold on the activity of the catalyst.

For the catalysts in the calcination study, hopcalite catalysts were precipitated from a 0.5 M solution of copper and manganese nitrate premixed in a 1:2 ratio. A 2M solution of sodium carbonate in a 1:2 was used as the precipitating agent. A Metrohm Titrando auto-titrator was used in order to maintain the pH at the desired 8.3.

In the experiments regarding hopcalite doping, hopcalite catalysts were produced using a premixed 0.5M solution of copper manganese nitrate in a 1:2 ratio, precipitated by a 0.25M sodium carbonate solution as described in previous work by Solsona *et al.* [16]. It has been determined by previous work that 2M is the optimum concentration for the precipitating sodium carbonate solution, however 0.25M was chosen in this case, to make a better

comparison with the work by Solsona on gold doping for propane oxidation and was used for all doped catalysts.

A Metrohm Titrando autotitrator was used in order to maintain the pH at the desired 8.3. Copper was replaced by 1, 3 or 6 wt% Au or Ag as appropriate to produce the desired catalyst. So that an accurate comparison may be made an undoped catalyst was also produced. All catalysts were calcined at 400 °C. Full details of all catalysts preparations can be found in section 2.1.1.

3.2 Results of undoped catalyst calcination study

3.2.1 Precursor characterisation

X-ray diffraction of the catalyst precursor is shown in Figure 20. The observed diffraction pattern shows the presence of a manganese(II) carbonate phase with no corresponding copper phase present. Previous work suggests that the copper may be present as an amorphous or nanocrystaline phase, not detectable by XRD [19]. Another explanation that is discussed at further length in Chapter 4 is that the copper has been incorporated into the lattice of the $MnCO_3$ to form a $Cu_xMn_{1-x}CO_3$ phase [20] and this is supported by the shift in peak position in the precursor when compared with manganese carbonate. This has been shown to occur in the naturally occurring $MnCO_3$ phase; Rhodacrosite [21]. Work by Thomas and co-workers also supports this hypothesis showing that CuMn mixed carbonates can be synthesised [22].
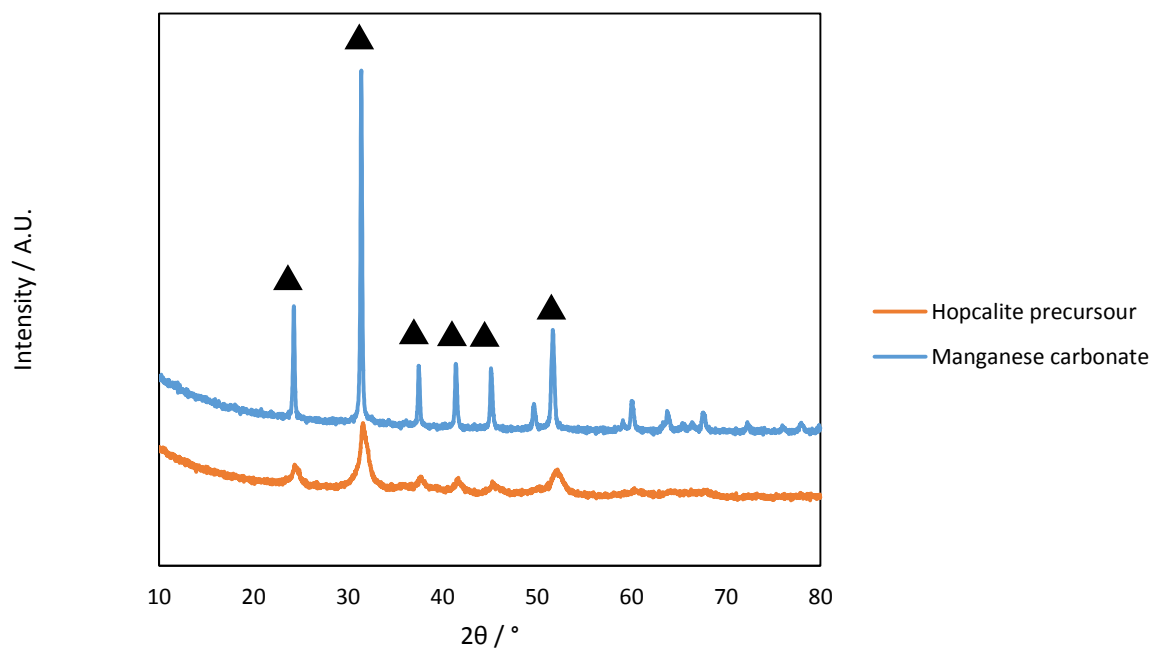
Figure 20: XRD of the undoped hopcalite precursour along with a reference manganese carbonate 40mA 40 kV Cu source ▲ = $MnCO_3$ (ICDD: 01-071-3820)
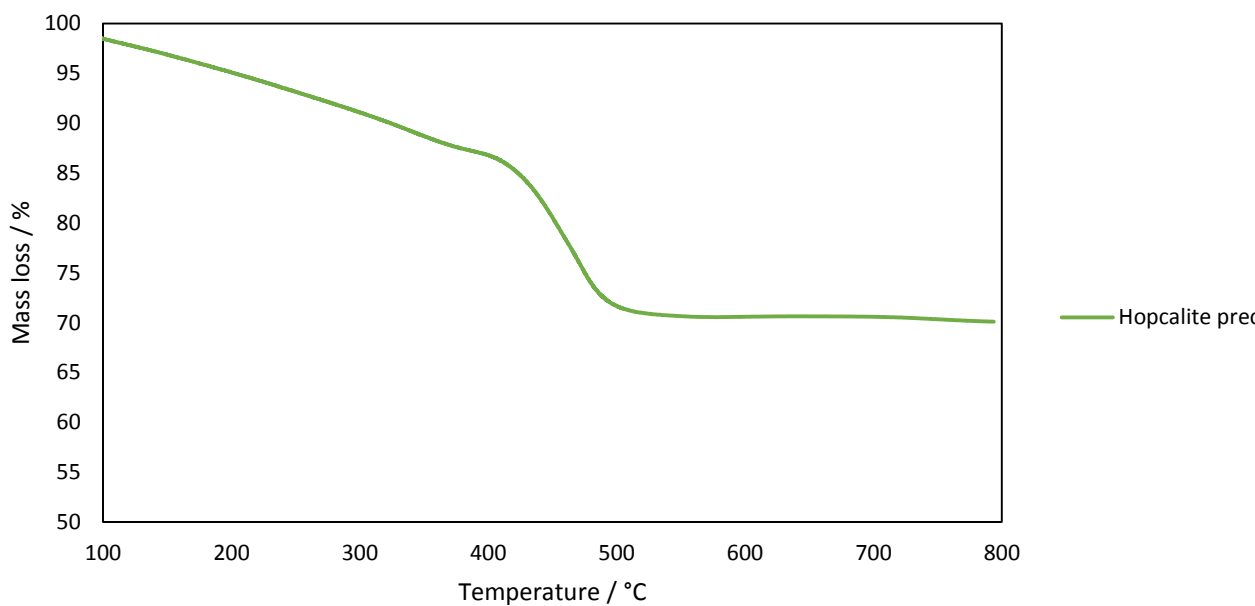
Figure 21: TGA of the uncalcined hopcalite precursor, Air atmosphere, flow rate 50 mLmin^{-1}

TGA (Figure 21) of the catalyst precursor shows a gradual mass loss associated with evolution

of physisorbed water followed by a sharp mass loss at *ca.* 415C. 13% of the total initial mass

of the precursor was physisorbed water and the second sharp mass loss associated with the

decomposition of the carbonate phase was 20% of the initial mass. The DTA trace also suggests that the process observed is endothermic. From the XRD and the endothermic nature of the mass loss event it is reasonable to deduce that the mass change is due to the thermal decomposition of the metal carbonate phase to form an oxide, with the resulting evolution of CO_2. If the mass loss was associated with the loss of $MnCO_3$ or $Cu_xMn_{1-x}CO_3$ alone then we would expect a mass loss in the region of 30%, this suggests that $MnCO_3$ is not the only phase present and there is another phase that does not show in the XRD. Further work would be needed to offer a definitive explanation.

3.2.2 XRD of the calcined catalysts

The catalysts were calcined as described in section 2.2.1 at 300, 400 500 and 600 °C. After calcination at 300 °C there is still evidence of the $MnCO_3$ precursor phase being present in the catalyst and no evidence of any oxide formation. This is in agreement with the TGA data presented in Figure 21, as the calcination temperature is below the temperature at which mass loss, and hence oxide formation by the thermal decomposition of the carbonate phase, is observed. Compared with the precursor XRD however there has been a significant broadening of the reflections, indicating a loss of long range order and the formation of more domains with amorphous or nanocrystaline character.
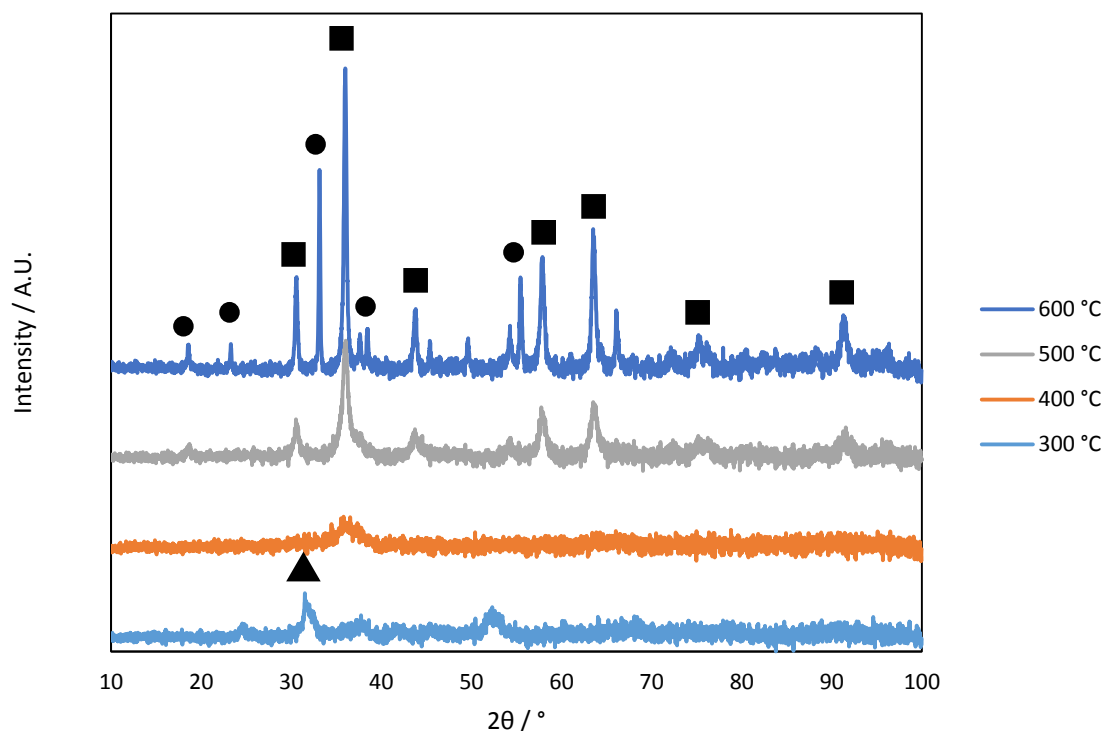
Figure 22: XRD of the calcined hopcalite catalysts. 40mA 40 kV Cu source. ■ = CuMn$_2$O$_4$ (ICDD: 01-075-0826) ●= Mn$_2$O$_3$ (01-071-3820) ▲ = MnCO$_3$ (01-071-3820)

Figure 22 shows the XRD of the calcined catalysts. Calcination at 400 °C results in a sample that exhibits no sharp diffraction peaks, the only observable feature is a broad diffraction around 35°. Previous work has shown that this broad feature can be indicative of amorphous or nanocrystaline CuMn$_2$O$_4$[23]. Further work by Cole has shown that this amorphous phase is the most active phase for CO oxidation [23]. This high CO oxidation activity is associated with mobile lattice oxygen that is available for use in a Mars van krevelen type reaction mechanism [24]. Wang suggested that in the oxidation of single ring aromatic species on manganese oxide that the availability of labile lattice oxygen was a key contributor toward catalyst activity [25]. This suggests that this material may be active for naphthalene oxidation also.

When calcined at 500 °C there is a well-defined CuMn$_2$O$_4$ phase observed, with clear evidence of reflections at 36°, 57° and 63° corresponding to the (311), (511) and (440) planes

of copper manganese oxide respectively. All the reflections observed correspond to copper manganese oxide.

At a calcination temperature of 600 °C, the reflections at 36°, 57° and 63° are observed to be sharper and more well-defined, this is due to an increase in the crystallinity and long range order of the sample. Use of the Scherrer equation demonstrates that the crystallite size increases from 44 nm to 53 nm with this increase in calcination temperature (Table 1). Also observable upon calcination at 600 °C are a number of new reflections not observed at 500 °C. Principle amongst these new reflections is one at 33.1°. This corresponds to the principle reflection of Mn_2O_3 (222) plane. This is unexpected as there is no evidence of a manganese oxide phase in any of the samples calcined at lower temperatures. This suggests that there is either an undetected, amorphous manganese phase present in the other samples or that the sample has phase separated at high temperatures. The first explanation is more likely as there is no corresponding evolution of a copper only phase at 600 °C nor is there any shift in the position of the reflections associated with $CuMn_2O_4$ that could suggest a change in the Cu:Mn ratio of that phase that would bring about changes in unit cell dimensions.

3.2.3   TPR of the calcined catalysts

Figure 23 shows the temperature programmed reduction data for the four calcined hopcalite samples. The complex reduction pattern exhibited is typical of copper manganese oxide catalysts [26]. The accepted structure for the copper manganese species is a spinel type structure[27], however it has been shown that there is an inverted spinel component to the structure [28]. To add to this complexity there is also evidence that both the copper and manganese components can exist in multiple oxidation states [27]. When these factors are considered, alongside the presence of un-oxidised carbonate species, amorphous phases and the manganese oxide phase identified in Figure 23, unambiguous assignment of reduction events is difficult.
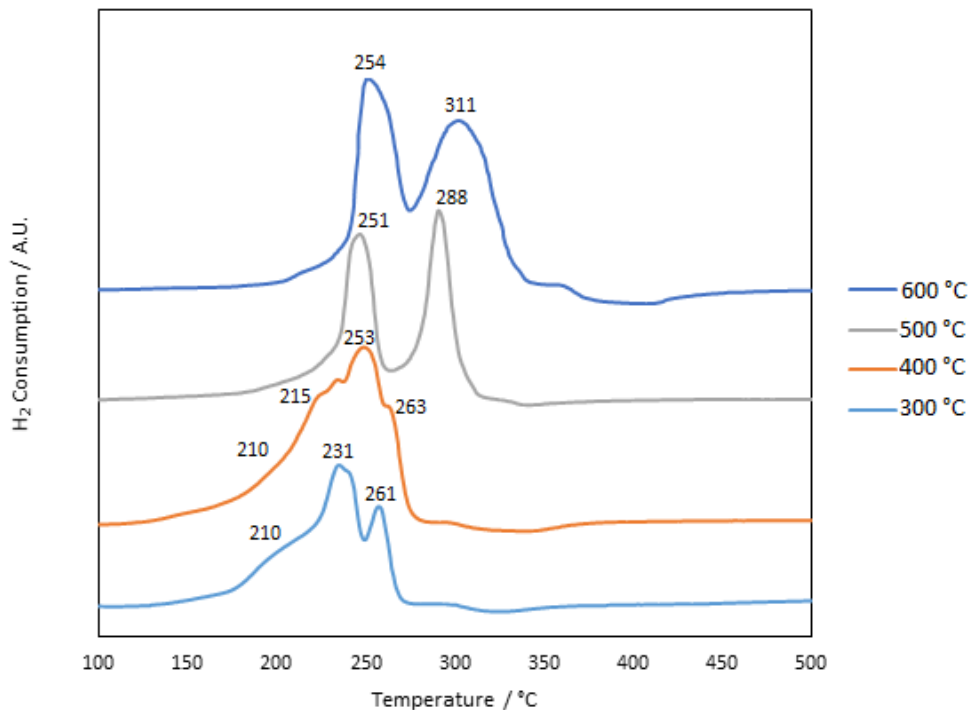
Figure 23: TPR of the calcined hopcalite catalysts illustrating the changing oxidation state of the catalysts as calcination temperature is increased. 20mL min^{-1} 10 % H_2/Ar, 5°C min^{-1}

The catalyst calcined at 300 °C exhibited little reduction in comparison with the materials calcined at higher temperatures (

Table 7), this is due to incomplete oxide formation and the presence of carbonate phases. The catalyst calcined at 400 °C was the catalyst that reduced at the lowest temperature of the three catalysts in which complete carbonate decomposition had occurred, and hence has the highest concentration of labile oxygen available for catalysis. Overall reducibility decreased with calcination temperature, presumably as the more crystalline materials bind the lattice oxygen more strongly than their amorphous analogues.

Calcination at 300 °C resulted in three peaks. The first is a broad peak centred at 202 °C with two sharper peaks at 232 °C and 259 °C. These are associated with the complex reduction of the metal carbonate phase that is present, as indentified by the XRD. The sample calcined at 400 °C resulted in one broad reduction centred at 250 °C, however there is evidence of

multiple reduction events happening within this broad feature, with multiple shoulders observable at 220 °C, 231 °C and 265 °C. This is typical of the reduction associated with a nanocrystaline or amorphous $CuMn_2O_4$ phase reducing to form MnO and copper metal with multiple oxidation states present in the material resulting in an overlapping pattern [26]. At 500 °C a two stage reduction was observed, this is typical for crystalline copper manganese oxide catalysts. The two reduction peaks observed at 250 °C and at 290 °C are associated with the reduction of the copper component from copper (II) to copper (0) [29] and the manganese from manganese (III) to manganese (I). Calcination at the highest temperature of 600 °C also resulted in a two-step reduction with peaks at 250 °C and 310 °C, however the peak at 310 °C appears broader than the equivalent peak for the sample calcined at 500 °C. This is due to the influence of the additional crystalline Mn_2O_3 that is observed in the XRD pattern for this material.

Table 7: physical properties of the calcined copper manganese oxide catalysts

Calcination temperature/ °C	Phases present from XRD	Surface Area / $m^2\,g^{-1}$	Crystallite size / nm		
			$MnCO_3$	$CuMn_2O$	Mn_2O_3
0	$MnCO_3$	-	67	-	-
300	$MnCO_3$	9	9	-	-
400	$CuMn_2O_4$	72	-	5	-
500	$CuMn_2O_4$	54	-	44	-
600	Mn_2O_3, $CuMn_2O_4$	9	-	53	56

3.2.4   Surface area analysis

The BET surface areas are tabulated in

Table 7. The sample calcined at 300C exhibited a low surface area, this was expected as $MnCO_3$ is known to have a low surface area and the XRD of this sample showed the presence of this phase alone. Of the other three samples the highest surface area was for the sample calcined at 400 °C. This is due to the formation of the amorphous copper manganese oxide phase and this surface area of 72 m^2g^{-1} was found to be comparable to previous work[30].

As the calcination temperature was increased, surface area decreased due to sintering of the material and at 600 °C the formation of the low surface area Mn_2O_3

3.2.5   Naphthalene oxidation activity

The naphthalene oxidation data for all 4 catalysts is detailed in Figure 24 and Figure 25, with Figure 24 detailing the percentage CO2 evolution and Figure 25 the percentage naphthalene consumption. A commercial hopcalite along with a standard 1% Pt / Al_2O_3 catalyst were tested as comparisons. T50 and T90 for the catalysts is detailed in Table 8 for both CO_2 production and naphthalene consumption.

Table 8: Naphthalene oxidation activity for the catalysts calcined at varying temperatures. A commercial hopcalite catalyst and a 1% Pt/Al_2O_3 industrial standard are *shown* for comparison

Catalyst	CO₂ production		Naphthalene consumption		CO₂ Selectivity at 50% conversion
	T50 / %	T90 / %	T50 / %	T90 / %	/%
300 °C	242	250	245	255	100
400 °C	229	238	230	238	90
500 °C	239	270	233	258	30
600 °C	269	290	245	265	20
Commercial catalyst	226	245	226	246	100
1% Pt / Al_2O_3	250	280	-	-	-

The data in Figure 24 and Figure 25 along with Table 8 demonstrates that of the catalysts prepared the optimum calcination temperature is 400 °C. This material has the lowest T50 and T90 of the calcined hopcalite samples for both naphthalene consumption and CO_2 production.   There also is no discrepancy between naphthalene oxidation and CO_2 production, suggesting that there is negligible partial oxidation occurring, or that any partial oxidation products formed are so rapidly oxidized by the catalyst that they are not detected. Previous data suggests that this sample along with being the most amorphous is the most reducible with the lowest reduction temperature and the highest amount of reducible material, and hence the most labile oxygen. This is in agreement with previous work by Garcia *et al.* In their study they showed that the availability of labile lattice oxygen was a

contributing factor towards catalyst activity [13].   This suggests that the nanocrystaline $CuMn_2O_4$ detected in the XRD is the most active phase in this study.
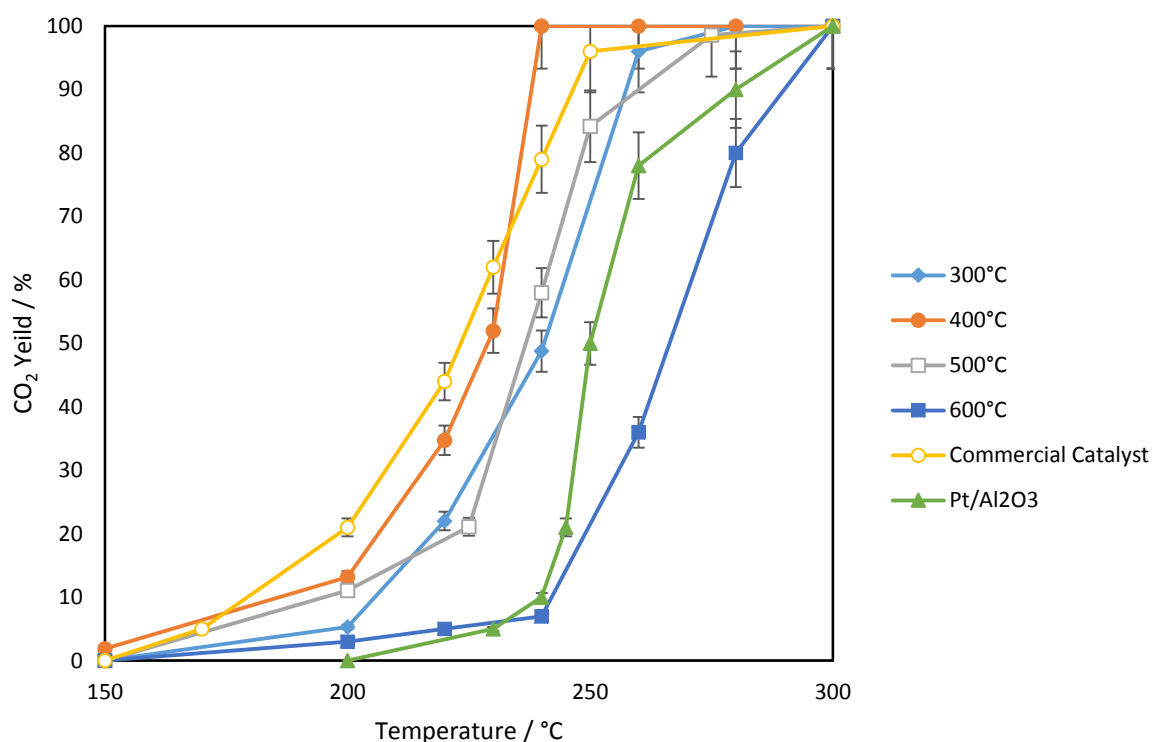

Figure 24: Naphthalene oxidation activity for hopcalite catalysts calcined at various temperatures in terms of the CO_2 produced with the comparison materials shown. 100 vppm naphthalene, 20% O_2/He, 45000 h^{-1}

As the calcination temperature was increased the T50 and T90 for both CO2 production and naphthalene oxidation increased, this is due to the less reducible nature of these materials as detailed by the previous TPR data supressing the ability of the catalysts to undergo Mars van Krevelen type reactions. It also suggests that the crystalline analogue of $CuMn_2O_4$ is less active than its amorphous counterpart. Notably however the T50 for naphthalene oxidation for the catalyst calcined at 600 °C was higher than the T50 for CO_2 production. This suggests that the material calcined at 600 °C was catalysing the partial oxidation of the naphthalene alongside its total oxidation, or that the naphthalene was irreversibly adsorbing to the catalyst surface. However, the trapping experiment to determine the exact nature of these products has not been done in this case[12]. It is worth noting that partial oxidation products

may be formed in all cases studied here but that they were rapidly converted to CO_2 before exiting the catalyst bed, especially when the larger surface areas of the catalysts calcined at 400 and 500 °C are considered. These materials have a far greater ability to reabsorb and further oxidise partially oxidised products. Work by Garcia et al has previously shown that manganese oxide catalysts can give rise to the partial oxidation of naphthalene [13], and as it is present in the XRD for the sample calcined at 600 °C, it could be responsible for this partial oxidation activity. The principle partial oxidation products that they observed were naphthenol, dimethyl phthalate and benzaldehyde [13].
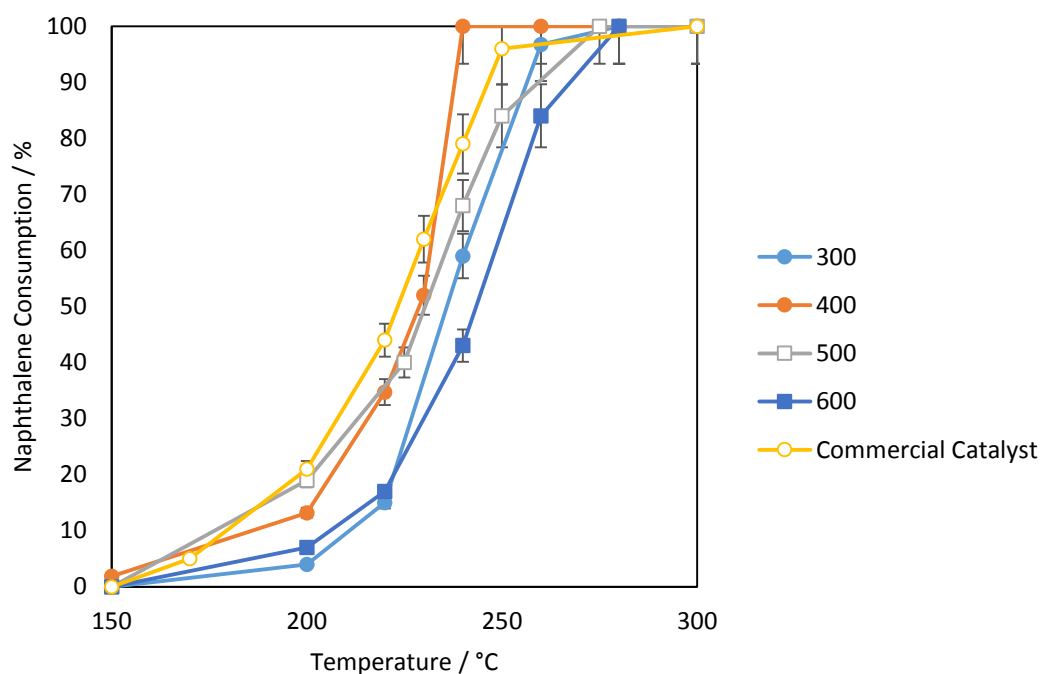
Figure 25: Naphthalene oxidation by hopcalite catalysts calcined at various temperatures in terms of the naphthalene consumption. 100 vppm naphthalene, 20% O_2/He, 45000 h^{-1}.

The catalyst calcined at 300 °C showed poor activity due to the lack of $CuMn_2O_4$ formation with the carbonate phase not very active for this reaction. However the catalyst showed some activity so it is possible that there are some undetected amorphous $CuMn_2O_4$ that is highly active for the reaction but present in low quantities.

When compared with the standard catalyst of 1% Pt / Al$_2$O$_3$ (Figure 25), it is clear that copper manganese oxide is more active, both in terms of T50 and T90. As naphthalene oxidation has not been reported using copper manganese oxide previously, a commercial copper manganese oxide catalyst was also tested. The commercial sample gave activity comparable to the sample calcined at 400 °C. The precise composition of this commercial material is not known, and most likely contains promoter materials not present in the co-precipitated samples.
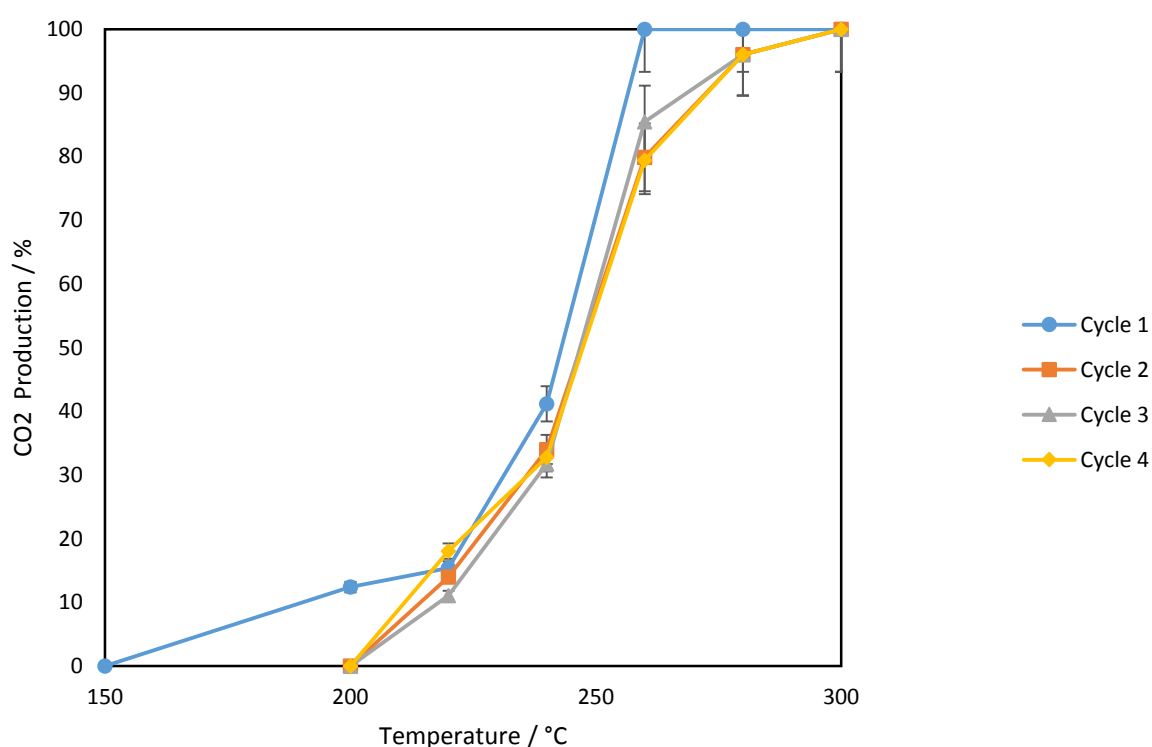
Figure 26: Naphthalene oxidation re-use test for coper manganese oxide catalyst calcined at 400 °C

The most active sample was also tested to determine its stability. In order to do this the sample calcined at 400 °C was tested four times successively (Figure 26). After the initial light off there was a slight deactivation upon subsequent reaction cycles. However, after this initial deactivation there was little change suggesting that there was no further change to the catalyst. The cause of this initial deactivation could be investigated in future studies. Though the experiments would be non-trivial, in situ techniques, such as XRD or IR could be

used to probe deactivation. Following this a time on line stability test was performed on the catalyst at 300 °C (Figure 27). After an intial deactivation period of 3-4 h, the conversion stabilised and activity maintained constant for 48 h, demonstrating its durability as a catalyst.

Previous work by Solsona et al on the oxidation of propane by hopcalite suggested that the catalyst deactivated over time [16]. This was attributed to increasing levels of Cu^+ and Mn^{4+} on the surface of the catalyst. This does not appear to hold true for naphthalene oxidation possibly due to the lower reaction temperature required for this reaction leading to less sintering and crystallisation of the catalyst.
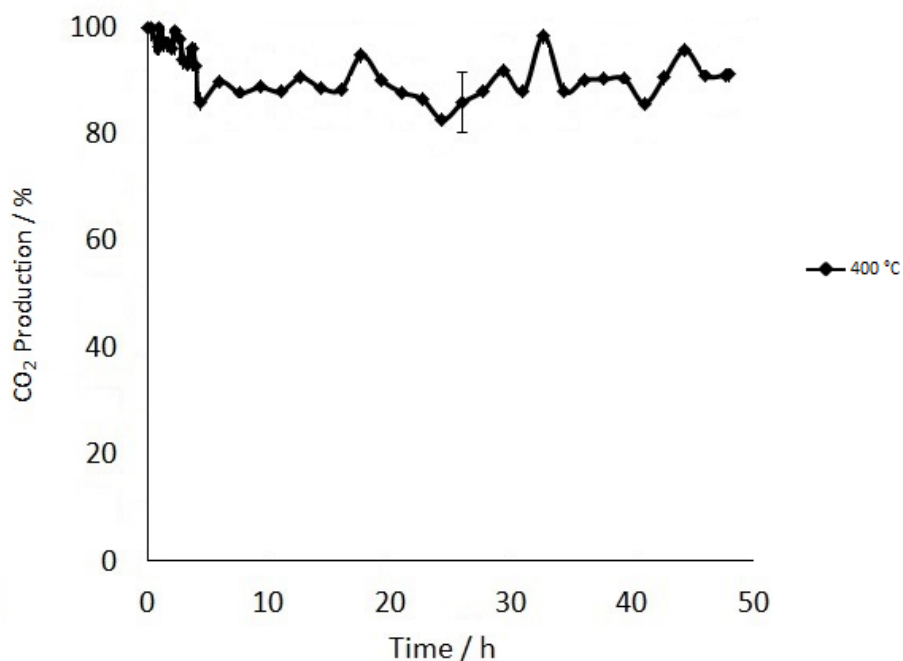
Figure 27: Production of CO_2 using catalyst calcined at 400 °C for naphthalene oxidation. 300 °C, 48h.

This deactivation could be attributed to a number of factors. Irreversible adsorbtion of partially oxidized carbonaceous products is one possibility. Another possibility is the physical change of the material from the amorphous active copper manganese oxide to a less active phase under reaction conditions. However, further investigation into the post reaction nature of the catalyst would be required to give a definitive answer to this.

3.3 Gold doped catalysts

As detailed in chapter 2 the catalysts discussed here were precipitated from a 1:2 molar mixture of copper manganese nitrate using a 0.25M sodium carbonate solution as the precipitant[16]. Copper was replaced with gold in amounts appropriate to give 1, 3 and 6 wt% gold catalysts whilst maintaining the overall molar ratio of copper and dopant to manganese at 1:2.

3.3.1   XRD of the gold containing catalyst precursor

The X-ray diffraction patterns of the three precipitated gold doped catalyst precursors (1, 3 and 6% gold) are shown, along with an undoped catalyst for comparison, in Figure 28.
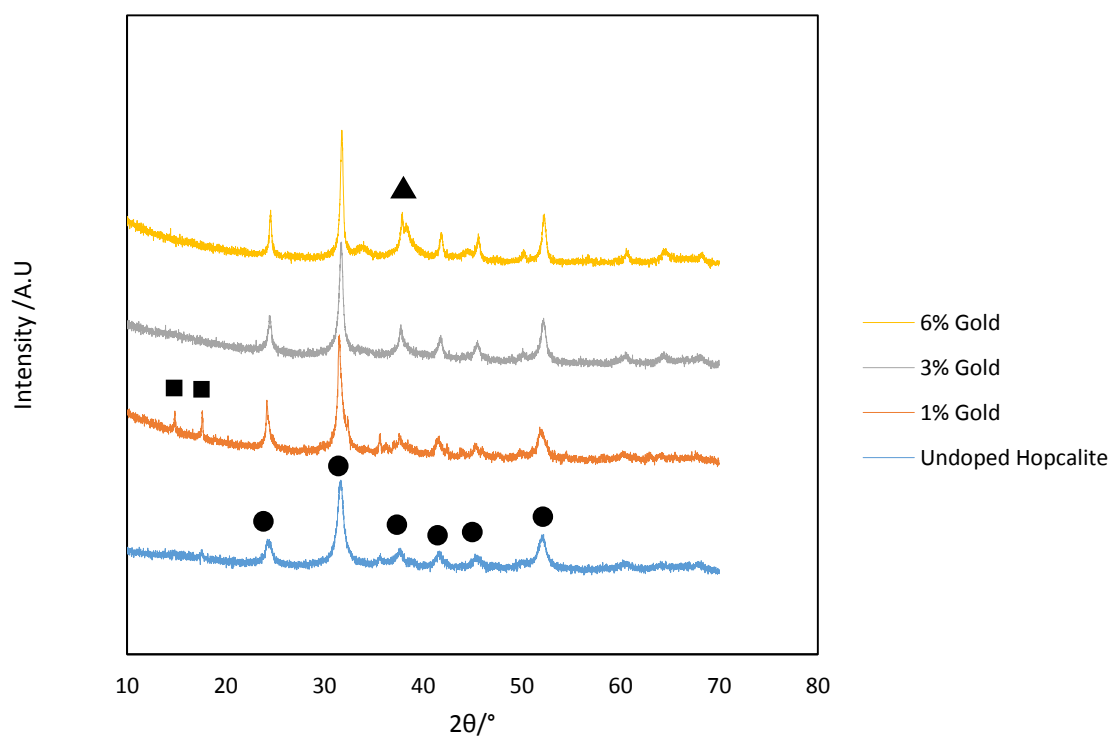

Figure 28: XRD of the gold doped hopcalite precursors. 40mA 40 kV Cu source.
■ = $Cu(OH)_2CO_3$ (ICDD: 00-001-0959), ▲ = Au (01-071-4614), ● = $MnCO_3$ (01-071-3820)

The undoped catalyst precursor XRD pattern consists of reflections that correspond with manganese carbonate with the principle reflection at 31.8° corresponding to the (104) plane of the manganese carbonate.

Unlike the undoped catalyst the material doped with 1wt% gold shows evidence of a separate copper phase with reflections at 13.5° and 18° corresponding to the (020) and (120) planes of $Cu_2(OH)_2CO_3$. In addition, the reflection corresponding to the (104) plane of $MnCO_3$ has shifted from 31.8° in the undoped catalyst to 31.5° in the sample containing 1 wt% Au. This suggests that less copper has been incorporated into the manganese carbonate lattice [21]. In their work on copper manganese carbonate materials Porta *et al*. demonstrated that incorporation of copper into the manganese carbonate lattice reduces the unit cell size causing a shift to higher 2θ angles in the XRD pattern. The opposite occurs in this case suggesting less Cu is incorporated. It is clear that the presence of a small amount of chloroauric acid solution has led to a more phase separated precipitant. RIR analysis suggests that the copper hydroxycarbonate phase in the 1% sample makes up 46% of the material with 53% $MnCO_3$ and 1% Au. This also points towards the existence of an amorphous manganese phase as there should be twice as much manganese as copper present in the material.

Table 9: Physical properties of the uncalcined catalysts containing gold

Expected gold content / wt%	Phases present	Crystalite size / nm		
		$Cu(OH)_2CO_3$	$MnCO_3$	Au
0	$MnCO_3$	-	14	-
1	$MnCO_3$, $Cu(OH)_2CO_3$	36	20	-
3	$MnCO_3$, Au	-	26	-
6	$MnCO_3$, Au	-	37	9

When Au content is increased to 3wt% there is no evidence of the $Cu_2(OH)_2CO_3$ phase observed in the 1 wt% Au sample. This suggests that perhaps in the 1% sample the gold is incorporated into the lattice and disrupting the copper incorporation into the manganese, and that in the sample containing 3 wt% Au the gold is not incorporated into the lattice of the carbonate and is instead aggregating together. This is supported by the broadening of the peak observed at 37.7°, this peak corresponds to the (110) plane of $MnCO_3$ but the (111)

plane of Au^0 also gives a diffraction peak at around this 2θ value. As it also corresponds with Au^0 it is likely that the broadening of this peak is due to the presence of gold being precipitated. As the peak is masked by the $MnCO_3$ reflection it is not possible to estimate a value for the crystallite size of gold in this sample.

When precipitated with 6 wt% Au the XRD clearly shows the presence of Au^0. Reflections corresponding with the (110), (200) and (220) planes of Au^0 are clearly observable at 37°, 45.7° and 65°. This clearly indicates the presence of gold particles. A crystallite size of 9nm was recorded for the gold in this sample.

It is clear from the Scherrer calculations that the crystallite size of $MnCO_3$ in the precursors is increasing with the further addition of gold to the hopcalite precursor. In the absence of gold the crystallite size is 14nm, however this has more than doubled with the addition of 6 wt% gold.

3.3.2   TGA of the catalyst precursors containing gold.

The thermal gravimetric analysis of the catalyst precursors is shown in Figure 29. The undoped catalyst is also shown for reference. The undoped material exhibits a three-step mass loss. There is an initial loss of mass associated with water. This is followed by two mass loss events corresponding to the thermal decomposition of an amorphous copper hydroxycarbonate phase alongside manganese carbonate.
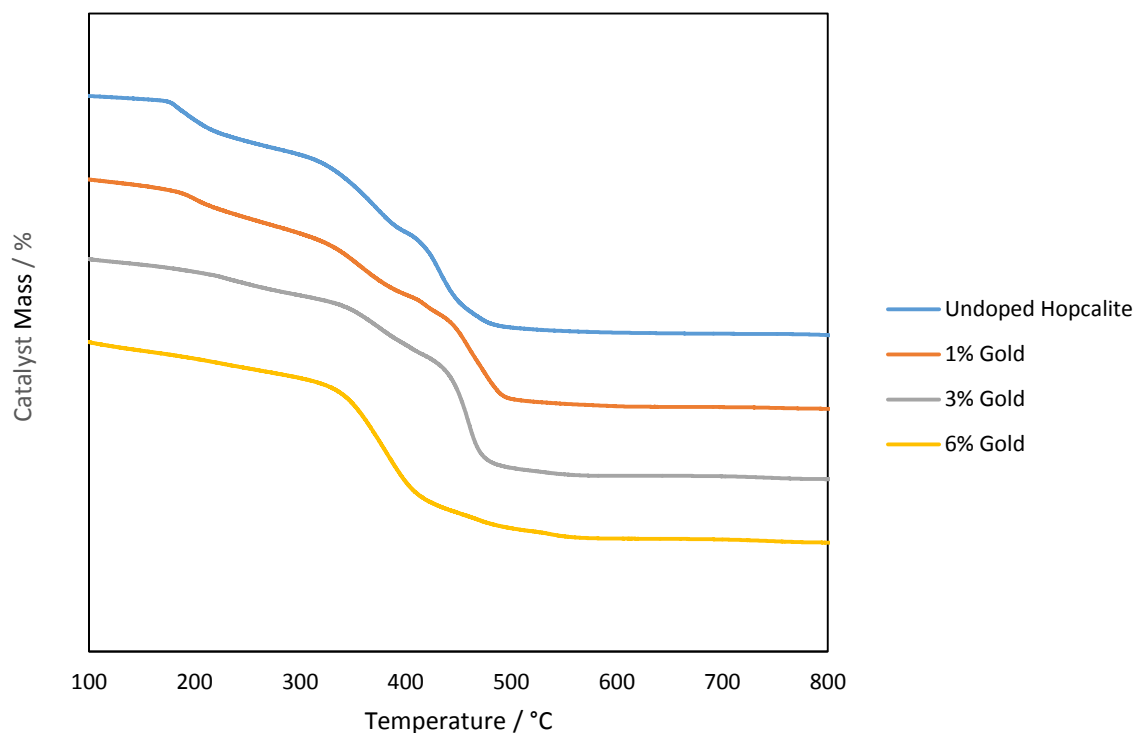
Figure 29: TGA of the catalyst precursours precipitated with gold showing the termal decomposition of the carbonate precursour. 5 °C min^{-1}, static air.

The sample precipitated with 1% gold exhibits a similar mass loss profile to the undoped sample with a slight shift to higher decomposition temperatures. This is reflected again in the sample containing 3 wt% gold, however there is a decrease of the temperature by which the mass loss ceased. 1% Au stabilises around 500 °C, whereas 3% stabilised at 475 °C, a change of 25 °C. 6 wt% gold leads to a change in the mass loss profile with only one major mass loss observed, which suggests that only one phase is present, and there is no amorphous copper phase as in the other materials. The thermal decomposition of the sample with 6 wt% gold stabilises around 500 °C, similarly to the sample containing 3 wt%, however the thermal decomposition begins earlier and takes place over a broader temperature range. This suggests that there is a broad range of particle sizes present in the material as particles of differing dimensions will decompose at different temperatures, giving rise to broad mass loss profiles.

It is worth noting at this point that previous work with copper manganese oxide catalysts reported in this thesis displayed a single mass loss around 415 °C. However the previous catalyst was precipitated using a 2M Na_2CO_3 solution whereas the catalysts discussed here were precipitated using a 0.25M Na_2CO_3 solution. What is clear is that the sample precipitated using the less concentrated base is more phase separated than when using the stronger base. This has not been studied in detail in this work however it is clear that more of the less concentrated base is needed to maintain the pH at the desired value the concentration gradient of the system is greater than when a more concentrated base is used. This leads to precipitation of multiple phases. The co-precipitation process is very easily disrupted by slight changes in conditions and method[31].

3.3.3   XRD of the calcined catalysts

XRD patterns of the calcined catalysts are shown in Figure 30. Calcination of all the precursors resulted in a poorly crystalline catalyst, with few identifiable reflections. The un-doped catalyst contains a reflection at 36° and one at 39° corresponding to the (311) and (222) planes of copper manganese oxide.

The catalyst containing 1 wt% Au also exhibits the characteristic $CuMn_2O_4$ reflections, however there is also a reflection at 32° 2θ and the reflection at 39° 2θ is broader than in the un-doped sample. The reflection at 32° is indicative of residual $MnCO_3$ in the catalyst, it corresponds with the reflection resulting from the (104) plane. This correlates with the TGA that shows a shift to higher temperatures for the thermal decomposition of the $MnCO_3$ present in the precursor. The broadening of the reflection at 39° is possibly the result of the Au^0 cubic (110) reflection overlaying the $CuMn_2O_4$ orthorhombic (222) reflection.
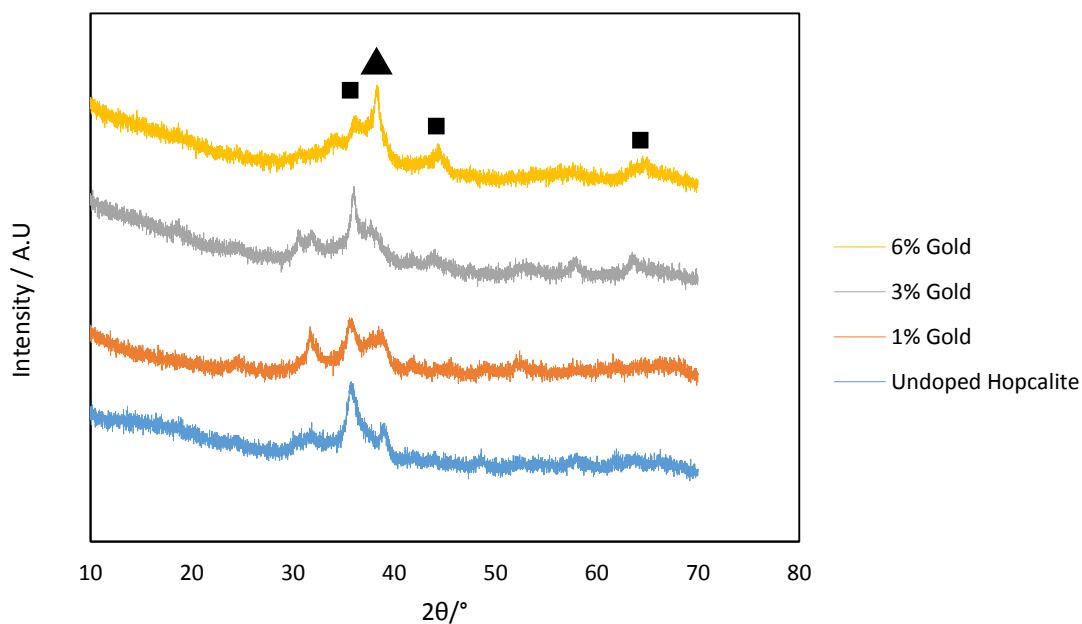
Figure 30: XRD of the calcined gold doped catalysts showing increasing intensity in the Au phase as loading increases. 40mA 40 kV Cu source . ▲= Au (ICDD: 01-071-4614), ■= $CuMn_2O_4$ (01-075-0826)

Table 10: Physical properties of the calcined gold containing hopcalite catalysts

Expected gold content / wt%	Phases present	Crystalite size / nm		Surface Area / m² g⁻¹
		$CuMn_2O_4$	Au	
0	$CuMn_2O_4$	9	-	82
1	$MnCO_3$, $CuMn_2O_4$, Au	4	5	78
3	$MnCO_3$, $CuMn_2O_4$, Au	10	5	42
6	$CuMn_2O_4$, Au	5	11	43

Increasing Au content to 3 wt% and to 6 wt% increases the intensity of this Au^0 (110) reflection at 39° as would be expected. The sample containing 3 wt% gold exhibits some signs of residual $MnCO_3$, however the sample with 6 wt% Au does not. This is in agreement with the previously discussed TGA data that suggests a decrease in the thermal decomposition temperature as more Au is added.

3.3.4   TPR of the calcined catalysts

Figure 31 shows the TPR data for hopcalite catalysts doped with gold. For comparison the undoped TPR profile is also shown. All four catalysts exhibit the same behaviour with three

reduction events corresponding to $Cu^{II} \rightarrow Cu^{0}$ and $Mn^{III} \rightarrow Mn^{II} \rightarrow Mn^{I}$ [20, 26]. There is no reduction event associated with the gold species suggesting that it is present as Au^{0} as inferred from the observations made of the XRD of the samples.
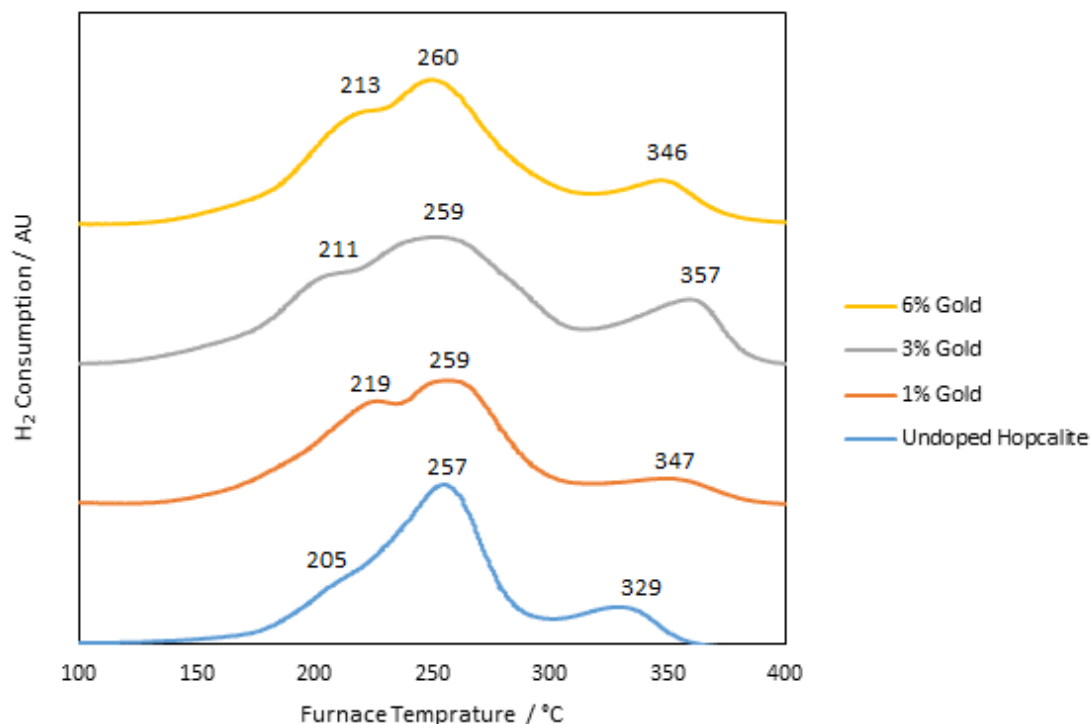
Figure 31: TPR data for hopcalite catalysts doped with gold showing little change in the reduction properties of the catalysts with additional gold. 20mL min^{-1}, 10% H$_2$/ Ar, 5 °C min^{-1}.

The $Cu^{II} \rightarrow Cu^{0}$ reduction occurs in one step around 220 °C. The reduction centred at 250 °C is due to the first stage of the $Mn^{III} \rightarrow Mn^{II} \rightarrow Mn^{I}$ reduction. This is followed by the $Mn^{II} \rightarrow Mn^{I}$ reduction at 335 °C. The reduction is complicated by the presence of other species, previous work has shown that Mn^{IV} and Cu^{I} are present in the spinel lattice[32].

When doped with gold the low temperature reduction shoulder is broadened. Solsona et al attribute this event tentatively to the presence of Mn^{IV} species in the material as this will have a lower reduction temperature than Mn^{III} species [16, 33]. Their conclusion that gold

improves the reducibility and hence oxygen mobility of the catalyst appears to hold true in this case[16].

3.3.5 Surface area analysis

The surface area of the catalysts decreases as gold is added to them as detailed in Table 10. With 1wt% Au loading the surface area is similar to that of the undoped catalyst, at 78 $m^2\,g^{-1}$.However, when the gold loading is increased to 3 and 6 wt% the surface area drops by roughly 50 %. This could be either the result of gold blocking pores on the surface of the catalyst surface or a textural change in the catalyst surface with the result of it being smoother and less porous. Our hypothesis is that a textural change has occurred. If the change in surface area was due to the influence of gold within the porous surface there would be further decrease in surface area from 3 wt% to 6 wt% however this is not observed. The increased acidity of the precipitating liquor due to the presence of chloroauraic acid however could be an explanation for a textural change with more Na_2CO_3 needed to maintain the pH at the desired pH of 8.3. This would lead to more carbonate rich conditions and possibly a slightly different phase precipitated.

3.3.6 SEM analysis of calcined materials.

Table 11: EDX data for copper manganese oxide catalysts containing gold.

Expected loading of gold / wt%	Copper		Manganese		Cu:Mn Atomic Ratio	Gold		Au:Mn Atomic Ratio
	Weight %	Atomic %	Weight %	Atomic %		Weight %	Atomic %	
0	26	16	55	40	1:2.5	-	-	
1	29	14	36	20	1:1.4	1	0.14	1:143
3	22	11	32	16	1:1.45	3	0.45	1:35
6	25	13	39	24	1:1.8	6	0.91	1:26

Figure 32 shows SEM images of the three catalysts containing gold. All three images were obtained using the backscatter detector functionality of the microscope. Bright areas corresponding to high concentrations of gold are clearly visible on all three samples, with gold particles becoming more populous as the weight loading of gold is increased. The expected loadings of gold are present in all the catalysts.

It is known that the size of gold particles is the primary factor determining their catalytic activity, work by Haruta proved that gold nanoparticles in the region of 4nm are needed to be active for CO oxidation [34]. However larger nanoparticles, in the region of 25nm have been shown to be active in the oxidation of propane[35], indeed this study shows that the active sites for CO oxidation and propane oxidation are not the same. Bulk gold has long been known to be unreactive and the large particles observed here are unlikely to be active for oxidation reactions. However as particles in the nanometer size range are possible with coprecipitated gold catalysts [36] it is likely that there are some smaller particles that are unobserved by this study as particles less than 50 nm are unlikely to be observed. Further TEM and STEM EDX studies would be useful to see if this is indeed the case.
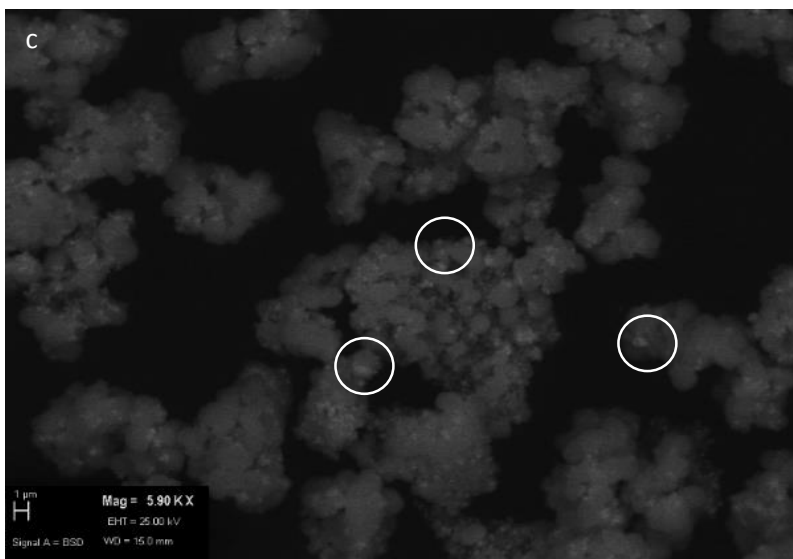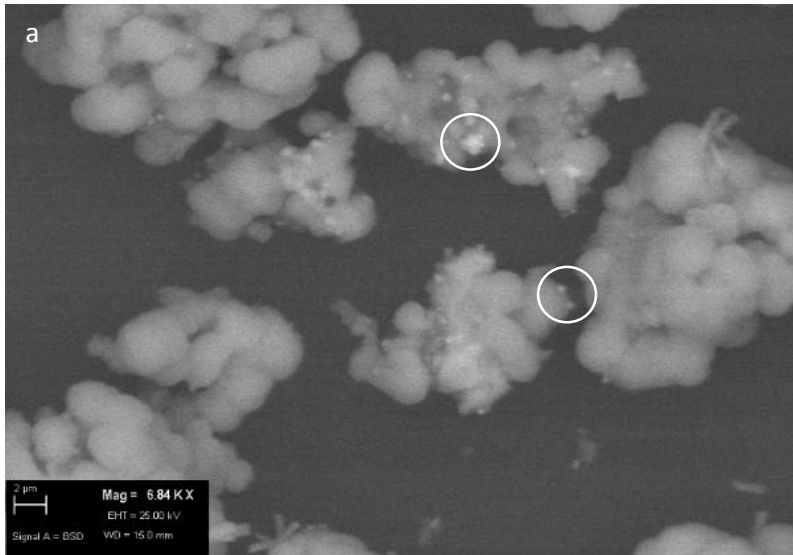
Figure 32: Backscattered SEM images of catalysts containing gold a) 1 wt% gold b) 3 wt% gold c) 6 wt% gold. Circled areas show gold particles

3.3.7 XPS analysis of calcined catalysts
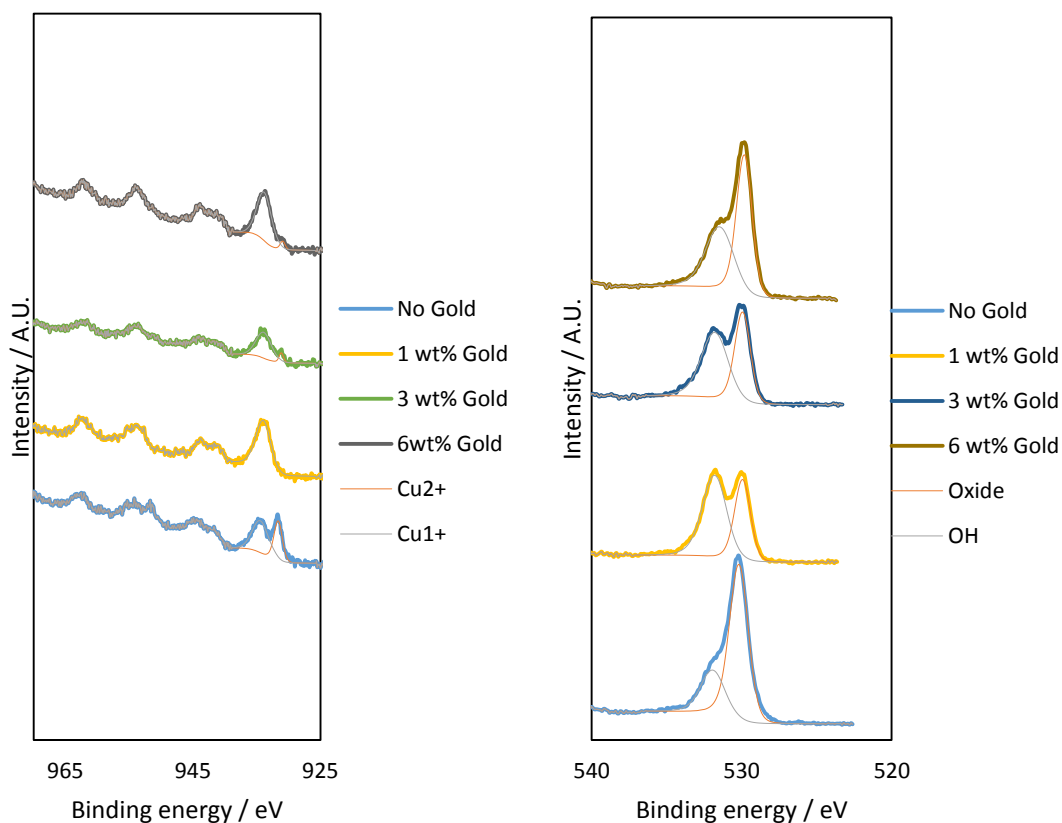
Figure 33a) XPS of gold containing hopcalite catalysts showing the Cu 2p region with evidence of both Cu^{1+} and Cu^{2+} species alongside multiple shakeup and satellite features. b) XPS of gold containing hopcalite catalysts showing the O 1s region with evidence of O^{2-} and OH^- species.

Figure 33a displays evidence that the copper on the surface of the undoped catalyst is a mixture of the Cu^{1+} and Cu^{2+} oxidation states. This is in agreement with work published by Einaga et al [37] whereupon they observe both Cu^{1+} and Cu^{2+} on the surface of their hopcalite type material. Doping with 1 wt% gold completely supresses the expression of Cu^{1+} on the surface of the sample with none observed in the XPS. Further doping increases the amount of Cu^{1+} marginally. Further study is required to explain why this is the case. Cole et al showed that doping with gold increased the levels of Cu^{1+}[38] however their undoped sample did not show evidence of Cu^{1+} suggesting that the precipitation technique is closely linked with the level of Cu^{1+} in the catalyst.

Precipitation with 1 wt% gold also leads to a change in the oxidation state of the oxygen on the surface of the catalyst as demonstrated in Figure 13b. OH species are promoted on the surface of the catalyst containing 1 wt% gold with a near 1:1 ratio of OH to oxide (Table 6). As further gold is doped this ratio increases in favour of the oxide species. This indicates that small quantities of gold is changing the catalyst surface significantly.
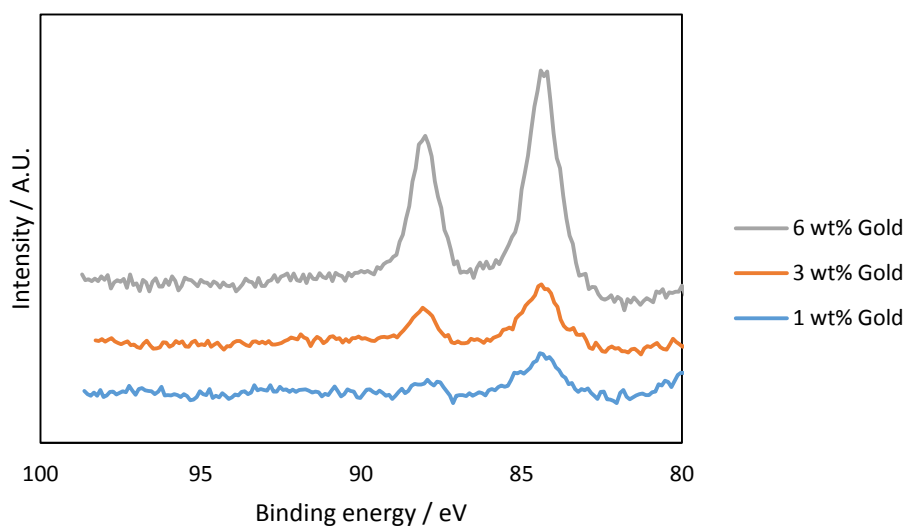
Figure 34. Au 4f XPS of gold doped hopcalite catalysts illustrating evidence of Au^0

The gold 4f region as shown in Figure 14 clearly shows the presence of Au^0 [39] with the intensity of the peak increasing as the gold loading is increased. The Au:Mn ratio suggests that a large proportion of the gold is on the surface. For the 1 wt% sample if the gold was evenly distributed through the material the Au:Mn molar ratio would be *ca* 1:160. As the ratio is much lower than that it suggests that there is a higher gold concentration on the surface.

Table 12: Atomic ratios of species on the surface of the gold containing hopcalite catalysts as determined by XPS

Gold loading / wt%	OH^- : O^{2-} Ratio	Cu^{1+}: Cu^{2+} Ratio	Cu:Mn Ratio	Au: Mn Ratio
Undoped	1 : 3	1:1.5	1: 5.6	N/A
1	1 : 0.64	N/A	1: 3.9	1:85
3	1:0.82	1:10	1: 5.7	1:51
6	1:1.25	1:9	1:5.9	1:22

What is also clear from the XPS is that there is an excess of manganese on the surface. Table 6 clearly shows that the typical Cu:Mn ratio is in the region of 1:5.6 rather than the 1:2 that is expected from the desired stoichiometry. This suggests that there is some manganese oxide material on the surface of the catalysts that consists of crystallites too small to be detected by XRD.

3.3.8   Naphthalene oxidation activity

It is worth noting at this point that it is possible that the catalysts containing gold will also have trace amounts of chloride within them from the chloroauric acid used as the gold source in their preparation. The effect of chloride as a catalyst poison has not been studied for this reaction/catalyst system however it is a well-known poison for many catalysts [40].
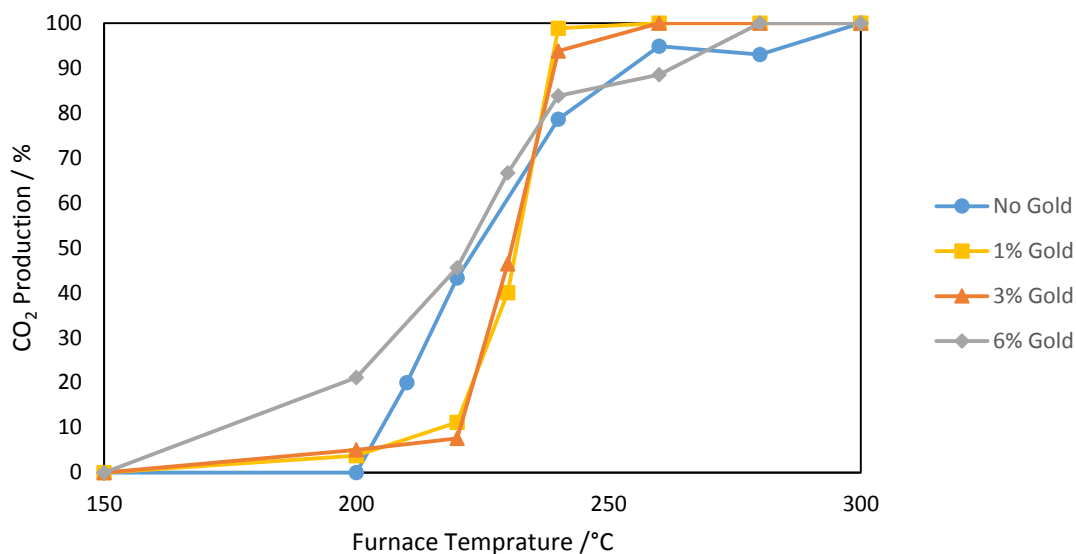
Figure 35: Naphthalene oxidation activity of the gold doped catalysts. 100 vppm naphthalene, 20% O_2/He, 45000 h^{-1}

Figure 35 displays the naphthalene oxidation light off curves for the gold doped hopcalite catalysts. Doping with small amounts of gold leads to an increase in light off temperature, and hence a reduced catalytic performance, when compared with the undoped catalyst with both 1% and 3% gold loading resulting in a T50 for CO_2 production of around 232 °C. The undoped catalyst by comparison has a T50 of around 225 °C.

It was determined that the addition of 1% gold did not decrease the surface area of the catalyst, however addition of further gold led to a drop in the overall surface area. This drop can be attributed to the possible presence of larger particles in these materials.

When doped further the activity of the catalyst increases to become more comparable with the undoped sample (T50 of 224 °C).

The doped catalysts (1 and 3 wt%) exhibit low activity of 5% at 200 °C whilst the undoped catalyst is not active at this temperature. The low temperature activity of the sample doped with 6% gold is much improved, however with 21% CO_2 production at 200 °C this suggests that gold has promoted the oxidation of naphthalene at low temperatures. This coincides with the onset of low temperature reduction in the TPR that Solsona *et al.* attributed to Mn^{IV}

species [16]. This would be an indication of mobile oxygen in the material that potentially is available for reactions via Mars van Krevelen type mechanisms.

Previous work by Sellick et al suggests that catalysts consisting of platinum supported on silica, catalysts consisting of large platinum particles performed better than those populated with smaller ones[41]. This was attributed to the larger particles ability to accommodate more naphthalene molecules adsorbing to the surface lying flat and not forcing them into binding vertically. Whilst there is no direct evidence of the size of any possible nanoparticles on the surface of the hopcalite materials discussed in this section it is possible that the relative size of the nanoparticles present is increasing as more gold is loaded into the catalyst.
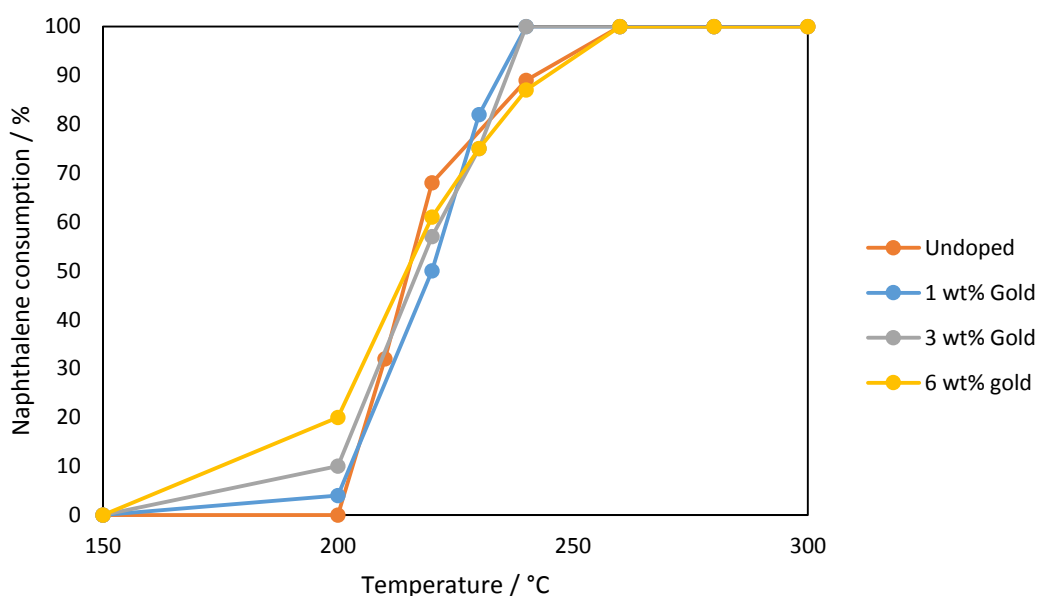
Figure 36: Naphthalene oxidation activity of gold doped catalysts in terms of naphthalene consumption. 100 vppm naphthalene, 20% O_2/He, 45000 h^{-1}

The catalysts that were less active for production of CO_2 had a common theme of low copper to manganese ratios. Both the catalyst containing 1 and 3 wt% gold had a Cu:Mn ratio of about 1:1.4 whereas the two active materials had a Cu:Mn ratio of closer to 1:2 as would be expected for the stoichiometric $CuMn_2O_4$ spinel. The copper richness of the less active

catalysts seems to supress their activity, possibly due to the disruption of the previously discussed copper manganese redox couple that exists within the spinel.

3.4 Effect of doping hopcalite catalysts with silver

As detailed in chapter 2 the catalysts discussed here were precipitated from a 1:2 molar mixture of copper manganese nitrate using a 0.25M sodium carbonate solution as the precipitant. Copper was replaced with silver in amounts appropriate to give 1, 3 and 6 wt% silver catalysts whilst maintaining the overall molar ratio of copper and dopant to manganese at 1:2. Silver was part of the original hopcalite formulation developed by Lamb et al at John Hopkins University[15] and as such is an ideal candidate to dope copper manganese oxide materials.

3.4.1 XRD of the catalyst precursors containing silver

Figure 37: XRD patterns of the silver doped catalyst precursors. 40mA 40 kV Cu source**.** ■ = MnCO3 (ICDD: 01-071-3820), ▲ = Ag details the XRD patterns of the silver doped catalyst precursors. There is clear evidence for the presence of the $MnCO_3$ phase in all the catalysts. The (104) reflection of manganese carbonate is visible in all three precursors at 31.6° 2θ . Unlike the gold containing materials there is no evidence of a copper containing hydroxycarbonate phase in any of the materials, suggesting the presence of silver nitrate in the precipitation mixture has had less of an effect on the precipitation compared with the chloroauric acid.
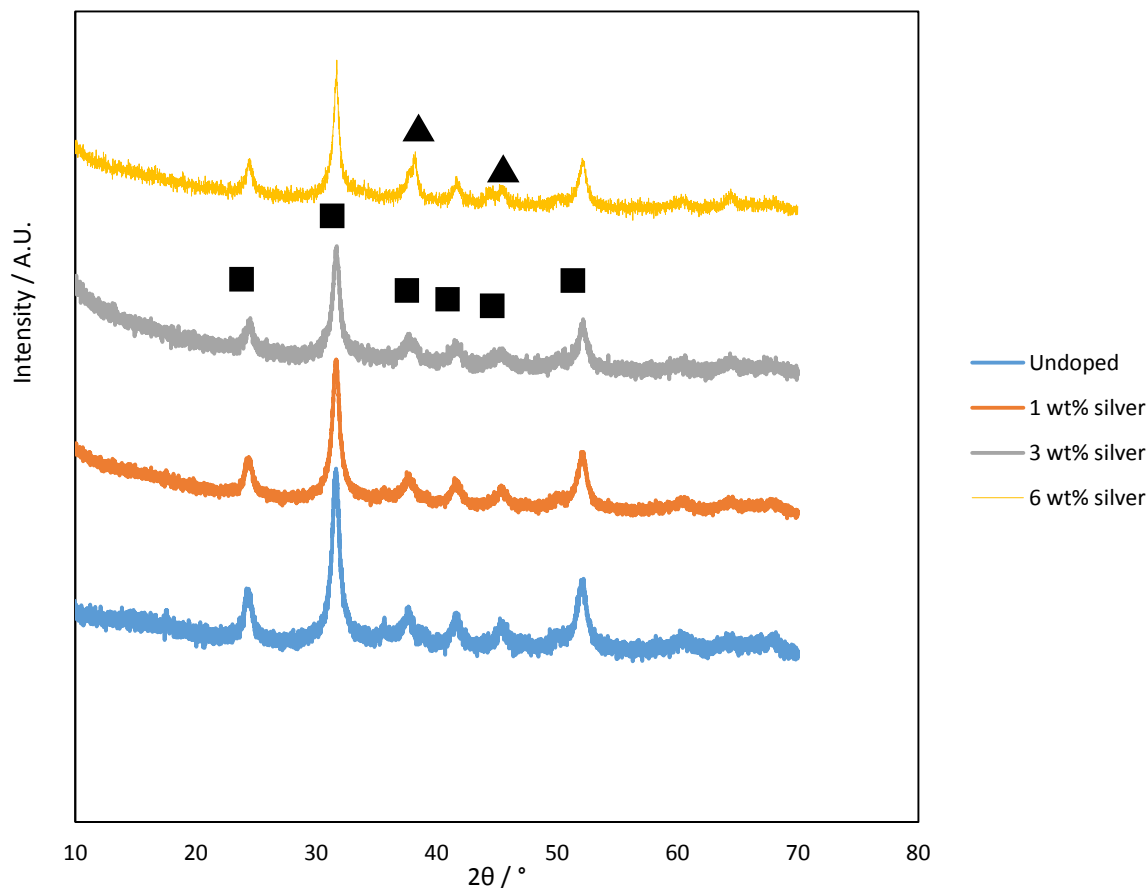
Figure 37: XRD patterns of the silver doped catalyst precursors. 40mA 40 kV Cu source. ■ = MnCO$_3$ (ICDD: 01-071-3820), ▲ = Ag (01-071-4613)

There is no change in the crystallite size of the manganese carbonate phase, or any peak shift that could suggest a change in unit cell parameters.

Neither the 1 or 3 wt% catalyst show any evidence of a silver phases suggesting that it is present in a form that is not detectable by XRD, such as very small nanoparticles or as a solid solution within the carbonate lattice. There is evidence of a silver phase in the 6 wt% sample, with a shoulder corresponding to the (111) plane of metallic silver observable at 38.3° 2θ. As with the gold reflections previously discussed this reflection intersects with the (110) reflection of MnCO$_3$, and as such could be masked in 1 and 3 wt% samples.

Table 13: Physical properties of the hopcalite precursors containing silver

Expected silver content / wt%	Phases present	Crystalite size / nm	
		$MnCO_3$	Ag
0	$MnCO_3$	14	-
1	$MnCO_3$	14	-
3	$MnCO_3$,	14	-
6	$MnCO_3$, Ag	15	10

3.4.2   TGA of the washed catalyst precursor

Figure 38 details the thermal gravimetric analysis of the silver doped catalyst precursors. With no dopant added there are three mass loss events, as discussed previously in this chapter. When 1 wt% silver is substituted into the material there are only two mass loss events suggesting that there is only one species decomposing alongside the loss of water. This is possibly the result of silver incorporation into the precursor, resulting in formation of a single phase forming. When more silver is added the pattern of a single thermal decomposition is maintained, however the temperature of this decomposition is shifted to higher temperatures indicating that these materials are more thermally stable. It is unclear as to the exact reason why this is the case, one possibility is that with low loadings the silver is present within the structure of the precursor material and acts as a defect, and de-stabises the structure. Whereas higher loadings leads to larger areas of silver rich material that do not de-stabilise the structure to the same degree. The precursor XRD of 6 wt% material shows evidence of an Ag^0 species, however the 1 and 3 wt% precursors do not.
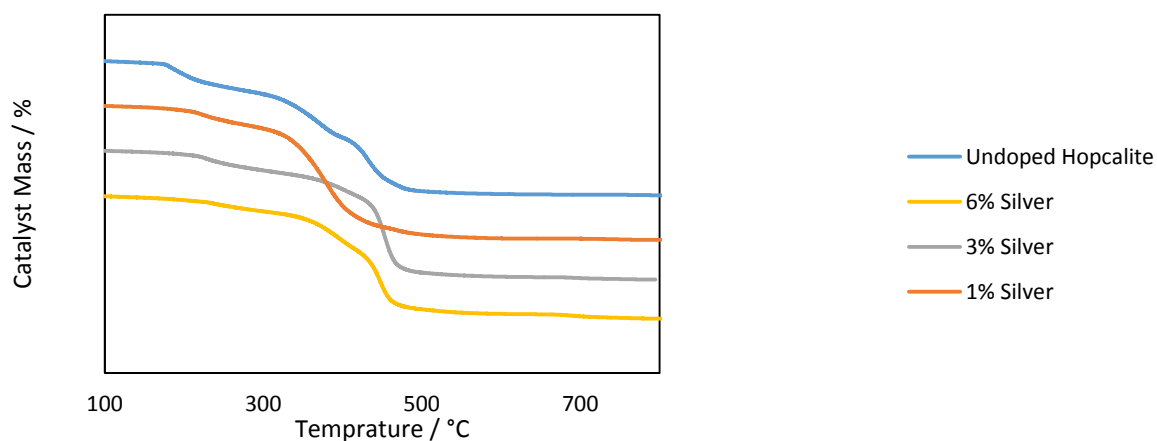
Figure 38: TGA of the silver doped copper manganese catalyst precursors showing multiple carbonate decompositions.

3.4.3   XRD of the calcined catalysts

XRD of the materials after calcination are shown in Figure 39. Broadly speaking the three catalysts are similar in their patterns with the principle reflection at 36° corresponding with the principle (311) reflection of $CuMn_2O_4$ and the other observed reflections also corresponding with this phase. The catalyst containing 1 wt% Ag is slightly less crystalline than the catalysts containing 3 and 6 wt% Ag. It has the smallest crystallite size of the three doped materials (Table 8). This is possibly for the reason detailed in the previous TGA discussion, with the small amount of silver acting to disrupt the lattice of the $CuMn_2O_4$. It is interesting to note that there is no evidence of either silver oxide with its principle reflection at 32° 2θ or silver metal whose principle reflection is observed at 45° 2θ. This suggests that any silver within the material either consists of particles too small to observe by means of XRD, exists as a solid solution or has been incorporated into the lattice of the material.
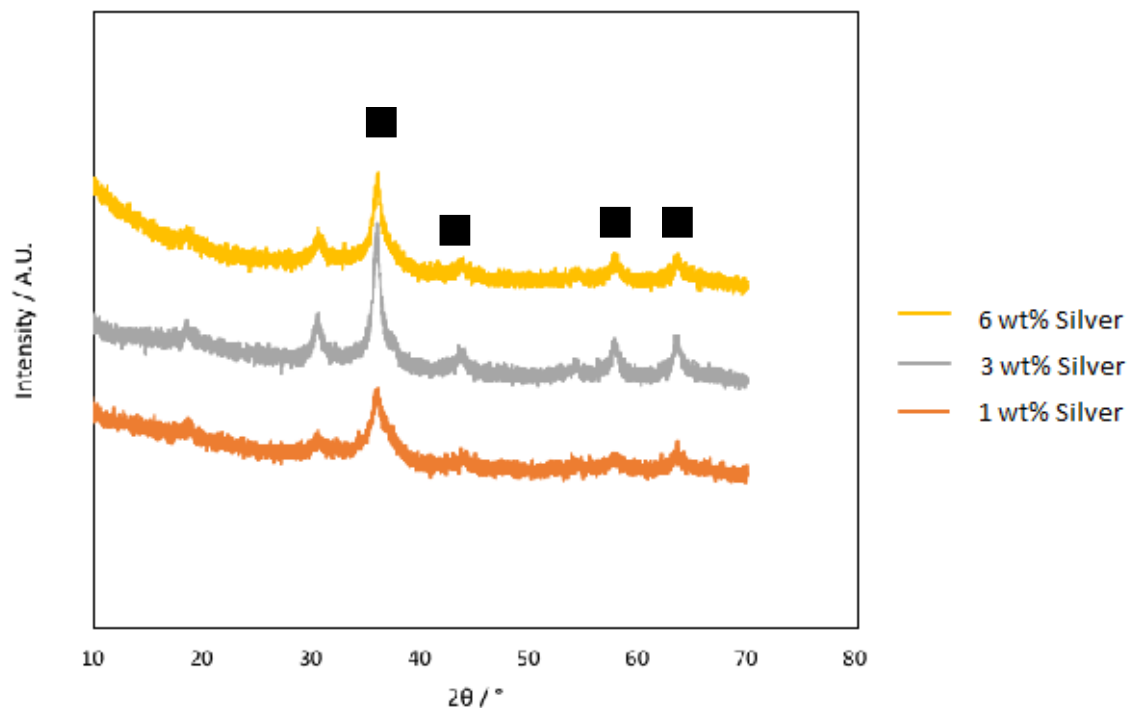
Figure 39: XRD of the calcined silver containing catalysts showing the presence of the $CuMn_2O_4$ spinel but no silver phase. 40mA 40 kV Cu source. ■ = $CuMn_2O_4$ (ICDD: 01-075-0826)

Table 14: Physical properties of the calcined hopcalite catalysts doped with silver

Expected silver content / wt%	Phases present	Crystallite size / nm		Surface Area / m² g⁻¹
		$CuMn_2O_4$	Ag	
0	$CuMn_2O_4$	9	-	82
1	$CuMn_2O_4$	7	-	74
3	$CuMn_2O_4$,	12	-	60
6	$CuMn_2O_4$,	9	-	48

3.4.4   SEM analysis of calcined catalysts

Images of the calcined catalysts captured using the back scatter detector are shown in **Error! Reference source not found.**. It is clear that there is no immediately observable difference between the three materials. All three catalysts consist of uniform particles roughly 1 μm in diameter.   **Error! Reference source not found.** contains the EDX data for the silver containing catalysts. The undoped catalyst prepared by this method has a Cu:Mn ratio of

1:2.5 indicating a slightly manganese rich material compared to the stoichiometric 1:2 Cu:Mn ratio desired. However when silver is introduced into the material the resultant materials are slightly copper rich with a Cu:Mn ratio in the region of 1:1.8. This suggests that the presence of silver nitrate in the precipitation mixture promotes the precipitation of copper. The influence of pH on the precipitation of hopcalite has not been investigated in great detail. Work by Hutchings et al describes the effect of pH on the CO oxidation activity of hopcalite, They suggest that copper rich materials are precipitated in acidic conditions[14]. However as the pH of the solution was maintained at 8.3 for all the samples this cannot be the cause.
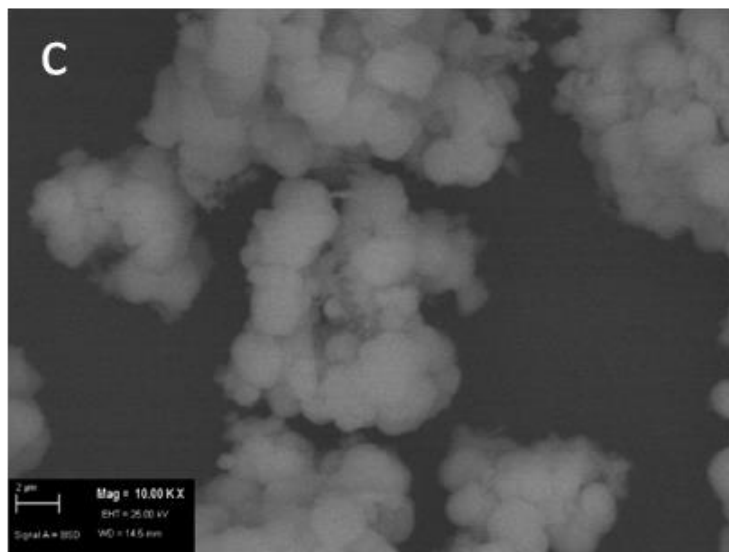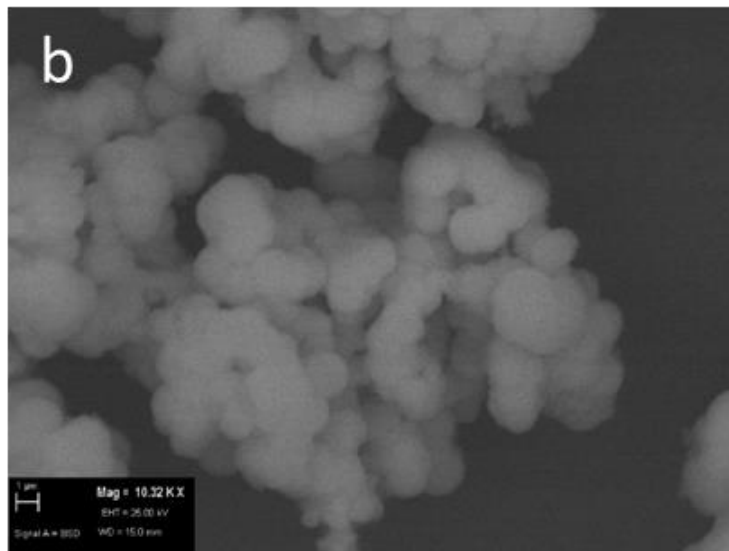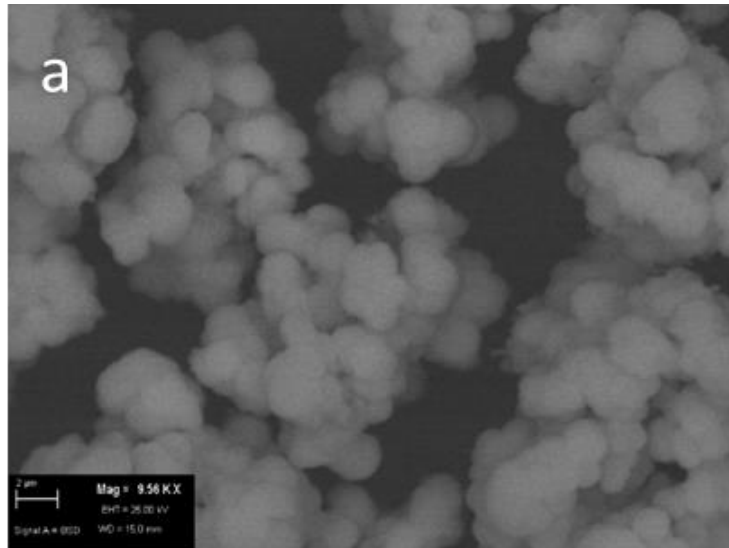
Figure 40: Backscattered SEM images of catalysts containing silver a) 1 wt% silver b) 3% silver c) 6% silver.

Table 15 : EDX data for copper manganese oxide catalysts containing silver.

Expected Silver content	EDX						
	Copper		Manganese		Cu:Mn Atomic Ratio	Silver	
	Weight %	Atomic %	Weight %	Atomic %		Weight %	Atomic %
0	26	16	55	40	1:2.5	-	-
1	27	14	43	26	1:1.8	1	0.4
3	32	20	47	35	1:1.75	3	1.2
6	26	14	40	25	1:1.78	6	1.6

None of the three images exhibit the bright spots associated with large particles of heavier atoms in the material. In this case any large concentrations of silver within the material would appear bright as silver has a considerably higher atomic number than copper and manganese. This suggests any silver present within these materials is present either well dispersed within the catalyst or as nanoparticles that are smaller than the resolution of the microscope. Figure 41, 42 and Figure 43 show the EDX mapping data for the catalysts with 1, 3 and 6 wt% silver content respectively. It is clear from the three sets of EDX mapping that there is no large silver particles observed and that both copper and manganese are well dispersed within the catalysts. This is in contrast to the catalysts precipitated with gold that were discussed previously in this chapter, all three of those catalysts displayed large gold particles which were clearly visible in the back scattered SEM images. The gold precursor used in that case was chloroauric acid, whereas the silver precursor used was silver nitrate. It seems like the nitrate precursor was able to mix better with the nitrate copper and manganese precursor and as a result the silver has been better dispersed. Also the nitrate silver precursor has less of an effect on the overall pH of the precipitating system than the acidic gold species, this leads to less use of base to maintain pH at the desired 8.3. This leads to a catalyst with a more favourable Cu:Mn ratio. This could be confirmed by investigating the precipitation of this material using a silver chloride precursor rather than the silver nitrate used in this case. STEM EDS analysis would be helpful in this case in order to

investigate the nature of the silver nanoparticles, as would EXAFS analysis as none of the

characterisation techniques used thus far have lent much understanding into the nature of

the silver species in the catalyst.
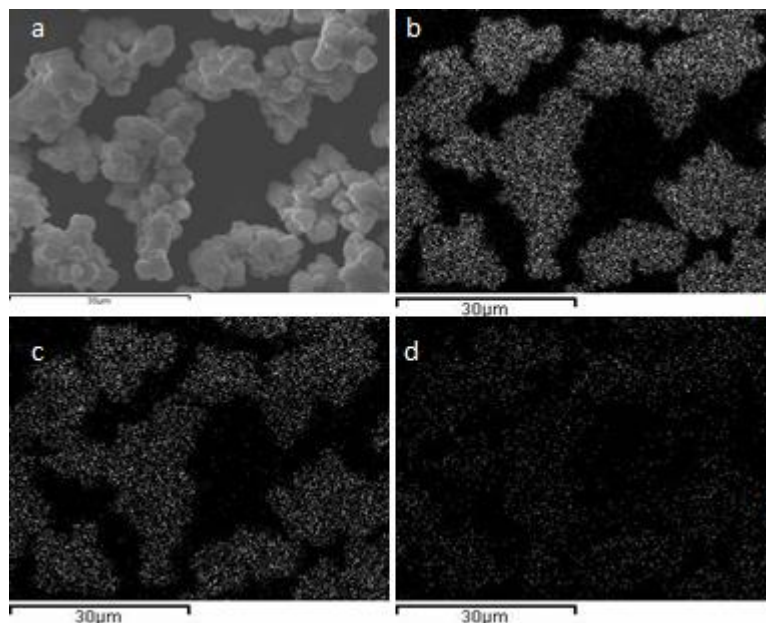
Figure 41: EDX mapping of the 1 wt% Ag catalyst. a) SEM image b) Mn map c) Cu map d) Ag map
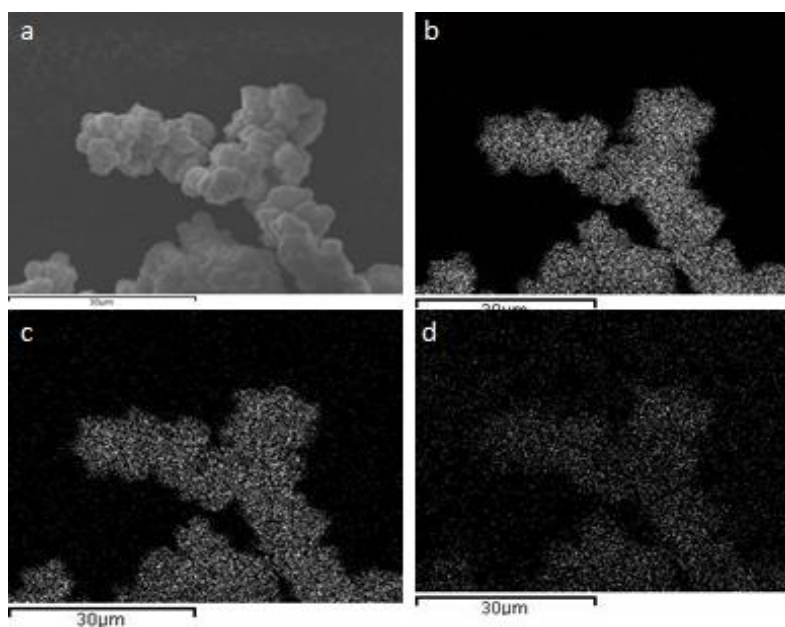
Figure 42: EDX mapping of the 3 wt% Ag catalyst. a) SEM image b) Mn map c) Cu map d) Ag map
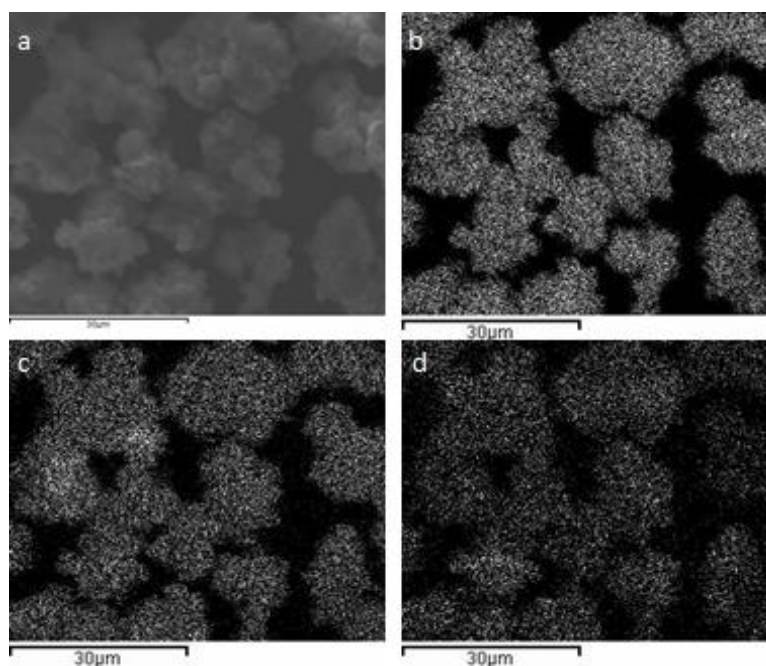
Figure 43: EDX mapping of the 6 wt% Ag catalyst. a) SEM image b) Mn map c) Cu map d) Ag map

3.4.5 TPR of the calcined catalysts

The TPR data for the calcined silver containing materials are detailed in Figure 44 . Unlike the addition of gold, silver changes the reduction profile of the materials significantly. Doping with 1 wt% silver there is a peak at 202 °C, with a shoulder at 190 °C. This is followed by a more intense reduction feature at 263 °C. These two reductions are attributed to the reduction of the copper manganese spinel phase. The shouldered peak at 202 °C is due to the reduction of copper and silver. The Handbook of Chemistry and Physics states that silver oxide reduces at 230 °C, with copper within the spinel known to reduce at a similar temperature, it is difficult to determine which is responsible for which, this is complicated by the difficulty resolving individual peaks in the TPR [42].
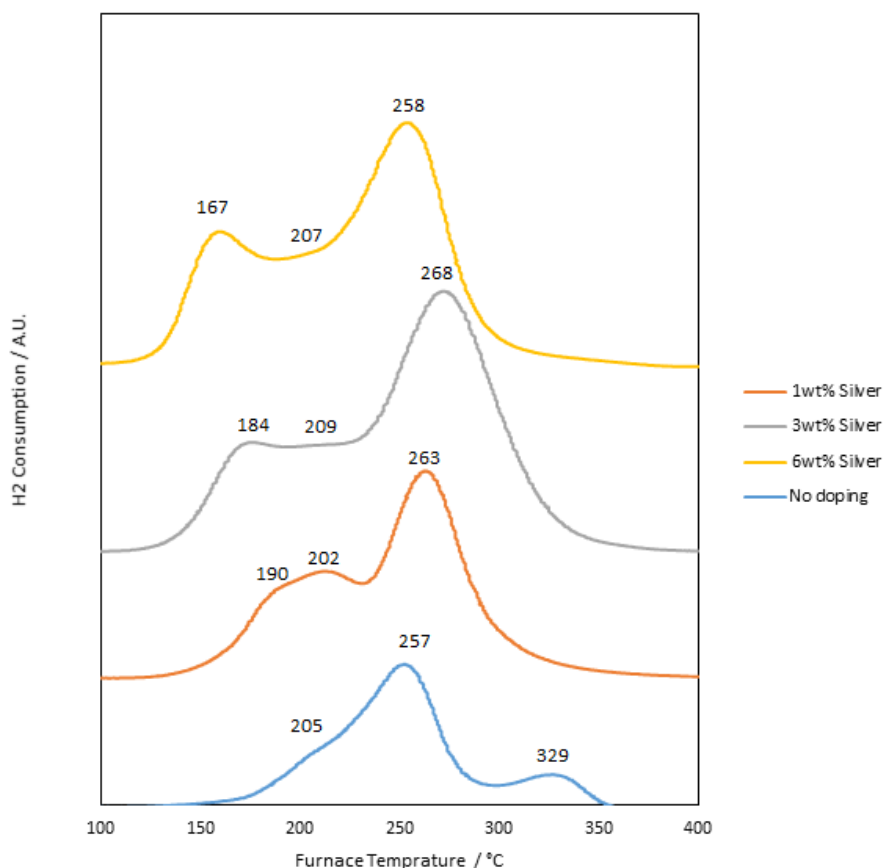
Figure 44: TPR of the calcined catalysts containing silver illustrating the lowering of the onset of reduction as a result of silver incorporation. 20mL min^{-1}, 10% H$_2$/ Ar, 5 °C min^{-1}.

The second peak at 263 °C is the result of the manganese reduction of the spinel. Unlike the undoped material the catalysts containing silver do not exhibit a further reduction at around 330 °C. This was attributed to the second stage of the Mn^{III} → Mn^{II-III} → Mn^{II} reduction. In this case it seems that this must occur in one step, possibly due to the influence of silver in the lattice of the material introducing defects within the material.

As further silver is added to the catalyst there is a shift in the reduction temperature. The reduction of the manganese appears to remain stable, however the reductions at lower temperatures appear to change. The shoulder observed at 190 °C in the catalyst containing 1 wt% silver increases in magnitude to form a distinct peak at a slightly lower temperature of 184 °C in the 3 wt% sample. This continues in the 6 wt% sample with a shift to 167 °C. The increase in peak size suggests that this feature is related to the reduction of a silver

species within the sample, however with an increase of only a few wt% it is unlikely that the total increase is attributable to the reduction of a bulk silver oxide phase. More likely is that this reduction is the result of the decomposition of a $Cu_{1-x}Mn_2Ag_xO_4$ spinel like phase with silver replacing copper in the unit cell of the material.

3.4.6   Surface area analysis

As silver is doped into the catalyst there is a trend towards materials with lower surface areas. This suggests that silver on the surface is filling pores on the hopcalite surface leading to a drop in surface area. In order to investigate this a catalyst was prepared by impregnating 6wt% silver onto the surface of an undoped hopcalite. A small drop in of $1 m^2\,g^{-1}$ of surface area was observed, far less than what is observed for the catalyst coprecipitated with 6 wt% silver. This suggests that silver on the surface is not responsible for the drop in surface area, rather a textural change must have occur.

Table 16: Physical properties and reactivity of copper manganese oxide catalysts doped with silver

Catalyst	Surface Area / $m^2\,g^{-1}$	CO$_2$ production	
		T50/ %	T90/ %
Undoped	82	225	255
1 wt% Silver	74	235	235
3 wt% Silver	60	206	225
6 wt% Silver	48	208	218
6 wt% Silver IMP	81	230	255

3.4.7   XPS analysis of the calcined silver containing hopcalite catalysts

Figure 25a shows the oxygen XPS of the silver doped catalyst materials. Unlike the previously discussed gold doped materials there is no change in the ratio of OH$^-$ to oxide present on the surface as more silver is added. There is an initial increase in the OH- concentration as the silver is added. However this does not continue to increase as further silver is added, nor as in the case of the gold catalyst does it drop. This suggests that the addition of silver is having an effect on the nature of the oxygen on the surface of the material but that this is not directly related to the concentration of silver metal.
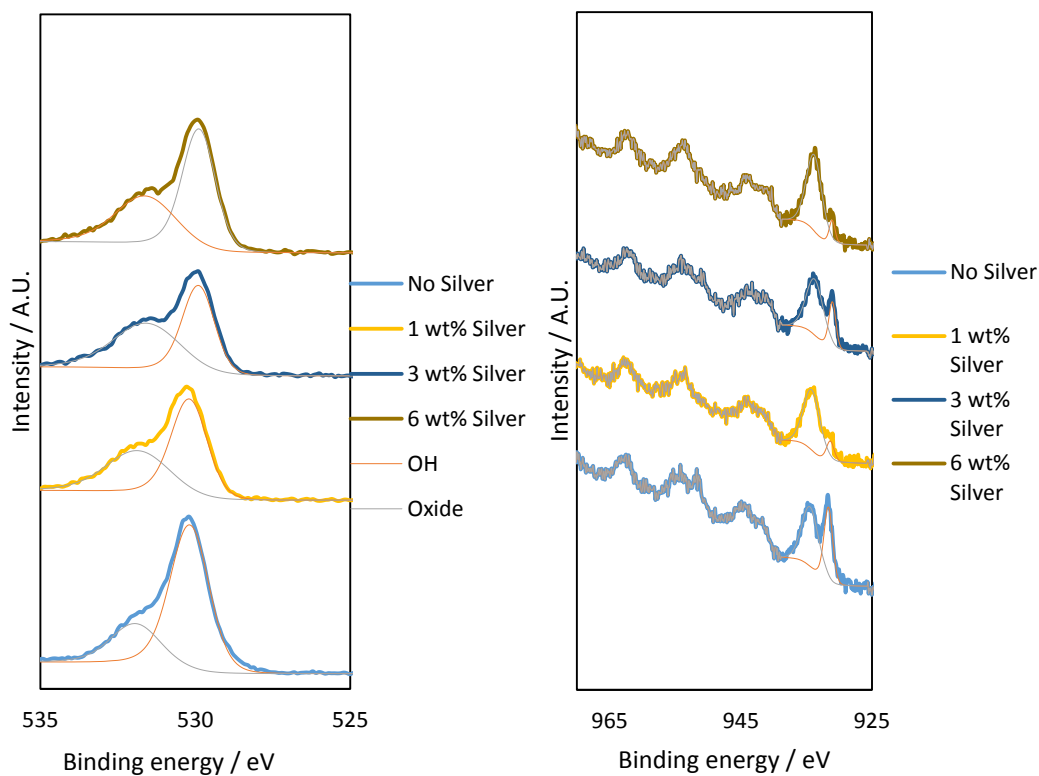
Figure 45 a) XPS of silver containing hopcalite catalysts showing the O 1p region with evidence of both OH⁻ and O²⁻ species b) XPS of silver containing hopcalite catalysts showing the Cu 2p region with evidence of both Cu^{1+} and Cu^{2+} species alongside multiple shakeup and satellite features

The copper XPS is shown in figure 45b. There appears to be both Cu1+ and Cu2+ present in both catalysts [43]. As with the gold catalysts discussed earlier in this chapter, the addition of silver leads to a reduction in the levels of Cu^{1+} in the sample. There is no observable trend in the Cu^{1+} : Cu^{2+} ratio. Doping with 1 wt% silver leads to a drop in the Cu^{1+} concentration on the surface. The sample containing 3 wt% Ag has far more Cu^{1+} whilst doping with 6 wt% Ag results in a drop in the Cu^{1+} concentration (Table 17). The reason for this is unclear.

Figure 46 shows the XPS spectra of silver for the doped catalysts. The presence of metallic silver is clearly observed with the typical emission for Ag^0 at 368.2 eV present [44]. As more silver is added from 1 up to 6 wt% the ratio of silver to manganese drops as would be expected (Table 11).
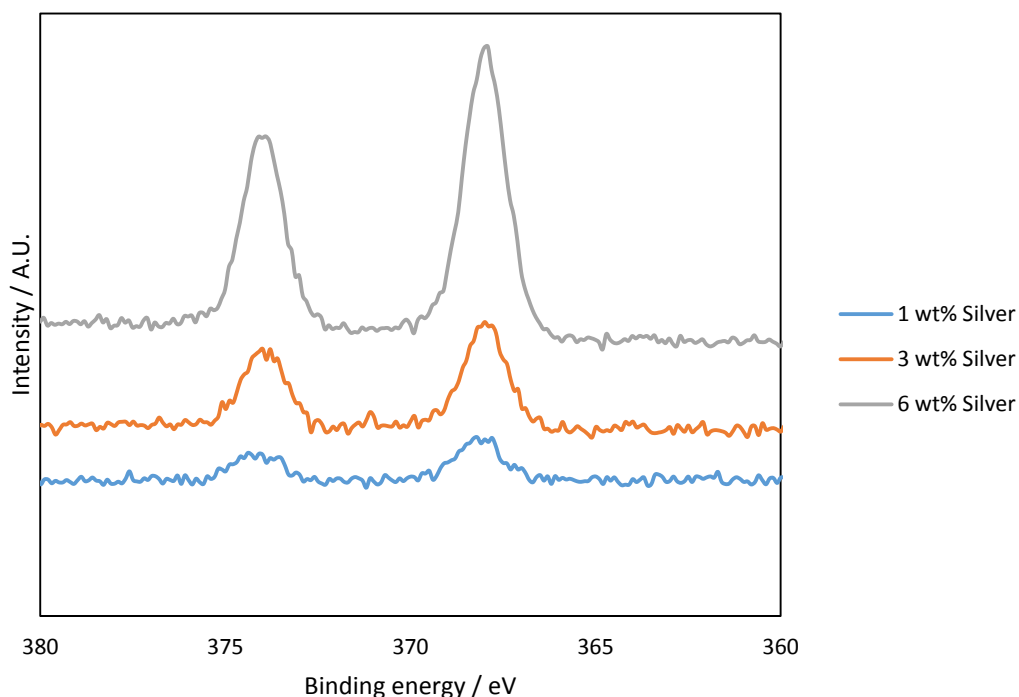
Figure 46: XPS of gold containing hopcalite catalysts showing the Ag 3d region with evidence of Ag^0 species on the surface

Table 17: Atomic ratios of species on the surface of the silver doped hopcalite catalysts as determined by XPS

Silver loading / wt%	$OH^-:O^{2-}$ Ratio	$Cu^{1+}: Cu^{2+}$ Ratio	Cu:Mn Ratio	Ag: Mn Ratio
Undoped	1 : 3	1: 1.5	1: 5.6	N/A
1	1: 1.3	1: 6.7	1: 4.8	1: 42.7
3	1:0.9	1: 3	1: 3.8	1: 14
6	1:1.4	1:10	1:4.4	1: 6.86

However the silver to manganese ratio is lower than would be expected if the silver was distributed evenly throughout the material. For the 1 wt% catalyst this expected value would be one silver atom to every 90 manganese atoms. However the observed ratio is to 1:43 suggesting that there is roughly double the silver on the surface as expected if the silver was distributed evenly.   This remains true as the silver content is increased with roughly twice

the silver content expected on the surface. However comparison with the EDX data does suggest that there is some subsurface silver that is not detected by XPS.

3.4.8   Naphthalene oxidation activity

The catalysts were tested for naphthalene oxidation and the results in terms of CO_2 production are displayed In Figure 47. As shown in Table 16 the addition of 1 wt% silver does not affect the T50 of the catalyst as it remains relativel unchanged with a 5 °C increase with regard to the undoped sample. However the T90 of the catalyst is improved significantly from 255 °C to 235 °C. In addition to this the low temperature activity of the catalyst is increased with 14% CO_2 production observed at 200 °C compared to the 0% conversion of the undoped catalyst at this temperature. This suggests that the addition of silver is improving the low temperature oxygen mobility of the catalyst. This is supported by the increase in low temperature reduction observed in the TPR (Figure 44).
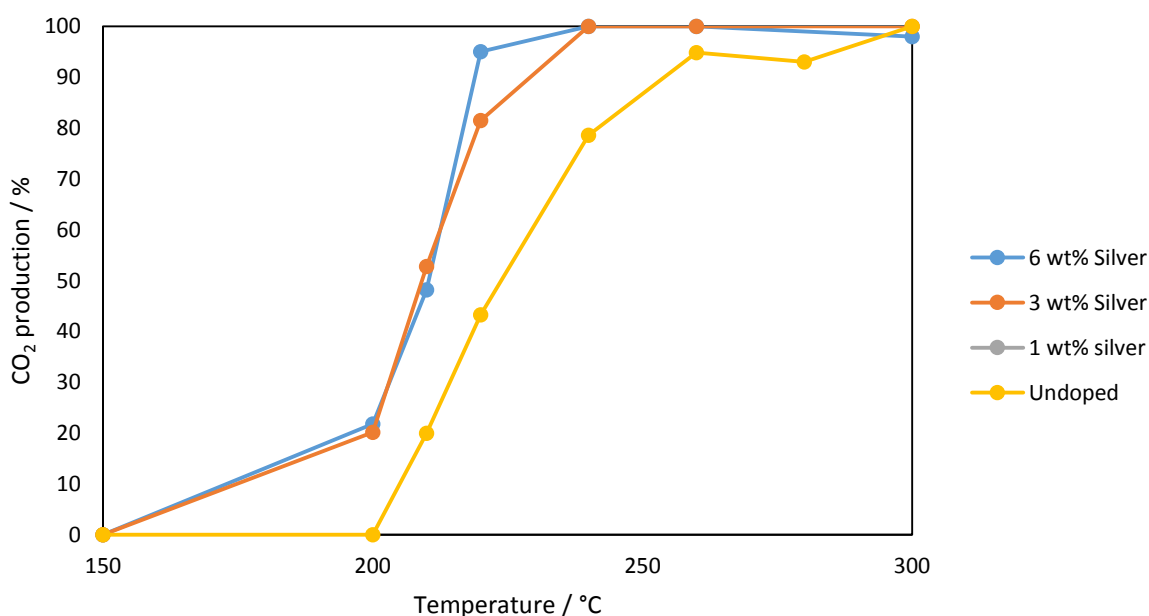
Figure 47: Naphthalene oxidation activity of silver doped catalysts in terms of CO_2 production. 100 vppm naphthalene, 20% O_2/He, 45000 h^{-1}

As more silver is doped into the materials there is an increase in CO_2 production, with both the catalysts containing 3 and 6 wt% silver having a T50 of 206 °C and 208 °C respectively.

The T90 of both catalysts is increased also to 225 °C and 218 °C respectively. As previously discussed the surface area of the materials decreases with increased silver content so it is not simply the case that the oxidation activity is linked to the surface area. Indeed the most active catalyst, 6 wt% silver, is the catalyst with the lowest surface area. More likely the increased activity is linked to the change in the oxygen mobility of the material with silver addition. There is an increase in the low temperature reducibility of the catalysts with the addition of silver, and it is our hypothesis that this allows the catalysts to oxidise naphthalene more efficiently at low temperatures.

Figure 48 shows the change in activity between a material that was precipitated containing 6 wt% silver, its equivalent that has had 6 wt% silver impregnated onto the surface and the undoped catalyst. What is clear from this chart is that the addition of silver exclusively on the surface does not lead to an improvement in the catalyst activity. This suggests that the incorporation of silver into the material where it can affect the redox properties of the catalyst, rather than the presence of surface silver species is important for the production of more active catalysts.
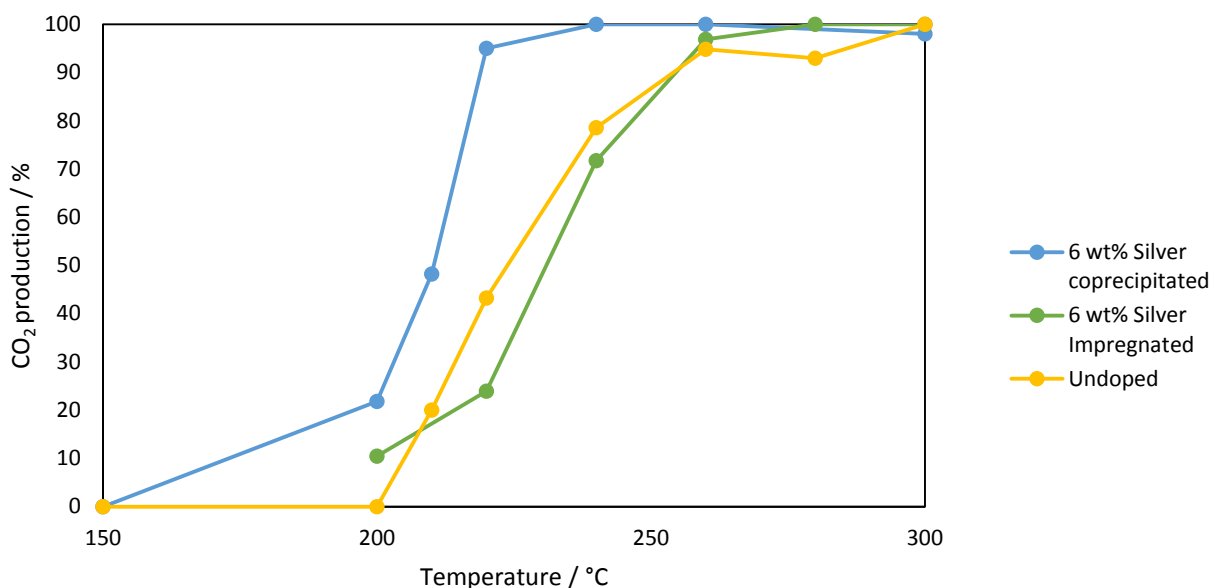
Figure 48: A comparison of the CO$_2$ production of catalysts doped with 6 wt% silver prepared by co-precipitation and impregnation with an undoped comparison. 100 vppm naphthalene, 20% O$_2$/He, 45000 h^{-1}

Indeed the catalyst impregnated with silver is outperformed by the undoped catalyst, suggesting that the presence of large quantities of silver on the surface of the hopcalite is blocking active sites where the catalyst is active.

The only point at which the impregnated catalyst outperforms the undoped material is at low temperatures. At 200 °C it has an activity of 10% CO$_2$ production, which is half of the conversion exhibited by the coprecipitated 6 wt% silver catalyst. This, along with the fact that the undoped catalyst is inactive at this temperature suggests that silver on the surface of the material has some low temperature naphthalene oxidation activity.
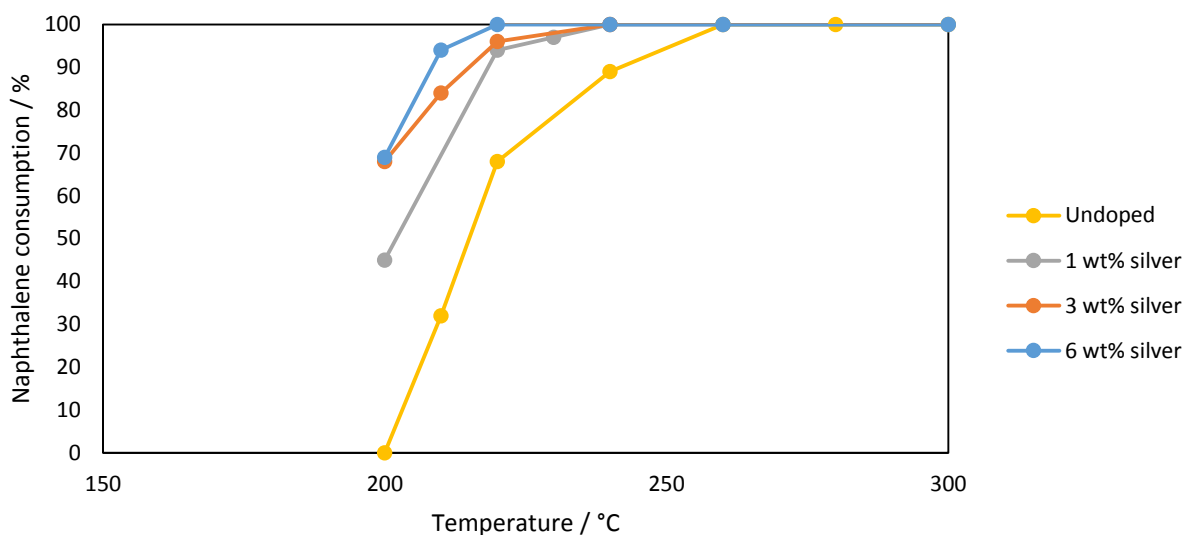
Figure 49: Naphthalene oxidation data for silver doped catalysts in terms of their naphthalene consumption showing high consumption at low temperature. 100 vppm naphthalene, 20% O_2/He, 45000 h^{-1}

When the naphthalene consumption of the catalysts is considered it is clear that there is a significant amount of partial oxidation occurring. The catalyst containing 1wt% silver is oxidising 45% of the naphthalene feed at 200 °C whilst only converting 14% of that to CO_2. This continues for the catalysts containing 3 and 6wt% silver with increasing naphthalene conversion into undetected products. Due to the nature of the columns used in the GC analysis partial oxidation products cannot be detected on line. Previous offline studies have suggested that such products include the bicarboxylic acid and the anhydride derivatives of naphthalene [13], it is not unreasonable to expect that these products are produced in this case, however further studies are clearly required to investigate this.

3.5 Conclusions

3.5.1 Effect of calcination on the undoped hopcalite catalyst

This work demonstrates that copper manganese oxide catalysts are active for the total oxidation of naphthalene. It is shown that the disordered nanocrystaline/amorphous hopcalite spinel phase is more active than its crystalline analogue, as demonstrated by the fact that the catalyst calcined at 400 °C was the most active of the four catalysts tested and

no other phases were observed in this sample. This material also had the highest concentration of reducible material, which suggests a link between the mobility of lattice oxygen and catalyst activity. This suggests that the reaction may proceed through a Mars van Krevelen type reaction as previously suggested by Wang for the total oxidation of aromatic hydrocarbons [25] and Garcia for naphthalene oxidation using manganese oxide catalysts[13].

This catalyst was stable upon reuse with only a slight deactivation from first use to second, upon which there was no further deactivation of the material. Time on-line study suggests that after an initial deactivation there is little drop in activity over a 48h period.

Increasing the calcination temperature served to supress the total oxidation of naphthalene, shifting T50 and T90 to higher temperatures due to the more crystalline nature of these materials alongside their lower overall reducibility. It was noted that higher calcination temperatures not only promoted the formation of the crystalline $CuMn_2O_4$ phase but also a manganese (II) oxide phase which, along with the lower surface area of these samples, may have contributed to the higher level of partial oxidation observed for these materials.

3.5.2   Effect of doping hopcalite with gold

The studies on gold doped hopcalite catalysts show that small gold loadings depress the activity of the materials with higher T50 values observed as a result of the doping. The TPR studies of the materials demonstrated that the addition of gold did not change the reducibility of the catalysts by a large degree, with no shifting of reduction temperature or profile upon the addition of gold. As such the changes in reactivity are not linked with changes in oxidation state of the materials in this case. There was a change in the thermal stability of the catalyst precursors with gold addition, with mass loss occurring at progressively lower temperatures with the addition of gold. The reason for this is unclear and does not seem to have had a direct effect on the activity of the catalyst. However, it was

observed that the catalytic performance of the materials was linked to the copper to manganese ratio of the catalysts. This suggests that the formation of the stoichiometric $CuMn_2O_4$ phase is significant.

Addition of gold serves to slightly lower the activity of the samples. For other gold containing catalysts it has been shown that large gold particles are inactive for many reactions and that gold nanoparticles are needed for the reaction to take place. The EDX images clearly show that the gold is present as large particles and as such may not be actively contributing to the oxidation of naphthalene. It is possible that gold nanoparticles on the surface are present however none of the characterisation techniques used can detect whether this is the case. Further work should focus on identifying these gold species by use of TEM.

3.5.3   Effect of doping hopcalite with silver.

The above work demonstrates that there are clear advantages in doping hopcalite with silver for the total oxidation of naphthalene. Small amounts of silver (1 wt%) cause the T50 of the material to increase slightly, however larger amounts of silver doping (6 wt%) result in a significant drop from 225 °C to 208 °C. The comparison between the coprecipitated and impregnated catalysts suggests that the CO_2 production is the result of silver incorporated into the structure of the catalyst rather than particles on the surface.

Work by Garcia suggests that for manganese oxide the Mars van Krevelen mechanism predominates for the oxidation of naphthalene[13]. It has been shown also by Hutchings et al in their TAP study of hopcalite that doping with noble metals promotes oxygen mobility [24]. The data presented in this chapter suggests that the Mars van Krevelen mechanism is predominantly responsible for the total oxidation of naphthalene on these silver catalysts and that silver incorporated into the lattice of copper manganese oxide is responsible for this increase in oxygen mobility. The shifting of the reduction to lower temperature,

observed in the TPR, seems to corroborate this and is in agreement with previous work by

Solsona et al[16].

3.6 References

[1]   EU, Council Directive 1999/13/EC 1999.
[2]   EU, Directive 2004/42/CE European Union, 2004.
[3]   B. Bems, M. Schur, A. Dassenoy, H. Junkes, D. Herein, R. Schlögl, Chemistry – A European Journal 9 (2003) 2039-2052.
[4]   S.H. Taylor, B. Garcia, T., in: F.C. D. Duprez (Ed.), Advanced Processes in Catalytic Oxidation. From Laboratory Studies to Industrial Applications, Imperial College Press.
[5]   E. Union, PAH Position Paper ISBN92-894-2057-X, Office for Official Publications of the European Communities, Luxembourg, 2001
[6]   E. Ntainjua N, S.H. Taylor, Top Catal 52 (2009) 528-541.
[7]   J.I. Levy, E.A. Houseman, J.D. Spengler, L. Penn, L. Ryan, Environmental health perspectives 109 (2001) 341-347.
[8]   X.-W. Zhang, S.-C. Shen, L.E. Yu, S. Kawi, K. Hidajat, K.Y. Simon Ng, Applied Catalysis A: General 250 (2003) 341-352.
[9]   J.-L. Shie, C.-Y. Chang, J.-H. Chen, W.-T. Tsai, Y.-H. Chen, C.-S. Chiou, C.-F. Chang, Applied Catalysis B: Environmental 58 (2005) 289-297.
[10]   F. Klingstedt, A. Kalantar Neyestanaki, L.E. Lindfors, T. Salmi, T. Heikkilä, E. Laine, Applied Catalysis A: General 239 (2003) 229-240.
[11]   E. Ntainjua N, A.F. Carley, S.H. Taylor, Catalysis Today 137 (2008) 362-366.
[12]   T. García, B. Solsona, S.H. Taylor, Applied Catalysis B: Environmental 66 (2006) 92-99.
[13]   T. Garcia, D. Sellick, F. Varela, I. Vázquez, A. Dejoz, S. Agouram, S.H. Taylor, B. Solsona, Applied Catalysis A: General 450 (2013) 169-177.
[14]   G.J. Hutchings, A.A. Mirzaei, R.W. Joyner, M.R.H. Siddiqui, S.H. Taylor, Applied Catalysis A: General 166 (1998) 143-152.
[15]   A.B. Lamb, W.C. Bray, J.C.W. Fraser, J. Ind. Eng. Chem. (Washington, D. C.) 13 (1920) 213-221.
[16]   B. Solsona, T. Garcia, S. Agouram, G.J. Hutchings, S.H. Taylor, Applied Catalysis B: Environmental 101 (2011) 388-396.
[17]   H.C. Genuino, S. Dharmarathna, E.C. Njagi, M.C. Mei, S.L. Suib, The Journal of Physical Chemistry C 116 (2012) 12066-12078.
[18]   V.H. Vu, J. Belkouch, A. Ould-Dris, B. Taouk, Journal of Hazardous Materials 169 (2009) 758-765.
[19]   A.A. Mirzaei, H.R. Shaterian, M. Habibi, G.J. Hutchings, S.H. Taylor, Applied Catalysis A: General 253 (2003) 499-508.
[20]   T.J. Clarke, T.E. Davies, S.A. Kondrat, S.H. Taylor, Applied Catalysis B: Environmental 165 (2015) 222-231.
[21]   P. Porta, G. Moretti, M.L. Jacono, M. Musicanti, A. Nardella, Journal of Materials Chemistry 1 (1991) 129-135.
[22]   P.A. Wright, S. Natarajan, J.M. Thomas, P.L. Gai-Boyes, Chemistry of Materials 4 (1992) 1053-1065.
[23]   C. Jones, K.J. Cole, S.H. Taylor, M.J. Crudace, G.J. Hutchings, Journal of Molecular Catalysis A: Chemical 305 (2009) 121-124.
[24]   K. Morgan, K.J. Cole, A. Goguet, C. Hardacre, G.J. Hutchings, N. Maguire, S.O. Shekhtman, S.H. Taylor, Journal of Catalysis 276 (2010) 38-48.
[25]   S.C. Kim, W.G. Shim, Applied Catalysis B: Environmental 98 (2010) 180-185.

[26]   F.C. Buciuman, F. Patcas, T. Hahn, Chemical Engineering and Processing: Process Intensification 38 (1999) 563-569.
[27]   R.E. Vandenberghe, G.G. Robbrecht, V.A.M. Brabers, Mater. Res. Bull. 8 (1973) 571-580.
[28]   N.K. Radhakrishnan, A.B. Biswas, Phys. Status Solidi A 44 (1977) 45-49.
[29]   G. Fierro, M. Lojacono, M. Inversi, P. Porta, R. Lavecchia, F. Cioci, Journal of Catalysis 148 (1994) 709-721.
[30]   A.A. Mirzaei, H.R. Shaterian, R.W. Joyner, M. Stockenhuber, S.H. Taylor, G.J. Hutchings, Catalysis Communications 4 (2003) 17-20.
[31]   B. Bems, M. Schur, A. Dassenoy, H. Junkes, D. Herein, R. Schlogl, Chem.--Eur. J. 9 (2003) 2039-2052.
[32]   Y. Tanaka, T. Takeguchi, R. Kikuchi, K. Eguchi, Applied Catalysis A: General 279 (2005) 59-66.
[33]   M.R. Morales, B.P. Barbero, L.E. Cadús, Applied Catalysis B: Environmental 67 (2006) 229-236.
[34]   M. Haruta, S. Tsubota, T. Kobayashi, H. Kageyama, M.J. Genet, B. Delmon, Journal of Catalysis 144 (1993) 175-192.
[35]   B.E. Solsona, T. Garcia, C. Jones, S.H. Taylor, A.F. Carley, G.J. Hutchings, Appl. Catal., A 312 (2006) 67-76.
[36]   C. Sze, E. Gulari, B.G. Demczyk, Materials Letters 36 (1998) 11-16.
[37]   H. Einaga, A. Kiya, S. Yoshioka, Y. Teraoka, Catalysis Science & Technology 4 (2014) 3713-3722.
[38]   K. Cole, A. Carley, M. Crudace, M. Clarke, S. Taylor, G. Hutchings, Catalysis Letters 138 (2010) 143-147.
[39]   M.P. Casaletto, A. Longo, A. Martorana, A. Prestianni, A.M. Venezia, Surface and Interface Analysis 38 (2006) 215-218.
[40]   H.S. Oh, J.H. Yang, C.K. Costello, Y.M. Wang, S.R. Bare, H.H. Kung, M.C. Kung, Journal of Catalysis 210 (2002) 375-386.
[41]   D. Sellick, D. Morgan, S. Taylor, Catalysts 5 (2015) 690-702.
[42]   Handbook of Chemistry and Physics, 73 ed., Chemical Rubber Publishing Company, 1993.
[43]   Kalchev, M. G., Andreev, A. A., Zotov, N. S., Water-gas shift reaction on CuO;ZnO catalysts. I: Structure and catalytic activity, Maik Nauka/Interperiodica, Moscow, RUSSIE, FEDERATION DE, 1995.
[44]   Y. Lai, H. Zhuang, K. Xie, D. Gong, Y. Tang, L. Sun, C. Lin, Z. Chen, New Journal of Chemistry 34 (2010) 1335-1340.

Chapter 4

Investigating the mechanochemical synthesis of CuMn$_2$O$_4$ catalysts

4.1 Introduction

As discussed in chapter 1 there is a drive towards more green catalyst preparation methods. Co-precipitation generates large amounts of aqueous waste from the precipitation step and from any washing steps required to remove unwanted by products that may poison the final material[1]. Nitrate waste generated by this process is a major pollutant causing ecological damage to waterways and its production and disposal is heavily regulated. As discussed in chapter 1 there are also many variables that can affect the resulting materials produced by co-precipitation including ageing time, precipitation pH and temperature [2-4] so a method that is more reproducible is advantageous.

Mechanochemical grinding is a very attractive process for catalyst preparation in that it is straightforward to perform, gives consistent results and does not generate any unwanted waste products or contain catalyst poisons[5]. As discussed in the comprehensive review by Hardacre *et al.* it has been applied to many catalytic preparations[6], but not widely investigated for the preparation of hopcalite.

Three precursor materials were investigated in order to determine which material was the most promising from which to prepare hopcalite. These were oxides, acetates and carbonates.

Saito et al recently demonstrated that lanthanum manganate perovskites can be directly synthesised from their component oxides[7]. The advantage to this method is that there is no requirement for a calcination step to generate the active catalytic material after milling.

Acetates have been investigated as potential $CuMn_2O_4$ precursors within the group previously by Kondrat *et al.* [8]. They ground copper and manganese acetate in a pestle and mortar and investigated the effects of calcination on phase formation for these materials. As they were able to obtain good CO conversions using a pestle and mortar it was logical to investigate the effects of high energy milling on this system.

Finally carbonates are the precursor material that are generated from co-precipitation when synthesising $CuMn_2O_4$. The precursor material precipitated is usually identified as $MnCO_3$ alongside an amorphous copper hydroxycarbonate[4] phase, mechanochemically grinding these two precursors will allow the investigation of this system. This work has been published in Applied Catalysis B: Environmental [9].

4.2 Preparing hopcalite catalysts from oxide precursors via a mechanochemical route.

The mechanochemical synthesis of catalysts using oxide precursors was performed as detailed in Section 2.1.5.1. Copper(II) oxide and manganese(III) oxide in a 1:2 copper to manganese molar ratio were ground in a planetary ball mill for up to 72 h at 400 rpm.

4.2.1 XRD of the materials prepared from oxides

The oxides of both copper and manganese can exist in multiple oxidation states. Figure 50 shows the XRD patterns of the precursor materials prior to the grinding process. The pattern clearly shows that the precursors contained only one crystalline phase.
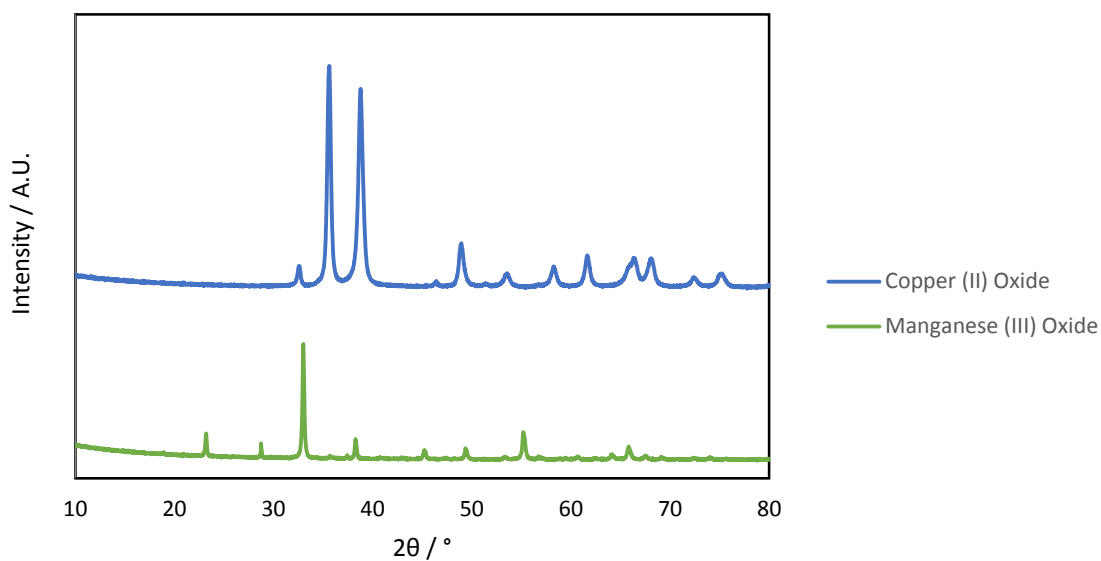
Figure 50: XRD of the oxide catalyst precursor materials used to prepare catalysts. 40mA, 40kV Cu source.

The copper oxide and manganese oxide consisted of CuO and Mn_2O_3 phases exclusively with no evidence of phases with other oxidation states. Moreover the XRD shows that the materials are very crystalline with well-defined, sharp reflections with no peak overlap that could confuse identification.
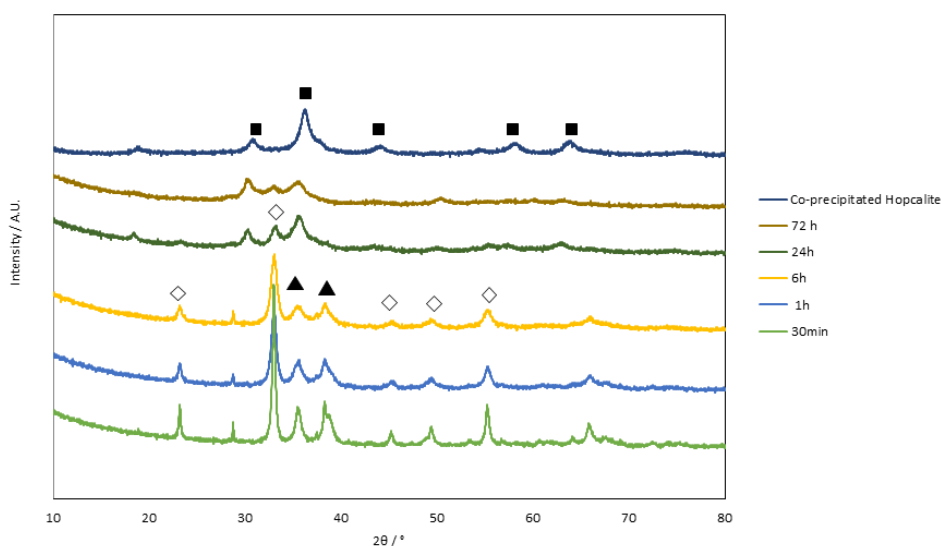
Figure 51: XRD Pattern of mechanochemically produced catalysts from oxides ▲ = CuO (ICDD: 01-089-5895), ◇ = Mn2O3 (01-071-3820), ■ = CuMn2O4 (01-075-0826). 40mA, 40kV Cu source

Figure 51 shows the XRD patterns of the materials after grinding. Copper manganese oxide material, prepared by a co-precipitation route, is also shown for comparison. In samples ground up to 6 h, CuO is clearly observed with reflections at 35.2° and 38.3° corresponding with the ($\bar{1}$11) and (111) planes respectively. Reflections corresponding to Mn_2O_3 are also observed in these materials, specifically the (222) plane gives rise to a reflection at 33° with less intense reflections at 23.2° and 53.4° corresponding to the (211) and (440) planes respectively.

After 24 h of grinding a new phase was observed with its principle reflection at 35.9°. This could correspond with the reflection due to the (311) lattice plane of $CuMn_2O_4$.The potential formation of this mixed phase coincides with the disappearance of reflections associated with CuO. This suggests that the copper is being consumed and incorporated into the manganese lattice to form the mixed phase. It is worth noting at this stage that decrease in crystallite size or a loss of the crystallinity of the sample could also account for this loss of detected CuO. The principle reflection associated with the Mn_2O_3 (222) plane is still observed at 33°, suggesting that if it is being incorporated, not all the CuO has been consumed, if all the CuO had been consumed the Mn_2O_3 would all have been converted to the $CuMn_2O_4$ phase. The nature of this remaining CuO is unknown. It is interesting to note that amorphous copper oxide hydrates are known to be stabilised by manganese oxide material and this could be an explanation for the missing copper[10].

As grinding continues up to 72 h both the $CuMn_2O_4$ phase and the Mn_2O_3 phase are still observed with again no evidence of the CuO phase observed in the XRD. It is important to consider the possibility that the new phase observed is Mn_3O_4, rather than $CuMn_2O_4$. Mn_3O_4 is also of the spinel structure group and as such exhibits similar diffraction behaviour. The principle reflection of the Mn_3O_4 phase is at 36.1°, this is within 1 degree of the peak observed and the peaks are quite broad, making positive identification difficult. However

the weak reflections at 57.4° and 64.1° suggest the presence of the mixed spinel phase rather than the manganese (II,III) oxide as they correspond with the (511) and (440) planes of the $CuMn_2O_4$ phase, these reflections are not present in Mn_3O_4. Rather, present in Mn_3O_4 are reflections at 58.7° and 60° due to the diffraction of the (321) and (224) planes.

Also of note, in the sample ground for 72h the principle $CuMn_2O_4$ peak has become markedly broader with the impact of additional grinding. The FWHM (full width half maximum) of the peak is increased from 1.59° to 1.69°. Using the Scherrer equation it is possible to determine that this broadening is equivalent to a crystallite size change from 55 to 51 Å. However this reduction is within the margin of error for crystallite size calculations using the Scherrer equation. very poorly with co-precipitated analogues of these catalysts which routinely have surface areas in the region of 100 m2 g-1[11].

Table 18 contains information regarding the physical properties of the catalysts produced by the mechanochemical method. There is little change in the surface area of the materials with all the ground catalysts remaining ± 1 m^2 g^{-1} of the precursors from which they were ground. This compares very poorly with co-precipitated analogues of these catalysts which routinely have surface areas in the region of 100 m^2 g^{-1}[11].

Table 18: Physical properties of catalysts synthesised by mechanochemical grinding of oxide precursors

Grind Time / h	Phases present	Surface Area	CO oxidation	Crystalite size / Å		
		/ m^2 g^{-1}	/ %	$CuMn_2O_4$	Mn_2O_3	CuO
0.5	Mn_2O_3, CuO	9	1.4	-	404	110
1	Mn_2O_3, CuO	6	0.2	-	179	75
6	Mn_2O_3, CuO	7	0.35	-	129	71
24	Mn_2O_3, $CuMn_2O_4$	8	0.36	55	119	-
72	Mn_2O_3, $CuMn_2O_4$	7	0.5	51	110	-
CuO	CuO	8	-	-	-	276
Mn_2O_3	Mn_2O_3	7	-	-	876	-

4.2.2 CO oxidation testing of the oxide catalysts

Figure 51 shows the CO oxidation activity of the catalysts. Activity for all catalysts was *ca* 1% and within the margin of error for each other (as discussed in chapter 2). CuO and Mn_2O_3 have been shown to be active for CO oxidation at elevated temperatures [12, 13], it is expected that the catalysts that contain these two phases are inactive for oxidation at room temperature. It was also expected that the catalysts containing $CuMn_2O_4$, a well-known CO oxidation catalyst would be more active. The lack of activity can be partially attributed to the very low surface area of these materials. The co-precipitated analogue commonly has surface areas in the region of 100 m^2 g^{-1} [11] far higher than the 6-9 m^2 g^{-1} range shown in Table 18

When activity was normalised for surface area (Figure 52) the catalysts exhibited the same trend with the rate for all materials falling within the margin of error. The sample ground for 0.5 h was the most active material per unit surface area despite also being the material with the highest surface area.

Another possibility that was considered was that H_2O adsorbed onto the surface of the material was inhibiting the activity of the catalyst. As there was no heat treatment or desiccation step involved with the preparation of these materials it is not unreasonable to assume that a considerable amount of H_2O had adsorbed to the surface of the catalyst and H_2O has been shown previously to be a prime agent in the deactivation of $CuMn_2O_4$ catalysts[14].

In order to rule out this possibility M5 was dried in in an oven for 16 h at 120 °C to remove any water adsorbed to the surface. There was no increase in activity observed. This proved that the catalysts were not being deactivated by water, rather they are not especially active for this reaction.
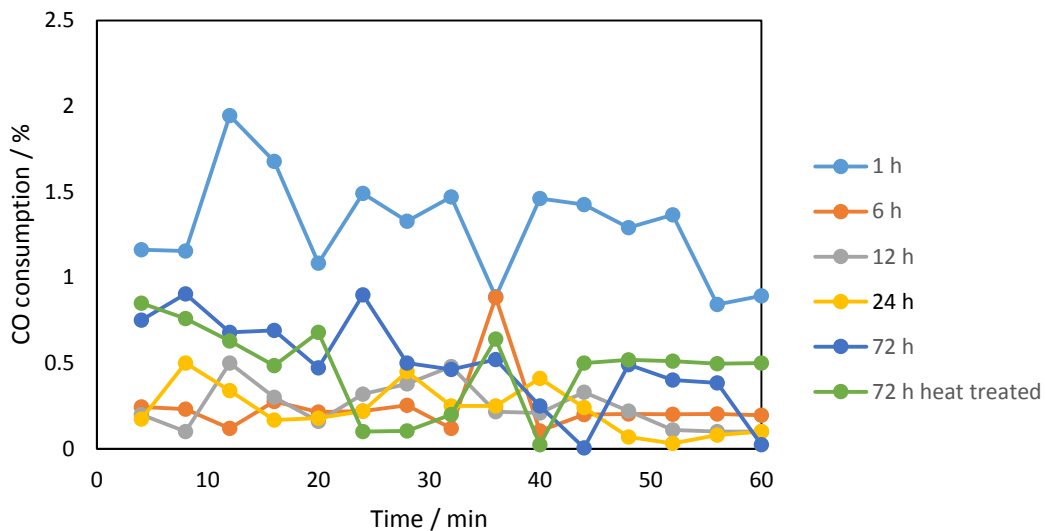
Figure 51: CO oxidation activity for mechanochemically prepared oxide catalysts. 5000 ppm CO / synthetic air, 21 mL min^{-1}, 25°C.

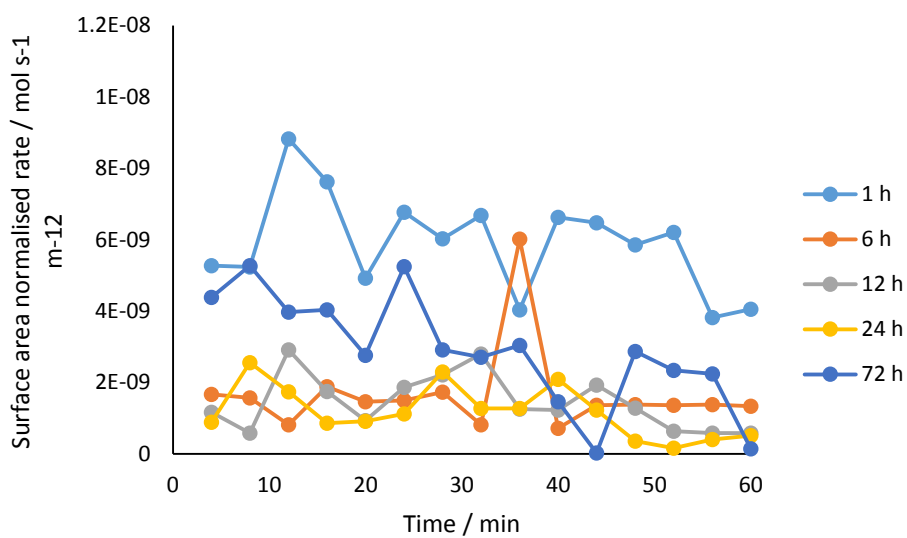
Figure 52: Surface area normalised CO oxidation rates of the catalysts prepared from oxide precursors. 5000 ppm CO / synthetic air, 21 mL min^{-1}, 25°C.

4.3 Preparing hopcalite catalysts from oxide precursors via a mechanochemical route

This section of work was carried out with the assistance of Korrin Saunders and also is presented as part of her MChem final year project.

The mechanochemical synthesis of catalysts using acetate precursors was performed as detailed in section 2.1.5.3. As detailed, copper (II) acetate hydrate and manganese (III) acetate hydrate in a 1:2 copper to manganese molar ratio were ground in a planetary ball mill for up to 72 h at 400 rpm.

4.3.2 XRD of the acetate reagents and ground catalyst precursors

XRD of the reagents before grinding in the planetary ball mill (Figure 53) showed reflections corresponding to the monoclinic phases copper (II) acetate and manganese (II) acetate respectively.
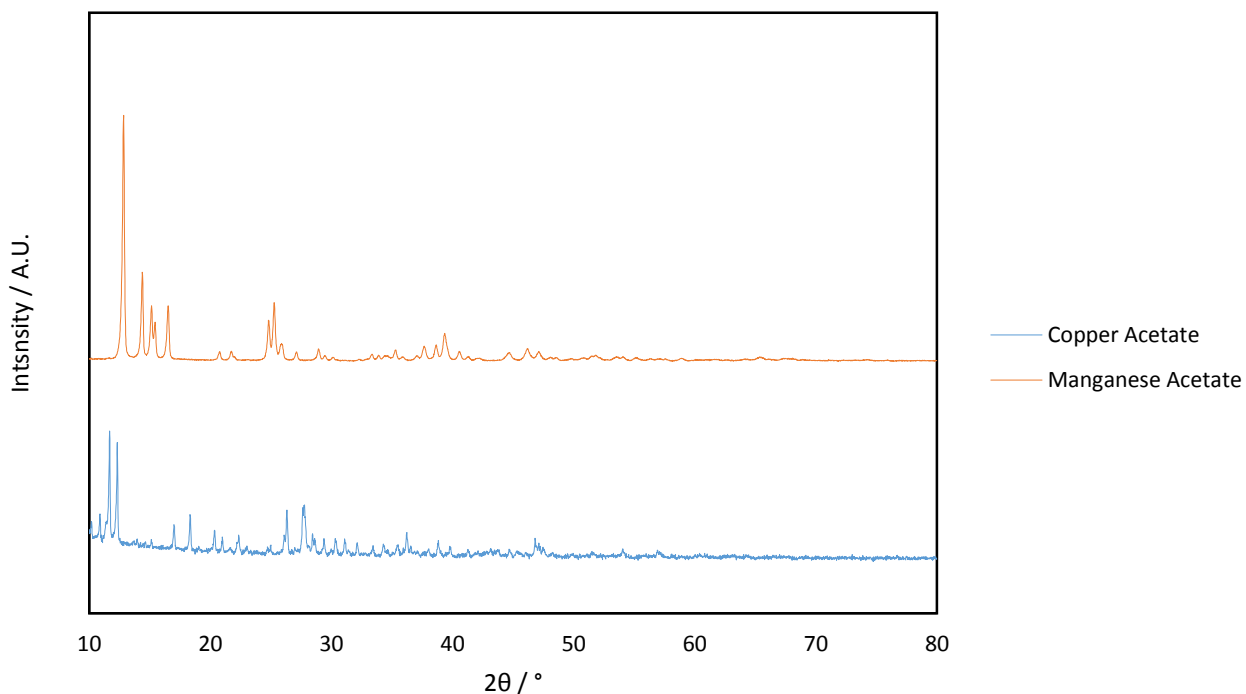
Figure 53: XRD of precursors before grinding. 40mA, 40kV Cu source.

Figure 54 shows the XRD pattern of the precursor materials after grinding. The phase makeup of all the materials is the same with both copper acetate and manganese acetate phases present in all materials. The intensity of the manganese acetate reflections decreases with increased grinding time, this suggests that the particles are becoming smaller. This trend was expected as grinding has long been known as an efficient method of reducing particle size. During the grinding process it is possible that there is an evolution and loss of acetone and water from the samples over the prolonged grinding period that also will have an effect on the observed pattern. It is known that manganese acetate will dissolve in its own water of hydration when heated, this almost certainly is the case during the grinding process [8].
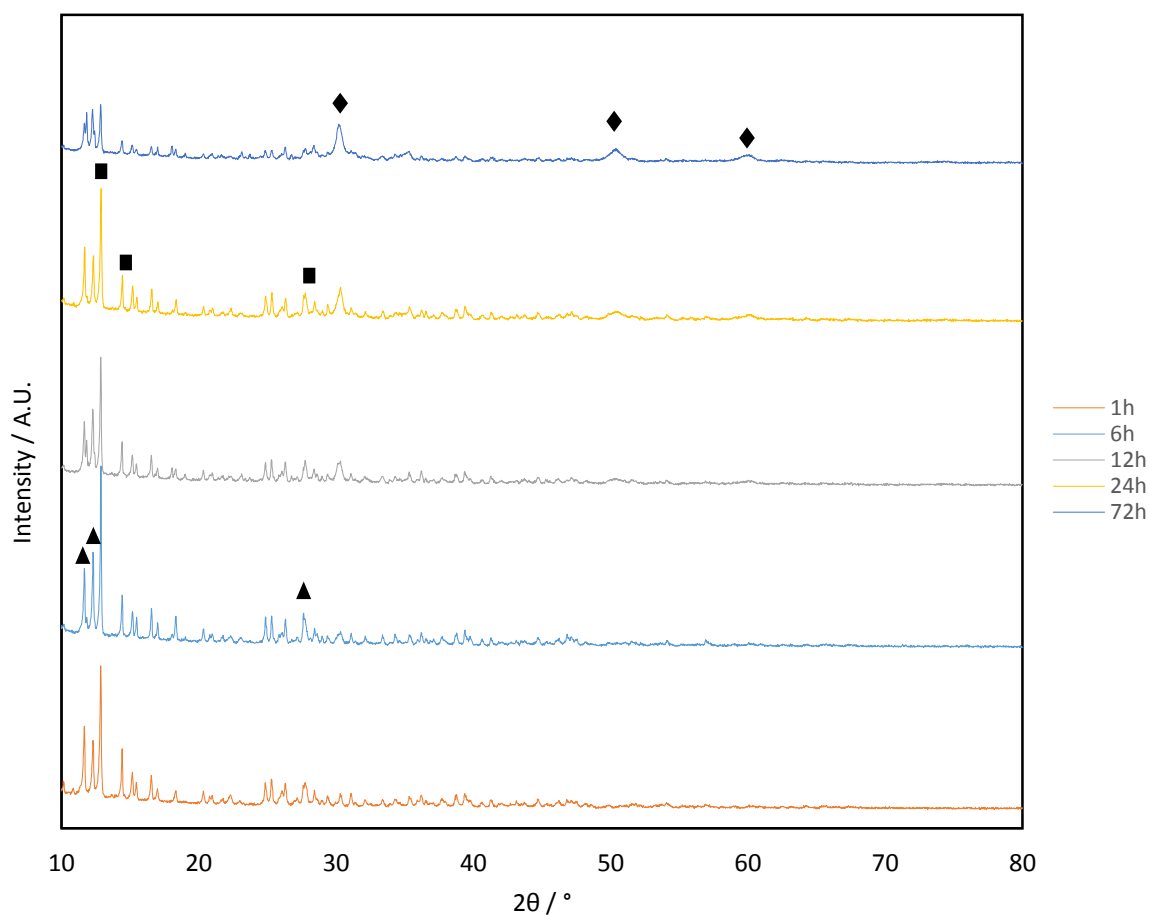
Figure 54: XRD of acetate catalyst precursor materials after grinding illustrating the decreasing intensity of the patterns along with the increasing contamination with zirconia. 40mA, 40kV Cu source.▲ = Manganese acetate hydrate (ICDD: 00-014-0724) ■= Copper acetate hydrate (00-046-0849) ◆ = Zirconium oxide (01-083-0937).

After grinding for 72 h a third phase is evident. This phase matches cubic zirconium oxide that makes up the grinding bowl and milling balls. The main peak observed at 30.4° corresponds to the (111) plane and further reflections at 50.6° and 60.2° to the (220) and (311) planes respectively. This ZrO_2 contamination is the result of the hardness of the manganese and copper acetates acting upon the grinding vessel and milling balls during the

milling process. Zirconia alone is not active for CO oxidation. As such the contaminant will simply act as a diluent within the catalyst.

4.3.3   Thermal gravimetric analysis of the ground acetate precursors

In order to investigate the behaviour of the samples under calcination conditions the samples were subjected to TGA analysis. Figure 55 shows the TGA traces of all the catalyst precursors. All samples have consistent mass loss profiles. Initially there is a mass loss associated with evolution of H_2O. Around 250 °C (Table 19) there is a mass loss event; this is followed by a second mass loss event at around 280 °C. These mass losses correspond with the thermal decomposition of the copper and manganese acetate precursors. With the first event due to the copper and the second due to the manganese acetate[15]. Thermal decomposition of metal acetates is a complex process, with multiple gasses evolved during the process.
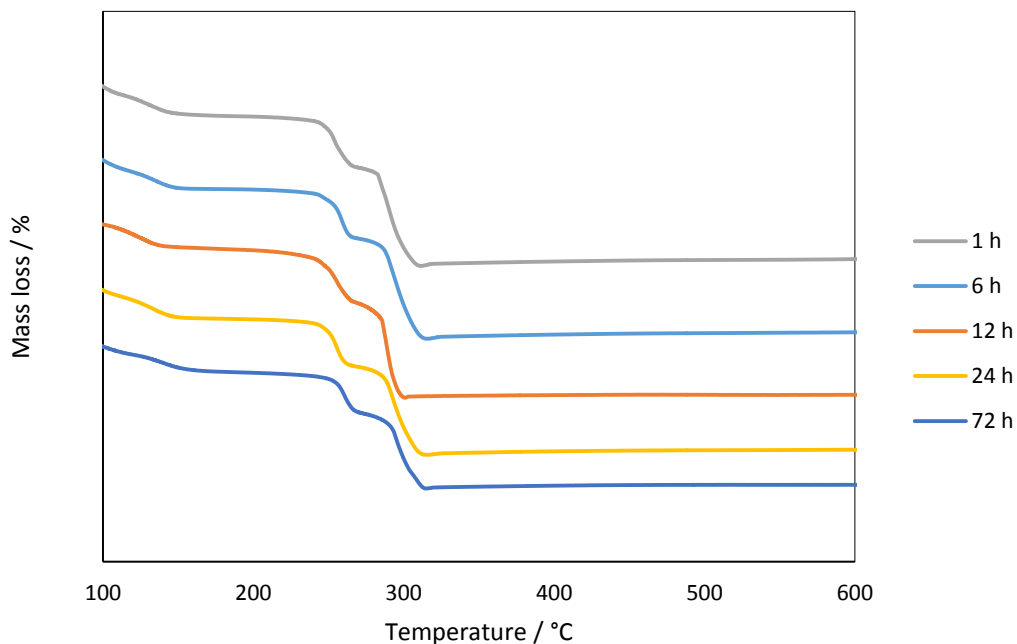

Figure 55: TGA of ground acetate precursors showing distinct, sharp mass loss events indicative of distinct phases decomposing. 5 °C min^{-1}, Air, 50 mL min^{-1}

Table 19: Physical properties of catalysts prepared by mechanochemical grinding of acetates.

| Grinding Time /h | TGA | | | | | Zr Contamination From EDX / wt% | Calcined Surface Area /m²g⁻¹ |
| | Mass loss / % | | | Temperature of mass loss / °C | | | |
	Total	1	2	1	2		
1	62	13	25	252	282	0	12
6	63	12	26	253	281	0	7
12	61	12	23	252	283	3	10
24	57	12	23	251	284	5	10
72	47	10	20	252	281	10	15

In the samples ground up to 12 h the magnitude of the mass losses remains constant. However, after 24 h and especially after 72 h there is a decrease in the overall mass loss. This is due to the influence of the ZrO_2 contaminant present as it does not thermally decompose under these heating conditions. EDX determined that up to 5 wt% of the 24 h sample and 10 wt% of the sample ground for 72 h is made up of the ZrO_2 contaminant. However, the changes in the mass loss could also be due to the loss of acetone and water during the grinding process. The presence of the ZrO_2 contaminant could also be masking any mass loss from these factors and it should be considered as a possibility.

The TGA data shows that by 300 °C the final mass loss event is underway, for this reason it was decided to calcine the materials at this temperature. Calcination at lower temperatures also serves to avoid the possibility of the formation of very crystalline oxide phases. Previous work on $CuMn_2O_4$ has shown that the presence of amorphous $CuMn_2O_4$ is preferred for the oxidation of CO[4].

4.3.4 XRD of calcined catalytic materials prepared from acetates

After calcination the samples were characterised by XRD (Figure 56). The sample ground for 1 hour showed clear evidence of the mixed $CuMn_2O_4$ phase with the principle reflection at 36.3° corresponds to the (311) plane and the reflections at 57.4° and 64.1 the (511) and (440) planes. Also present are small amounts of Mn_2O_3 with the peak at 32.5 corresponding with

the (222) plane. There is no strong evidence for the presence of reduced phases as detected

by Kondrat *et al*[8] when the samples were decomposed in the absence of oxygen.

As grinding time progresses the same phase composition is observed however there are

increasing amounts of ZrO_2 detected in the sample, as also seen in the precursor material.
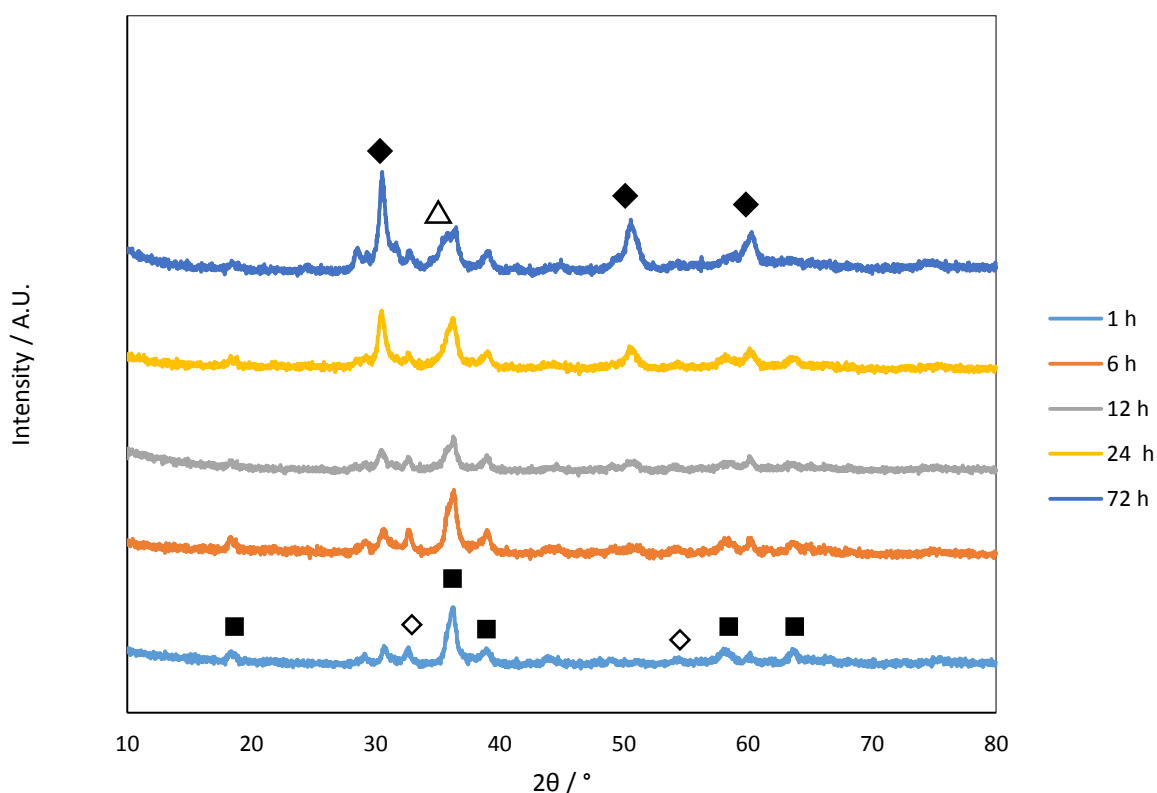
Figure 56: XRD of the catalysts prepared from acetate precursors after calcination. 40mA, 40kV Cu source. ◆ = ZrO_2 (ICCD: 01-083-0937), △= Mn_3O_4 (01-075-1560), ■= $CuMn_2O_4$ (01-075-0826), ◇ = Mn_2O_3 (01-071-3820)

 After 72 h of grinding there is a small shoulder observed on the principle $CuMn_2O_4$ reflection.

This could be attributed to the presence of the Mn_3O_4 phase. Both phases are of the AB_2O_4

spinel type and have very similar patterns so this assignment is not certain.

4.3.5 CO oxidation testing of the catalysts prepared from acetates

When tested for CO oxidation (Figure 57), all the materials exhibited similar, low activity. The range of conversions between 1 and 2 % at steady state is within the margin of error for the instrument. There is a decrease in the activity observed with higher grinding times however this is most likely due to the increasing effects of ZrO_2 acting as a diluent.
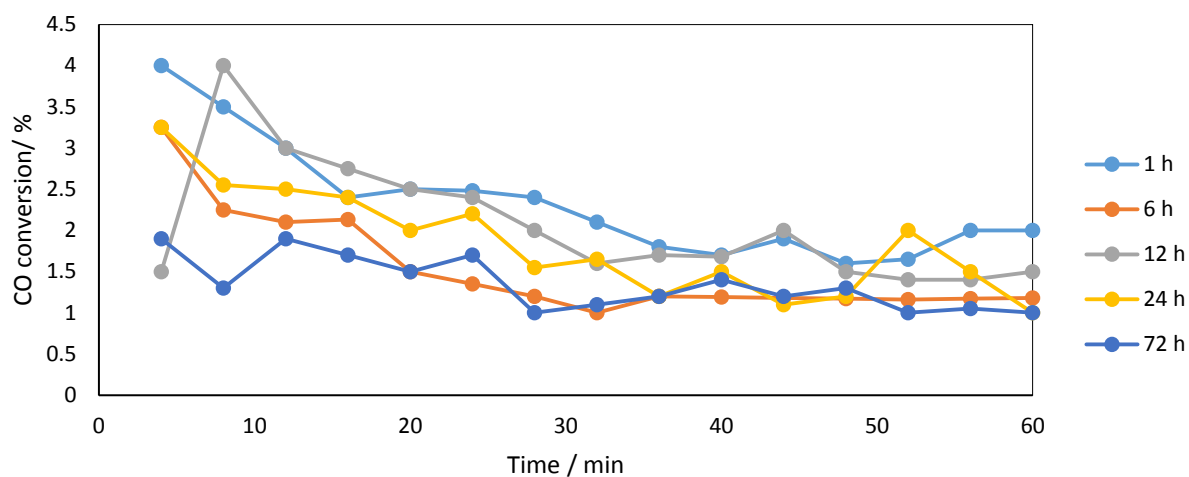
Figure 57: CO oxidation activity of catalysts produced from acetate precursors. 5000 ppm CO / synthetic air, 21 mL min^{-1}, 25°C.

4.4 Catalysts produced from carbonate precursors

The mechanochemical synthesis of catalysts using carbonates as precursors was performed as detailed in section 2.1.5.2. In summary, copper (II) hydroxycarbonate and manganese (III) carbonate in a 1:2 copper to manganese molar ratio were ground in a planetary ball mill for up to 72 h at 400 rpm. The resulting powders were then calcined at 415 °C for 2 hours to give the active catalyst material.

4.4.2   XRD of the carbonate reagents and catalyst precursours.

The XRD of the reagents used to prepare the catalysts is shown in figure 58 The only phases present in the precursor materials were the copper hydroxycarbonate phase and the manganese carbonate phase.
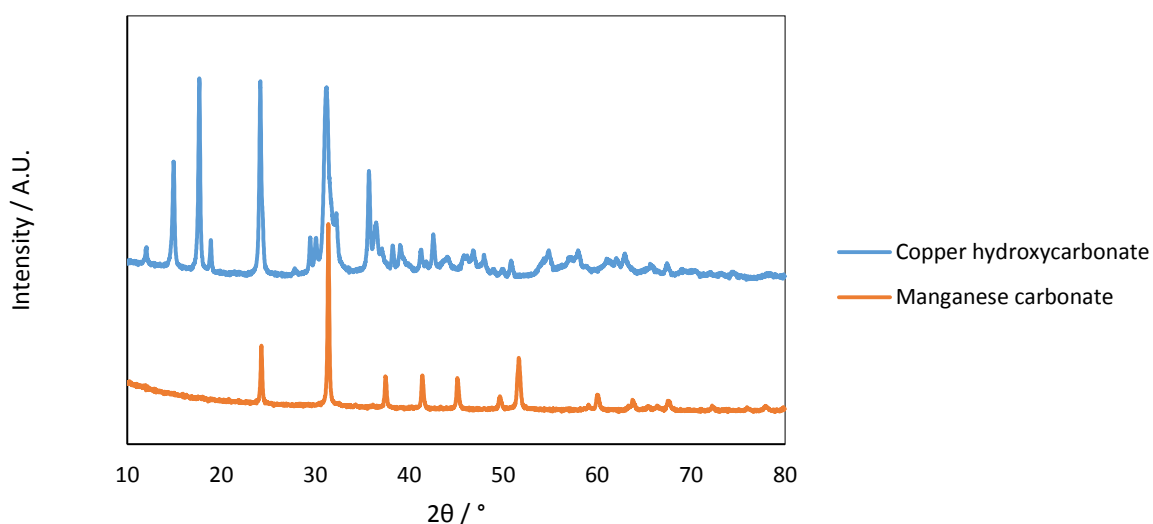
Figure 58: XRD of reagents used to make catalysts from carbonate precursors. 40mA 40kV Cu source.

The XRD patterns of the precursors ground for times between 0.5 and 72 h can be seen in Figure 59. The dominant reflections after all grinding times correspond with the $MnCO_3$ phase. The principle (104) reflection can be seen at around 31.4° 2θ. After 0.5 h grinding the (020) and (120) reflections from the $Cu_2(OH)_2CO_3$ phase are also visible at 14.9 and 17.6° 2θ respectively. After 1 h the intensity of both visible $Cu_2(OH)_2CO_3$ peaks has decreased and after 12h they were not visible at all. This loss of discernible $Cu_2(OH)_2CO_3$ reflections can be attributed to a number of factors. A reduction in crystallite size, phase change and loss of crystallinity are all possible explanations. Indeed when ground in the absence of manganese carbonate $Cu_2(OH)_2CO_3$ the reflections lost intensity with grinding time, eventually giving a pattern with no visible reflections after 72h (Figure 60). When ground in the presence of copper hydroxycarbonate, the reflections assigned to the $MnCO_3$ phase do not lose intensity

in the same manner as the $Cu_2(OH)_2CO_3$, although some broadening is observed as the grinding time is increased. However the position of the reflections moves towards larger 2θ values with an increase in grinding time, caused by a reduction in the unit cell volume of the $MnCO_3$ phase.
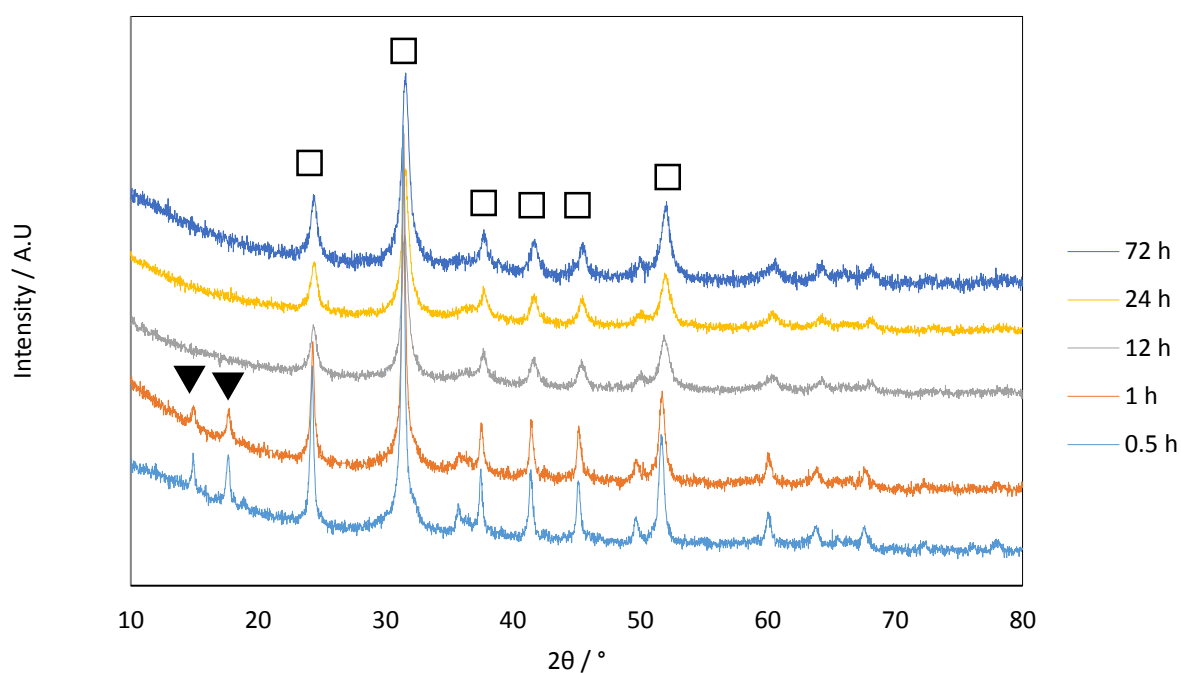
Figure 59: XRD of catalyst precursors prepared from carbonate reagents. 40mA 40kV Cu source □ = $MnCO_3$ (ICDD: 01-071-3820), ▼ = $Cu_2(OH)_2CO_3$ (00-001-0959)

Table 20: Physical properties of catalysts prepared by mechanochemical grinding of carbonates.

Time /h	Crystallite size /nm	Cell parameters				TGA				Surface area /m^{2}g^{-1}
		a/Å	b/ Å	c/Å	Vol/Å	Mass loss / wt%		Temperature / °C		
						1	2	1	2	
MnCO$_3$	61	4.7993	-	15.6783	312.824	-	-	-	-	-
CuO	-	-	-	-	-	-	-	-	-	13
MnOx	-	-	-	-	-	-	-	-	-	60
0.5	35	4.7983	-	15.6666	312.380	8	16	300	495	65
1	27	4.7985	-	15.6693	312.367	6	16	307	483	45
12	15	4.7717	-	15.6086	307.629	-	21	-	480	50
24	14	4.7690	-	15.5901	306.954	-	22	-	475	21
72	14	4.7664	-	15.5757	306.451	-	21	-	438	78

Figure 60: XRD pattern of copper hydroxycarbonate ground alone

Lattice parameters for the MnCO$_3$ phase were determined using Rietveld refinement as detailed in chapter 3. The parameters are detailed in Table 20.

There is a clear trend for both the a and c lattice constants to shrink with grinding time. In unground $MnCO_3$ they are 4.799 and 15.678 Å respectively, shrinking to 4.766 and 15.576 Å after 72 h grinding. This reduction of the unit c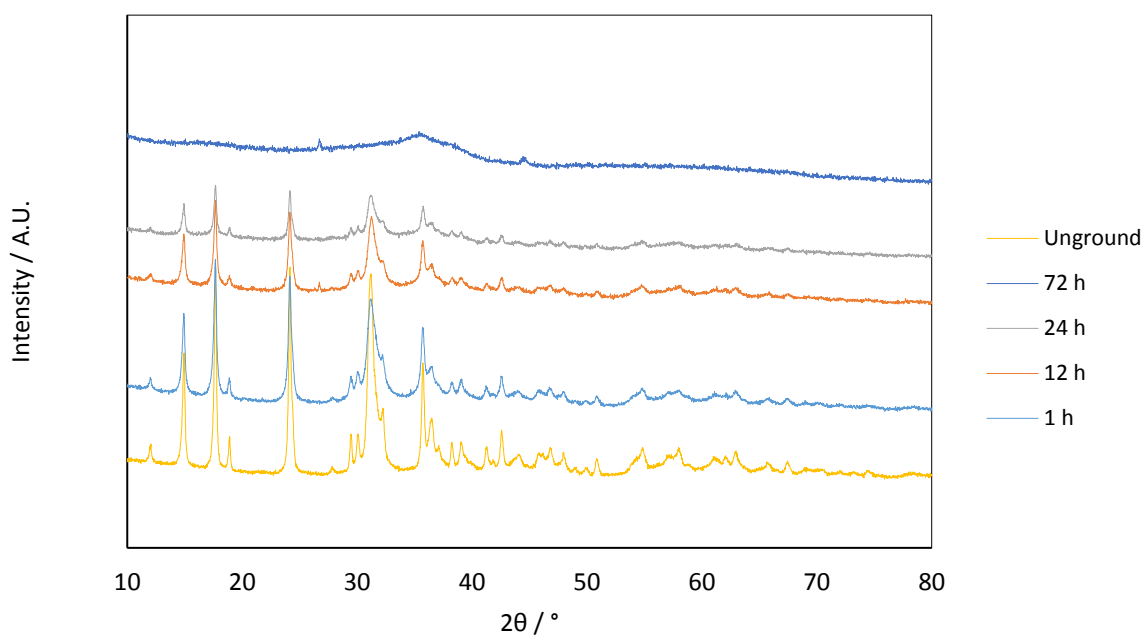ell volume is reflected in the volume change with a reduction of 6 Å^3 over the course of the grinding process. Figure 61 a and b shows the XRD pattern from 30 - 33° focusing on the (104) reflection of $MnCO_3$ after various grinding times. In Figure 61a the $MnCO_3$ was ground alone and clearly there is no change in the peak position, and thus no contraction of the unit cell. In Figure 61b however the shift in the (104) reflection is clear. This contraction is therefore a result of the mechanochemical interaction between the copper hydroxycarbonate and manganese carbonate phases during grinding. Porta et at showed that when Cu^{2+} is substituted into the lattice of manganese carbonate, to form a $Mn_{1-x}Cu_xCO_3$ phase, there is a contraction in the unit cell[16]. This process was found to be more facile than the incorporation of manganese into the copper hydroxycarbonate lattice. The contraction is a result of both the smaller ionic radius of Cu^{2+} and the higher covalency of the CuO_6 polyhedra along with site distortion due to the d9 electron configuration of Cu^{2+}. They found that Cu^{2+} incorporation was limited to around 30%, the decrease of 6 Å^3 corresponds to a Cu^{2+} incorporation of only around 15 %[16]. Vergads law does not apply in this case[17] as Porta et al show that the change in lattice parameter is not linearly related to the Cu^{2+} concentration.

Also shown in Table 20 is the crystallite size of the carbonate precursor phases as a function of grinding time. It is shown that there is a decrease in the average crystallite size as grinding time increases. Unground, the average crystallite size is 61 nm decreasing to a minimum of 14 nm after 24 h. This corresponds with the incorporation of Cu^{2+} into the $MnCO_3$ lattice as the smaller crystallite size leads to a larger surface area to volume ratio, allowing solid state reactions such as this to proceed more readily.
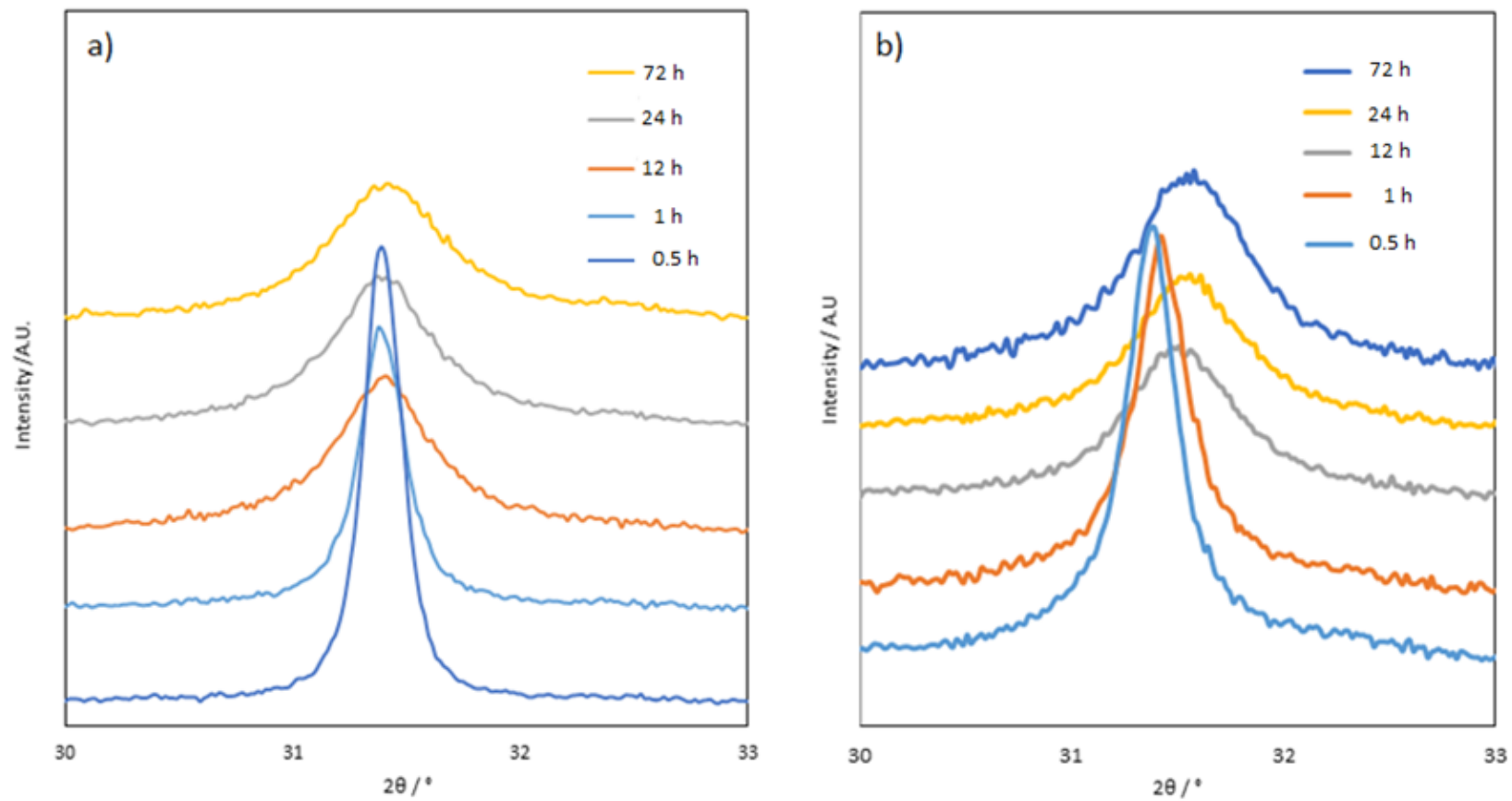
Figure 61: a) XRD of $MnCO_3$ ground alone showing no peak shift with grinding. b) XRD of $MnCO_3$ ground with $Cu_2(OH)_2CO_3$ and the shift in 2θ values to higher angles as a result of unit cell contraction

4.2.3 Thermal gravimetric analysis

The precursors were subjected to thermal gravimetric analysis (Figure 62: TGA of catalyst precursors prepared from carbonate reagents Up to 200 °C there is weight loss due to the desorption of physisorbed and chemisorbed water. It was found that the catalysts that exhibited evidence of copper hydroxycarbonate alongside manganese carbonate In the XRD had two distinct mass loss events, one at around 300 °C corresponding to copper hydroxycarbonate and a broader weight loss around 420 °C corresponding to manganese carbonate.
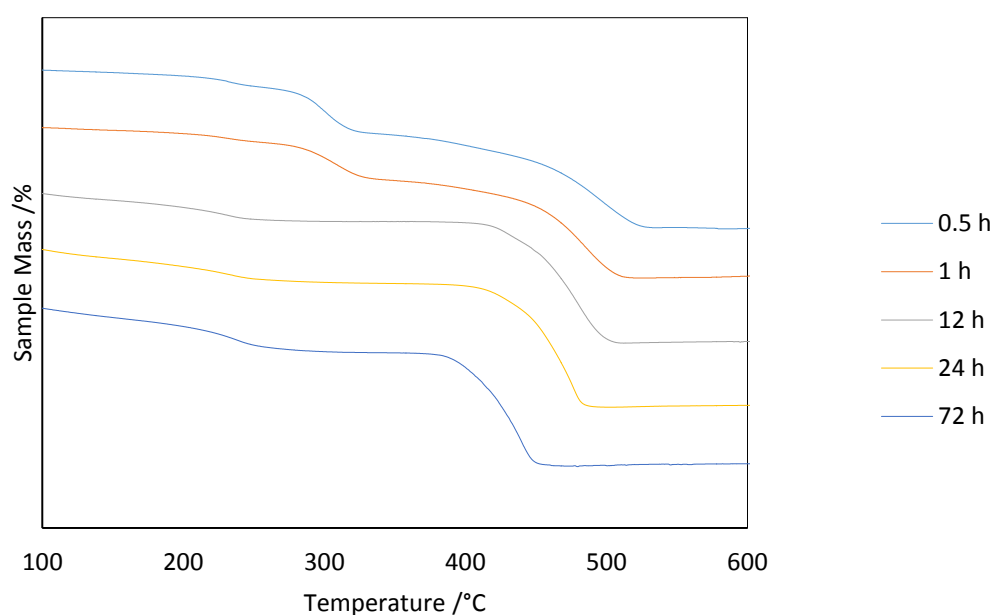
Figure 62: TGA of catalyst precursors prepared from carbonate reagents. Air atmosphere, flow rate 50 mL min^{-1}

The samples that only showed one phase in the XRD only had one mass loss event in the TGA. This is attributed to the thermal decomposition of the $Mn_{1-x}Cu_xCO_3$ phase. There is a trend towards lower thermal decomposition temperatures as the grinding time increases. This could be the effect of forming smaller particles that thermally decompose more readily.

4.2.4 XRD of calcined catalytic materials

As detailed earlier the active catalyst was generated by calcining the precursor materials in static air for 2 h at a temperature of 415 °C heated by a ramp rate of 2 °C min^{-1}. This was found by Hutchings

et. al. to be the most effective calcination temperature for $CuMn_2O_4$ catalysts as it generated an amorphous $CuMn_2O_4$ phase[11].
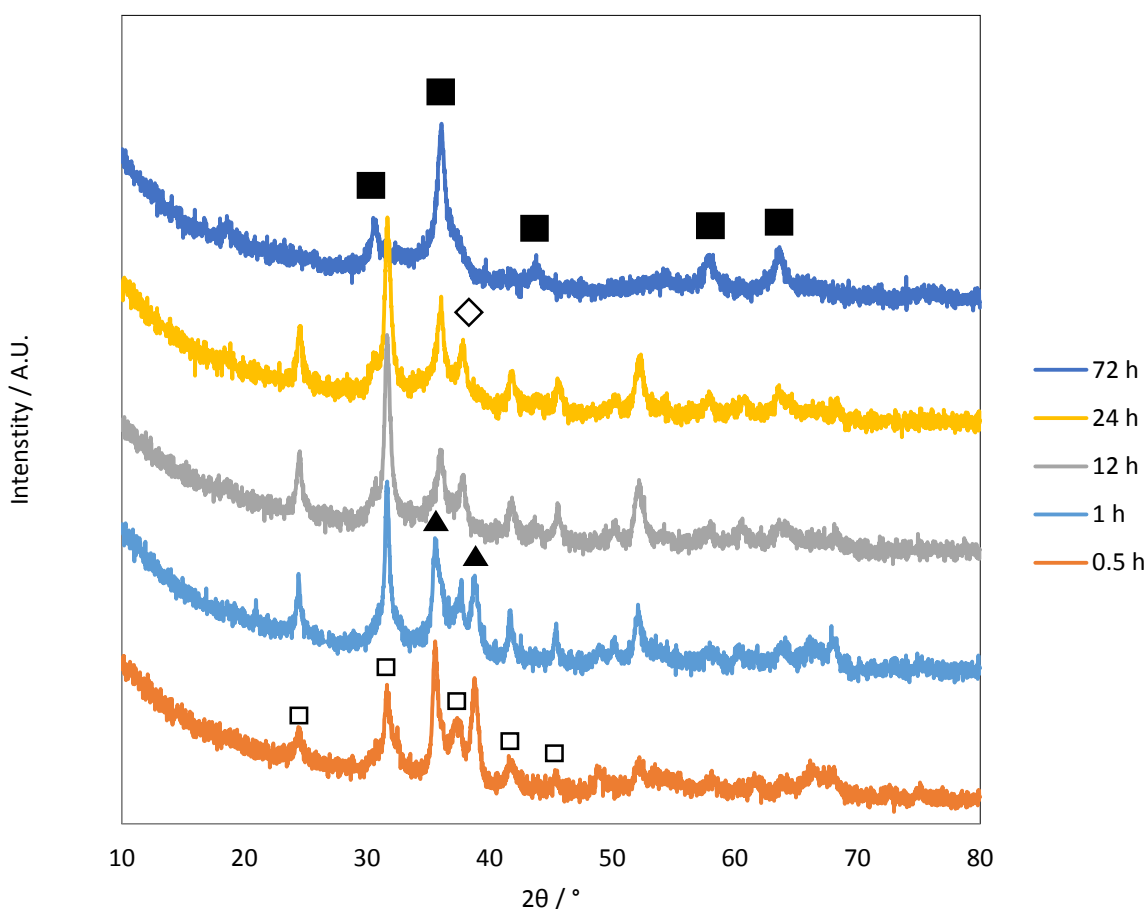
Figure 63: XRD of the calcined catalysts generated from carbonate precursors showing the evolution from phase separated materials to mixed metal oxide with grinding. □ = $MnCO_3$ (ICDD: 01-071-3820), ▲ = CuO (01-089-5895), ■ = $CuMn_2O_4$ (01-075-0826) ◇ = Mn_2O_3 (01-071-3820). 40mA 40kV Cu source.

Figure 63 shows the X-ray diffraction patterns for the calcined catalysts. The catalysts ground for 30mins and 1h showed evidence of CuO and $MnCO_3$, in keeping with the TGA data (Figure 62) that suggests that the decomposition of $MnCO_3$ is only complete at 500 °C. After grinding for 12 h and 24 h there is evidence of $CuMn_2O_4$ formation alongside residual $MnCO_3$. Again this is in agreement with the TGA data, as the weight loss event associated with $Cu_2(OH)_2CO_3$ is no longer observed and the weight loss associated with the $Mn_{1-x}Cu_xCO_3$ decomposition does not end until 500 °C in the case of the 12 h catalyst and 480 °C for the 24 h ground material. After grinding for 72h the only phase

detected was nanocrystaline $CuMn_2O_4$. Indeed $CuMn_2O_4$ formation appears linked to $MnCO_3$ decomposition, due to incorporation of Cu^{2+} into the $MnCO_3$ lattice during the preparation. The incorporation of Cu^{2+} ions into the $MnCO_3$ lattice appears to be a favoured, but kinetically limited process.

4.2.5   In situ XRD

In situ XRD was used to determine if the decomposition of the copper substituted $MnCO_3$ phase was responsible for the formation of the nano-crystaline spinel, or whether the single oxide phases (CuO, Mn_2O_3) are formed before reacting to form the spinel. Two catalysts were studied, the samples ground for 1 h and 72 h. The materials were heated from 25 °C to 600 °C and scans taken every 25 °C. Figure 64a shows the phase evolution of the sample ground for 1 h over the temperature range. The (104) reflection of $MnCO_3$ is clearly visible at 31.4° from 25 °C. By 300 °C the reflections associated with the CuO ($\bar{1}11$) and (111) planes become visible at 35.5° and 38.7°, this is in agreement with the TGA data (Figure 62) that suggests that the $Cu_2(OH)_2CO_3$ phase decomposes at around 300 °C. At 450 °C the $MnCO_3$ phase begins to lose intensity and a reflection corresponding with the (311) lattice plane of $CuMn_2O_4$ is observed at 35.7°. This corresponds with the decomposition of $MnCO_3$ in the TGA. As temperature increases further to 500 °C, a reflection corresponding to the (222) plane of Mn_2O_3 is observed at 33.1°. There is no evidence in the TGA to associate with this phase formation suggesting that a highly amorphous manganese oxide phase had formed during the decomposition of $MnCO_3$. In comparison Figure 64b shows the *in situ* XRD of the material ground for 72 h. No evidence of the CuO ($\bar{1}11$) and (111) planes at 35.5° and 38.7° are observed at any temperature. This re-enforces our supposition that the copper is being incorporated into the $MnCO_3$ lattice during grinding. However if all Cu^{2+} had been incorporated, a total of 33 % incorporation would be required. When compared with Porta's studies[16] the XRD analysis only suggests an incorporation of around 15 % (Figure 61). This suggests the presence of an undetected copper phase within this material alongside the $Cu_xMn_{1-x}CO_3$. Within the literature it is known that amorphous copper oxide hydrates such as Hydrocuprite and Melaconite are stabilised by manganese oxides [10]. If a phase of this type is indeed present in
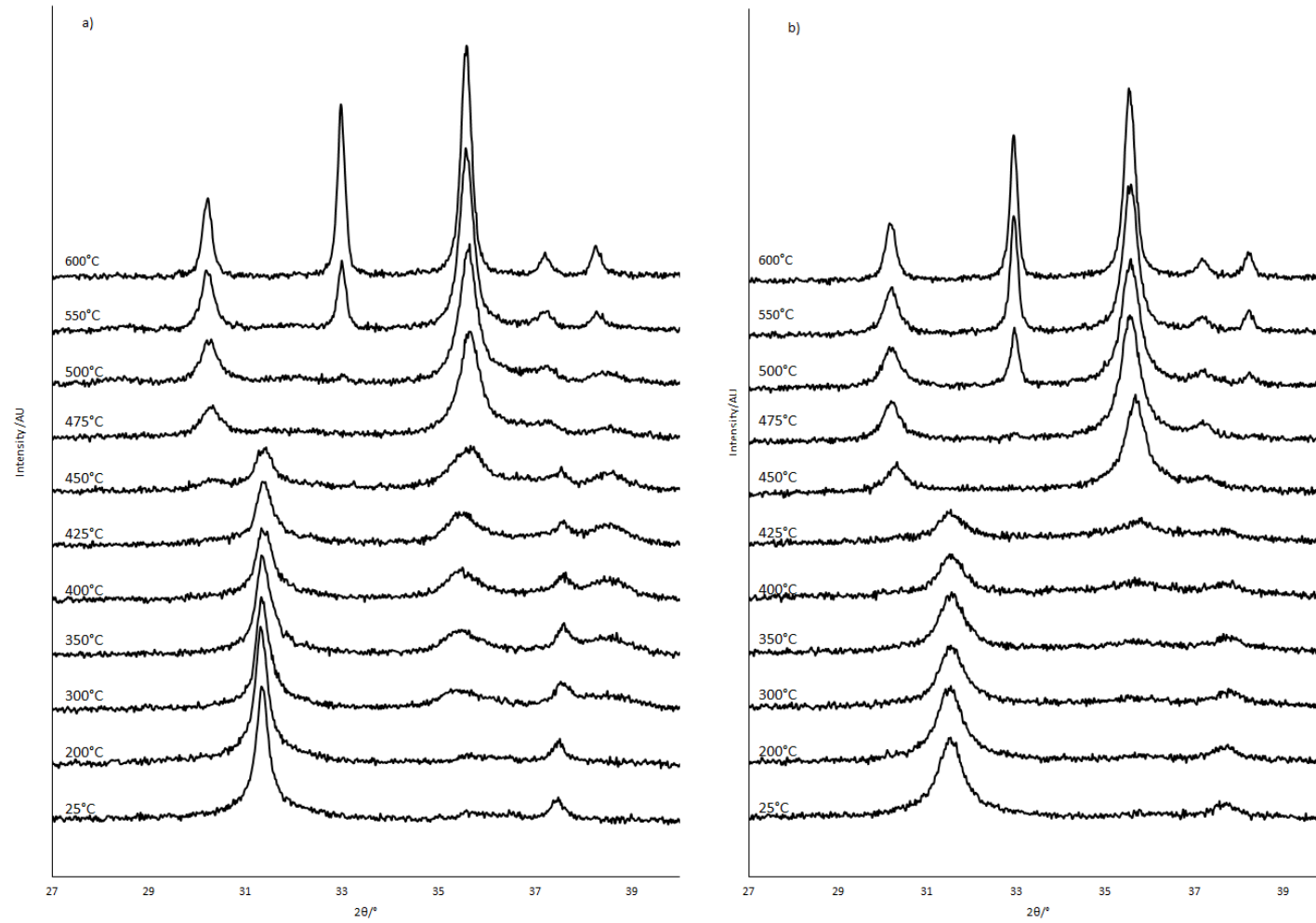
Figure 64: In situ XRD of carbonate catalyst precursors a) 1 h b) 72 h. 40mA 40kV Cu source, ramp rate of 3 °C min^{-1} held for 8 min scans, 4mL min^{-1} flow of air.

this case, the energy requirement for formation of the spinel during calcination would be lower than for separate crystalline materials. With the data available it is not possible to state that the $Mn_{1-x}Cu_xCO_3$ phase is the only source of spinel formation. What can be said however is that with prolonged grinding the formation of this phase proceeds more readily. This is reflected in the *in situ* XRD. At 400 °C a broad reflection at 35.7° was observed, this corresponds with the (311) plane of $CuMn_2O_4$. This is 50 °C lower than the sample ground for 1 h. At 450 °C this is a well-defined, crystalline phase. By 500 °C the presence of Mn_2O_3 is once again observed, despite the absence of CuO. It is possible that excess copper could be residing within the vacant tetrahedral sites of the $CuMn_2O_4$ or remaining as a stabilised amorphous phase as the Cu:Mn ratio has been determined to be 1:1.84 by MP-AES.

4.2.6 Elemental analysis

Table 21: Cu:Mn Ratio of catalysts prepared from carbonate precursors as determined by MP-AES

Grinding Time / h	Cu:Mn ratio
0.5	1:1.84
1	1:1.83
6	1:1.83
24	1:1.86
72	1:1.84

Elemental analysis (Table 21) shows that the Cu:Mn ratio remains constant independent of grinding time. The ratio of 1:1.84 is slightly lower than the expected 1:2 ratio however the materials are very hygroscopic and water absorption can lead to inconsistencies in the mass weighed out.

4.2.7 Temperature programmed reduction

In order to further investigate the phase evolution of the materials with grinding the calcined catalysts were characterised by temperature programmed reduction. Figure 65 shows the H_2 consumption profiles of the catalysts and the total hydrogen consumption is detailed in Table 22.

The catalysts ground for 24 h or less exhibited similar H_2 consumption. After 72 h the hydrogen consumption was seen to increase by *ca.* 50%. This is attributed to the full formation of the mixed metal oxide phase with no residual carbonate or single oxide phases present.

Figure 65 contains the TPR profiles of the catalysts. After 0.5 h of grinding one broad reduction peak is observed at 297 °C with a shoulder at 255 °C. This is due to the reduction of the CuO observed in the XRD (Figure 63), CuO has previously been shown to exhibit a shoulder of this type and is attributed to multiple CuO species existing in conjunction with other metal oxides[18]. This is followed by the complex reduction of $MnCO_3$ and its reduction products. After 1 h the reduction of CuO is more prominent with the previous shoulder at 255 °C now a prominent peak at 254 °C. A new peak is observed at 404 °C due to the second step of the $Mn_2O_3 \rightarrow Mn_3O_4 \rightarrow MnO$ reduction. Grinding for 6 h results in a lowering of the CuO reduction temperature and a shoulder is observed at 292 °C due to the first step of the $Mn_2O_3 \rightarrow Mn_3O_4 \rightarrow MnO$ reduction no longer being masked by the sifting CuO $\rightarrow$ Cu reduction. The reduction of the materials becomes more facile with increased grinding as signified by the shift of the highest reduction peak from 404 °C to 390 °C. This trend of lowering reduction temperatures continues in the sample ground for 24 h.

Table 22: Summary of H_2 consumption data acquired from TPR studies of the catalysts prepared from carbonate precursors

Time / h	Hydrogen consumption / mol g^{-1}
0.5	0.018
1	0.016
12	0.018
24	0.016
72	0.024
Theoretical yield for CuMn$_2$O$_4$	0.021

After 72 h the reduction profile has changed significantly, however with the characteristic two step reduction of the spinel phase now observed [19].

A low temperature TPR shoulder is observed consistently within all samples. This shoulder consistently shifts to lower temperatures with an increase in grinding time. If the activity of the

catalysts is linked to a redox mechanism then this reducible species could be a good indicator of catalyst activity as the lattice oxygen is increasing becoming more mobile with longer grinding times potentially promoting Mars van Krevelen type reaction mechanisms.
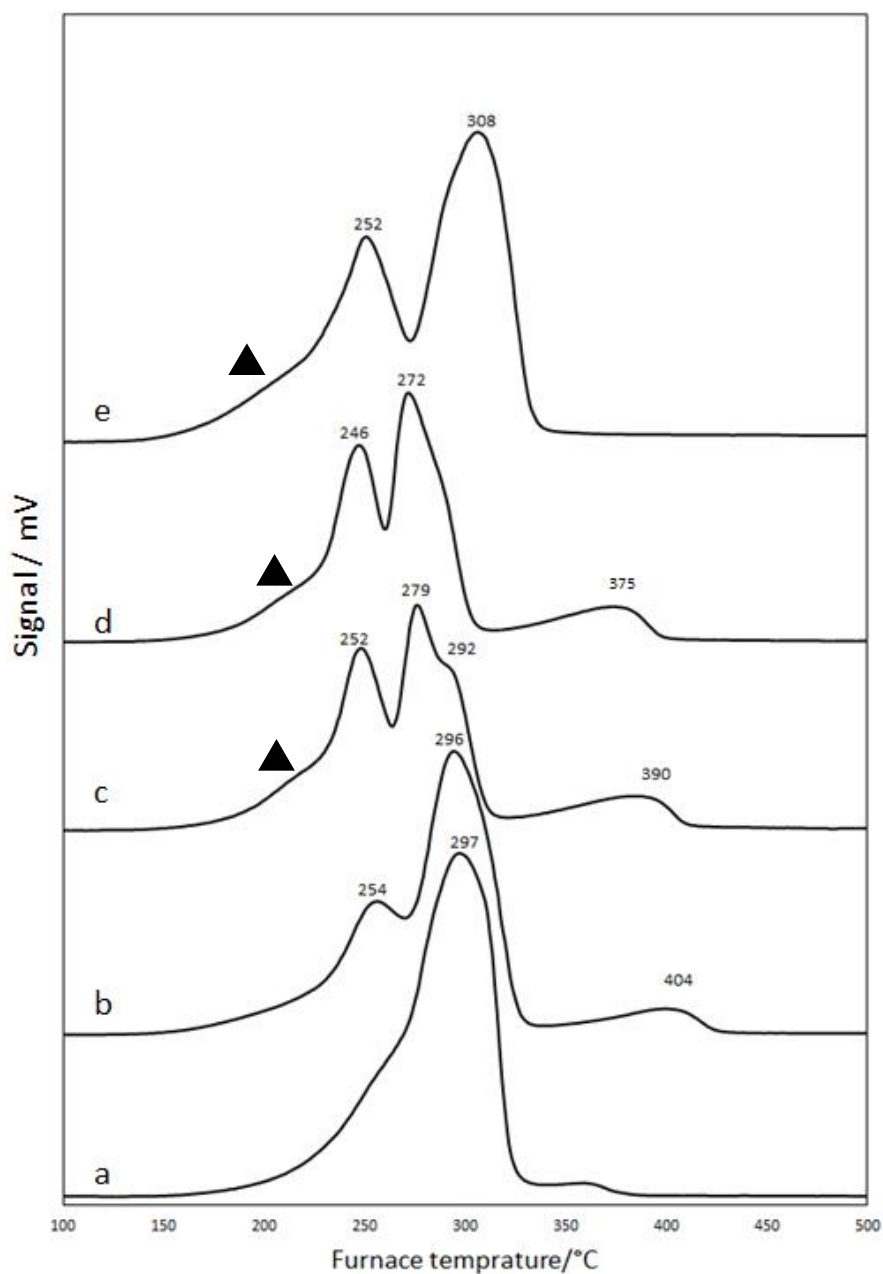
Figure 65:   TPR profiles of calcined catalysts prepared from carbonate precursors a) 0.5 h, b) 1 h, c) 6 h, d) 24 h e) 72 h ▲ = low temperature shoulder. 20mL min $^{-1}$ 10 % H_2/Ar, 5°C min^{-1} heating rate

4.2.8   Microscopy and elemental mapping

One of the main advantages of the co-precipitation method of catalyst synthesis is the homogeneous nature of the final precipitated material.   In order to assess the homogeneity of the mechanochemically prepared catalysts they were analysed by SEM-EDX mapping.

Figure 66 contains representative EDX mapping images of the calcined catalysts prepared by mechanochemical grinding from carbonate precursors. From the images it is clear that after 72 h the materials have become homogenous on the micro scale whilst the catalysts ground for less time still contain large and distinct copper and manganese rich domains.   EDX showed no zirconium contamination in any of the samples as was observed in materials generated from acetate precursours.
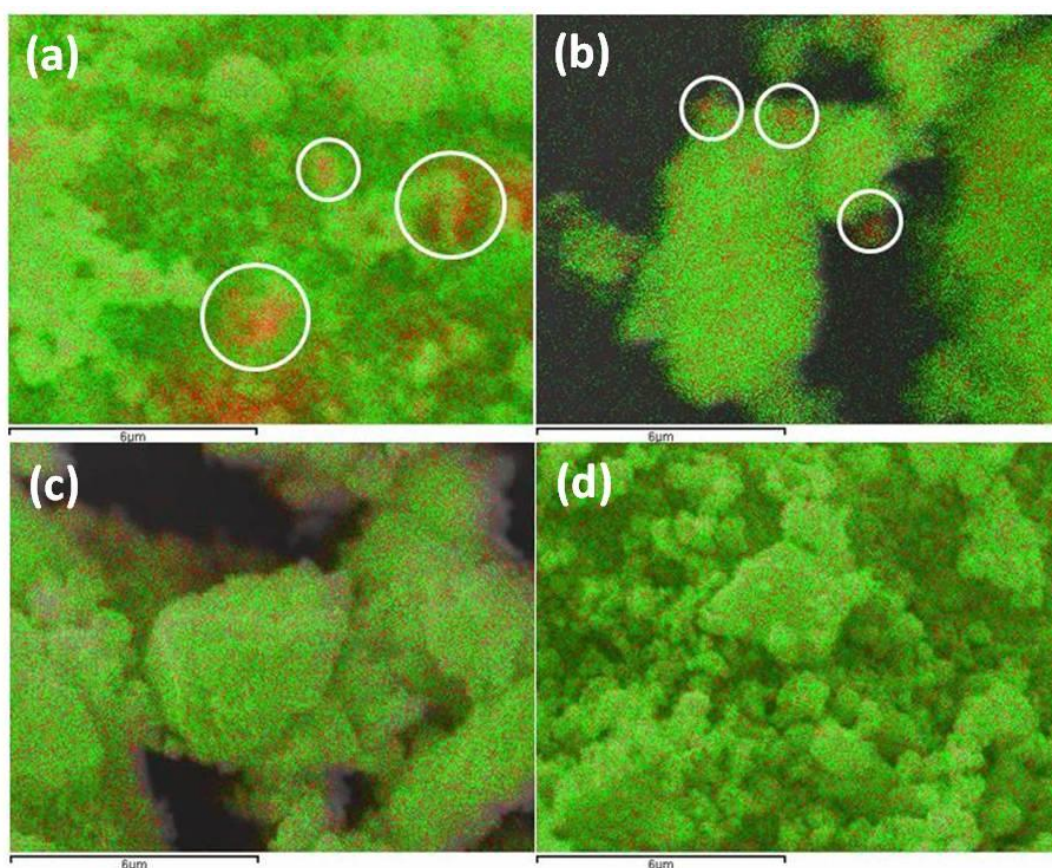
Figure 66: SEM EDX mapping of the calcined catalyst prepared from carbonate precursours. a) 0.5 h, b) 1 h, c) 24 h, d) 72h. Green = Manganese, Red = Copper
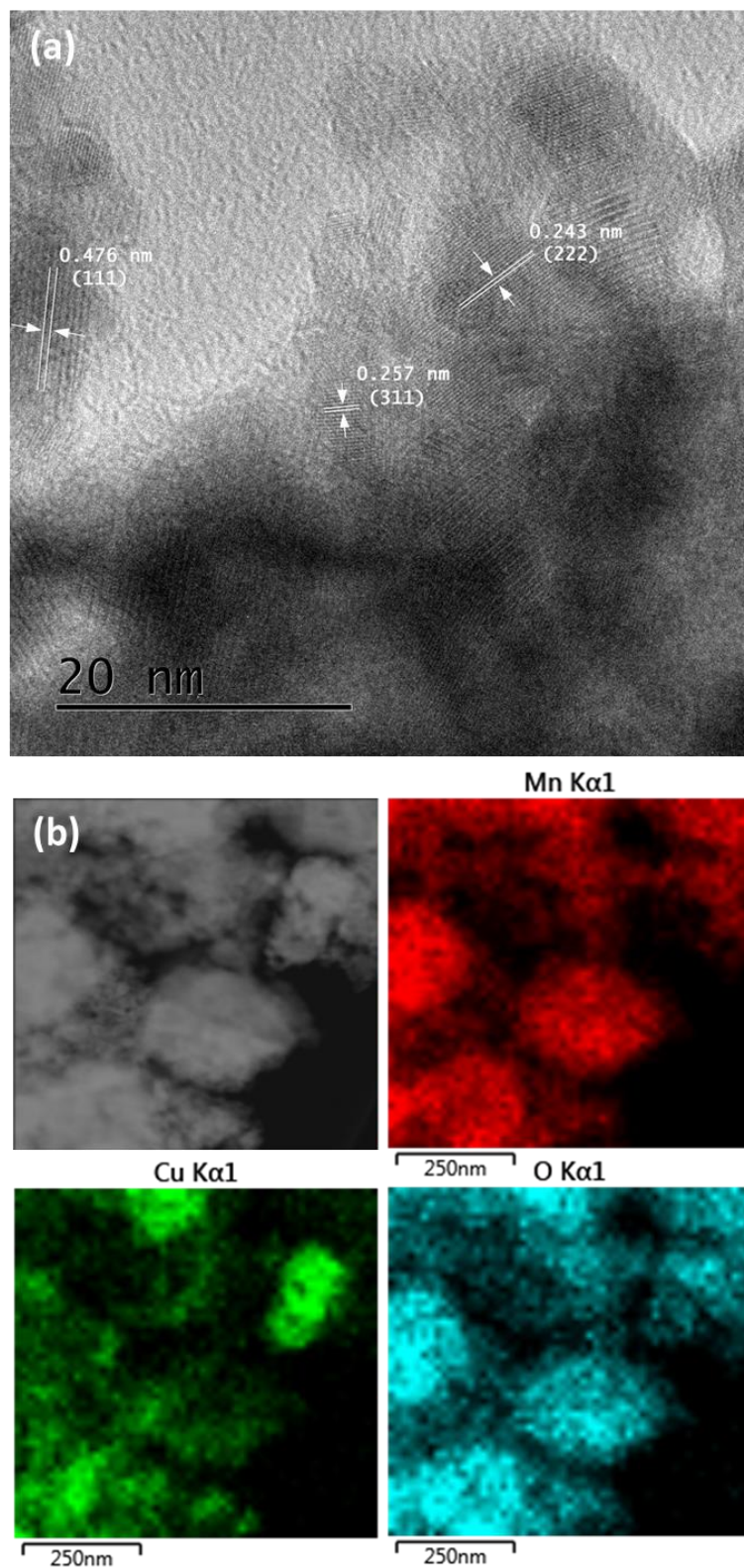
Figure 67: a) Representative TEM of catalyst ground for 72 h. b) Representative TEM - EDS of sample ground for 72 h.

In order to determine the extent of the homogeneity on a sub micrometre scale TEM studies of the material ground for 72 h were undertaken. Figure 67a clearly shows well defined lattice fringes resulting from the (311), (222) and (111) lattice planes of the $CuMn_2O_4$ spinel phase, no fringes associated with any other phase were observed. However, EDX mapping presented in Figure 67b shows clearly that there are areas of high Cu and Mn content with the mixed phase residing between these grains. It is our hypothesis that the friction between these grains could be involved in providing energy for copper to migrate into the manganese lattice during grinding.

4.2.9   CO oxidation testing
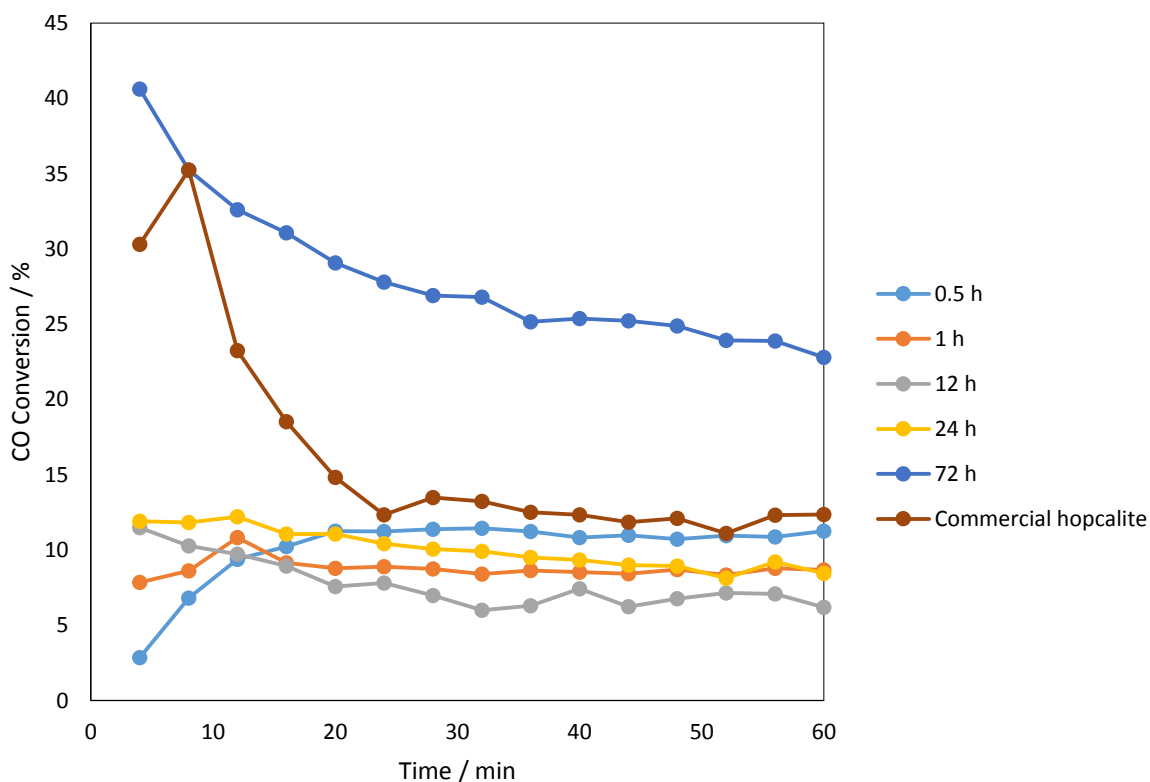
Figure 68: CO oxidation activity of the catalysts prepared from carbonate precursors. 5000 ppm CO / synthetic air, 21 mL min^{-1}, 25°C.

All the catalysts were tested for CO oxidation at room temperature (25 °C) as detailed in chapter 3. The results are shown in Figure 68 and summarised in Table 23. Even after a very short grinding period of 0.5 h 10% of the CO was oxidised to form CO_2. This level of activity

was consistent for catalysts ground for up to 24 h. When individual oxides were tested there was no measurable activity at room temperature, hence the mixture of oxides and carbonates probably contain isolated $CuMn_2O_4$ domains resulting in low observed levels of activity. After 72 h of grinding the activity is significantly increased with an initial rate of 40 % conversion rapidly stabilising at ca 25% after 1 h of testing. When taken with the previous characterisation data, this reinforces previous suggestions that the $CuMn_2O_4$ phase is required to form active materials rather than suggestions that a mixture of the individual oxides is preferable due to the prevalence of a spill over mechanism[19] as the catalysts composing of individual oxides perform poorly when compared with materials predominantly containing the mixed phase.

Table 23: Summary of CO oxidation catalytic behaviour of catalysts prepared from carbonate precursours.

Catalyst	Steady state activity / %	Calcined surface area / m^2g^{-1}	Surface area normalised rates at steady state / $mol\ s^{-1}m^{-2}$
0.5 h	11	65	1.76×10^{-7}
1 h	6	45	2.52×10^{-7}
12 h	12	50	1.26×10^{-7}
24 h	8	21	4.09×10^{-7}
72 h	23	78	2.97×10^{-7}
Commercial catalyst	12	-	-
CuO	0	-	-
Mn_2O_3	0	-	-

A commercial Hopcalite catalyst was also tested under identical conditions to benchmark the activity of the mechanochemically prepared material. The catalyst ground for 72 h was found to be roughly twice as active as the commercially available material. The initial activity of the commercial catalyst is similar to that of the 72h ground material, however activity rapidly decreases to become more comparable with the other materials tested.

In terms of surface area normalised rates (Figure 69) the catalysts up to 24 h all seem to have similar rates, however the drop in surface area after 24h results in it having the highest normalised rate. It is not possible to draw definitive conclusions from this as the catalysts are made up of multiple phases, some of which are active and some are not, all with differing surface areas.
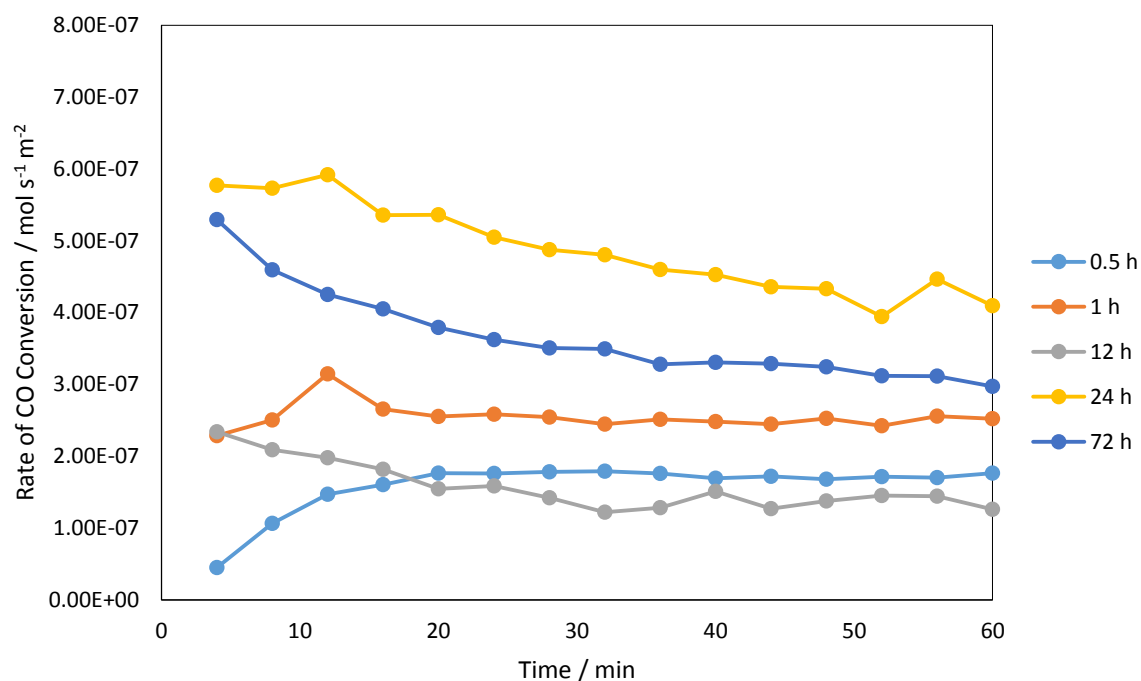
Figure 69: Surface area normalised rate of CO oxidation for catalyst prepared from carbonate precursors by a mechanochemical route. 5000 ppm CO / synthetic air, 21 mL min^{-1}, 25°C.

4.5 Conclusions

$CuMn_2O_4$ catalysts have been produced by mechanochemical methods from oxide, acetate and carbonate precursors. In the case of oxides and carbonates it was found that prolonged grinding led to larger degrees of mixed phase formation. In both cases this was due to the increased migration of copper ions into the lattice of the manganese phase caused by the prolonged energy input from the grinding process. The opposite trend was observed for the materials formed from acetate precursors. There was no evidence of copper migration during grinding from X-ray diffraction measurements or the thermal gravimetric analysis.

Samples ground for short periods formed the mixed $CuMn_2O_4$ phase, as reported by Kondrat et al. However samples ground for prolonged periods formed phase separated materials consisting of Cu_2O and Mn_3O_4 due to the effects of auto reduction possibly caused by the evolution of CO during the calcination process. Why this affected samples ground for prolonged periods rather than samples ground for shorter periods is unclear however.

When tested for CO all samples showed some activity, however the sample produced from grinding of carbonates for 72 h was clearly the most active. The high activity of this material was attributed to full formation of the high surface area, disordered, $CuMn_2O_4$ phase whereas the other materials did not form this phase with the same properties.

This work demonstrates that by grinding copper and manganese carbonates together an environmentally sound, simple method for the production of copper manganese oxide is possible, one that produces no unwanted waste streams. This is in contrast to the co-precipitation method that produces large volumes of nitrate waste and can be difficult to execute reproducibly . When ground for sufficient time this material exhibits appreciable CO oxidation activity with activity in excess of that found in commercial catalysts. The increased reducibility of the catalysts as the precursor is ground for longer is related to the increasing activity of the materials. As the materials become more reducible the Mars van Krevelan (MvK) mechanism of oxidation is promoted due to the mobility of lattice oxygen. Morgan et al suggest that there is a mixture of MvK and Langmuir oxidation taking place on the surface of hopcalite and that promoting the MvK mechanism can lead to increased activity [20]. This work is in agreement with this.

Further work should focus on exploring the effects of prolonging the grinding process further. Further mixing of the copper and manganese phases could lead to further increases in activity. Another subject of interest is the effect of the overall grinding energy on the activity of the sample, these materials were all ground at 400 rpm, however an increase in

rotational velocity and the consequent increase in energy could lead to further increases in atomic migration, a material with more defects and shorter grinding times. On the other hand lower rotational velocity could lead to a final material that may take more time to form but is less crystalline in nature. Also worth investigating is the effect of the oxidation state of the initial materials as Jones et al discuss in their review on mechanochemical preparation techniques, using a more reduced precursor can facilitate its mixing with the second phase [21]. Finally studies should be made into isotopic labelling studies to shed further light on the contribution of MvK and Langmuir mechanisms to these materials activity.

4.6 References

[1]   A.A. Mirzaei, H.R. Shaterian, R.W. Joyner, M. Stockenhuber, S.H. Taylor, G.J. Hutchings, Catalysis Communications 4 (2003) 17-20.
[2]   G.J. Hutchings, A.A. Mirzaei, R.W. Joyner, M.R.H. Siddiqui, S.H. Taylor, Catal. Lett. 42 (1996) 21-24.
[3]   G.J. Hutchings, A.A. Mirzaei, R.W. Joyner, M.R.H. Siddiqui, S.H. Taylor, Applied Catalysis A: General 166 (1998) 143-152.
[4]   A.A. Mirzaei, H.R. Shaterian, M. Habibi, G.J. Hutchings, S.H. Taylor, Applied Catalysis A: General 253 (2003) 499-508.
[5]   P. Baláž, A. Aláčová, M. Achimovičová, J. Ficeriová, E. Godočíková, Hydrometallurgy 77 (2005) 9-17.
[6]   K. Ralphs, C. Hardacre, S.L. James, Chemical Society Reviews (2013).
[7]   Q. Zhang, F. Saito, Journal of Alloys and Compounds 297 (2000) 99-103.
[8]   S.A. Kondrat, T.E. Davies, Z. Zu, P. Boldrin, J.K. Bartley, A.F. Carley, S.H. Taylor, M.J. Rosseinsky, G.J. Hutchings, Journal of Catalysis 281 (2011) 279-289.
[9]   T.J. Clarke, T.E. Davies, S.A. Kondrat, S.H. Taylor, Applied Catalysis B: Environmental 165 (2015) 222-231.
[10]   A.F. Rogers, The Journal of Geology 25 (1917) 515-541.
[11]   C. Jones, K.J. Cole, S.H. Taylor, M.J. Crudace, G.J. Hutchings, Journal of Molecular Catalysis A: Chemical 305 (2009) 121-124.
[12]   T.-J. Huang, D.-H. Tsai, Catalysis Letters 87 (2003) 173-178.
[13]   M.I. Zaki, M.A. Hasan, L. Pasupulety, K. Kumari, Thermochimica Acta 311 (1998) 97-103.
[14]   E.C. Njagi, C.-H. Chen, H. Genuino, H. Galindo, H. Huang, S.L. Suib, Applied Catalysis B: Environmental 99 (2010) 103-110.
[15]   M. Afzal, P.K. Butt, H. Ahmad, Journal of Thermal Analysis 37 (1991) 1015-1023.
[16]   P. Porta, G. Moretti, M.L. Jacono, M. Musicanti, A. Nardella, Journal of Materials Chemistry 1 (1991) 129-135.
[17]   L. Vegard, Z. Physik 5 (1921) 17-26.
[18]   G. Fierro, M. Lojacono, M. Inversi, P. Porta, R. Lavecchia, F. Cioci, Journal of Catalysis 148 (1994) 709-721.
[19]   F.C. Buciuman, F. Patcas, T. Hahn, Chemical Engineering and Processing: Process Intensification 38 (1999) 563-569.
[20]   K. Morgan, K.J. Cole, A. Goguet, C. Hardacre, G.J. Hutchings, N. Maguire, S.O. Shekhtman, S.H. Taylor, Journal of Catalysis 276 (2010) 38-48.

[21]   S.L. James, C.J. Adams, C. Bolm, D. Braga, P. Collier, T. Friscic, F. Grepioni, K.D.M. Harris, G. Hyett, W. Jones, A. Krebs, J. Mack, L. Maini, A.G. Orpen, I.P. Parkin, W.C. Shearouse, J.W. Steed, D.C. Waddell, Chemical Society Reviews 41 (2012) 413-447.

Chapter 5

Investigating the synthesis of CuMn$_2$O$_4$ catalysts by co-precipitation from non-aqueous solvents.

5.1 Introduction

As discussed in chapter 1, a number of factors have been identified as having a role in the production of active hopcalite catalysts using the co-precipitation method [1-6]. One of the factors that has not been investigated is the role of the solvent in the precipitation process. To investigate this, a number of non-aqueous solvents and mixtures of non-aqueous solvents with water were investigated as precipitation media for copper manganese oxide catalysts. The effect of changing the solvent environment, specifically the interaction between the containing solvent nitrates and the precipitating reagent, on the activity of the materials was explored.

Linear alcohols ranging from ethanol up to n-pentanol were used in place of water to prepare the nitrate solution used to co-precipitate the catalysts. As alcohols possess an OH group at the terminus of their hydrocarbon chain they can dissolve ionic solids such as nitrates. This allowed the substitution of water for other solvents whilst still using nitrates as the precursors for the preparation of coper manganese oxide catalysts. As the carbon chain length increased the solubility of the alcohols in water decreased [7]. The effect of this was to change the rate of mixing between the nitrate solution and the sodium carbonate precipitation agent. The effect of this changing rate on the precipitated materials was investigated.

Table 24: Precipitation conditions of the Hopcalite catalysts studied

Solvent	Co solvent	Precipitation Temp / °C
Water	N/A	80
Ethanol	N/A	60
Propanol	N/A	80
n- Butanol	10% H_2O	80
n- Pentanol	10% H_2O	80

When aged at 80 °C the sample precipitated from ethanol lost too much solvent to evaporation to give a comparable result and as such this sample was precipitated at 60 °C to prevent this from occuring. The two longest alcohols investigated, n-butanol and n-pentanol required the addition of 10% water in order to allow the nitrate salts used to dissolve and as such the results are presented separately to the samples prepared from pure alcohol solutions.

5.2 Catalysts precipitated from pure solvents

5.2.1 XRD of catalyst precursors precipitated from pure solvents

The XRD of the catalyst precursors precipitated using the various pure solvents is shown in Figure 70: XRD of the hopcalite catalyst precursors precipitated from various solvent systems ■ = MnCO3 (ICDD: 01-071-3820)▲ = CuO. The material precipitated in the control experiment from the traditional H_2O solvent displays the typical XRD pattern for copper manganese oxide precursors. The principle reflection at a 2θ of 31.6° corresponds to the (104) reflection of $MnCO_3$ (ICDD 00-044-1472), this reflection appears shifted relative as it is expected that the reflection should be observed at 31.3° 2θ. As discussed in chapter 4 work by Porta et al attributes this shift to incorporation of Cu^{2+} ions into the manganese carbonate lattice causes a contraction in the unit cell volume and results in a shift of reflections to higher 2θ than would be observed in the pure $MnCO_3$ phase[8]. Without the presence of Cu^{2+} the peak position of the (104) reflection is 31.3° 2θ ,suggesting a shift of 0.3°.
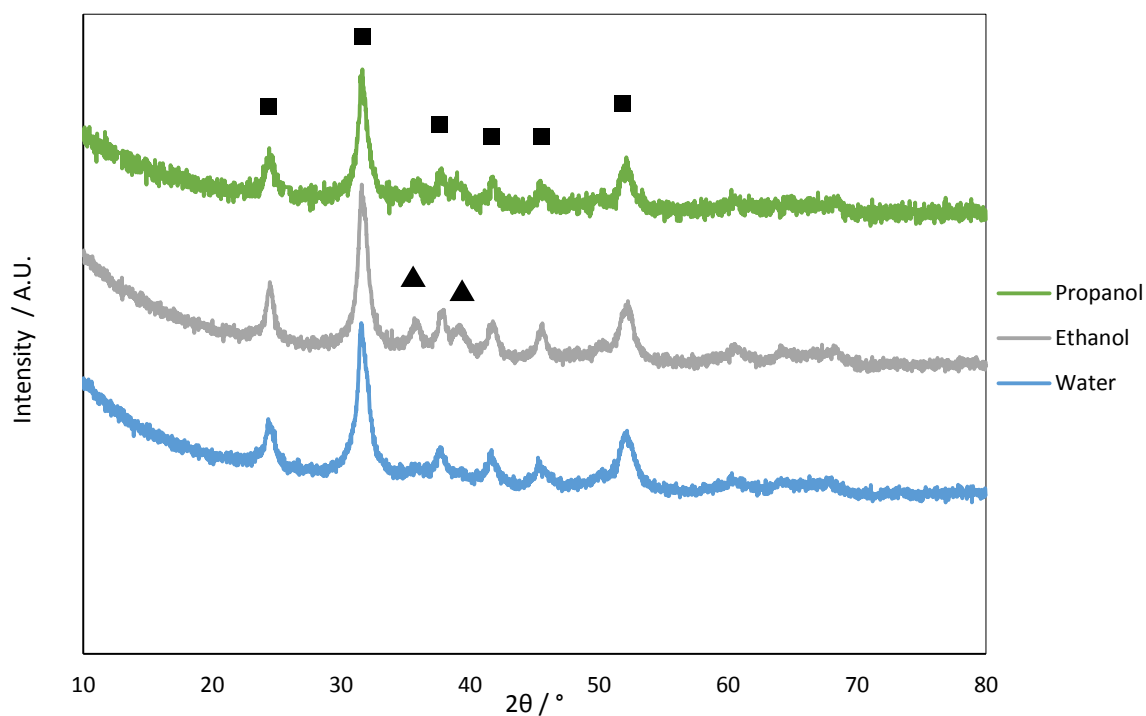
Figure 70: XRD of the hopcalite catalyst precursors precipitated from various solvent systems ■ = MnCO₃ (ICDD: 01-071-3820)▲ = CuO (01-089-*5895*)

As previously observed no copper containing phase is observed in the XRD (Chapter 3, Chapter 4). This suggests that there may be an undetected amorphous or nanocrystaline copper phase present within the material. The pattern of the material precipitated from the ethanol solution also clearly shows the presence of the $MnCO_3$ phase with a 2θ of 31.6° for the (104) plane. This suggests a similar level of Cu^{2+} incorporation into the $MnCO_3$, as observed in the control H_2O system. However a second phase is also observed with reflections at 35.7° and 39.5. These peaks correspond to the ($\bar{1}11$) and (111) planes of copper (II) oxide (ICDD 01-089-5895). This has previously been observed in copper zinc systems by Soler-Illia et al who attributed its formation to the re-dissolution and subsequent precipitation of an amorphous copper hydroxycarbonate phase[9].

Table 25: Crystalite size values for copper manganese oxide materials precipitated from pure solvents

Solvent	Crystallite size / Å	
	Precursor	Calcined
Water	163	44
Ethanol	105	44
Propanol	115	72

The precursor calcined from propanol again has a reflection at 31.6° corresponding to the (104) plane of the copper incorporated $MnCO_3$ and the copper oxide reflections observed in the sample precipitated from ethanol are again present. This suggests that changing the properties of the solvent is having an effect on the structural outcome of the precursor.

5.2.2   TGA of the catalyst precursours precipitated from pure solvents

As seen in Figure 71, TGA of the samples shows two distinct behaviours. The sample precipitated from H_2O shows one well defined mass loss at around 400 °C as observed previously (Section 3.2.1). This corresponds to the thermal decomposition of the mixed copper manganese carbonate phase to form the mixed metal oxide (see Figure 73). There is no observed mass loss observed that would correspond with a copper containing phase, such as malachite, which shows a characteristic mass loss at 325 °C [10]. It is possible however that some mass loss is obscured by the gradual evolution of physisorbed and chemisorbed water observed at low temperatures in the TGA profile.

Table 26: Physical properties of the materials precipitated from pure solvent systems

Sample	TGA	TPR	BET	EDX
	Mass loss percentage / %	H_2 consumption / mol g^{-1}	Calcined surface area / $m^2 g^{-1}$	Cu:Mn Ratio
Water	28	0.012	85	1:2
Ethanol	26	0.009	75	1:1.8
Propanol	26	0.004	3	1:1.4

The samples precipitated from ethanol and propanol display a significant shift in the decomposition temperature observed with additional decomposition steps. There is a broad

decomposition from around 300 °C to about 400 °C and a smaller one at around 500 °C. In their study on the effect of preparation conditions on copper manganese oxide catalysts, Mirzaei *et al* attributed broad reductions around this temperature to the decomposition of hydroxycarbonate materials, indeed malachite is known to decompose in this temperature range, and decomposition at higher temperatures to carbonates[6]. In this case the magnitude of the decomposition is so high any crystalline copper or manganese hydroxycarbonate species would be visible in the XRD, however as seen in Figure 1 they are not, suggesting that any phase is amorphous or nanocrystaline in character.
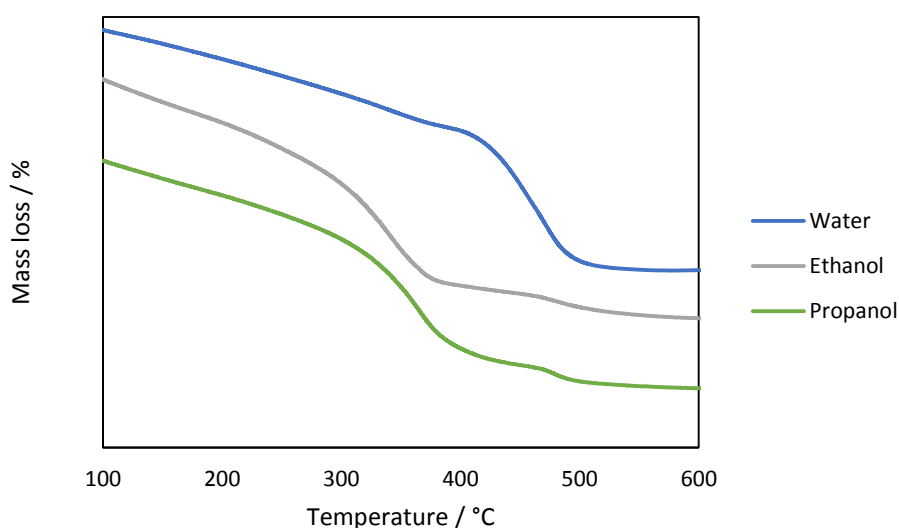
Figure 71: TGA of catalyst precursors precipitated from pure solvent systems, 5 °C min^{-1}, Air, 50 mL min^{-1}

As there is no observable change in the phases present as illustrated by the XRD pattern (Figure 70), a possible explanation is that the precursors precipitated from the alcohol solutions is composed of smaller particles that thermally decompose at a significantly lower temperature. due to their higher surface area to volume ratio, than the larger particles formed in the water precipitation.

5.2.3 SEM and EDX of the catalyst precursors precipitated from pure solvents

SEM micrographs of the precursor materials is limited to low magnification images in order to limit the effect of charging on the samples. As the samples are non-conducting and sample

coating was unavailable for these samples, higher magnifications lead to samples moving under the beam in such a manner that images could not be acquired. However even at the low magnification presented here it is possible to see some significant differences in the nature of the catalyst precursors precipitated from water and those precipitated from alcoholic media.

Figure 72a shows the precursor precipitated from water, the particles for the most part are in the region of 10 µm with little evidence of smaller particles.   In comparison the materials precipitated from ethanol and propanol (Figure 72b and c) respectively display a range of particle sizes, the large particles observed in the water precipitated material are still observed, however there is also a large range of smaller particles. Previous TEM microscopy studies have shown that copper manganese catalysts produced by coprecipitation consist of poorly defined needle like structures that agglomerate to form the larger structures seen in SEM[11].   One possibility to explain the changes in morphology is that these nanoscale structures are agglomerating to differing extents when precipitated from different solvents, however further TEM studies would be required to confirm this. This serves to explain the lower onset of thermal decomposition observed in the TGA for these samples (Figure 71), as smaller particles are likely to be more susceptible to thermal decomposition due to their higher surface area to volume ratio when compared with larger particles.
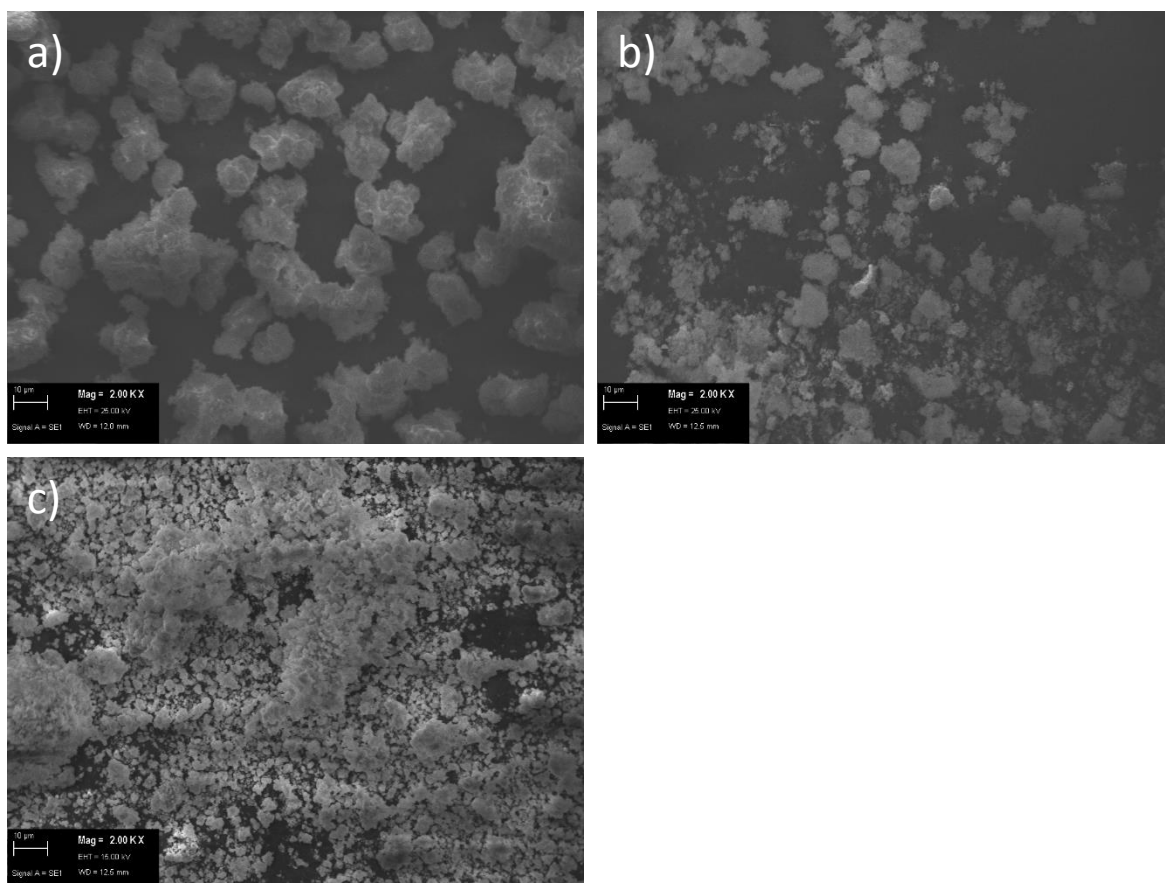
Figure 72: SEM Micrographs of co-precipitated catalyst precursors co-precipitated from pure solvents. a) Sample precipitated from water, b) Sample precipitated from ethanol, c) Sample precipitated from propanol. All images EHT 25kV 1000pa 2000x mag

5.2.4   XRD of the calcined catalysts precipitated from pure solvents

As detailed in chapter 2 the catalysts were all calcined in static air, to a temperature of 415 °C at a rate of 2 °C min^{-1} for 2 h. These calcination conditions have previously been shown to be optimal for preparation of copper manganese oxide catalysts prepared by the standard co-precipitation method[5]. Figure 73 shows the XRD patterns of the calcined catalysts precipitated from the pure solvents.

All three materials show evidence of the presence of a poorly crystaline $CuMn_2O_4$ phase. The broad peak observed at 36° corresponds to the (311) plane of $CuMn_2O_4$. A second broad reflection is observed around a 2θ of 40° and this corresponds to the (400) plane of $CuMn_2O_4$.

The samples precipitated from water and ethanol show no other reflections and the reflections, as described, are very broad.
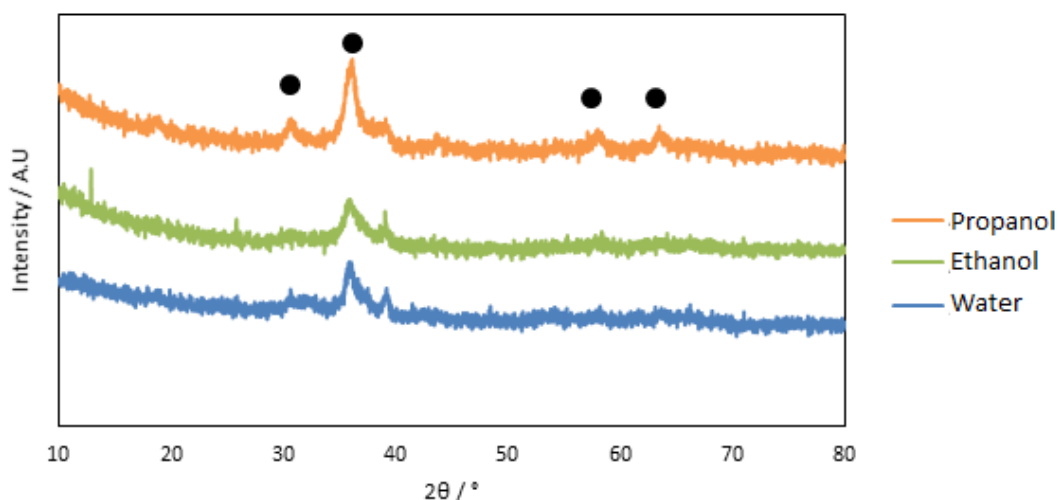

Figure 73: XRD of the calcined copper manganese oxide catalysts precipitated from single solvent systems   40kV 40 mA Cu Source ●= $CuMn_2O_4$ (ICDD: 01-075-0826)

This suggests a highly disordered nanocrystaline or partially amorphous copper manganese oxide phase. Calcination of the sample precipitated from the propanol solution result in the observation of more reflections than the other two samples. Specifically the main (311) reflection at 36.1° appears more distinct and other reflections being observable at 30.8°, 58.3° and 63.5° corresponding to the (220), (511) and (440) planes respectively.

This is in contrast to the precursor materials, where the reflections of the catalyst precipitated from propanol were slightly broader and less defined than the water and ethanol samples. A similar effect has been observed previously by Tang *et al.* in their study of supercritically prepared copper manganese oxides[12].   When their precursor was amorphous the calcined material was highly crystalline, conversely when they had a crystalline precursor it resulted in a less crystalline material upon calcination. This was attributed to the presence of crystalline carbonate materials in the precursor material decomposing slower upon calcination temperature, resulting in less crystaline materials.

Neither materials precipitated from ethanol or propanol show any observable evidence of a CuO phase present in the calcined materials as is seen in the precursors (Figure 70). This suggests that the CuO acted as a source of copper for spinel formation alongside the copper manganese carbonate phase during the calcination process.

5.2.5 TPR precipitated from pure solvents

The calcined materials were analysed by temperature programmed reduction (Figure 74) as described in Chapter 2. The catalyst precipitated from water displayed the reduction of disordered copper manganese oxide spinels [11]. The principle reduction event is centred at 245 °C. Multiple reduction events are clearly taking place with clear shoulders at 225 °C, 229 °C and 265°C. This is typical as there are multiple possible oxidation states for both the copper and manganese species within the spinel[13]. When the spinel is disordered, as is the case for this material, these species may exist in multiple structural environments. In addition, it is possible that there are trace amounts of the individual oxides present, complicating the pattern further.
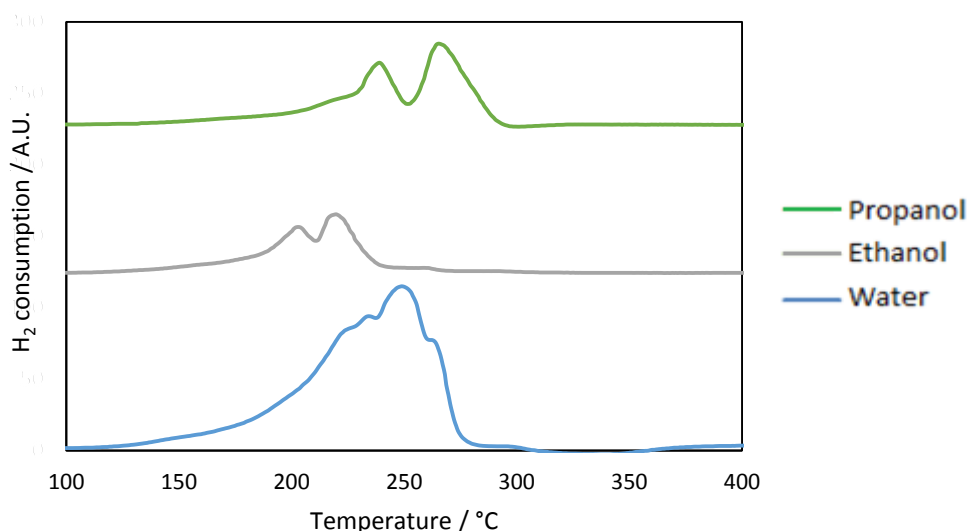

Figure 74: H_2 TPR of the calcined catalysts precipitated from pure solvents . 20mL min $^{-1}$ 10 % H_2/Ar, 5°C min^{-1}

The TPR profile for the material precipitated from ethanol shows two reduction events at 210 °C and 220°C. These could correspond to the reduction of the copper and manganese

species within the spinel. The reduction temperature is depressed compared to the sample precipitated from water.

The sample precipitated from propanol shows the same reduction trend as the sample precipitated from ethanol with a two stage reduction at 243 °C and 277 °C. This is significantly higher in temperature than the sample precipitated from ethanol. This shift to higher temperature is due to the increased crystallinity of this material in comparison with the sample precipitated from ethanol (Figure 73 and Figure 74).

TPR hydrogen consumption is presented in Table 26. It is clear that the total reducibility of the material is decreasing as the solvent is changed from water to ethanol to propanol. This is significant as previous work has shown that the Mars van Krevelan mechanism is a key contributor to the CO oxidation activity of hopcalite materials [14]. The reducibility of the catalysts is linked to their oxygen mobility hence lower reducibility could be an indicator of lower oxidation activity.

5.2.6   SEM and EDX of the calcined catalysts precipitated from pure solvents

Representative SEM micrographs of the calcined catalysts are shown in Figure 75. A micrograph of the sample precipitated from water, shows the typical globular morphology associated with copper manganese oxide catalysts on the microscale. Figure 75b shows the catalyst precipitated from ethanol, the typical globular morphology is observed again, however there is also a larger amount of smaller particles than observed in the water precipitated catalyst. Finally Figure 75c shows the sample precipitated from propanol. There is a total absence of particles with a radius of 1 µm or greater in this sample and the majority of the particles have radii of between 0.05 and 0.5 µm.   The change in particle size distribution is illustrated in Figure 76 with a clear trend towards a smaller particle size in the samples precipitated from ethanol and propanol. This could be caused by changes in viscosity of the solvent system with the formation of small aqueous domains where the

precipitation occurs during the mixing of the alcoholic nitrate mixture and the aqueous carbonate solution. Whilst both alcohols are miscible with water, ethanol is slightly more polar than propanol so mixing with the aqueous carbonate solution would occur more rapidly leading to a larger particle size distribution.
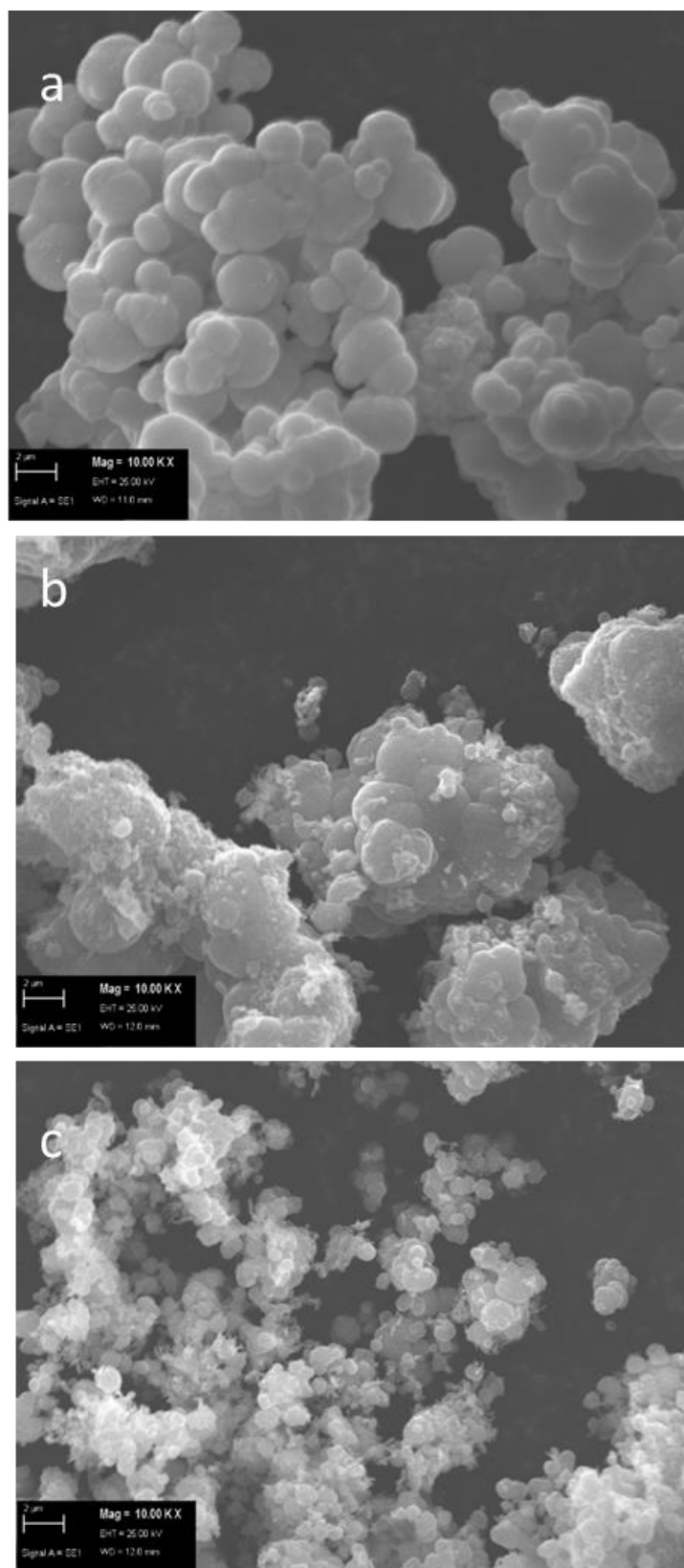
Figure 75: SEM micrographs of the calcined samples co-precipitated from pure solvents a) Sample precipitated from water, b) Sample precipitated from ethanol, c) Sample precipitated from propanol. All images EHT 25kV 1000pa 10000x mag.

EDX analysis was performed in conjunction with the imaging. The Cu:Mn ratio that was determined from this analysis is displayed in Table 26. The catalyst precipitated from water had the expected 1:2 Cu:Mn ratio. This was not the case for the other two catalysts with the ratio changing to 1:1.8 for the catalyst precipitated from ethanol and 1:4 for the material precipitated from propanol. This demonstrates a clear trend of increasing concentrations of copper as the solvent is changed from water to ethanol to propanol. This could be an effect of the changing solubility of manganese carbonate as the solvent is changed. Another possibility is that there is a change in the local pH as the samples are mixed. The nitrate solutions in propanol and ethanol are not going to mix with the aqueous carbonate solution as rapidly as the aqueous nitrate solution. This will lead to short term imbalances in pH which could explain the change in Cu:Mn ratio along with the presence of CuO in the catalyst precursors (Figure 70: XRD of the hopcalite catalyst precursors precipitated from various solvent systems ■ = $MnCO_3$ (ICDD: 01-071-3820)▲ = CuO) Other co-precipitation systems have shown that pH is a crucial factor in the precipitation process with changes in pH leading to different phases being precipitated[15]. It should be noted however that this is not reflected in the XRD with no shift in the position of the $CuMn_2O_4$ reflections (Figure 74). However the disordered nature of the catalysts and the resulting broad reflections could mask any shift. The change in Cu : Mn ratio is significant as the activity of hopcalite has been linked to the Cu^{2+}+ Mn^{3+} ⇌ Cu^{1+}+ Mn^{4+} redox couple (Section 1.2.3). Whereby the Cu^{2+} and Mn^{4+} oxidation states interact with Cu^{1+} and Mn^{3+} species within the spinel[16, 17]. Any change in the Cu : Mn ratio is going to effect this system and by extension the activity of the catalyst.
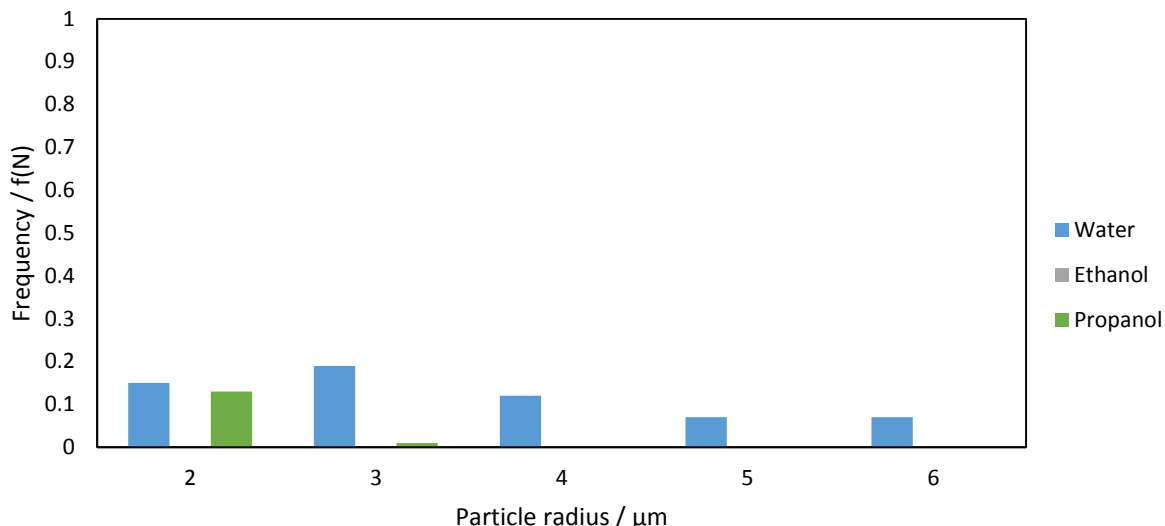
Figure 76: Particle size distributions as determined by SEM for calcined catalysts precipitated from pure solvents.

5.2.7 XPS of the calcined catalysts precipitated from pure solvents

Whilst the bulk ratios determined by EDX gives insight into the changing precipitation conditions that the materials are exposed to as the solvent is changed, it does not give information about the composition of the catalytically active portion of the catalyst: the surface. In order to investigate the composition of the surface XPS analysis was undertaken and the results are displayed in Table 27.

The sample precipitated from water exhibits a slightly manganese rich surface compared to the 1:2 Cu:Mn ratio expected from a spinel material[2]. This suggests that there is some stratification of the material with more copper rich material in a layer near the surface.

Table 27: XPS of the catalysts precipitated from pure solvents.

Sample	Cu: Mn ratio	Na: Mn Ratio
Water	1 : 2.4	1:24
Ethanol	1 : 1.93	1:22
Propanol	1 : 3.9	1:11

When precipitated from ethanol, there is a decrease in the Cu:Mn ratio, so it is closer to the 1:2 ratio that was expected. Whereas the precipitation from propanol results in a 1:3.9 ratio with an extremely manganese rich surface. This is especially manganese rich when the 1:1.4 ratio of the bulk material is considered. Again there may be exposed surfaces giving rise to these changes in Cu:Mn ratio or concentration of manganese rich material near the surface. The highly manganese rich nature of the surface suggests the presence of a manganese phase on the surface of this material.

XPS also showed changes in the levels of Na^+ on the surface of the materials. The catalyst precipitated from water exhibited a Na:Mn ratio of 1:24 on the surface. This is similar in the sample precipitated from ethanol, and doubled to 1:11 in the propanol precipitated sample. As each catalyst was washed in the same manner this suggests that the residual Na^+ from the precipitation of the catalyst from propanol is bound more strongly to this material than to the material precipitated from water or ethanol. Alternatively the less polar nature of propanol and the resulting slower mixing with water could simply make removing Na^+ by washing with hot water more difficult. As Na^+ has been shown to be a key catalyst poison this increase in surface concentration is significant[1].

5.2.8 Surface area analysis precipitated from pure solvents

Surface area of the catalysts is displayed in Table 3. The catalyst precipitated from water exhibits the highest surface area of the three, with an area of 85 $m^2 g^{-1}$. The surface area decreases slightly to 75$m^2 g^{-1}$ when ethanol is used as the solvent. When propanol is used the surface area decreases significantly to 3 $m^2 g^{-1}$. This drop in surface area is possibly the result of less efficient mixing when the solvents become less polar leading to a more basic pH environment when the precipitation takes place. Another possibility is that there is residual propanol adsorbed to the surface of the catalyst that remains after drying and upon calcination combusts, leaving a carbonaceous layer supressing the surface area.

5.2.9   CO Oxidation precipitated from pure solvents

The three catalysts were tested for CO oxidation as described in chapter 2. The catalyst precipitated from water was the most active with a steady state activity of ca 50 % after 20 minutes. The ethanol precipitated material showed slightly lower activity with steady state activity of around 40%. The propanol precipitated sample exhibited lower activity with a steady state activity of 15 %.
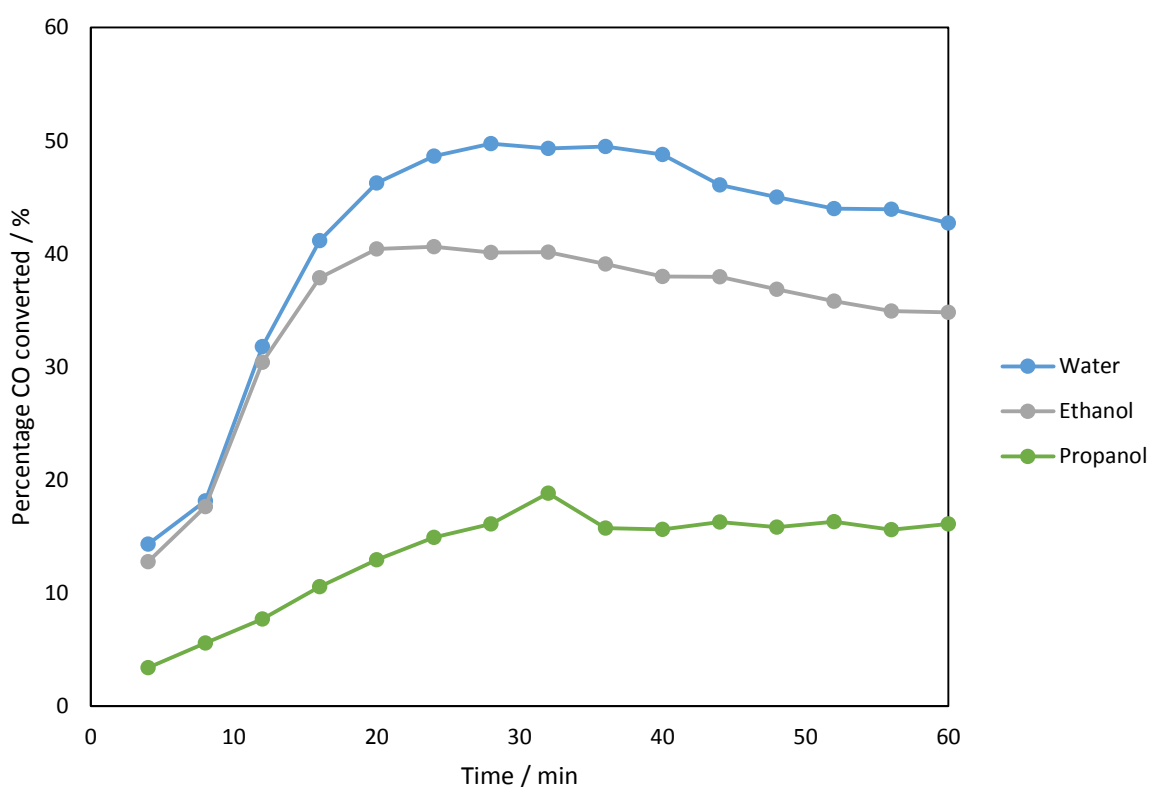
Figure 77: CO oxidation activity of the catalysts precipitated from pure solvents. 5000 ppm CO / synthetic air, 21 mL min^{-1}, 25°C.

The slightly lower activity for the sample precipitated from ethanol can be attributed to the slightly lower surface area of the sample. Indeed when the surface area normalised rate of CO oxidation is calculated the ethanol precipitated sample has the same activity as the aqueous sample. The catalyst precipitated from propanol demonstrates the highest surface area normalised rate by far, due mainly to the very low surface area exhibited by this

material. The material must contain isolated active domains in association with inactive low surface area materials.
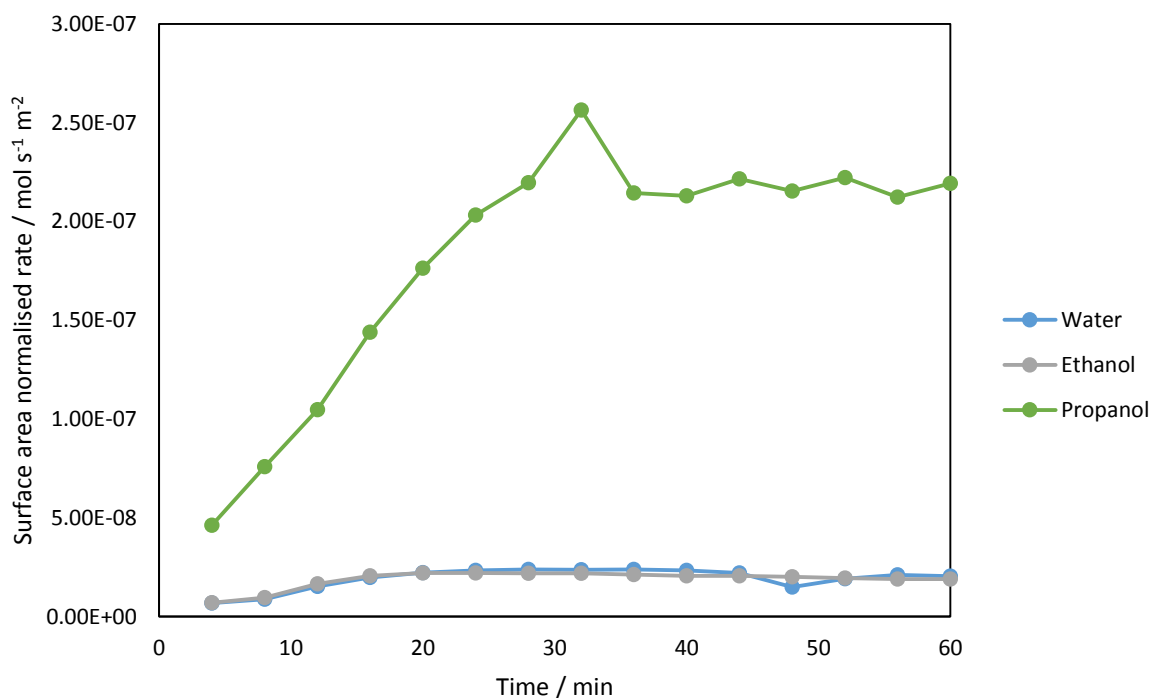

Figure 78: Surface area normalised CO oxidation rate for the catalysts precipitated from pure solvents.

5.3 Catalysts precipitated from water alcohol mixtures

5.3.1   XRD of the catalyst precursors precipitated from water alcohol mixtures

The XRD patterns for the catalyst precursors precipitated from water alcohol mixtures are

shown in Figure 79 alongside the sample precipitated from water as a comparison. Both

samples show evidence of both a manganese carbonate phase, as seen in the sample

precipitated from water. Very broad reflections at 37.2° and 40.1° corresponding to a copper

oxide phase ($\bar{1}11$) and (111) planes) were seen, as in the previous materials precipitated from

alcoholic media. The (311) plane of the manganese carbonate phase shows evidence of

shifting to higher 2θ angles in the material precipitated from 10% water in n-butanol with a

2θ of 31.6°, the same as the sample precipitated from water. As before this is attributed to

incorporation of Cu^{2+} into the lattice of the $MnCO_3$. The material precipitated from 10%

water in n-pentanol exhibits a smaller shift of 31.5°, this suggests a smaller amount of copper

incorporation in this material compared with the other two materials.

Table 28: Crystallite size values for copper manganese materials precipitated from water alcohol mixtures

Solvent	Crystallite size / Å		TGA Mass loss / %
	Precursor	Calcined	
10% Water n-butanol	95	81	27
10% Water n-pentanol	218	52	27
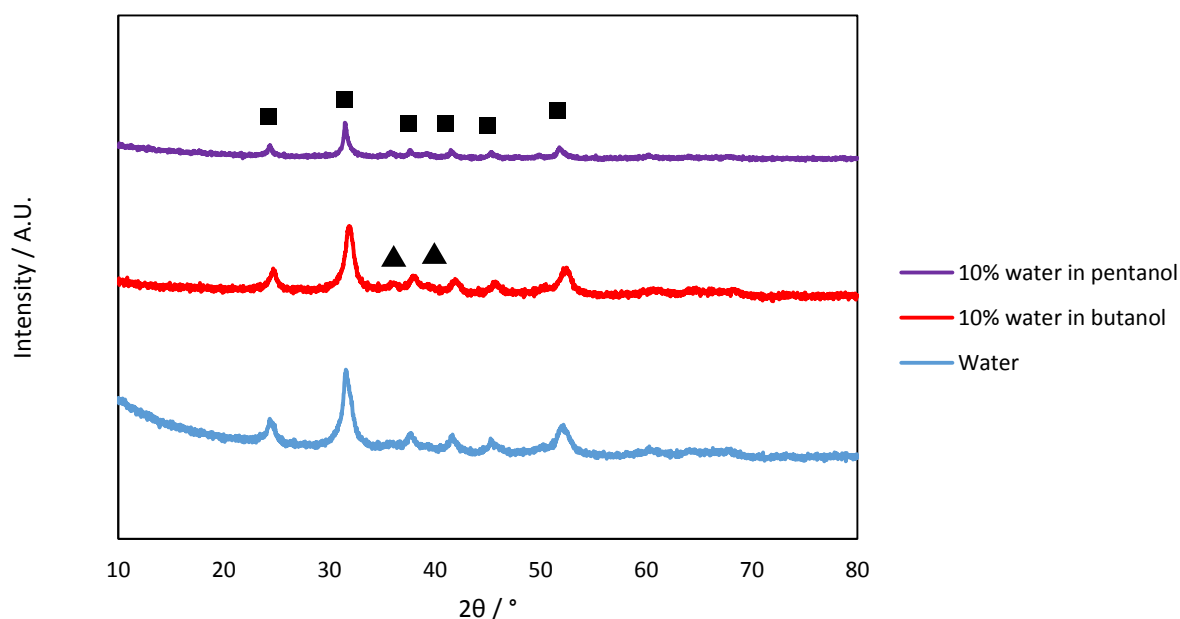
Figure 79: XRD patterns of the catalyst precursors precipitated from alcohol water mixtures. 40 kV, 40 mA, Cu source. ■ = $MnCO_3$ (ICDD: 01-071-3820) ▲ = CuO (01-089-5895)

The material precipitated from 10% water in butanol was composed of smaller crystallites

than when precipitated from water. The crystallite size of the precursor (Table 5)

precipitated from butanol was 95 Å compared with 163 Å for the sample precipitated from

water. This is in a similar range to the catalysts precipitated from ethanol and propanol.

However the pentanol precipitated material consisted of larger crystallites of 218 Å in size.

The intensity of the propanol precipitated XRD is also much lower than the other materials,

this suggests that there is more amorphous content in this sample with fewer crystalline

planes for x-ray diffraction to take place.

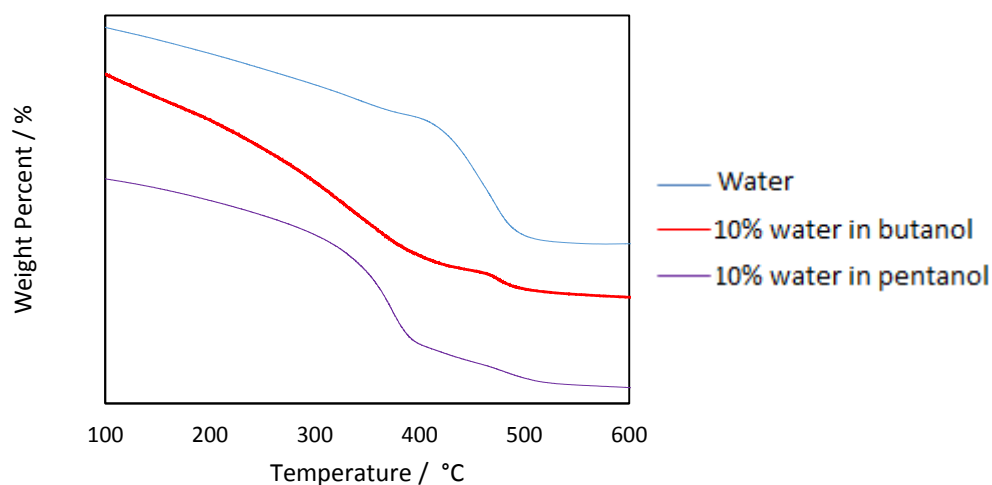## 5.3.2   TGA of the catalyst precursors precipitated from water alcohol mixtures

Figure 80: TGA of catalyst precursors precipitated from water alcohol mixtures. 5 °C min^{-1}, Air, 50 mL min^{-1}

Thermal gravimetric analysis of the precursors precipitated from water alcohol mixtures is

shown in Figure 80: TGA of catalyst precursors precipitated from water alcohol mixtures.

along with the TGA of the sample precipitated from water as a comparison. The sample

precipitated from 10% water in butanol exhibits a long gradual weight loss up to around 400

°C before a smaller mass loss at around 500 °C. There is an overall mass loss of 27%. The

initial mass loss is due to the loss of chemisorbed water within the sample along with the

thermal decomposition of small manganese carbonate particles as seen in the previous

alcohol work. The smaller mass loss around 500 °C corresponds to the end of the mass loss

seen in the water sample and can be attributed to the thermal decomposition of larger

carbonate particles. The sample precipitated from the propanol/water mixture also loses

164

27% of its mass over the course of the analysis. It exhibits a gradual initial mass loss due to physisorbed water also, but this is followed by a far sharper mass loss starting at 300 °C followed by a second broad mass loss at 400 °C. This possibly suggests the loss of two distinct phases.

5.3.3 XRD calcined catalysts precipitated from water alcohol mixtures

After calcination the only phase observed in the XRD of both the butanol precipitated and pentanol precipitated material is $CuMn_2O_4$, however the two patterns seen are both very different. The sample precipitate from 10% water in butanol exhibits reflections that are well defined compared with both the sample precipitated from water. The (311) reflection at 36.1° 2θ is clearly defined and less intense reflections are observed at 30.9°, 58.3° and 64.2° corresponding to the (220), (511) and (440) planes respectively. Whilst less broad than the sample precipitated from water, the broadness of the reflections in this sample suggest that there is a significant nanocrystaline or amorphous component present. The crystallite size of the catalyst precipitated from butanol was 82 Å (Table 5), this was larger than the 44 Å crystallites of sample precipitated from water. There was a slight shift to higher 2θ angles in this material compared with the reference pattern, this could be the result of a change in the Cu:Mn ratio influencing the unit cell dimensions, or simply be due to the broad nature of these reflections compared with the crystalline reference pattern. Another possibility is that there is some error in the measurement associated with sample height displacement. This is less likely than the other two possibilities as the sample holders, along with the procedure for filling them, are designed to minimise the possibility of this.
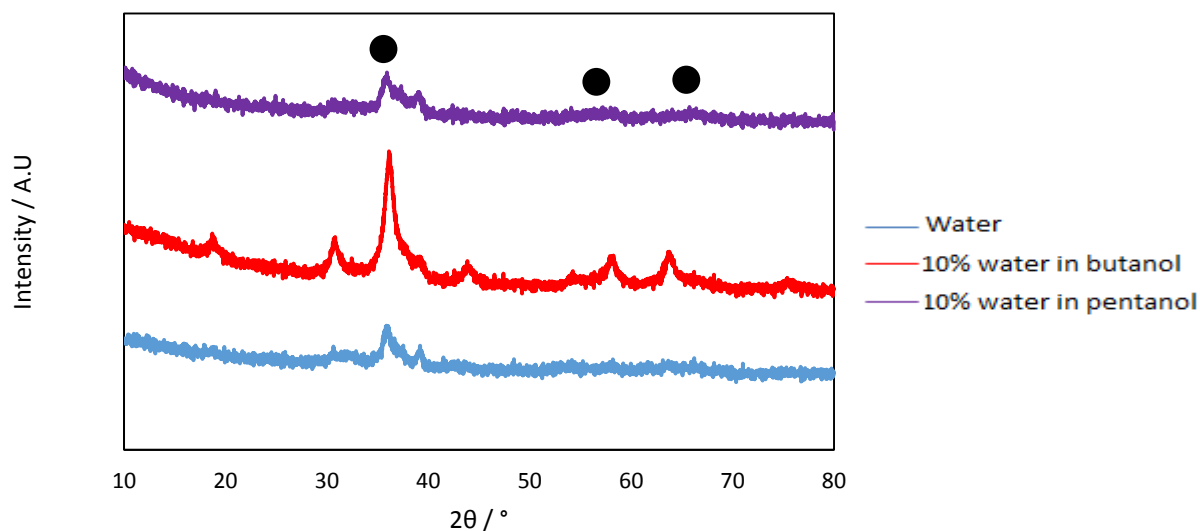
Figure 81: XRD of calcined catalysts precipitated from water alcohol mixtures. . 40 kV, 40 mA, Cu source. ● = $CuMn_2O_4$ ICDD (01-075-0826)

The pentanol precipitated sample on the other hand exhibited a very broad reflection at around 35.9° ((311) plane) and a smaller reflection at 39.5° ((222) plane) with no other observed reflections. This, similarly to the sample precipitated from water suggests a material with a large nanocrystaline or amorphous component. The crystallite size of this material was 52 Å, this re-enforces the previous observation of large crystallite size precursors resulting in small crystallite size catalysts.

5.3.4 TPR of calcined samples precipitated from water alcohol mixtures.

The temperature programmed reduction data for the calcined samples precipitated from water alcohol mixtures is shown in Figure 82. The sample precipitated from the butanol solution exhibits a similar trend of a number overlapping peaks as the traditional aqueous precipitated sample.
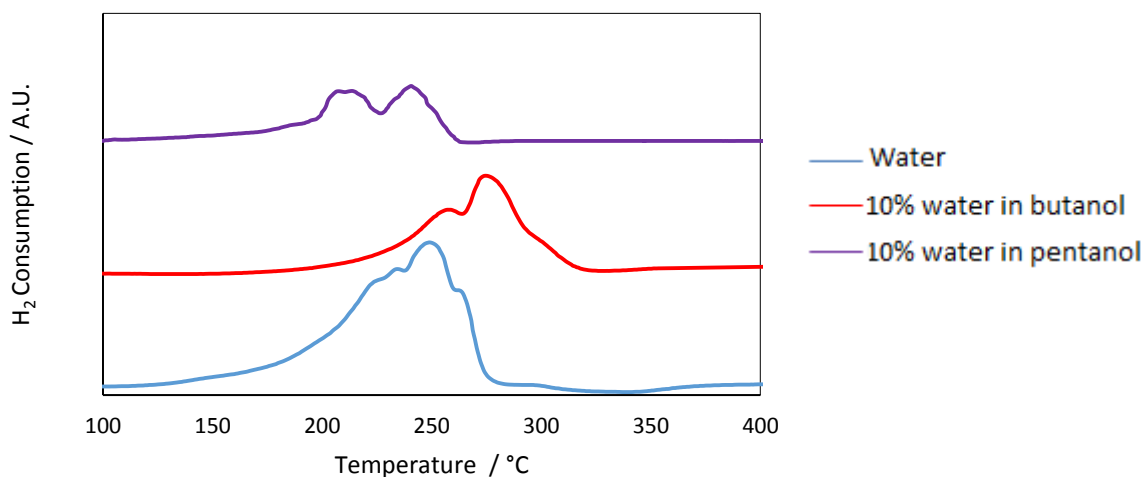
Figure 82: H_2 TPR of calcined catalysts precipitated from water alcohol mixtures

This is caused, as mentioned previously, by a number of species reducing at similar temperatures. In this case however the material is less susceptible to reduction with a shift to higher temperature for the reduction to take place. The sample precipitated from 10% water in pentanol however shows two distinct reduction events centred at 220 °C and 244 °C. This suggests two distinct species present possibly the reduction of copper (II) and manganese (III) oxide individually.

The total hydrogen consumption of the samples is shown in Table 30. There is a clear decrease in total H_2 consumption when the pentanol precipitated material is compared with the butanol precipitated. This is significant as it may give an indication as to the relative activity of each material, due to the influence of the Mars van Krevelan mechanism in CO oxidation using copper manganese oxide catalysts [14].

5.3.5 Scanning electron microscopy calcined catalysts precipitated from water alcohol mixtures

Scanning electron microscopy (Figure 83) clearly illustrates the differing morphology of the sample precipitated from the butanol solution compared with the sample precipitated from the pentanol precipitated sample.
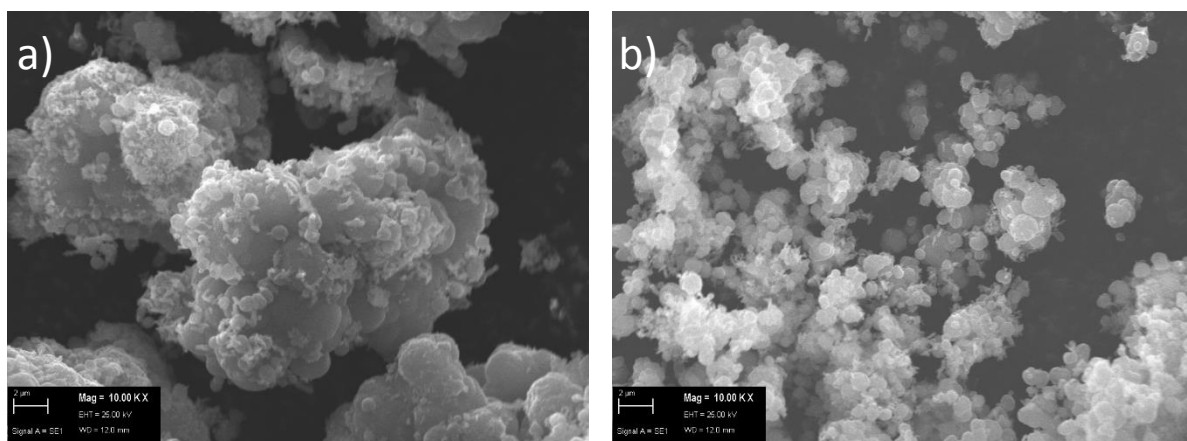
Figure 83: SEM micrographs of calcined catalysts co-precipitated from water alcohol mixtures a) Sample precipitated from 10% water in butanol, b) Sample precipitated from 10% water in pentanol. All images EHT 25kV 1000pa 2000x mag

In Figure 83a the large particle size range of the sample precipitated from the n-butanol solution is clearly visible with large particles in the region of 2-3 μm in diameter alongside smaller particles 10% of that size. Figure 83b however depicts the sample precipitated from 10% water in n-pentanol. The particle size distribution is much narrower with only small particles in the size range of 0.2 μm in diameter observed. This size difference is possibly the result of the changing miscibility with the aqueous sodium carbonate component of the co-precipitation mixture. The n-butanol (solubility in water: 73 g L^{-1} at 75 °C [7]) water mixture is more miscible than the n-pentanol (22gL^{-1} at 75°C [7]) water mixture. In the butanol precipitated system mixing between the two solutions will occur more rapidly resulting in a more phase separated solvent. In the pentanol precipitated system however diffusion from the less polar pentanol precipitated nitrate solution into the basic carbonate solution may result in precipitation occurring within small droplets before mixing can occur, resulting in smaller particles. Indeed after a large amount of carbonate addition the solution will separate into aqueous and organic layers, further complicating the precipitation environment.

EDX analysis was also undertaken in conjunction with the imaging, the results are displayed in Table 30. There is a decrease in the Cu:Mn ratio as the solvent becomes more non polar.

168

This suggests that Mn ions are not precipitating from the solution and are remaining as nitrates. This could be the result of interaction between the ions and solution forming a solvation shell around the ions, stabilising them in solution. Another possible explanation is that there is insufficient mixing preventing a homogeneous pH environment forming, preventing the desired 1:2 Cu:Mn ratio precipitating.

5.3.6 XPS of the calcined catalysts precipitated from water alcohol mixtures

XPS data for the two catalysts is shown in Table 6. The Cu:Mn ratio of the material precipitated from butanol is nearly 1:1 whereas the Cu:Mn ratio for the propanol precipitated material is 1:1.4. This is contrary to the bulk trend where the less polar solvent had a lower copper content. This suggests that there is some phase separation occurring with the surface being relatively more manganese rich than the bulk.

Also noteworthy is the levels of sodium on the surface of the two materials. As seen in Figure 15, the catalyst precipitated from butanol has no sodium detectable on the surface of the material. Mirzaei has previously shown that Na^+ is a poison for hopcalite catalysts [1] therefore its absence is significant.

Table 29: XPS data for calcined catalysts precipitated from water alcohol mixtures

Sample	Cu:Mn ratio	Na:Mn Ratio
10% Water in Butanol	1: 1.05	-
10% Water in pentanol	1: 1.40	1: 14

Figure 84: XPS of hoclalite precipitated from water alcohol mixtures showing the Na 1s emmision peak
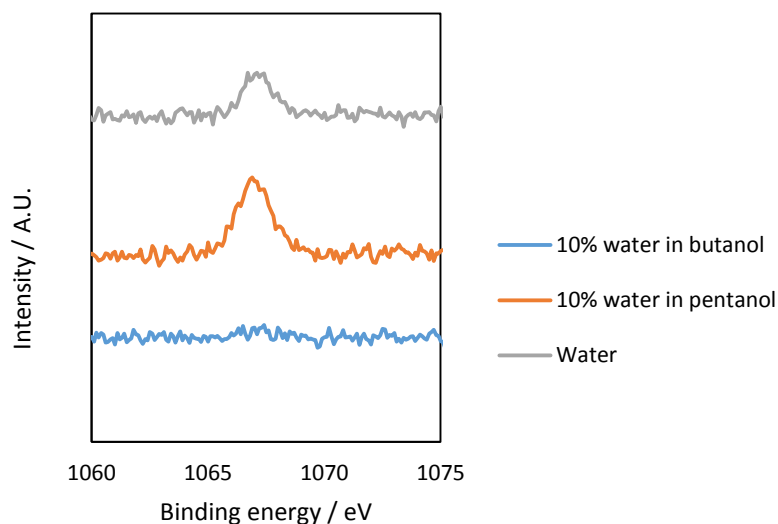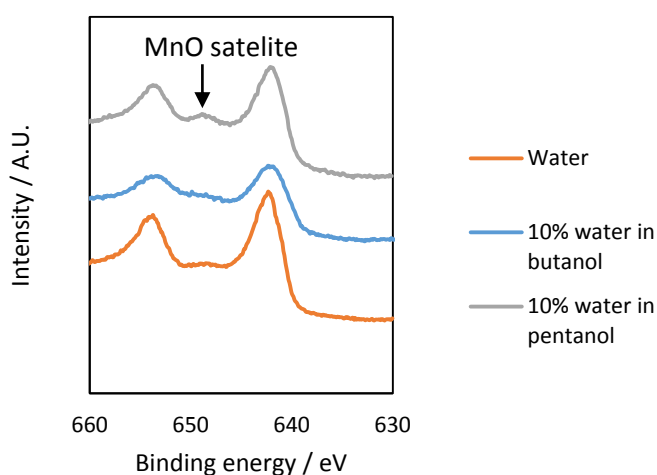
Figure 85: XPS of hopcalite precipitated form water alcohol mixtures showing the Mn 3p emission peak and associated satellite indicating the presence of MnO

Figure 16 shows the manganese 3p XPS for the aforementioned materials. Analysis of this region is complicated by the overlapping emission from the Cu auger emission along with the possibility for multiple manganese oxidation states. However it is possible to identify the presence of a MnO satellite in the sample precipitated from pentanol[18]. This is significant as previous work suggests that the activity of the $CuMn_2O_4$ spinel is at least partially due to the presence of the $Cu^{2+} + Mn^{3+} \rightleftharpoons Cu^{1+} Mn^{4+}$ redox couple. The samples precipitated from butanol and water exhibited less of this MnO satellite and as such contained less MnO.

5.3.7 Surface area measurements of the calcined catalysts precipitated from water alcohol mixtures

Surface area measurements of the catalysts are shown in Table 30: Physical properties of the materials precipitated from water alcohol mixtures. There is a slight increase from   55 $m^2 g^{-1}$ to 66 $m^2 g^{-1}$ when the solvent is changed from butanol to pentanol. This is not a very large change in surface area when the error associated with the BET measurement is taken into account and any changes are the result of the precipitation environment as a result of the changing solvent. It is however lower than when Hopcalite is precipitated from water alone, 85 $m^2 g^{-1}$. This suggests that there is either some sintering of these materials upon calcination, or that they are texturally distinct from the material precipitated from water. The TGA of the precursors shows that they both decompose at lower temperatures than the precursor precipitated from water, future work should investigate the effect of calcination temperature on these materials. A lower calcination temperature may be able to generate the active oxide while maintaining a higher surface area.

Table 30: Physical properties of the materials precipitated from water alcohol mixtures

Sample	TPR H$_2$ consumption / mol g^{-1}	Calcined surface area / m^2 g^{-1}	EDX Cu:Mn ratio
10% water n-Butanol	0.012	52	1:1.8
10% water n-Pentanol	0.004	66	1: 1.6

5.3.8 CO Oxidation activity data for the calcined catalysts precipitated from water alcohol mixtures

Both of the catalysts were tested for CO oxidation as described in chapter 2. The sample precipitated from 10% water in butanol exhibited the higher activity of the two (Figure 86) with a steady state activity of 47% achieved after 16 minutes. When error is taken into account this is comparable with the sample precipitated from water and has a shorter

induction period. The sample precipitated from 10% water in pentanol exhibited far lower activity, with a steady state activity of only 8.5%.   This was not the expected result as previous studies have shown that amorphous copper manganese oxide materials are more active for CO oxidation than crystalline ones. The sample precipitated from butanol is markedly more crystalline in nature than the sample precipitated from pentanol (Figure 81). When compared with the catalysts precipitated from water the butanol precipitated catalyst is also more crystalline, therefore it is not the case that more amorphous catalysts are always more active than crystalline ones when precipitations is from a water/alcohol mixture. The high activity of the catalyst is In part due to the fact that there were no traces of Na$^+$ on the surface [1].
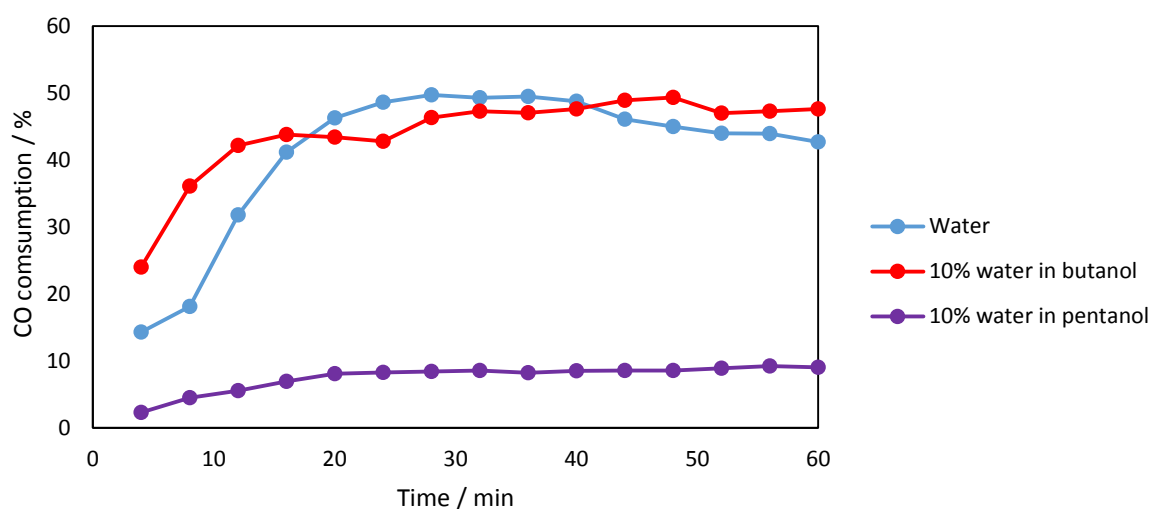
Figure 86: CO oxidation activity of the catalysts precipitated from water alcohol mixtures. 5000 ppm CO / synthetic air, 21 mL min^{-1}, 25°C.

The catalyst precipitated from pentanol exhibits low activity in comparison, this is possibly due to the MnO present within the catalyst disrupting the Mn Cu redox couple. It also had higher levels of sodium on the surface with a Na:Mn ratio of 1:14 compared with 1:24 for the sample precipitated from water.
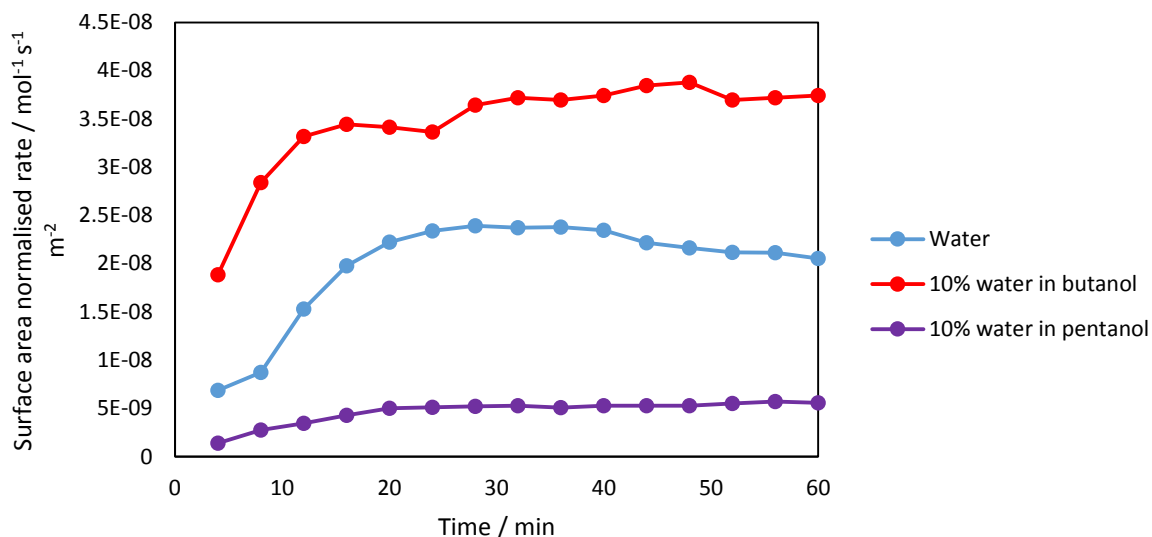
Figure 87: Surface area normalised CO oxidation rate for the catalysts precipitated from water alcohol mixtures

When the surface area normalised rates are considered the sample precipitated from butanol is the more active of the two materials and is more active than the sample precipitated from water. The suppressed surface area of the butanol catalyst leads to its activity per square meter to be higher than the traditionally precipitated water catalyst. This suggests that there is a matrix of inert material that contains small domains of active material that is performing the reaction.

5.4 Conclusions

When the catalysts are compared it is clear that the catalyst precipitated from butanol is as active as the catalyst precipitated from water. The catalyst precipitated from water and butanol have the typical characteristics that have been identified in previous work by various authors for good copper manganese oxide catalysts. The catalyst contains the appropriate copper to manganese ratio for the formation of the spinel phase, a low level of sodium ions on the surface and an XRD pattern that suggests that the calcined catalyst is nanocrystaline in nature.

The catalyst precipitated from ethanol shares many of these traits with a bulk Cu:Mn ratio of close to 1:2 and a nanocrystaline XRD. The CO oxidation data for this material demonstrates a slightly lower steady state oxidation activity however when surface area normalised rates are taken into account the two materials have similar performance. There is a clear difference in the morphology of the materials on the micro scale. Before calcination the sample precipitated from water consists of regular particles in the region of 10 μm across, the sample precipitated from ethanol consists of a range of particles ranging from 10 μm down to small particles that could not be measured using the images acquired. Sintering of the smaller particles during calcination leads to the observed lower surface area. This morphological difference could be the result of the different rate of mixing between the aqueous carbonate precipitating agent and the non-aqueous nitrate solution when compared with the catalyst precipitated from water

The catalyst precipitated from propanol exhibits a depressed activity compared to the other two catalysts, this is related to the very low surface area of the material. Again like the catalyst precipitated from ethanol there is a large proportion of small particles observed in the SEM, these are more susceptible to sintering than their larger counterparts on account of the difference in surface area to volume ratio. However the main point of difference between the catalyst precipitated from propanol and the two others is the large amount of Na^+ remaining on the surface. Previous work has shown that sodium is a prime agent in the poisoning of hopcalite catalysts. It is unclear as to why the level of sodium is ten times higher on the surface of the propanol precipitated catalysts than the other two studied.

By precipitating hopcalite from the water butanol mixture it is possible to form a catalyst that is comparable in its activity to the catalyst precipitated from water. However the lower surface area of this material leads its activity per square meter to be superior than the catalyst precipitated from water. This is despite the fact that the sample has a lower Cu:Mn

ratio when compared to the catalyst precipitated from water, is less reducible and more crystalline. The factor that contributes to its increased activity is the lack of Na^+ ions on the surface of the catalyst. This is interesting as the catalyst was prepared in the same manner as the others yet resulted in a sodium free surface. This suggests that the solvent system itself had an effect in removing Na^+ from the surface. Rogers and Armentrout found that, of the short chained alcohols they studied ($C_nH_{2n+2}O$, n = 1-4), n-butanol had the highest enthalpy of binding with Na^+ [19] due to its polarizability. This suggests that butanol should bind more strongly to Na^+. The branched chain alcohols exhibited higher binding enthalpies than their linear analogues and they should be investigated in future work.   Another possibility that should be investigated is the levels of sodium impurities within the alcohols used for precipitation as this may be significant.

Precipitation from the pentanol precipitated mixture is not as effective as the butanol. The catalyst exhibited lower CO oxidation activity than the butanol precipitated catalyst. This is attributed to the presence of MnO on the surface of the catalyst inhibiting the manganese copper redox couple [20]. This along with a relatively large concentration of Na^+ contributes to the low activity observed.

What is clear is that the precipitation of hopcalite from this system is even more complex than the traditional co-precipitation. Alongside the precipitation and aging processes which in of themselves are not well understood there is the additional factor of the changing rate of mixing two phases. Because of this there is a diffusion of ions from the organic phase into the aqueous carbonate solution at which point the precipitation occurs. This leads to a change in the morphology of the catalyst precipitated with the particle size of the pentanol precipitated catalyst smaller than its butanol precipitated counterpart. This work has identified that interesting Hopcalite catalysts can be prepared by precipitation from solvents

of alcohols and alcohol/water mixtures, and further studies are now required to start to

understand more fully the interesting preliminary observations presented in this chapter.

5.5 References

[1]   A.A. Mirzaei, H.R. Shaterian, R.W. Joyner, M. Stockenhuber, S.H. Taylor, G.J. Hutchings, Catalysis Communications 4 (2003) 17-20.
[2]   G.J. Hutchings, A.A. Mirzaei, R.W. Joyner, M.R.H. Siddiqui, S.H. Taylor, Catal. Lett. 42 (1996) 21-24.
[3]   A.A. Mirzaei, H.R. Shaterian, M. Habibi, G.J. Hutchings, S.H. Taylor, Applied Catalysis A: General 253 (2003) 499-508.
[4]   L.-N. Cai, Y. Guo, A.-H. Lu, P. Branton, W.-C. Li, Journal of Molecular Catalysis A: Chemical 360 (2012) 35-41.
[5]   C. Jones, K.J. Cole, S.H. Taylor, M.J. Crudace, G.J. Hutchings, Journal of Molecular Catalysis A: Chemical 305 (2009) 121-124.
[6]   G.J. Hutchings, A.A. Mirzaei, R.W. Joyner, M.R.H. Siddiqui, S.H. Taylor, Applied Catalysis A: General 166 (1998) 143-152.
[7]   Handbook of Chemistry and Physics, 73 ed., Chemical Rubber Publishing Company, 1993.
[8]   P. Porta, G. Moretti, M.L. Jacono, M. Musicanti, A. Nardella, Journal of Materials Chemistry 1 (1991) 129-135.
[9]   G.J.d.A.A. Soler-Illia, R.J. Candal, A.E. Regazzoni, M.A. Blesa, Chemistry of Materials 9 (1997) 184-191.
[10]   G.J. Millar, I.H. Holm, P.J.R. Uwins, J. Drennan, Journal of the Chemical Society, Faraday Transactions 94 (1998) 593-600.
[11]   C. Jones, S.H. Taylor, A. Burrows, M.J. Crudace, C.J. Kiely, G.J. Hutchings, Chemical Communications (2008) 1707-1709.
[12]   Z.R. Tang, S.A. Kondrat, C. Dickinson, J.K. Bartley, A.F. Carley, S.H. Taylor, T.E. Davies, M. Allix, M.J. Rosseinsky, J.B. Claridge, Z. Xu, S. Romani, M.J. Crudace, G.J. Hutchings, Catalysis Science and Technology 1 (2011) 740-746.
[13]   F.C. Buciuman, F. Patcas, T. Hahn, Chemical Engineering and Processing: Process Intensification 38 (1999) 563-569.
[14]   K. Morgan, K.J. Cole, A. Goguet, C. Hardacre, G.J. Hutchings, N. Maguire, S.O. Shekhtman, S.H. Taylor, Journal of Catalysis 276 (2010) 38-48.
[15]   B. Bems, M. Schur, A. Dassenoy, H. Junkes, D. Herein, R. Schlogl, Chem.--Eur. J. 9 (2003) 2039-2052.
[16]   I. Spassova, D. Mehandjiev, React. Kinet. Catal. Lett. 69 (2000) 231-237.
[17]   N.K. Radhakrishnan, A.B. Biswas, Phys. Status Solidi A 44 (1977) 45-49.
[18]   M.C. Biesinger, B.P. Payne, A.P. Grosvenor, L.W.M. Lau, A.R. Gerson, R.S.C. Smart, Applied Surface Science 257 (2011) 2717-2730.
[19]   M.T. Rodgers, P.B. Armentrout, The Journal of Physical Chemistry A 103 (1999) 4955-4963.
[20]   D.L. Cocke, S. Vepřek, Solid State Communications 57 (1986) 745-748.

Investigating the effect of washing CuMn$_2$O$_4$ catalyst precursors on the activity of the calcined material for CO oxidation

6.1 Introduction

There has been much work over the years on the various factors that affect the activity of the Hopcalite catalyst when preparing it by coprecipitation. Areas studied include the aging of the coprecipitation liquor[1], calcination of the precursor[2] and sodium content on the surface of the material[3]. This has led to the identification of factors that can, in part, contribute to the preparation of an active Hopcalite catalyst by coprecipitation.

In their 2003 paper Mirzaei *et al.* determined that the activity of a hopcalite catalyst can be related to the levels of sodium on the surface of the material [3]. In this study levels of sodium on the surface was determined after aging the catalyst for differing periods of time and after varying the pH of the precipitation. However, the modification of these parameters can also lead to changes in other characteristics of the catalyst, such as the nature of the precipitated phase [4, 5].

When co-precipitation is performed with an undesirable counter ion in the precipitant, such as sodium in this case, the precipitate is often washed with a certain amount of water to remove it. There is no published literature on the systematic study of the effect of this washing step on the activity of the final catalyst. It was decided therefore to investigate the effect of washing on the levels of sodium in the catalyst, and as a consequence the effect of sodium on their activity as CO oxidation catalysts.

A second investigation that is discussed in this chapter is into washing using chelating agents. The most commonly used precursor salts for co-precipitation are nitrates. As large volumes of water are required to remove sufficient sodium from the catalysts precipitates to produce active materials, large volumes of waste water contaminated with nirates can be generated. This has adverse environmental effects as nitrates are linked with waterway pollution and algal blooms[6]. We investigated minimising the amount of washing required by washing with dilute chelating agents. Compounds such as 15-crown-5 ether are commonly used in inorganic synthesis to selectively remove Na^+ ions from solutions[7]. By washing with dilute solutions of these chelating agents our intention was to remove Na^+ with less washing than by using water alone and as a result minimising nitrate waste.

6.2 Results of washing catalyst precursors with water

6.2.1 XRD of the washed catalyst precursors

Figure 1 shows the XRD patterns for the catalyst precursors washed with increasing amounts of water. XRD of the uncalcined catalysts shows the presence of the typical $MnCO_3$ phase that has been discussed at length in Chapters 3 and 4. The most intense reflection is at 31.6° and corresponds to the (104) reflection of manganese carbonate (ICDD 00-044-1472). The unwashed sample also shows a weak reflection at 30° which appears to correspond with sodium carbonate (00-019-1130). This sodium carbonate phase is unobserved after 200 mL of washing, a small volume of washing clearly removed any trace of bulk sodium carbonate.
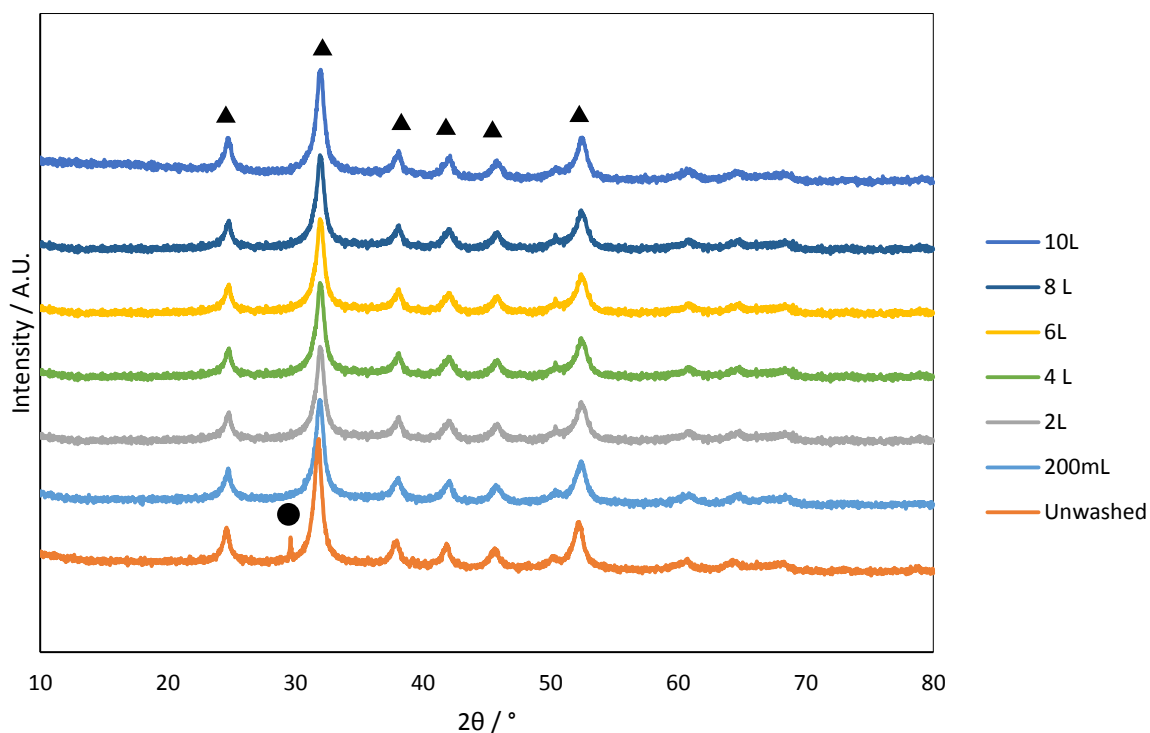
Figure 88: XRD of the washed catalyst precursors showing presence of $MnCO_3$ and Na_2CO_3. 40mA 40 kV Cu source. ▲ = MnCO3 (ICDD 00-044-1472) ● = Na2CO3 (00-019-1130)

There is no evidence of a crystalline copper phase in any of the XRD patterns. This suggests that the copper is present as an amorphous or nanocrystaline phase that is not observed or has been incorporated into the $MnCO_3$ phase to form a $Mn_xCu_{1-x}CO_3$ phase [8]. The slight increase in the 2θ angle for the principle reflection from 31.3° to 31.6° suggests that this incorporation is occurring.

It is clear that despite the increasing volume of washing there is not a major change in the phase composition of the catalyst precursor. There is no observed change in the crystallite size of the $MnCO_3$ phase with increased washing (Table 31) with all values falling within the margin of error of each other. This suggests that the washing is not changing the manganese carbonate precursor structure.

Table 31: Physical properties of the washed catalyst materials

Volume of washing / L	Surface area / $m^2 g^{-1}$	Cu :Mn Ratio	Na Content / ppm	Precursor crystallite size / nm	Calcined crystallite size / nm
0	38	1:2	11377	12	-
0.2	37	1:2	7563	11	7
2	85	1:1.84	2538	12	8
4	84	1:1.83	2348	11	7
6	87	1:1.8	2211	12	7
8	92	1:1.73	1921	12	7
10	110	1:1.62	1121	10	7

6.2.2   XRD of the calcined catalysts

The XRD after the calcination process (415 °C, 2 °C min^{-1} and 2h) is displayed in Figure 89.

The unwashed catalyst exhibits one broad feature centred around 36°. This suggests that there is no crystalline material present in this calcined material and possibly there is a nanocrystaline or amorphous copper manganese phase, the broad feature could correspond with the (311) plane of $CuMn_2O_4$ (ICDD 01-075-0826). No sodium carbonate is observed, as it was in the precursor, suggesting that the Na_2CO_3 has thermally decomposed under calcination and the products of this are not apparent or that it is present as very small crystals.

Washing with 200mL causes the distinctive $CuMn_2O_4$ phase to form after calcination. The (311) reflection of $CuMn_2O_4$ is clearly visible at 36°.

There is no further change in the phase observed with additional washing. This is interesting as the relatively small washing amount is enough to induce a structural change in the calcined product from amorphous to crystalline.   As further washing does not seem to induce structural change observed in the XRD of the precursor materials, other than the presence of Na_2CO_3 in the unwashed sample, it suggests that it is the presence of the sodium carbonate phase that causes this change.   Previous work has demonstrated that the presence of amorphous $CuMn_2O_4$ is preferable for activity in CO oxidation[9], so influencing

the crystallinity of the catalyst is important. There is no link between the crystallinity of the precursor and the crystallinity of the calcined material as demonstrated by the lack of relationship between the crystallite size of the precursor and that of the calcined material (Table 31)
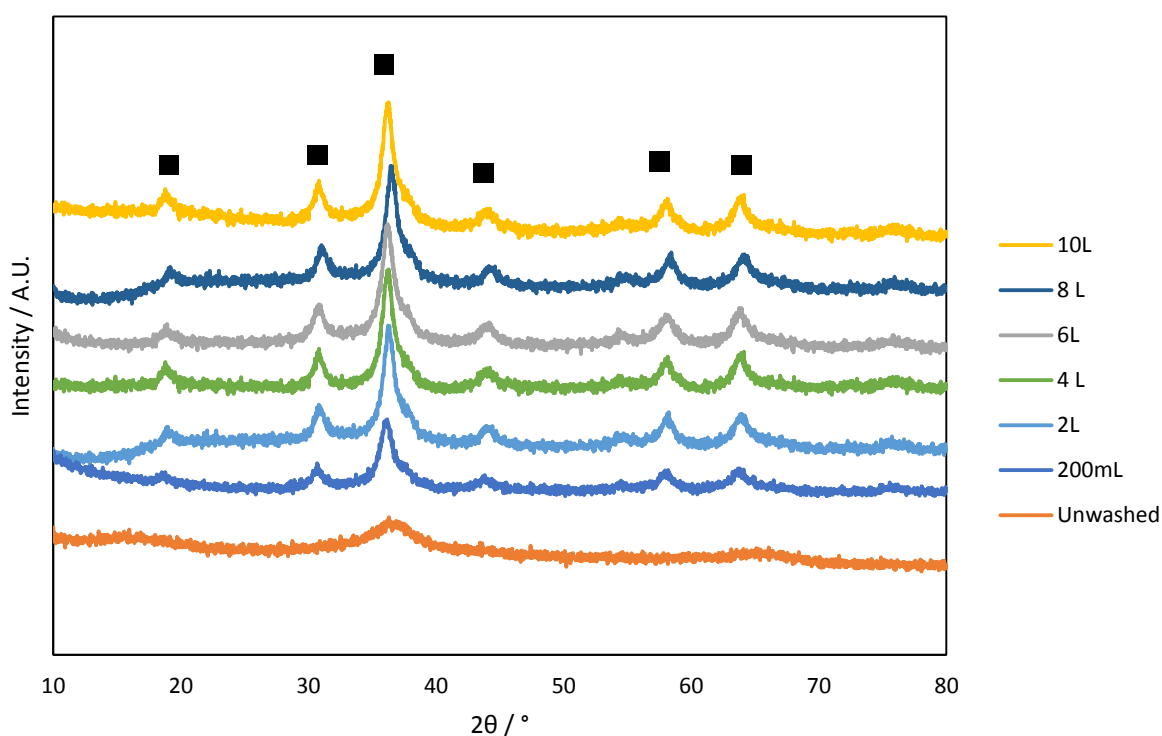

Figure 89: Representative XRD of the calcined washed catalysts showing the presence of copper manganese oxide . 40mA 40 kV Cu source. ■ = $CuMn_2O_4$ (ICDD 01-075-0826)

6.2.3 Surface Area

There is a clear trend of an increase in surface area with increased washing (Figure 90). The unwashed sample exhibits a surface area of 35 m^2 g^{-1}. The surface area plateaus at 85 m^2 g^{-1} after 2 L of washing and remains unchanged with up to 6 L of washing. After this point there is a gradual increase up to 110 m^2 g^{-1} following washing with 10 L of water. This suggests that as washing proceeds there is an initial removal of material that when calcined becomes low surface area and that the removal of this material is very facile, possibly this is related to the presence of sodium carbonate in the unwashed precursor. The material that

remains after this removal appears to be relatively stable upon further washing until a point is reached and a higher surface area material is formed.
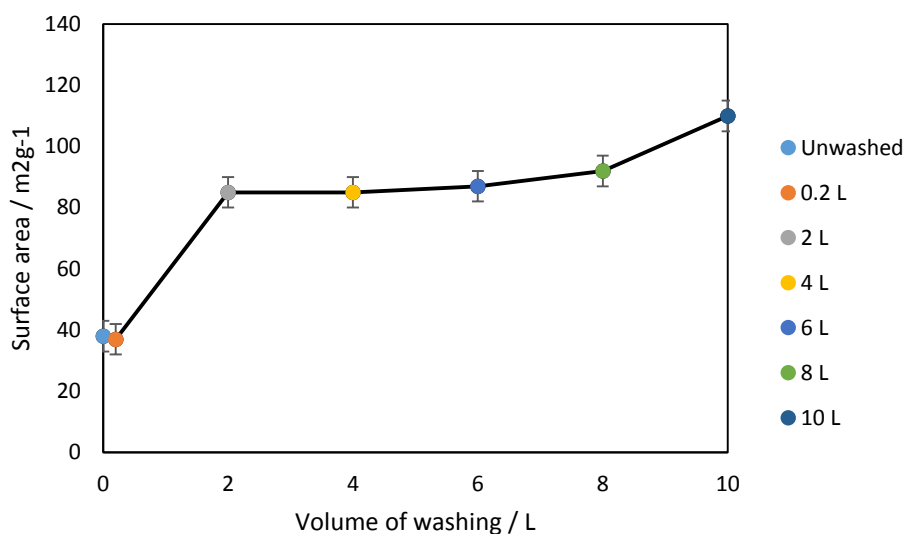

Figure 90: Surface area of the calcined catalysts as a function of the volume of washing undertaken.

6.2.4   Elemental analysis of the calcined catalysts

The elemental composition measured by MP-AES for the washed catalysts is detailed in Table 31 and summarised in Figure 91. There is a clear initial removal of sodium from the material associated with the loss of the Na_2CO_3 phase in the XRD. After washing with 2 L the rate of Na^+ removal slows, with only a gradual loss of Na^+ taking place with additional washing. This is expected as the initial washing step removes the most soluble sodium species. Any sodium that is bound more strongly to the surface requires more washing to remove and as such the levels drop more slowly after the facile sodium is removed. Sodium also will be located in the centre of particles as they are formed by coprecipitation. This sodium would not be removed by washing.

This change in the sodium concentration mirrors the change in surface area (Figure 90) this could suggest that the removal of sodium carbonate from the surface is related to the increasing surface area.
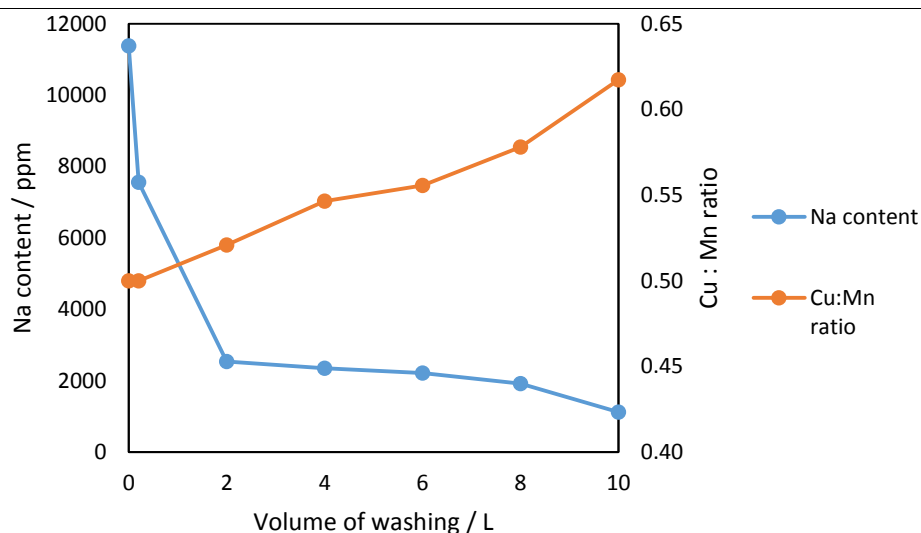
Figure 91: Elemental compositions of washed catalysts determined by MP:AES showing trend of decreasing Na content alongside increasing Cu:Mn ratio with increased washing

Removal of sodium is not the only change observed in the materials with increased washing, there is also a consistent change in the Cu : Mn ratio of the catalysts. Initially the Cu : Mn ratio is the expected 1:2 ratio. As washing increases the Cu : Mn changes as the catalysts become more copper rich. This suggests that with increased washing there is a removal of $MnCO_3$ from the precursor leaving a more copper rich material. The change is from 1:2 when unwashed to 1:1.6 after 10 L of washing.   Manganese carbonate is only sparingly soluble in water, with the 73rd edition of the handbook of chemistry and physics stating its solubility product at 2.24 x10^{-11} at 25 °C [10], which explains the slow rate of manganese removal. Copper hydroxycarbonate is not reported as soluble so it is likely that any copper removal would be at a much slower rate.

6.2.5   CO oxidation activity

CO oxidation of the materials is detailed below. From the work of Mirzaei *et al.* [3] where they studied the effect of surface Na^+ on CO oxidation activity of hopcalite it would be expected that CO conversion would increase as Na^+ is washed out of the catalyst (Figure 91).

Whilst this is true initially there does come a point at which activity drops with further washing.
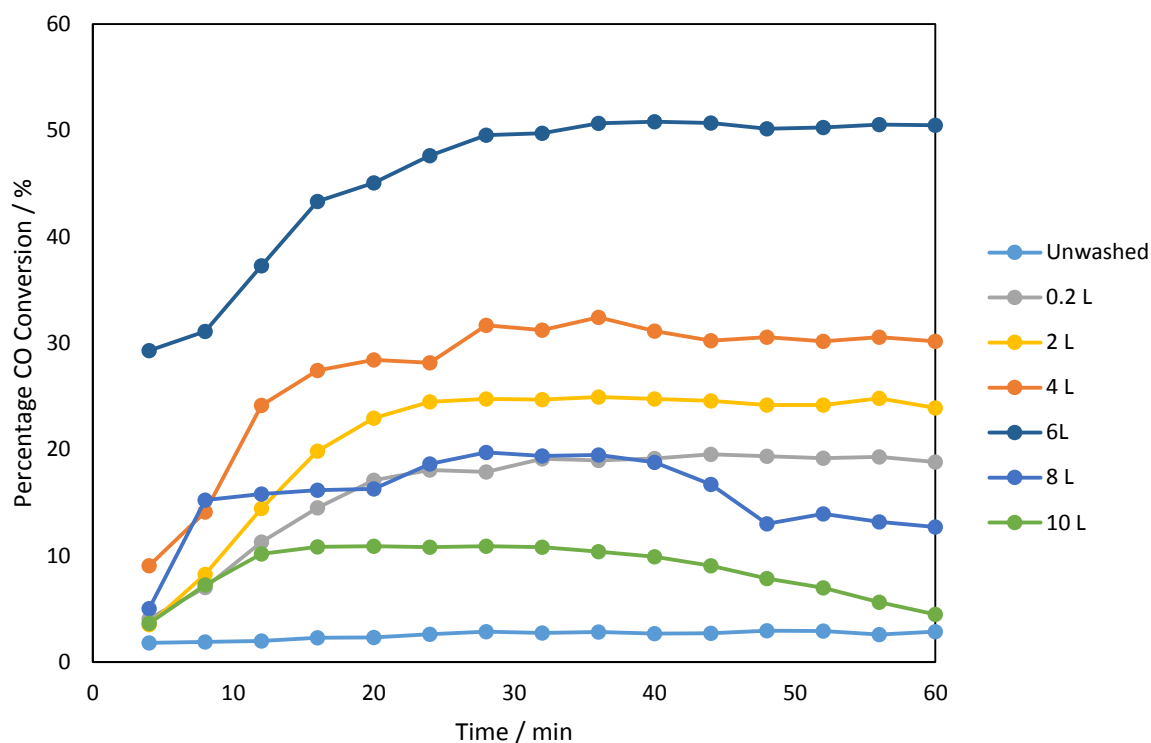

Figure 92: CO oxidation activity of the washed Hopcalite catalysts.

As shown in Figure 92 the unwashed catalyst exhibits little CO conversion. Washing with 0.2L increases the activity by an order of magnitude, further washing slowly increases the CO oxidation activity untill it peaks at 50% conversion after washing with 6 L of water. The large increase in activity corresponds with a large drop in sodium concentration within the catalyst. It also correlates with the loss of bulk Na_2CO_3 removal as expected.

Further washing leads to a reduction of the CO conversion. After 8 L of washing the CO conversion was 14% at steady state and drops further to 7% after 10L of washing. This was not expected as the MP-AES (Table 31) indicates that sodium levels continue to fall with increased washing. Figure 93 illustrates this with a volcano relationship between sodium content and CO conversion. This suggests that another factor is affecting the activity of the catalyst.
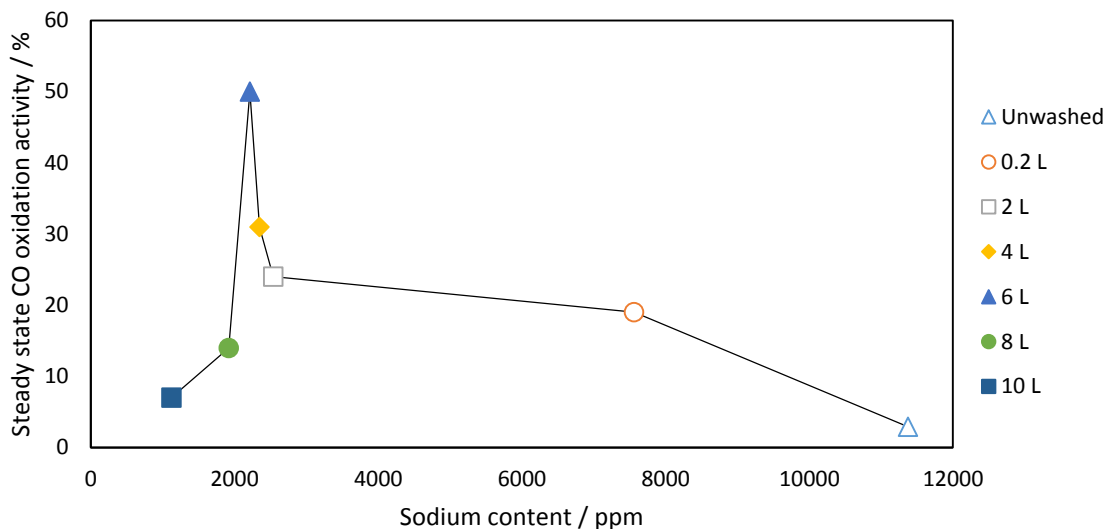
Figure 93: The relationship between steady state CO conversion and sodium content

As the catalyst is washed manganese is removed alongside sodium. This causes the Cu:Mn ratio to become more copper rich. Previous work has shown that a 1:2 copper to manganese ratio is the optimum for active hopcalite CO oxidation catalysts and that materials prepared with higher Cu:Mn ratios are less active for CO oxidation, this may explain the drop in CO oxidation activity with increased washing [9].

6.2.6   Conclusions

Washing the catalysts leads to an increase in CO oxidation as Na$^+$ is removed. It is clear however that the levels of Na$^+$ in the catalyst is not the only factor that determines CO oxidation activity. Despite an increase in surface area with 10 L of washing compared to 6 L there is a clear decrease in activity. This is associated with the gradual change of the Cu:Mn ratio with washing to become more copper rich. It is clear that there is a point at which the change in the manganese composition of the catalyst becomes an inhibiting factor for the CO oxidation activity of the material. The mechanism by which hopcalite oxidises CO is poorly understood with multiple theories attempting to explain it, it is accepted however that changing the ratio of Cu$^+$ and Mn^{4+} to Cu^{2+} and Mn^{3+} leads to deactivation of the catalyst [11]. It follows therefor that changing the overall Cu to Mn ratio will also have an adverse

effect and this could be an explanation as to the reduction of activity with additional washing. XPS studies would be useful to give insight into the ratio of these species directly.

It is interesting that the washing step leads to a structural change in the calcined catalyst material. The unwashed sample resulted in an amorphous material after calcination wheras after washing the materials were more crystalline. This suggests that unremoved sodium carbonate can inhibit crystallisation upon calcination.

If this could be replicated with a carbonate that did not contain a catalyst poison, as Na_2CO_3 does, it would be interesting as previous work has demonstrated clearly that amorphous $CuMn_2O_4$ phases outperform crystalline ones [9]. Future studies should focus on doping catalysts with controlled sodium amounts, this will allow direct correlation of activity with sodium content on the surface.

6.3 Effect of washing catalyst precursors with chelating agents

As shown in section 6.2, washing can be used as a method of removing Na^+ from catalysts. However the amount of water required is significant to remove the optimum amount of sodium. In addition washing can remove components of the catalyst that are required to maintain high activity. Chelating agents are widely used in inorganic and organic synthesis to scavenge unwanted Na^+ ions from reaction solutions. This work details investigations into the effectiveness of chelating agent solutions for removal of Na^+ from hopcalite catalyst precursors and the effect this has on their activity.

The experimental procedure for this study is detailed in Chapter 2. To recap, a single batch of copper manganese oxide was precipitated using 2M sodium carbonate at a pH of 8.3 using the Metrohm titrando auto titrator. The sample was then aged for 1 h then dried on a Buchner funnel. The sample was then weighed and then split into eight, 1 g portions. Each portion was washed with 100 mL of the solvents detailed in the table below and then rinsed with 100 mL of room temperature water. The samples were then dried and calcined as

discussed in chapter 2. The concentration of the chelating agents, other than HCl, was calculated to equal this in order to ensure an 1:1 ratio of chelating agent to sodium as determined by MP-AES (see Chapter 2: Experimental and Table 33)

Table 32: Concentration of chelating agents used to remove sodium from the catalyst precursours

Sample	Concentration / mol L^{-1}
Unwashed	N/A
Water (25°C)	N/A
Hot water (90 °C)	N/A
15-Crown-5	0.00403
Citric acid	0.00403
Oxalic acid	0.00403
EDTA (0.2M KOH)	0.00403
Hydrochloric Acid	0.1

6.3.1   XRD of the catalyst precursors washed with chelating agents

The XRD of the washed catalyst precursors clearly shows that the only phase present in all the materials is $MnCO_3$. The characteristic reflection present at 31.6° is indicative of the (104) plane of manganese carbonate and the distinctive trio of reflections at 38°, 41° and 46° are due to the (110), (113) and (202) planes. There is no change in the crystallite size of the precursors (Table 3) when washed with the different chelating agents that suggests that there is no change in the precursor phase induced by the washing.

It is unclear as to whether there has been any change in the lattice parameters of the materials in question that could relate to any change in the copper manganese ratio[8] as the samples were analysed using a non-diffractive silicon wafer and as such the error in the reflection position is much higher than usual due to the difficulty in getting a flat surface for analysis.

It is worth noting that the reflection associated with Na_2CO_3 as observed in the previous washing study is present in the unwashed precursor, however it is far less intense. This demonstrates the benefit of using the autotitrator system versus the manual technique. Less Na_2CO_3 is used and as a consequence there is no excess remaining in the final precursor. This is an area that could be investigated further for other precipitated materials.

Table 33: Physical properties of the materials washed with various chelating agent solutions

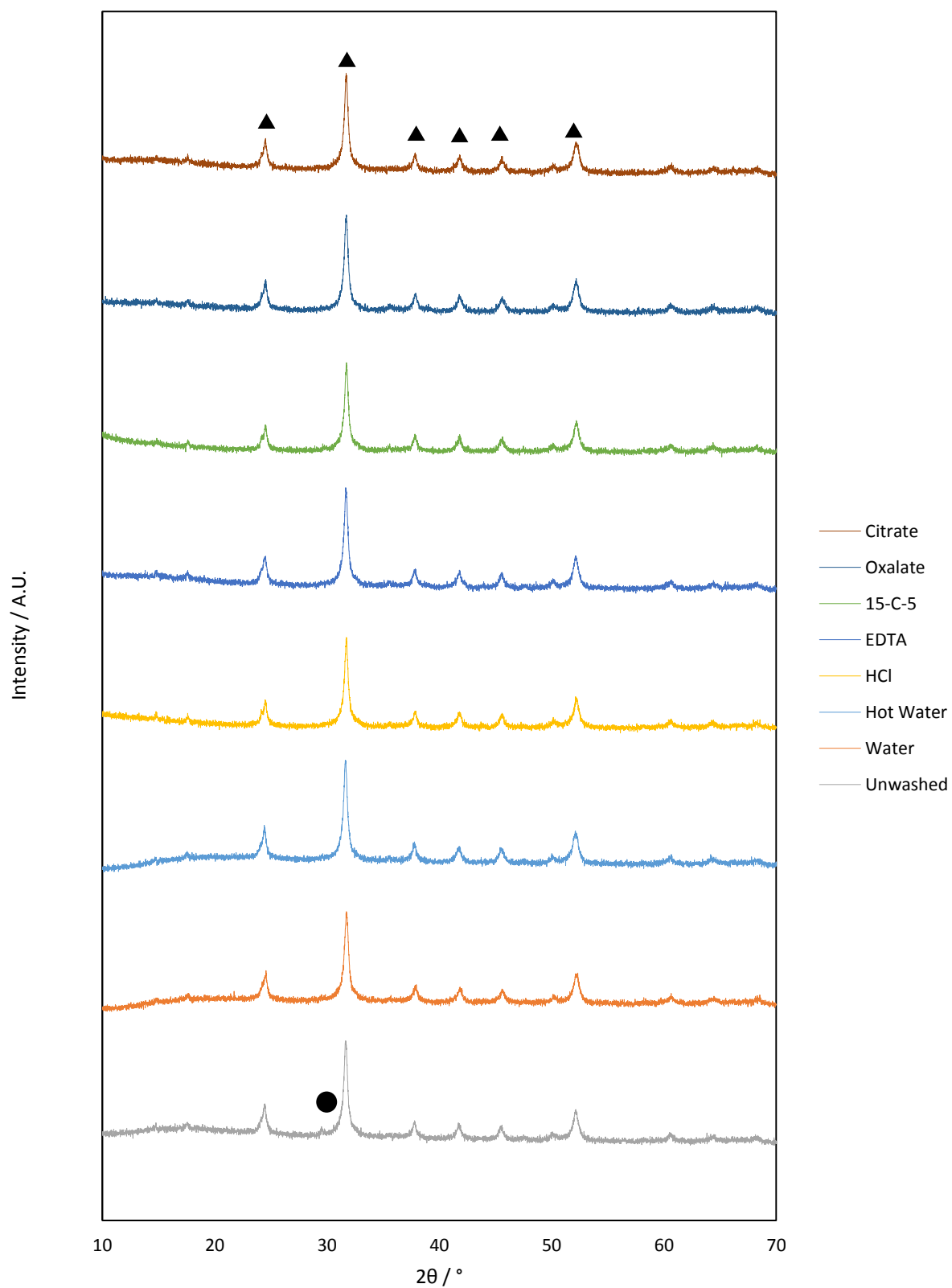| Sample	Surface area / $m^2\,g^{-1}$	Cu:Mn ratio	Sodium content / ppm	Precursour crystallite size / nm	Calcined crystallite size / nm	TGA mass loss / %
Unwashed	37	1:2	9262	26	8	31
Water	36	1:2	7294	23	9	31
Hot Water	35	1:2	5837	25	9	31
HCl	32	1:1.84	7579	25	10	31
EDTA	35	1:1.84	6946	21	9	30
15-C-5	36	1:1.83	2981	26	9	29
Oxalic acid	35	1:1.84	5993	25	10	30
Citric acid	35	1:1.84	5799	25	9	31

Figure 94: XRD of the catalyst precursours washed with various chelating agents. 40mA 40 kV Cu source ▲ = MnCO$_3$ (ICDD 00-044-1472), ● = Na$_2$CO$_3$ (00-019-1130)

Figure 95 below displays the TGA data for the catalyst precursors treated with chelating

agent solutions. When overlaid it is clear that the mode of decomposition is the same for all

the materials. There is an initial loss of physisorbed water up to about 200 °C. At around

350 °C there is a significant mass loss associated with the thermal decomposition of

manganese carbonate followed by a smaller loss of mass that is unattributed, however it is

possibly the result of a second thermally stable carbonate species. TGA MS studies could be

a method of identifying whether this is the case or not.
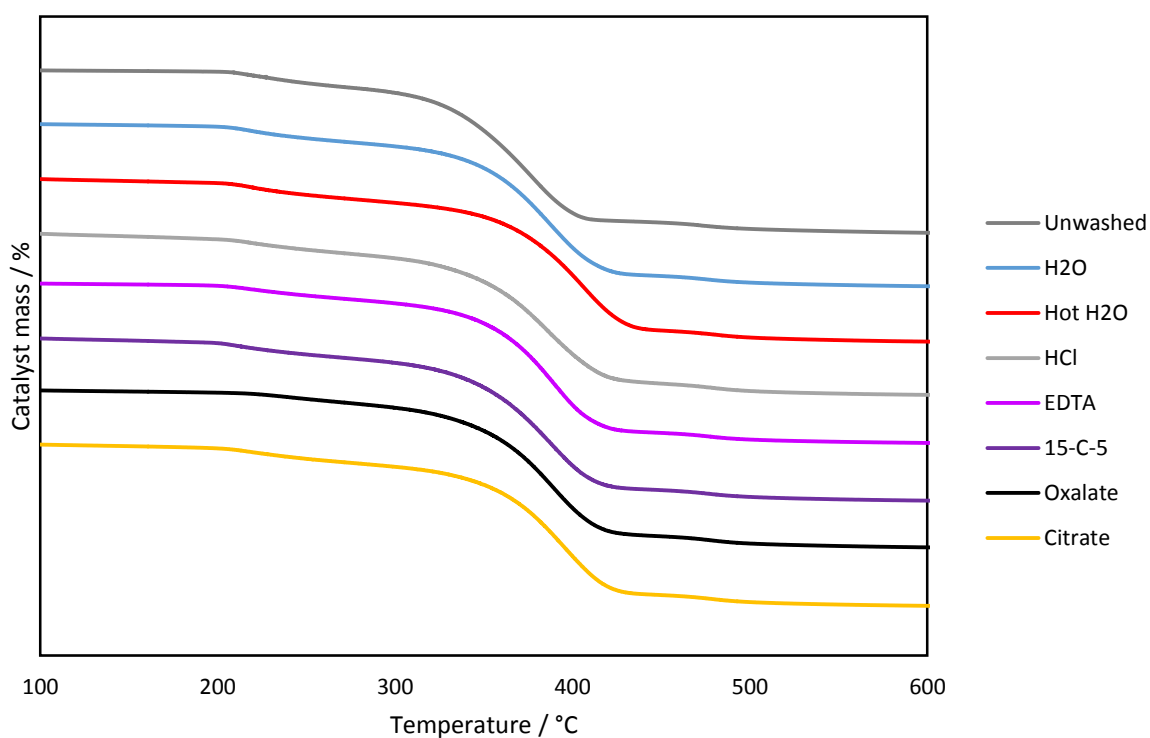
Figure 95: TGA analysis of the catalyst precursors washed with chelating agents showing
slight change in their mass loss profile

There is slight variance of the decomposition temperatures observed amongst the

precursors with the unwashed sample decomposing at a slightly lower temperature than the

other materials and the sample washed with hot water at a slightly higher temperature. In

addition the samples washed with oxalic acid and EDTA exhibit a lower overall mass loss than

the other samples. This could be the result of residual chelator bound to the surface not removed by the rinsing of the catalyst leaving carbonaceous species on the surface.

The overall mass losses are very similar. However the samples washed with bulky chelating ligands such as 15-crown-5 ether and EDTA exhibit a slightly lower mass loss suggesting that there is

6.3.3 XRD of the calcined catalysts washed with chelating agents

The XRD patterns of the calcined washed materials are visible in Figure 96. The only reflections visible are broad with the principle reflection centred at 36°. This corresponds with the (311) reflection of $CuMn_2O_4$ (ICDD 01-075-0826). This is reported to be observed at 35.73° however the shift observed can be attributed to the sample height displacement error resulting from the use of non-diffractive silicon wafers for the analysis rather than the more accurate stainless steel sample holder. This results in a more uneven surface and less accurate measurement of 2θ values.
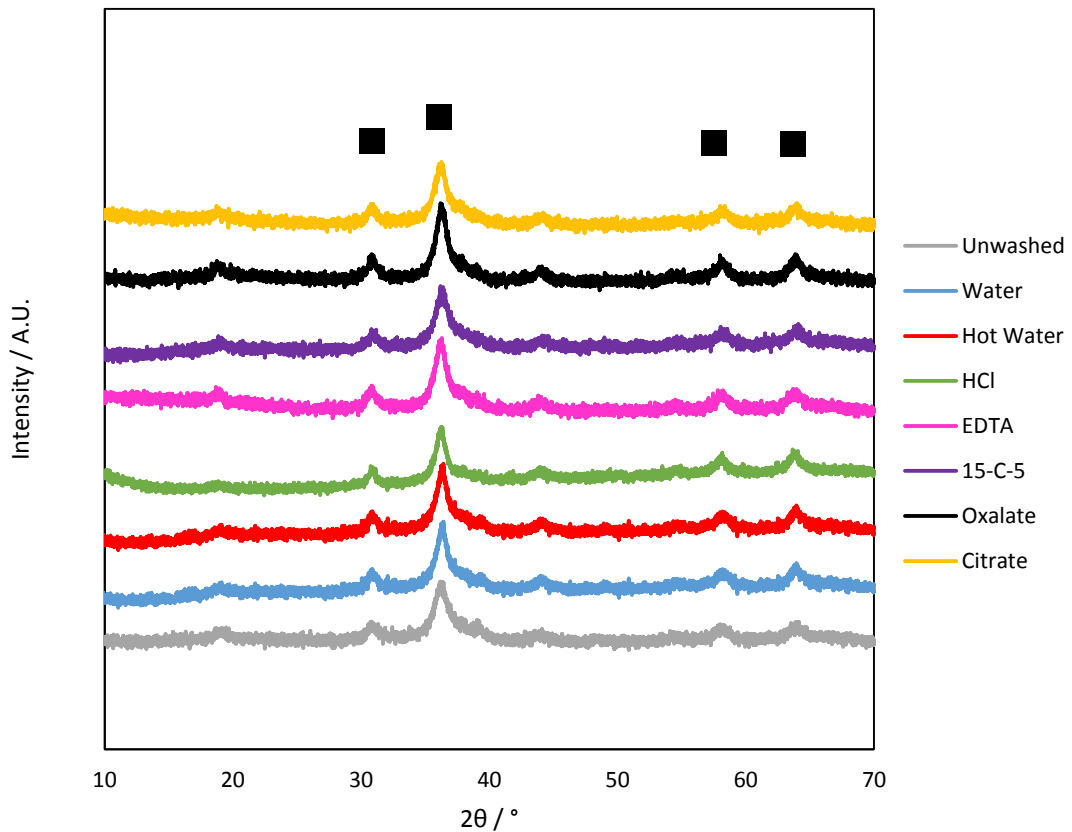
Figure 96: XRD patterns for the calcined materials washed with chelating agents illustrating no change in phase composition 40mA 40 kV Cu source. ■ = $CuMn_2O_4$ (ICDD 01-075-0826)

It is clear that the $CuMnO_4$ phase is poorly crystalline with small crystallites. Using the Scherrer equation the crystallite size of the materials was found to fall between 8 nm for the unwashed sample and 10 nm for the sample washed with HCl. Washing with hot and cold water resulted in the same crystallite size. It is clear that washing with small amounts of these chelating agent solutions is not having a large effect on the phase structure of the calcined material, however, there are small changes happening as expressed in the changing precursor crystallite size.

Interestingly the unwashed material also displays a reflection corresponding with the (311) diffraction plane. The previous unwashed catalyst did not exhibit this suggesting that the presence of the Na_2CO_3 in that material inhibited the formation of a crystalline $CuMn_2O_4$ phase.

6.3.4 Surface area analysis of the calcined catalysts washed with chelating agents

Surface area data for the calcined materials is tabulated in Table 33. It is clear that there is no significant change in the surface area upon washing with the various chelating agents as compared with washing with water. The sole exception to this is the sample washed with HCl where the surface area is slightly depressed possibly due to the removal of small particles by corrosive action.

6.3.5 Elemental analysis of the calcined catalysts washed with chelating agents

The MP-AES data for the washed materials is shown in table 3.   The levels of sodium in the materials was measured. The unwashed catalyst has 9262 ppm sodium. Washing with cold water removed ca 2000 ppm sodium and hot water about 3500ppm. Unexpectedly the solution of HCl did not remove any more sodium than the water rinsing alone. This was surprising as it is known that alkali metal ions are more soluble in acidic media.

The EDTA solution removed 3000ppm sodium, marginally more than the cold water rinse. The improvement was most likely limited by the chelation of potassium ions from the KOH solution used to prompt the EDTA to dissolve.

The two organic acid solutions removed in the region of 3500 ppm. This is clearly an improvement over the cold water wash as it is a similar amount to the hot water wash despite not requiring any heating.

Finally the sample rinsed with the 15-crown-5 solution removed 6000 ppm. This is a clear improvement over cold water alone. The level of sodium removal was expected as the cavity of the 15-crown-5 macrocycle is the appropriate volume to selectively chelate Na^+. The remaining sodium in the catalyst is likely not to be exposed in the surface, rather it is trapped within the lattice of the material where it cannot be rinsed out.

The copper to manganese ratio of the unwashed catalyst is the desired 1:2 ratio that has been shown to be the most active for CO oxidation in previous work. This 1:2 ratio is maintained in the samples washed with cold and hot water. When washing with other chelating agents however the ratio of copper to manganese has dropped to 1:1.8. This suggests that manganese has been removed from the material by the action of the chelating agents.

In the case of the sample washed with HCl the increased acidity of the wash is likely to have removed $MnCO_3$ as H^+ is well known to break down carbonates to form CO_2 and water. In this case manganese chloride would be formed which is soluble, however, CuCl is also soluble and would be also be formed. It is unclear therefore why more manganese is removed than copper.

6.3.6 XPS analysis of the catalysts washed with chelating agents after calcination.

The surface species on the calcined materials were investigated by XPS and the atomic ratios determined can be seen in table 4. The sodium to manganese ratio varies from 1: 5.4 for the unwashed material to nearly 1: 10 for the sample washed with citric acid. This clearly shows that the choice of washing solution has an effect on the levels of sodium on the surface of the materials.

Table 34: Atomic ratios of surface species of calcined catalysts as determined by XPS

	Cu^{1+} / Cu^{2+} Ratio	Cu / Mn Ratio	Na / Mn Ratio
Unwashed	1: 10.11	1: 4.61	1: 5.4
Cold Water	1: 4.55	1: 5.46	1: 5.9
Hot Water	1: 19	1: 6.13	1: 9.24
EDTA	1: 4.88	1: 5.50	1: 8.99
15-C-5	1: 6.14	1: 5.45	1: 7.48
Citrate	1: 5.67	1: 5.89	1: 9.92
Oxalate	1: 2.57	1: 6.44	1: 7.88
1M HCl	1: 2.80	1: 5.47	1: 7.01

The copper to manganese ratio is clearly increased from the 1:2 ratio that was desired. This suggests, alongside the EDX elemental analysis, that the various chelating agents are not only removing sodium from the surface of the material but are changing the copper to manganese ratio by removing manganese.

The copper species on the surface is a mixture of Cu^{1+} and Cu^{2+}. Interestingly the ratio of these two species is not constant depending on the solution used to wash the precursor. The unwashed material has a 1+: 2+ ratio of 1 :10. Washing with hot water suppress the levels of Cu^{1+} with a 1:19 ratio in that material. Conversely washing with other solutions promotes the levels of Cu^{1+}. This suggests that the chelating solutions are slightly reducing in character, as the XPS shows that electrons are being removed from the copper.

6.3.7 CO oxidation activity of the calcined catalysts washed with chelating agents.

There is clear differentiation in the activity of the catalysts washed with the different chelating agents. Figure 97 shows the activity of the various materials. As expected the unwashed catalyst shows very little activity. The sample washed with oxalic acid also exhibited no activity. This was not expected as the Na: Mn ratio suggested that there was less Na^+ remaining on the surface compared to other materials. This lack of activity could be the result of oxalic acid remaining strongly bound to the surface after rinsing, then leaving a carbonaceous later on the surface after calcination blocking the adsorbtion of CO to the surface.

The most active material was that washed with the citric acid solution with a steady state activity of 13%. The least active catalysts were those washed with cold water and EDTA. The catalysts washed with hot water, HCl and 15-crown-5 exhibited a similar activity in the region of 10% conversion. The least active materials were those washed with cold water and EDTA with a steady state activity in the region of 8% conversion.
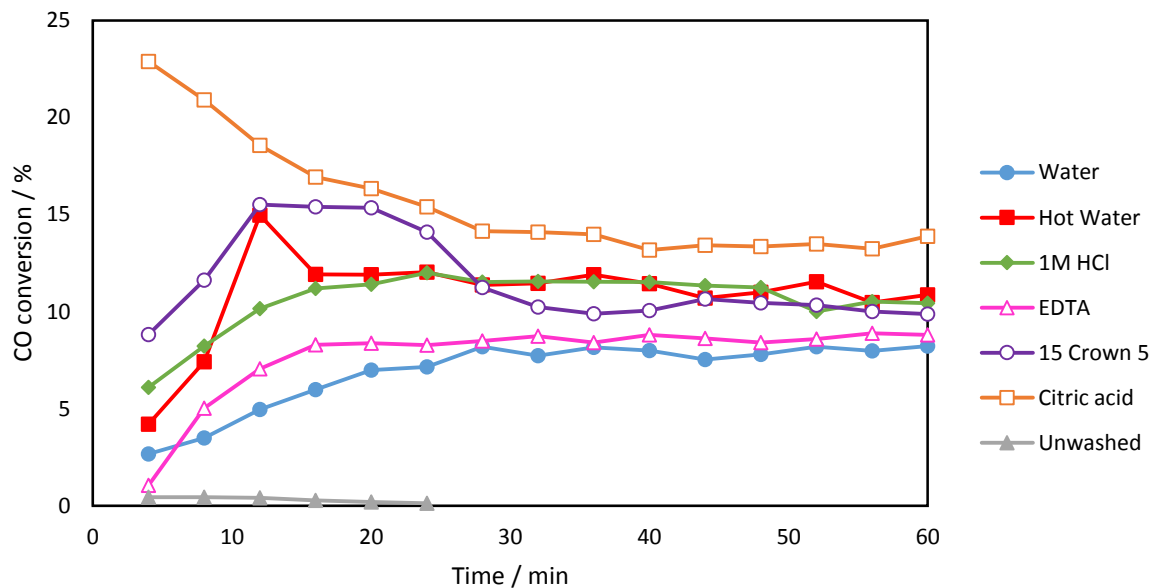
Figure 97: CO oxdiation activity of the calcined washed catalysts. 5000 ppm CO / synthetic air, 21 mL min^{-1}, 25°C.

When the surface area normalised rate of reaction is taken into account (the citric acid catalyst is the most active, followed by the HCl and hot water washed materials with the 15-crown-5, EDTA and cold water catalysts the least active. It is clear that washing with the citric acid solution has improved performance significantly with the surface area normalised rate improving by a factor of 2.5 compared with washing with cold water.
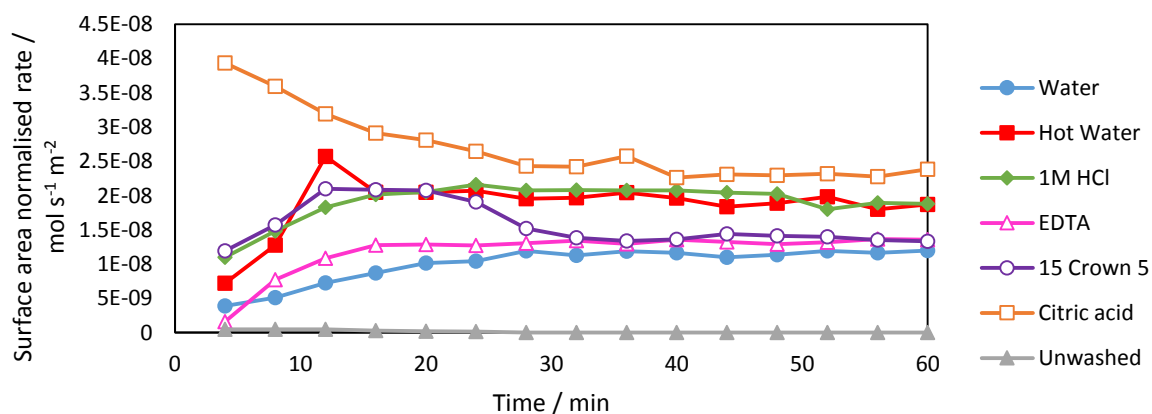

Figure 98: Surface area normalised rates of CO oxidation for the catalysts washed with chelating agents

By comparing the levels of sodium present in the material and the surface area normalised rate it is possible to determine that there is a direct relationship between the two. There is clearly a linear relationship between the sodium content and activity of the catalyst.

There are two outliers however. The catalyst containing the least sodium, and hence the one that we would expect to be most active, is the one washed with 15-crown-5. This material however exhibits a low surface area normalized rate for CO oxidation, nearly half that of the sample washed with citric acid despite its sodium content being only 50%. There is no major difference in surface area, copper to manganese ratio or crystallinity that could explain the difference in activity. The explanation therefore must be that the some of the 15-crown-5 ligand has bound to the surface blocking the adsorption of CO. The ligand is bulky and is known to coordinate with both copper and manganese. The slightly lower mass loss in the TGA seems to corroborate this hypothesis.

The second outlier is the sample washed with HCl. This material exhibits a higher surface area normalised activity than expected given its sodium content. The explanation for this is that it exhibits a lower surface area than the other materials for reasons explained previously and as such its surface area normalised rate is increased relative to the other materials. It suggests that possibly there are isolated high activity domains within a low surface area material that is inert.
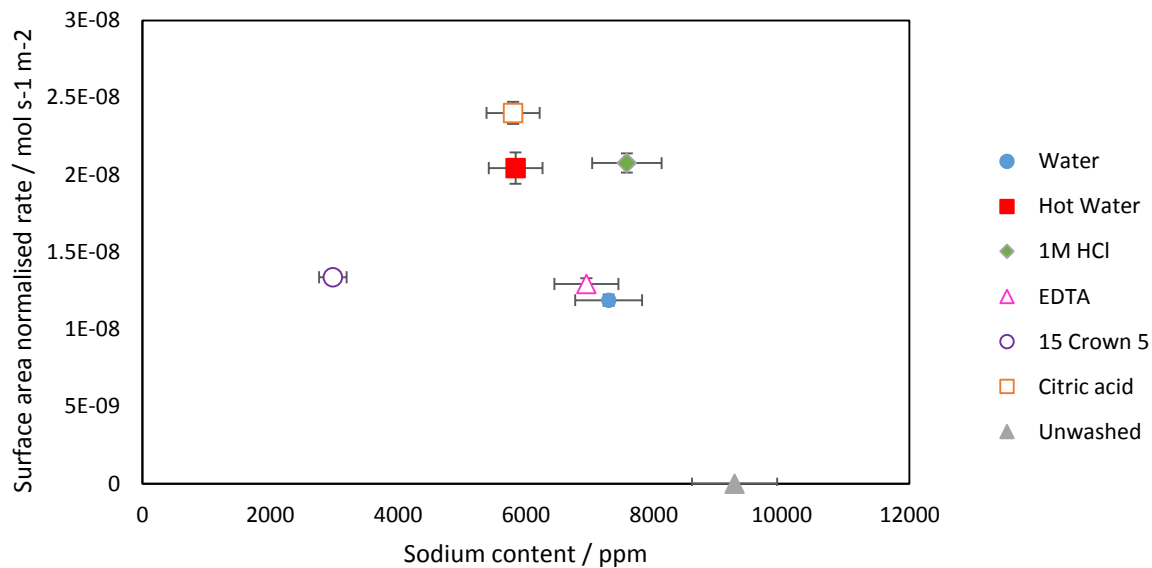
Figure 99: Relationship between sodium content and surface area normalised rate of CO oxidation

This relationship is also apparent when the sodium to manganese ratio on the surface of the material is taken into account. Figure 13 illustrates this and shows a linear relationship between surface area normalised rate and the sodium to manganese ratio. This suggests that sodium content is the key factor determining the activity of the catalysts.
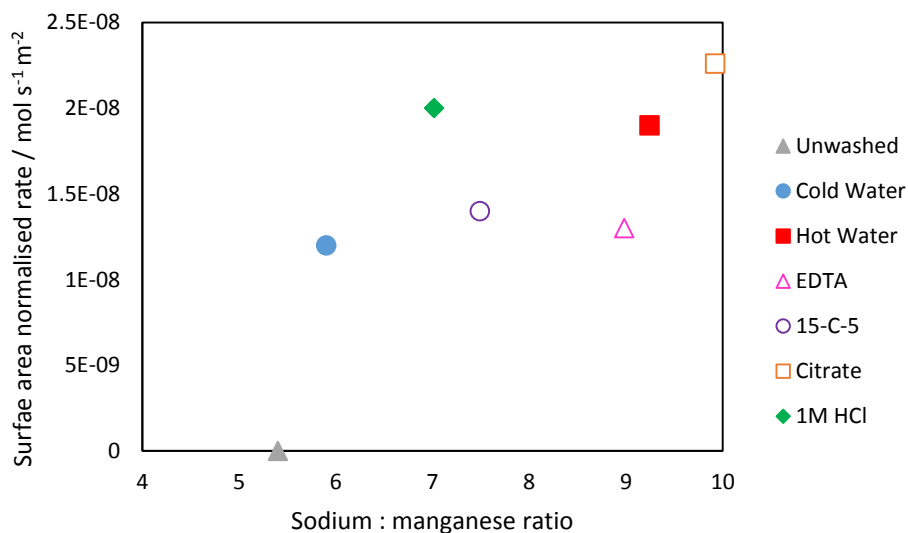

Figure 100: Surface area normalised rate against sodium to manganese ratio

6.3.8   Conclusions

The above work demonstrates that using appropriate chelating agent solutions to remove sodium from hopcalite catalysts can result in an appreciable increase in activity. This increase in activity has clearly been shown to be the result of superior removal of sodium by the citric acid solution as compared with cold water. The catalyst with most similar activity to the citrate is the sample washed in 80 °C water, however as solubility scales with temperature it is reasonable to infer that a citric acid solution at 80 °C would remove even more sodium from the material.

The aim of this initial study was to remove sodium without affecting the copper to manganese ratio of the catalysts as this was determined to be detrimental in the first study discussed in this chapter. This clearly has not been achieved with the decrease in Cu: Mn ratio upon washing with any of the chelating agent solutions. Even the sample washed in 15-crown-5, which is known to selectively chelate sodium [7], resulted in a net reduction in the manganese levels of the catalyst.

What is clear is that sodium content on the surface is an important factor with catalysts with low Na^+ concentrations on the surface outperforming those with high Na^+ concentration. It is apparent that the appropriate use of chelating agents in washing solutions can remove more sodium than water alone and as result lead to catalysts with higher activity whist avoiding environmentally problematic nitrate waste. Further work should be focused on investigating the effect of washing with larger volumes of chelating agents in order to bring the Na^+ levels down lower still. Testing of the hot chelating solutions should also be performed alongside synthesising sodium free catalysts[12] and doping sodium back onto the surface of the material to investigate the effect of sodium poisoning further.

6.4 References

[1]   G.J. Hutchings, A.A. Mirzaei, R.W. Joyner, M.R.H. Siddiqui, S.H. Taylor, Catal. Lett. 42 (1996) 21-24.
[2]   C. Jones, K.J. Cole, S.H. Taylor, M.J. Crudace, G.J. Hutchings, Journal of Molecular Catalysis A: Chemical 305 (2009) 121-124.
[3]   A.A. Mirzaei, H.R. Shaterian, R.W. Joyner, M. Stockenhuber, S.H. Taylor, G.J. Hutchings, Catalysis Communications 4 (2003) 17-20.
[4]   D.M. Whittle, A.A. Mirzaei, J.S.J. Hargreaves, R.W. Joyner, C.J. Kiely, S.H. Taylor, G.J. Hutchings, Physical Chemistry Chemical Physics 4 (2002) 5915-5920.
[5]   B. Bems, M. Schur, A. Dassenoy, H. Junkes, D. Herein, R. Schlögl, Chemistry – A European Journal 9 (2003) 2039-2052.
[6]   J. Heisler, P.M. Glibert, J.M. Burkholder, D.M. Anderson, W. Cochlan, W.C. Dennison, Q. Dortch, C.J. Gobler, C.A. Heil, E. Humphries, A. Lewitus, R. Magnien, H.G. Marshall, K. Sellner, D.A. Stockwell, D.K. Stoecker, M. Suddleson, Harmful Algae 8 (2008) 3-13.
[7]   S.-Y. Lin, S.-W. Liu, C.-M. Lin, C.-h. Chen, Analytical Chemistry 74 (2002) 330-335.
[8]   P. Porta, G. Moretti, M.L. Jacono, M. Musicanti, A. Nardella, Journal of Materials Chemistry 1 (1991) 129-135.
[9]   G.J. Hutchings, A.A. Mirzaei, R.W. Joyner, M.R.H. Siddiqui, S.H. Taylor, Applied Catalysis A: General 166 (1998) 143-152.
[10]   Handbook of Chemistry and Physics, 73 ed., Chemical Rubber Publishing Company, 1993.
[11]   G. Fortunato, H.R. Oswald, A. Reller, Journal of Materials Chemistry 11 (2001) 905-911.
[12]   H. Einaga, A. Kiya, S. Yoshioka, Y. Teraoka, Catalysis Science & Technology 4 (2014) 3713-3722.

Conclusions and future work

7.1 Conclusions

7.1.1 Use of copper manganese oxide catalysts for the total oxidation of naphthalene.

The work presented in chapter 3 on the total oxidation of naphthalene using hopcalite catalysts demonstrates their utility in this application. A calcination temperature of 400 °C was found to be the optimum temperature for total conversion of naphthalene to CO_2. Lower calcination temperatures resulted in a higher temperature of conversion while higher temperature gave rise to incomplete oxidation and partial oxidation products.

Doping with gold did not improve the naphthalene oxidation activity of the catalysts; low loadings served to reduce the activity of the catalysts. The reason for this is possibly the large size of the gold particles observed. SEM imaging clearly showed large agglomerations of gold which are known to be chemically inert.

Doping with silver, on the other hand, improved the activity of the catalysts. The increased activity of the silver containing catalysts was attributed to their increased reducibility. The silver species in these materials are unidentified at this time, however the lowering of the temperature at which reduction begins with addition of silver suggests that the reducibility of the catalysts is key for the total oxidation of naphthalene.

7.1.2 Mechanochemical synthesis of copper manganese oxide

Copper manganese oxide catalysts were prepared by a mechanochemical grinding method from oxide, acetate and carbonate precursors.

Of the three methods investigated, the use of copper hydroxycarbonate and manganese carbonate resulted in the most active catalysts. After 72 h of grinding, a single-phase copper manganese oxide phase was prepared. This resulted in the highest CO oxidation activity of the catalysts prepared. The single $CuMn_2O_4$ phase was produced as a result of Cu^{2+} migration into the lattice of the $MnCO_3$, allowing the facile formation of the active $CuMn_2O_4$ phase upon calcination[1]. This was observed using XRD to monitor the contraction of the $MnCO_3$ unit cell as a result of the Cu^{2+} incorporation.

The other materials prepared from oxides and acetates suffered from low surface area and phase separation, resulting in materials that did not have high CO oxidation activity despite formation of the $CuMn_2O_4$ phase.

7.1.3 Precipitation of copper manganese oxide catalysts from non-aqueous media

The investigation into precipitating copper manganese oxide catalysts from pure alcohol mixtures illustrated that catalysts precipitated from water were superior for CO oxidation to the catalysts prepared from ethanol and propanol. The catalyst precipitated from propanol had especially low activity. This was the result of low surface area as a consequence of sintering of the catalyst upon calcination.

Precipitation from the butanol-water mixture gave a material that was less active per gram than the water precipitated catalyst.   When the surface area normalised rate was calculated the activity of the butanol precipitated catalyst was comparable with the water precipitated catalyst. The high activity was a result of the exceptionally low sodium content of this material[2].

7.1.4 The effect of washing on copper manganese oxide catalysts

Washing the copper manganese oxide precursor with 6 L of boiling water was found give the most active catalysts for CO oxidation. Washing with less than this amount led to catalysts that were less active due to Na^+ poisoning[2]. Washing with more than 6 L

resulted in a drop in activity, despite the Na^+ concentration continuing to decrease. This was found to be the result of a loss of manganese from the materials and the disruption of the copper manganese redox couple.

Washing with chelating agents was found to have varying levels of effectiveness. Washing with oxalic acid, for example, prevented the catalysts from exhibiting any activity, whereas washing with citric acid increased the activity when compared with water. The increase in activity was related to the decreasing levels of Na^+ in the catalyst and as such the aim of reducing sodium content was realised. However more work is required to fully investigate this area.

7.2 Future work

In terms of the effectiveness of hopcalite as a naphthalene oxidation catalyst, more research is required into the effect of doping on the activity of the catalyst. In terms of the gold containing catalysts work should focus on identifying the reason why gold addition, whilst proven to beneficial for the total oxidation of other volatile organic compounds, was not beneficial for naphthalene oxidation. One possible reason is the phase separation of the materials; this could be combatted by modifying the preparation conditions[3]. For the catalysts containing silver there should be a focus on identification of the active silver species in the catalyst. The characterisation techniques used in this thesis could not identify the species, however transmission electron microscopy or X-ray absorbtion spectroscopy such as XAFS or XANES could be beneficial in identifying the active species.

The mechanochemical preparation of hopcalite has scope to be expanded further. In terms of using oxide precursors, the use of manganese species in different oxidation states could be a fruitful line of enquiry. Specifically the use of Mn_3O_4, which has the same crystal structure as $CuMn_2O_4$, should be investigated. The preparation using carbonates should be investigated further; the effects of longer grinding times than investigated in this work is an

area that should be investigated. This could lead to more Cu^{2+} incorporation into the precursor and more facile formation of the $CuMn_2O_4$ phase. Another route for synthesis that should be investigated is the use of a reduced metal in the mechanochemical grinding. It has previously been shown that this can lead to the more facile formation of mixed metal oxides than using oxidised materials alone[4].

Precipitating copper manganese oxide from n-butanol should be investigated further as it was as active in terms of activity per square meter as catalysts precipitated from water. If surface area could be maintained at the level found in the water precipitated materials then a highly active material could be synthesised. As the TGA analysis suggests that thermal decomposition of this material began at a temperature below that at which it was calcined, this could be potentially achieved by altering the calcination conditions to a lower temperature.

The work on washing the catalysts with water and chelating agents has many potential avenues to pursue. Principally to fully identify the role of sodium in inhibiting CO oxidation on hopcalite catalysts, sodium free materials should be synthesised and then poisoned by the addition of Na^+ to them[5]. Coupled with techniques such as FT-IR CO chemisorption to study the adsorbtion of CO to the catalyst, and temporal analysis of products to gain mechanistic insight, this could allow study into the poisoning mechanism. In terms of the study of the effects of chelating agents, study of heated solutions of the agents along with more concentrated solutions should be undertaken to maximise Na^+ removal and potentially improve activity.

7.3 References

[1]   P. Porta, G. Moretti, M.L. Jacono, M. Musicanti, A. Nardella, Journal of Materials Chemistry 1 (1991) 129-135.
[2]   A.A. Mirzaei, H.R. Shaterian, R.W. Joyner, M. Stockenhuber, S.H. Taylor, G.J. Hutchings, Catalysis Communications 4 (2003) 17-20.
[3]   G.J. Hutchings, A.A. Mirzaei, R.W. Joyner, M.R.H. Siddiqui, S.H. Taylor, Applied Catalysis A: General 166 (1998) 143-152.

[4]   S.L. James, C.J. Adams, C. Bolm, D. Braga, P. Collier, T. Friscic, F. Grepioni, K.D.M. Harris, G. Hyett, W. Jones, A. Krebs, J. Mack, L. Maini, A.G. Orpen, I.P. Parkin, W.C. Shearouse, J.W. Steed, D.C. Waddell, Chemical Society Reviews 41 (2012) 413-447.
[5]   H. Einaga, A. Kiya, S. Yoshioka, Y. Teraoka, Catalysis Science & Technology 4 (2014) 3713-3722.